Calcium nanodomains at spindles

Guolong Mo

Thesis submitted to the University of Ottawa

in partial Fulfillment of the requirements for the

Doctor of Philosophy

in Biochemistry

Department of Biochemistry, Microbiology, and Immunology

Faculty of Medicine

University of Ottawa

There are two ways to break a nut. One is to put the cutting edge of the chisel against the shell and strike hard. The other, is simply immersing the nut in some softening liquid. When the time is ripe, the shell opens like a perfectly ripened avocado.

Alexander Grothendieck

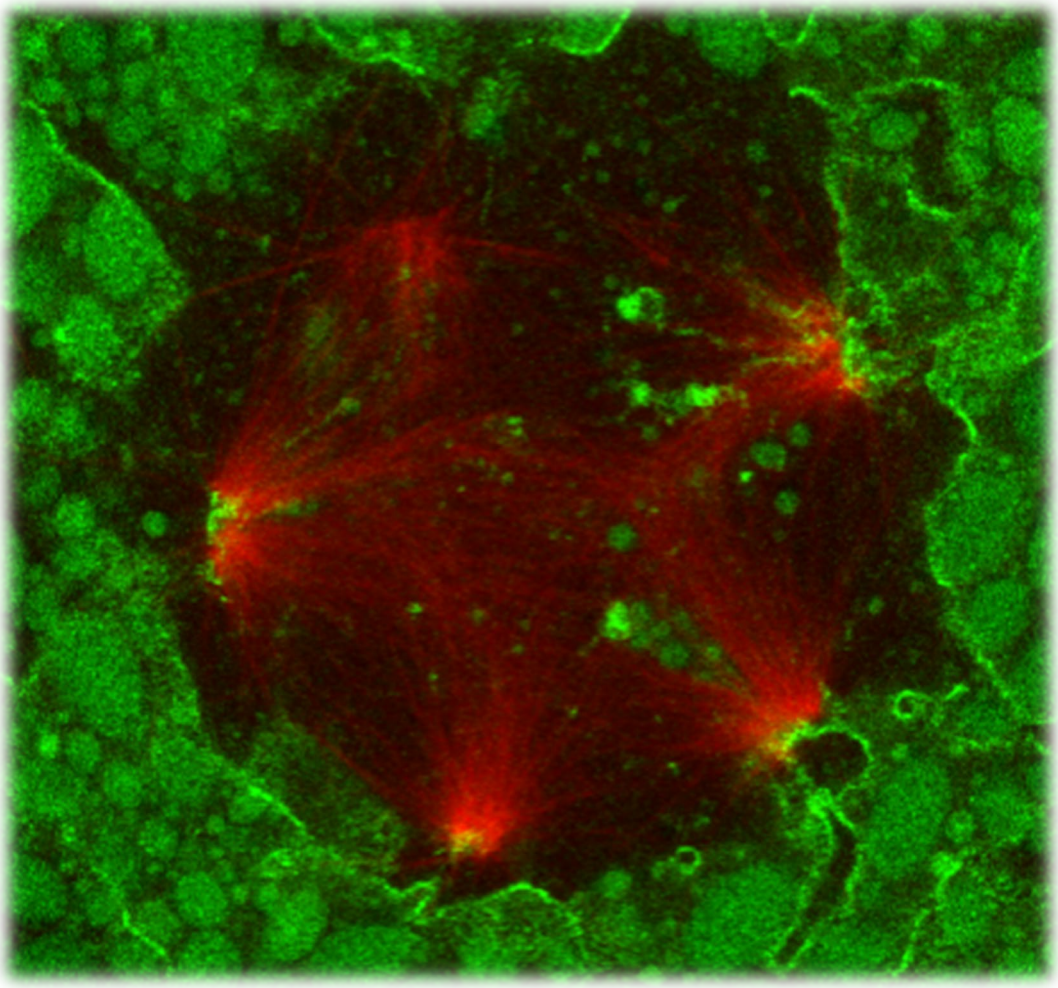

Abstract

The spindle apparatus is arguably the most important organelle in cell division. Despite the comprehensive characterization of microtubule regulatory proteins and protein complexes in the past decades, we are still far from being able to reconstitute a functional spindle using purified components. One important question remaining unanswered is whether calcium signaling participates in spindle assembly. Calcium signaling is involved in cell division but is thought to be dispensable for spindle assembly, mainly because excessive EGTA (ethylene glycol-bis(β-aminoethyl ether)-N,N,N',N'-tetraacetic acid) is present in the popular *in vitro* spindle assembly system – *Xenopus* egg extracts. However, a recent report showed that injection of the fast calcium chelator 1,2-bis(o-aminopheyoxy)ethane-N,N,N',N'-tetraacetic acid (BAPTA), but not the slow chelator EGTA, causes rapid depolymerization of spindle microtubules in *Xenopus* oocytes. Differential sensitivity to BAPTA is the defining characteristic of highly restricted, or nanodomain Ca^{2+} signaling, best known to function in presynaptic neurotransmitter release. However, no local Ca^{2+} signals have been identified to be functionally linked to spindle assembly.

In this project, a novel microtubule-binding calcium sensor, TubeCamp1 (TC1), was designed to test the hypothesis that spindles are associated with calcium nanodomains. Consistent with the hypothesis, confocal imaging with TC1 revealed microtubule-proximal calcium increase at the spindle poles in *Xenopus* oocytes and HeLa cells. Calcium nanodomains also formed in spindles assembled *in vitro* and at the center of monoastral spindles, suggesting that they are a general feature of spindle assembly. Disruption of nanodomain calcium signaling, via rapid chelation of calcium or perturbation of inositol-1,4,5-

trisphosphate pathway, resulted in rapid spindle disassembly in intact oocytes and in oocyte extracts. These results demonstrate the existence of spindle-associated calcium nanodomains and suggest that such domains are an important and common feature of spindles in vertebrates.

In addition, a Ca^{2+} transient was identified during polar body emission in *Xenopus* oocytes by using a novel ratiometric probe Tubecamp4 (TC4) and mobile probes Oregon Green-2 and -6f. A close examination of its spatiotemporal pattern with membrane-targeted probes revealed that the Ca^{2+} transient was associated with polar body abscission whereby the polar body is separated from the oocyte, suggesting a role of Ca^{2+} in ensuring the correct number of chromosomes and proper division of cytoplasm.

Collectively, these results expand our knowledge in highly localized Ca^{2+} control of spindle assembly and cell cycles, providing new angles for understanding disease pathology and drug intervention.

Acknowledgement

First and foremost, I want to thank my advisor Dr. X. Johné Liu. I appreciate all his contributions of time, ideas and feedback that help me accomplish my Ph.D. project. He has taught me, both consciously and unconsciously, how an all-around idea is proposed and how a good experiment is designed and performed. More importantly, he provides me with an excellent role model who is a scientist with endless energy, enthusiasm and perseverance in his research.

The lab members of Liu's group have contributed a lot to my personal and professional time in Ottawa. The group has been a source of friendships as well as good advice and collaboration. I appreciate the great help from Ms. Ruizhen Li, our lab technician and manager. As a project member, she provided remarkable academic and technical assists and we performed some crucial experiments together. As a senior and friend, she supported me through the ups-and-downs of my years in Ottawa. I also appreciate, and more importantly salute Dr. Yong Tao. Although never being formally appointed, Yong was regarded as my mentor during his time in Liu's lab. He was always the person I turned to whenever I wanted to discuss and share ideas with. I would also like to express my utmost gratitude to the other lab members. Dr. Dandan Liu, a bright and smart lady who taught and influenced me deeply when I first came to the Liu's Lab. We worked closely to publish a paper as co-first authors (Liu et al., 2017). Christopher Lavergne, a helpful, positive and easy-going buddy who was never too tired to cheer me up whenever my mood was down. Dr. Hua Shao, a wise and sophisticated gentleman who guided me with invaluable perspectives and shed light on my academic life and future career path. And of course, our dear administrative assistant, Ms.

Terri van Gulik, helped me greatly with the thesis proofreading and was always ready to listen to me.

Apart from my lab members, several external personnel provided significant support to my research. Special thanks to Dr. William Bement and Mr. Zachary Swider, who contributed useful tools and data to this project (Specifically, results in **III.2.2**) and offered great suggestions and discussions. I thank Dr. Chloë van Oostende-Triplet and Ms. Skye McBride from CBIA core of uOttawa (Cell Biology and Image Acquisition core) for their assistance and advice in operating the Spinning disk and Airyscan microscopy systems. I also thank my thesis advisory committee (TAC), Dr. Jay Baltz, Dr. Douglas Gray, Dr. John Copeland, for their constructive criticisms and illuminating suggestions to improve my project.

I am grateful to all my sponsors: China Scholarship Council, University of Ottawa and my supervisor. Their generous help makes it possible for my living and study in Ontario.

I would also like to appreciate my friends Dr. Yuefeng Li, Dr. Chao Ma, Mr. Runtian Hou, Dr. Zijie Huang, Mr. Weixin Ding, Mr. Wenqi Qian, Dr. Yumao Zhang, Dr. Dandan Wang, Dr. Xiongyi Huang and Dr. Xu Zhang for their encouragement and support in all aspects of my graduate years.

And at last, I thank my parents for all their love and devotion along the way.

Table of Contents

ABSTRACT ..... **III**
ACKNOWLEDGEMENT ..... **V**
TABLE OF CONTENTS ..... **VII**
LIST OF ABBREVIATIONS ..... **XI**
LIST OF FIGURES ..... **XIV**
LIST OF TABLES ..... **XV**
CHAPTER I GENERAL INTRODUCTION **1**
I.1 OOCYTE MATURATION IN *XENOPUS LAEVIS* 4
I.1.1 Prophase I arrest and resumption 4
I.1.2 Spindle assembly and organization in metaphase I 9
I.1.2.1 Four steps towards a metaphase spindle 9
I.1.2.2 Spindle microtubule organization: molecular aspects 10
I.1.2.3 Meiotic spindle pole formation and bipolarization 16
I.1.3 Anaphase I and polar body emission 19
I.1.3.1 Anaphase I spindles are characteristic of homologous chromosome separation and active depolymerization of microtubules 19
I.1.3.2 Molecular trigger of anaphase I onset 20
I.1.3.3 Polar body emission 22
I.1.4 Metaphase II arrest and exit 26
I.1.4.1 Molecular mechanism of metaphase II arrest 26
I.1.4.2 Fertilization breaks metaphase II arrest by a sweeping Ca^{2+} wave 27
I.2 CALCIUM NANODOMAINS IN SPINDLE REGULATION 28
I.2.1 Ca^{2+} signaling is required for oocyte maturation 28
I.2.2 Spindle collapse is caused by fast rather than slow Ca^{2+} chelators 30
I.2.3 Understanding nanodomain Ca^{2+} coupling by EGTA/BAPTA tests 37
I.2.3.1 A lesson from squids 37
I.2.3.2 A problem for visualization 40
I.2.4 Rationale for nanodomain Ca^{2+} signaling at spindles 41
I.3 PROBING CELLS WITH CA^{2+} INDICATORS 42
I.3.1 Bioluminescent Ca^{2+} indicators 43

I.3.2 Small-molecule organic Ca^{2+} indicators 44
I.3.3 Genetically encoded Ca^{2+} indicators (GECIs) 46
I.4 HYPOTHESIS AND OBJECTIVES 49
CHAPTER II METHODOLOGY 51
II.1 *XENOPUS LAEVIS* HANDLING AND OOCYTE PREPARATION 51
II.2 CONSTRUCTING GENETICALLY ENCODED CALCIUM PROBES 52
II.2.1 Tubecamp1（TC1, EMTB-GCaMP3） 52
II.2.2 Tubecamp4 (TC4, mCherry-EMTB-GCaMP3) 53
II.2.3 Plasmid DNA and mRNA preparation 54
II.2.4 Nucleic acid verification 55
II.3 MICROINJECTION METHODS 56
II.3.1 Equipment and operations 56
II.3.2 Artificial egg activation 56
II.4 CONFOCAL MICROSCOPY SYSTEMS AND IMAGE PRESENTATION 57
II.5 IMAGING SPINDLES IN *XENOPUS* OOCYTES 61
II.6 ASSEMBLING SPINDLES IN CELL EXTRACTS FROM A SINGLE OOCYTE 62
II.7 PHOTOLYSIS EXPERIMENTS 63
II.8 HELA CELL METHODS 65
II.9 IMMUNOFLUORESCENCE PROTOCOL FOR *XENOPUS OOCYTES* 66
II.10 OTHER REAGENTS 67
II.10.1 Organic Ca^{2+} probes 67
II.10.2 Plasmids 67
II.10.3 Primary Antibodies 69
II.10.4 Chemicals and organelle probes 69
II.11 STATISTICS 71
II.12 ARTWORKS 72
CHAPTER III PROBING SPINDLE-BASED CA^{2+} SIGNALS 73
III.1 INTRODUCTION 73
III.2 RESULTS 74
III.2.1 Constructing microtubule-tethered Ca^{2+} reporter TC1 74
III.2.2 Testing TC1: $[Ca^{2+}]_i$ elevation during wound healing 77
III.2.3 Probing spindle-based Ca^{2+} signal by TC1 and OG-2 in *Xenopus* oocytes 80

III.2.3.1 TC1 reports distinct Ca^{2+} signal at the spindle poles 80
III.2.3.2 TC1 reports spindle-based $[Ca^{2+}]_i$ elevation during egg activation 84
III.2.3.3 OG-2 reports diffuse Ca^{2+} signal at the spindle 87
III.2.4 TC1 reports distinct Ca^{2+} signals at monoastral poles 90
III.2.5 TC1 reports distinct Ca^{2+} signals at spindle poles in oocyte extracts 93
III.2.6 TC1 reports distinct Ca^{2+} signals at spindle poles in HeLa cells 97
III.3 DISCUSSION 100
III.3.1 Recap of the results 100
III.3.2 Pole-specific TC1 signals suggest that localized Ca^{2+} signaling is spatiotemporally correlated to spindle assembly in meiosis and mitosis 100
III.3.3 Relations between pole-specific $[Ca^{2+}]_i$ elevation and calcium nanodomains 102
III.3.4 Limitations 103
CHAPTER IV EXPLORING CALCIUM NANODOMAINS AT SPINDLES 105
IV.1 INTRODUCTION 105
IV.2 RESULTS 107
IV.2.1 Calcium nanodomains are required for spindle assembly in *Xenopus* oocyte-based systems 107
IV.2.1.1 DB-BAPTA causes rapid collapse of spindles in Xenopus oocyte extracts 107
IV.2.1.2 BAPTA causes fast depolymerization of monoastral spindles 111
IV.2.1.3 BAPTA attenuates the growth of spindle microtubules and inhibits bipolar formation in intact oocytes 112
IV.2.2 Evidence of ER's role in maintaining spindle integrity 113
IV.2.2.1 Spindles assembled in extracts are in close contact with ER 113
IV.2.2.2 Disruption of ER is accompanied by spindle disassembly 114
IV.2.3 IP_3Rs are required for spindle function 117
IV.2.3.1 IP_3Rs are concentrated at spindle poles 117
IV.2.3.2 Spindle-associated IP_3Rs are responsible for Ca^{2+} release 120
IV.2.3.3 IP_3R inhibitor causes spindle collapse 121
IV.2.4 Potential targets of nanodomain Ca^{2+} signaling 124
IV.2.4.1 Calmodulin is associated with Xenopus oocyte spindles 124

IV.2.4.2 Calcium nanodomain protects spindle microtubules by attenuating GTP-hydrolysis dependent depolymerization 127
IV.3 DISCUSSION 128
IV.3.1 Recap of the results 128
IV.3.2 ER-IP_3R based Ca^{2+} signaling at spindles 129
IV.3.3 Limitations 132
CHAPTER V CA^{2+} TRANSIENTS DURING POLAR BODY EMISSION 134
V.1 INTRODUCTION 134
V.2 RESULTS 136
V.2.1 Constructing TC4: a ratiometric Ca^{2+} reporter based on TC1 136
V.2.2 TC4 reports transient $[Ca^{2+}]_i$ elevation during polar body emission 140
V.2.3 OG-2 and OG-6f report asymmetric Ca^{2+} transient during polar body emission 144
V.2.4 Transient accumulation of PKCβ C2 at the intercellular bridge 147
V.3 DISCUSSION 151
V.3.1 Recap of the results 151
V.3.2 A local Ca^{2+} transient is associated with polar body abscission 151
V.3.3 Limitations 155
CHAPTER VI CONCLUSIONS AND OUTLOOK 157
VI.1 KEY DISCOVERIES 157
VI.2 IMPLICATIONS IN DISEASE PATHOLOGY AND TRANSLATIONAL MEDICINE 159
BIBLIOGRAPHY 162
APPENDIX 191
Homologous chromosome disjunction does not require Ca^{2+} signaling in *Xenopus* oocytes 191
Engagement of PLC-PIP_2-DAG pathway in spindle regulation 196
Vector information of TC1 and TC4 200
Microscopy in results 202
CONTRIBUTIONS OF COLLABORATORS 204
CURRICULUM VITAE 205

List of Abbreviations

2-APB	2-Aminoethoxydiphenyl borate
AA	Amino acid
AM	Acetoxymethyl
APC/C	Anaphase-promoting complex or cyclosome
BAPTA	1,2-bis(o-aminophenoxy)ethane-N,N,N′,N′-tetraacetic acid
BSA	Bovine serum albumin
Ca^{2+}	Cacium ion
$[Ca^{2+}]_i$	Intracellular free calcium concentration
CaM	Calmodulin
CaMKII	Calmodulin-dependent protein kinase II
cAMP	Cyclic adenosine monophosphate
CBP	Calcium buffer protein
Cdc	Cell division cycle protein
CDK	Cyclin dependent kinase
CIAP	Calf intestinal alkaline phosphatase
CMV	Cytomegalovirus
CPC	Chromosome passenger complex
cpEGFP	Circularly permutated enhanced green fluorescent protein
CSF	Cytostatic factor
DAG	Diacylglycerol
DB-BAPTA	Dibromo-1,2-bis(o-aminophenoxy)ethane-N,N,N′,N′-tetraacetic acid
DNA	Deoxyribonucleic acid
EB1	+TIP protein end binding 1
EGTA	ethylene glycol-bis(β-aminoethyl ether)-N,N,N′,N′-tetraacetic acid
EM	Electron microscope
EMTB	microtubule binding domain of ensconsin
EM-CCD	Electron multiplying – charge coupled device
ER	Endoplasmic reticulum
Erp1	Emi-related protein 1
F-actin	Filamentous actin

FBS	Fetal bovine serum
GCaMP	GFP-Calmodulin fusion protein
GECI	Genetically encoded Ca^{2+} indicators
GECO	Genetically encoded Ca^{2+} indicators for optical imaging
GFP	Green fluorescent protein
GMPCPP	Guanosine-5'-[(α,β)-methyleno]triphosphate
GTP	Guanosine triphosphate
GV	Germinal vesicle
GVBD	Geminal vesicle breakdown
IP_3(R)	Inositol-1,4,5-triphosphate (receptor)
LB	Lysogeny broth
Lck	Lymphocyte-specific protein tyrosine kinase
MAP	Microtubule-associated protein
MAPK	Mitogen-activated protein kinase
MCC	Mitotic checkpoint complex
MPF	Maturation promoting factor or M-phase promoting factor
MT	Microtubule
MTOC	Microtubule organization center
M13	M13 fragment of myosin light chain kinase
NPB buffer	Nuclear preparation buffer
NuMA	Nuclear mitotic apparatus protein
OCM	Oocyte culture medium
OG-2	Oregon Green BAPTA-2
Cdc2	cell division cycle protein 2
Ran	Ras-related nuclear protein
PBS	Phosphate-buffered saline
PCR	Polymerase chain reaction
PIP_2	Phosphatidylinositol 4,5-bisphosphate
PLC	Phospholipase C
Plk-1	Polo-like kinase 1
PKA	Protein kinase A
PKC	Protein kinase C

PMSG	Pregnant mare's serum gonadotropin
PtK cells	Potorous tridactylus kidney cells
RCC1	Regulator of chromosome condensation 1
RGECO	Red genetically encoded Ca^{2+} indicators for optical imaging
RyR	Ryanodine receptor
SAC	Spindle check point
SCF	Skp, Cullin, F-box containing complex
$SCF^{\beta\text{-}TRCP}$	SCF complex related to β-transducin repeat-containing protein
sfGFP	Super folded green fluorescent protein
SNR	Signal to noise ratio
STIM1	Stromal interaction molecule 1
TBS(T)	Tris buffered saline (plus Triton X-100)
TC	TubeCamp (probes fused microtubule-binding domain to GCaMP)
TIRF	Total internal reflection fluorescence
TMA	Transient microtubule array
TPEN	N,N,N′,N′-tetrakis(2-pyridinylmethyl)-1,2-ethanediamine
UV	Ultraviolet

Constant

K_d	Dissociation constant
K_{on}	Binding rate/association rate/on rate
K_{off}	Disassociation rate/off rate

List of Figures

Figure I.1 Oogenesis and oocyte maturation in Xenopus laevis 6

Figure I.2 Metaphase spindle assembly in *Xenopus* oocytes or oocyte extracts 12

Figure I.3 Anaphase I and polar body emission in *Xenopus* oocytes 24

Figure I.4 BAPTA/EGTA tests in understanding nanodomain Ca^{2+} coupling 33

Figure II.1 Methods for image presentation, *in vitro* spindle assembly and UV-photolysis ..59

Figure III.1 Schematic representation of TC1 production and working principle 75

Figure III.2 TC1 reports microtubule-proximal $[Ca^{2+}]_i$ during oocyte wound healing 78

Figure III.3 TC1 signals at spindles during oocyte maturation 82

Figure III.4 TC1 reports spindle-based $[Ca^{2+}]_i$ elevation during egg activation 85

Figure III.5 OG-2 signals during oocyte maturation 88

Figure III.6 TC1 signals at monoastral spindles 91

Figure III.7 TC1 signals during spindle assembly in cell extracts 95

Figure III.8 TC1 signals in HeLa cells 98

Figure IV.1 BAPTA's intervention in *Xenopus* oocyte-based systems 109

Figure IV.2 ER membranes are associated with spindle microtubules 115

Figure IV.3 Spindles are associated with functional IP_3Rs 118

Figure IV.4 Heparin intervention causes spindle collapse 122

Figure IV.5 Potential targets of Ca^{2+} nanodomain signaling 125

Figure V.1 TC4: a ratiometric Ca^{2+} reporter 138

Figure V.2 TC4 reports transient local $[Ca^{2+}]_i$ elevation 142

Figure V.3 Asymmetric $[Ca^{2+}]_i$ rise during polar body emission 145

Figure V.4 Transient recruitment of PKCβ C2 at the intercellular bridge 149

Figure V.5 Schematic representation of polar body abscission (theory) 153

Figure S1 Karyotyping *Xenopus* oocytes after DB-BAPTA treatment 194
Figure S2 Engagement of PLC-PIP_2-DAG pathway in spindle regulation.....197
Figure S3 Detailed vector maps of TC1 and TC4.....200
Figure S4 Visualization of the making of TC1 and TC4 in details.....201

List of Tables

Table I.1 DB-BAPTA *vs.* EGTA *vs.* TPEN intervention with the 1st polar body emission....35
Table I.2 Kinetics of Ca^{2+} buffers 36
Table S1 Microscopy in the results.....202

Chapter I General Introduction

Cell division, a process whereby a cell replicates by dividing itself, is a fundamental element of life (Koshland, 2002). In eukaryotic cells, there are two different kinds of cell divisions: *Mitosis* whereby two daughter cells possess the same amount of chromosome copies as the parent nucleus or *meiosis* whereby daughter cells have reduced copies (Ohkura, 2015). In both scenarios, *spindle apparatus* is arguably the most important organelle that mainly consists of chromosomes, microtubules and hundreds of regulating proteins. It plays a central role in eukaryotic cell division, ensuring the proper segregation of chromosomes and cytoplasm (Lee et al., 2012). On the other hand, spindle dysfunction could lead to serious consequences such as division failure or aneuploidy — the presence of incorrect chromosome numbers in cells (Potapova and Gorbsky, 2017). The clinical implication of spindle dysfunction in reproductive cells includes infertility, miscarriage and birth defects (Nagaoka et al., 2012). In somatic cells, spindle dysfunction significantly contributes to carcinogenesis and hence is a common characteristic of cancer cells (Simonetti et al., 2019; Stumpff et al., 2014).

Although the initial discovery of spindle apparatus can be traced back to 1873 by German zoologist Friedrich Anton Schneider, for more than 100 years people were merely watching its behaviors in the dividing cell like a marionette show, without grasping the underlying molecular mechanisms. The first functional model, *i.e.* “search and capture”, was only proposed three decades ago, which described the spindle as dynamic microtubule machinery undergoing frequent turnover to target and arrange chromosomes (Heald and Khodjakov, 2015; Kirschner and Mitchison, 1986). Today this model still dominates the field with much more

defined details. More than 800 proteins and 100 complexes have been identified to be associated with spindles, and several molecular pathways that account for spindle assembly and the fidelity of chromosome segregation are established (Hutchins et al., 2010; Sauer et al., 2005). While the list of proteins involved in spindle assembly is considered to be close to complete, the exact roles of these molecules and how they cooperate to shape and maintain spindles are still poorly understood (Gache et al., 2010; Oriola et al., 2018; Wuhr et al., 2014).

Our project is inspired by one specific problem that has remained elusive for decades: *to what extent does calcium signaling contribute to spindle assembly?* Historically, it has long been considered that Ca^{2+} signaling is not required for spindle assembly. In 1972, people had already known that microtubule formation is sensitive to high calcium concentration (~1.5–10 mM) in bulk solution: "The formation of microtubules is strongly inhibited by calcium ions" (Weisenberg, 1972). This was later confirmed in living organisms where injection of large amounts of Ca^{2+} (~1–10 mM) into echinoderm mitotic cells induces spindle microtubule depolymerization (Kiehart, 1981). In mammalian fibroblasts and epithelial cells, an increase of Ca^{2+} concentration during mitosis is thought to induce microtubule depolymerization leading to anaphase initiation (Tombes and Borisy, 1989). In *Xenopus* egg extracts, adding 600 μM Ca^{2+} causes depolymerization of spindle microtubules, which is however dependent on the activation of calmodulin-dependent kinase II (CaMKII) but not direct actions of calcium ions on microtubules (Reber et al., 2008). Therefore, excess amount of calcium chelator, EGTA (ethylene glycol-bis(β-aminoethyl ether)-N,N,N′,N′-tetraacetic acid), is routinely used for *in vitro* spindle assembly studies to maintain metaphase spindles (Field et al., 2017; Good and Heald, 2018; Hannak and Heald, 2006).

On the other hand, emerging evidence shows calcium regulation is extensively involved in the events during cell division including CDK (cyclin-dependent kinase) activation, nuclear envelope breakdown, metaphase checkpoints and anaphase regulation (Humeau et al., 2018). With improved techniques, discrete but localized calcium signals can be detected in syncytial *Drosophila* embryos (dividing nuclei/chromosomes within a common cytoplasm), although their involvement in general cell types remains far from clear (Whitaker, 2006b). Numerous studies reported that reduction or depletion of intracellular calcium has negative impacts on the spindle shape and size in both mitosis and meiosis (Groigno and Whitaker, 1998; Sun et al., 2008; Xu et al., 2003). Notably, a recent study suggested that exquisite spatial regulation of Ca^{2+}, rather than that at a global scale, might be at work (Li et al., 2016).

However, there is still a lack of reports that demonstrate highly localized calcium at the spindles, or associated complexes, that accounts for spindle assembly and maintenance. It is probably due to (1) lack of interest and motivation in the scientific community for a long time, as the conventional Ca^{2+} chelator EGTA has no effects on spindle assembly; (2) global calcium changes cannot be consistently detected during the cell cycle across species (FitzHarris et al., 2005; Whitaker, 2006b) and (3) the technical difficulties in revealing calcium signals at a proper spatiotemporal fashion (Augustine et al., 2003; Parry et al., 2005; Tay et al., 2012). We will discuss and attempt to address these questions mainly within *Xenopus* oocyte-based systems.

Our introduction will be organized into three main sections. First, the physiology of *Xenopus* oocytes (the major cellular model in our study) will be introduced with an emphasis on the functions of the spindle apparatus (**I.1**). Second, the possible involvement of Ca^{2+}

signaling in spindle assembly will be discussed (**I.2**). Finally, various calcium probes and their application in cell cycles will be briefly reviewed (**I.3**).

I.1 Oocyte maturation in *Xenopus laevis*

Xenopus oocytes have long been considered one of the best single cell models to study Ca^{2+} signaling, mainly for their convenience, robustness and being a faithful expression system and functional architecture (Lin-Moshier and Marchant, 2013). In this section, we will introduce the process of oocyte maturation and the contexts for spindle functions. In this thesis, "oocyte maturation" refers to a period during which oocytes progress through meiosis I and arrest at metaphase of meiosis II, resulting in reproductively competent eggs that are ready for fertilization and new life cycles (Yamashita et al., 2000). Some literature refer to the same period as "oocyte meiotic maturation".

I.1.1 Prophase I arrest and resumption

Oocyte meiosis is a special type of cell division whereby a primary oocyte divides two rounds without an intervening S-phase, resulting in 2–3 small cells (polar bodies) and a large oocyte containing half the original amount of genetic information (Yamashita et al., 2000). A primary oocyte of *Xenopus laevis* begins as a tiny cell at the regular somatic cell size (**Figure I.1A**). Following DNA duplication where sister chromatids bound by cohesin come into shape, the oocyte enters first meiotic prophase (prophase I, or G_2-like phase)[1]. Prophase I is the longest phase of meiosis and can be categorized into several substages based on the status of

[1] The Roman number (I or II) indicates the ordinal of meiosis. Despite calling the prophase in the first meiosis "prophase I", there does not exist a "prophase II" since the chromosomes do not change back to nucleus during the transition of two meiosis.

chromosomes: *leptotene*, *zygotene*, *pachytene* and *diplotene* (**Figure I.1A',** see figure legends). At the time prophase I initiates, the pairing of homologous chromosomes occurs and synaptonemal complexes are formed to bind homologous chromosomes (**Figure I.1A'**). Paired homologous chromosomes exchange genetic information via homologous recombination. This leads to physical crossovers at the chromosomal arms (**Figure I.1A'**). The oocyte arrests at the *diplotene* substage for months up to 3 years[2], where most of the synaptonemal complexes degrade and the homologous chromosomal arms begin to repel each other (**Figure I.1A'**) (Jessus et al., 2020). During prophase I, the yolk proteins accumulate in the cytoplasm. Depending on the size and morphology, prophase I oocytes can be classified into stage I to VI (**Figure I.1A**, see figure legend for development details). A stage VI oocyte is giant with a diameter of ~1.4 mm (**Figure I.1A**). In this full-grown oocyte, the enlarged nucleus, namely *germinal vesicle* (GV), reaches a diameter of ~400 μm, residing at the animal hemisphere of the *Xenopus* oocyte (Ferrell, 1999; Rasar and Hammes, 2006). The stage VI oocyte (or GV oocyte) is widely believed to be held at prophase I by cyclic AMP-dependent protein kinase A (PKA) activity. In this oocyte, constitutively active G protein-coupled receptors (GPCRs) such as GPRx (mammalian GPR3 equivalent) disassociate and release active G protein subunits $G_s\alpha$ and $G\beta\gamma$ that stimulate adenylate cyclase and thereby raise the cytoplasmic cyclic AMP (cAMP) concentration (**Figure I.1B**, prophase I arrest) (Deng et al., 2008; Rios-Cardona et al., 2008; Sheng et al., 2001).

[2] To compare, *Xenopus laevis* can survive ~15-20 years in the wild and 25-30 years in captivity.

Figure I.1 Oogenesis and oocyte maturation in *Xenopus laevis*

(A) Cartoons illustrate oogenesis at stage I to VI. Stage I: Transparent and roughly 50–300 μm in diameter. Stage II: White and 300–450 μm in diameter. Stage III: Pigmentation begins and becomes dark brown and 450–600 μm in diameter. Stage IV: Pigment polarizes, and animal (brown) and vegetal spheres (white) appear. 600–1000 μm in diameter. Stage V: Pigment fades to light brown and animal sphere is distinct from vegetal sphere. 1000–1200 μm in diameter. Stage VI: A white equatorial band is formed. The diameter is about 1.4 mm. The increasing sizes are mainly attributable to yolk accumulation in the cytoplasm. Parameters are from Rasar and Hammes, 2006.

(A') Schematic representation of chromosome morphogenesis during prophase I. Following DNA replication, sister chromatids form and are bound by cohesins. Homologous chromosomes are paired in early prophase I (*leptotene*) and gradually bound by synaptonemal complexes (*zygotene*). Homologous chromosomes exchange genetic information by homologous recombination between non-sister chromatids, where a physical crossover is formed (*pachytene*). Stage VI oocytes (or GV oocytes) arrest at the *diplotene* stage of prophase I where synaptonemal complexes partially degrade and homologous chromosome arms begin to repel each other.

(B) Schematic representation of prophase I arrest and release.

Prophase I arrest: High cAMP and PKA activities hold the oocyte at prophase by inhibiting the MPF activity and the protein synthesis of c-mos and cyclin B1. Cytosolic cAMP concentration is raised by activation of G-protein-responsive adenylyl cyclase, as a result of constitutive activities of GPCRs. The binding of cAMP to the regulatory subunits of PKA tetramers (inactive PKA) leads to the release and activation of catalytic subunits of PKA which subsequently inhibit the polyadenylation of c-mos and cyclin B1 mRNA, and thereby keep pre-MPF inactive.

Prophase I release: Meiosis I resumes by the action of progesterone through a nongenomic mechanism. Progesterone activates mPR and iPR which inhibit the G-protein-responsive adenylyl cyclase, leading to the inhibition of cAMP-dependent PKA activity. In the absence of PKA activity, c-mos and cyclin B1 are translated due to the polyadenylation of the corresponding mRNAs. Newly synthesized cyclin B1 binds to the pre-existing monomeric Cdc2 and thereby form a small pool of active-MPF that catalyzes the pre-MPF (cyclin B2/p-Cdc2) in an auto-amplification way. Meanwhile, c-mos triggers the ultrasensitive MAPK pathway that activates a wide array of proteins including Cdc25 that in turn activate pre-MPF by dephosphorylating p-Cdc2. Active-MPF ultimately triggers GVBD.

(C) A set of schematics shows **(a)** the progression of oocyte morphology, **(b)** cell cycle regulators, **(c)** spindle morphogenesis and **(d)** microtubule attachment to chromosomes during oocyte meiotic maturation. Hours in **(b)** indicate time after GVBD.

(a) A GV oocyte is stimulated by progesterone. 3–5 hours after progesterone addition, a large white GVBD spot takes shape at the animal pole. Roughly 1 hour after GVBD (prometaphase I), a tiny white spindle spot appears inside the GVBD spot, where a spindle is attached (underneath the cortex). Following the onset of anaphase I (~2 hour after GVBD), the GVBD spot shrinks while the spindle spot stays unchanged in terms of size. At metaphase II (~3 hour after GVBD), GVBD spot disappears and the spindle spot is circumscribed by a black-pigmented ring.

(b) The blue curve represents cytosolic APC/C/Cdc20 activity while the red curve represents cytosolic MPF/cyclin-B activity (Liu, 2012). Note that the patterns are different from typical mitosis or meiosis. At GVBD, both APC/C and MPF activities are peaked. Following GVBD, while APC/C activity stays unchanged, MPF activity gradually reduces and reaches lowest roughly 1 hour after GVBD (prometaphase I). Shortly prior to anaphase I, MPF activity returns to the peak while APC/C activity decline. These changes persist through metaphase II. MPF activity and APC/C inactivation are needed for metaphase II arrest.

(c)&(d) Inside a GV oocyte, GV isolates *diplotene* chromosomes from cytoplasm. Progesterone incubation causes oocyte GVBD where the synaptonemal complexes completely degrade and kinetochores assemble on the centromeres. Following GVBD, TMA forms and captures the chromosomes by attaching TMA microtubules to the kinetochores. In prometaphase (~1 hour after GVBD), a short bipolar spindle is formed and attached to the cortex in a paralleled fashion. The spindle grows and rotates to the position perpendicular to the cortex, where the oocyte reaches metaphase I. The metaphase I spindle continuously grows and elongates while the configuration of chromosomes aligns to a plane that is equidistant from two poles. During anaphase I (~2 hours after GVBD), paired homologous chromosomes are separated by the release of cohesins around the chromosome arms (at crossover) and the shortening of interpolar microtubules. Meanwhile, plasma membranes contacted with the spindle pole protrude and eventually become a polar body attached to the oocyte containing one set of separated homologous chromosomes. Anaphase I ends within ~15 minutes. Metaphase II oocyte (~3 hours after GVBD) has a smaller spindle with sister chromatids attached to bi-oriented kinetochore microtubules.

Figure I.1 Oogenesis and oocyte maturation in *Xenopus laevis*

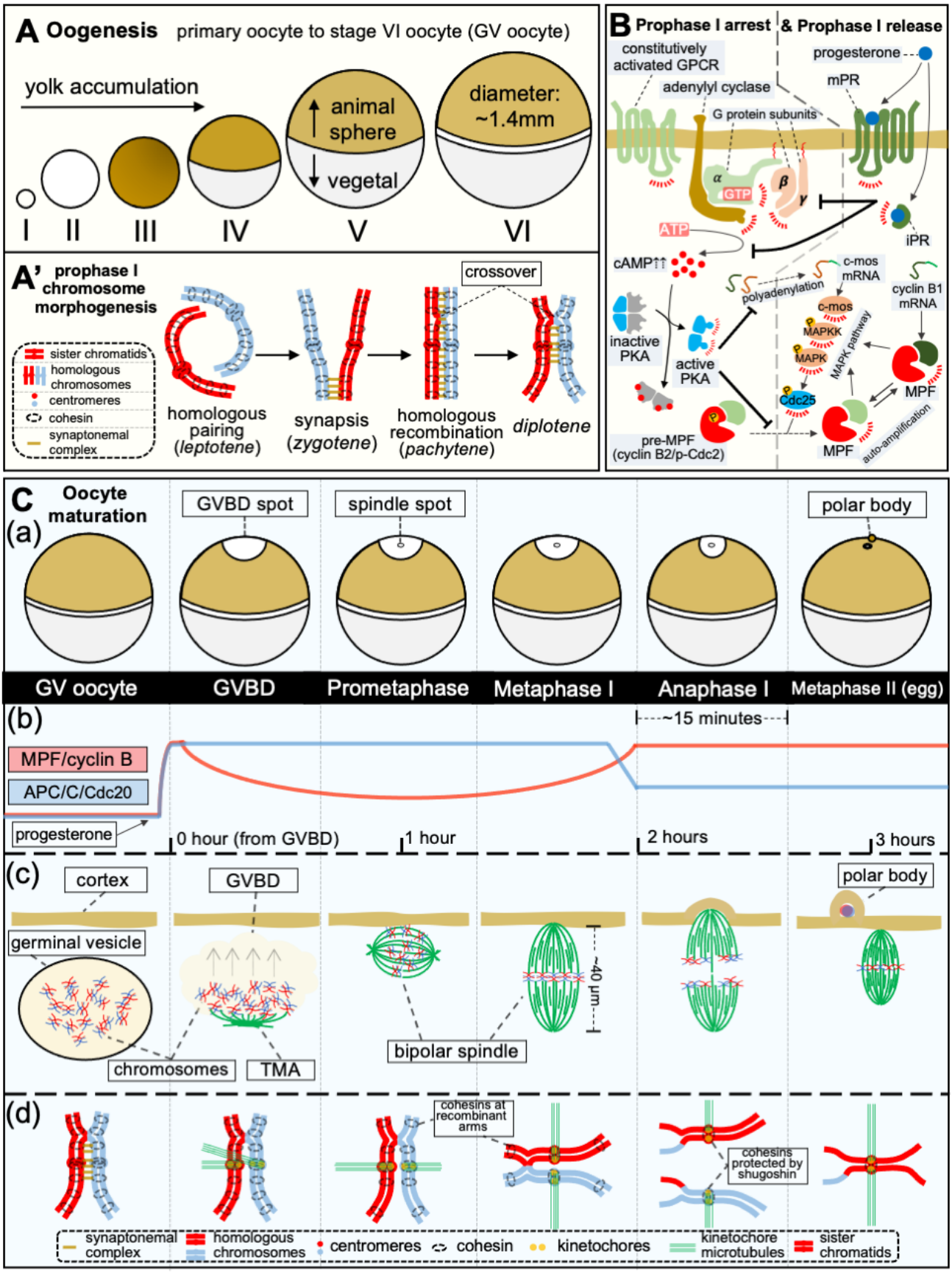

The resumption of meiosis is triggered by progesterone, produced by the follicle cells that surround the oocyte in response to pituitary-derived gonadotropic hormones. Progesterone activates both the intracellular progesterone receptor (iPR, a nuclear receptor) in the cytosol and the membrane progesterone receptor β (mPRβ, a GPCR) on the oocyte surface, and then oocyte maturation is initiated through transcription-independent mechanisms (**Figure I.1B**, prophase I release) (Bayaa et al., 2000; Josefsberg Ben-Yehoshua et al., 2007; Liu et al., 2005). The activation of progesterone receptors inhibits G protein-responsive adenylate cyclase, leading to a rapid drop of cAMP level and a subsequent inhibition of PKA activity (Sheng et al., 2001; Wang and Liu, 2004). Two key proteins — c-mos and cyclin B1 — are then synthesized following the polyadenylation of their mRNAs (Bayaa et al., 2000; de Moor and Richter, 1999; Mendez et al., 2000). The functional pathways underlying these two proteins are mutually promoted; microinjection of either protein alone into progesterone-free GV oocytes is sufficient to activate maturation-promoting factor (MPF) or cyclin B/Cdc2 complex, the universal cell cycle driver responsible for a wide range of protein phosphorylation (Haccard and Jessus, 2006). An inactive form of MPF — pre-MPF or cyclin B2/p-Cdc2 (Tyr-15 phosphorylated) — exists before progesterone stimulation. After stimulation, newly synthesized cyclin B1 binds to the cytosolic monomeric Cdc2 and forms a small pool of active-MPF, which causes auto-amplification of active-MPF by activating several phosphatases including Cdc25 that dephosphorylate the Tyr-15 site of the p-Cdc2 subunit of pre-MPF (Dupre et al., 2013; Karaiskou et al., 1999; Nebreda et al., 1995). In parallel, c-mos, as the mitogen-activated protein kinase kinase kinase (MAPKKK) of oocytes[3], triggers the highly

[3] In somatic cells, the major MAPKKK is also involved in *Xenopus* oocyte maturation, but the activation of MAPK by c-mos is independent of Raf (Shibuya, 1996).

sensitive MAPK cascade, leading to MAKP activation that in turn activates cyclin B2/p-Cdc2 through the actions of intermediate phosphatases (**Figure I.1C.b,** cyclin B/Cdc2 activity arises) (Ferrell and Machleder, 1998; Huang and Ferrell, 1996; Kosako et al., 1994; Shibuya et al., 1996). The active MPF induces germinal vesicle breakdown (**Figure I.1C.c**, GVBD, the term for oocyte version of nuclear envelope breakdown). GVBD is easy to score under a dissecting microscope because the rearrangement of cortical pigment granules results in an obvious white spot on the animal pole, a.k.a. GVBD spot (**Figure I.1C.a**, GVBD spot). At this stage, chromosomes and nuclear materials are in contact with cytoplasmic factors, leading to the assembly of the spindle apparatus.

I.1.2 Spindle assembly and organization in metaphase I

I.1.2.1 Four steps towards a metaphase spindle

In a classical paper, Gard categorizes the metaphase I spindle assembly into four significant steps: (1) Formation of microtubule organization center (MTOC) and transient microtubule array (TMA) with chromosomes, and the subsequent relocation of MTOC-TMA to the cortex of the animal pole; (2) reorganization of MTOC-TMA into a short bipolar spindle; (3) rapid growth and elongation of the spindle; (4) rotation of the spindle to be aligned with the oocyte animal-vegetal axis (Gard, 1992). **Figure I.1C.c** illustrates these steps (elongation and rotation occur simultaneously). Over the years, while this classification still holds, more evidence and molecular mechanisms have been added to our knowledge.

Coincident with GVBD, a disk-shaped MTOC-TMA is assembled in response to nucleoplasm materials releasing (**Figure I.1C.c**, GVBD). The MTOC-TMA captures the homologous chromosome pairs while translocating to the animal cortex with the assistance of

filamentous actins (F-actins) (Gard et al., 1995; Yamagishi and Abe, 2015, 2018). Thereafter, the MTOC-TMA gradually transforms into a short, bipolar meiotic spindle (Gard, 1992; Shao et al., 2012). This transformation is usually accomplished around 30 minutes to 1 hour after GVBD. The nascent bipolar spindle is initially paralleled to the oocyte surface (**Figure I.1C.c**, prometaphase). Thereafter, the spindle gradually rotates, eventually to an orientation perpendicular to the oocyte surface around 1.5 hours after GVBD, with one pole attached to the cortex (Gard, 1992; Li et al., 2016; Shao et al., 2012). There are two groups of microtubules at this stage[4]: (i) Kinetochore microtubules that attach the homologous chromosome pairs to spindle poles in a bi-orientational way. The kinetochore is a disc-shaped protein complex that consists of tens of proteins assembled on the centromere of chromosomes (**Figure I.1C.d**) (Musacchio and Desai, 2017). (ii) Short non-kinetochore microtubules (constitute 90%–95% of the spindle microtubule as estimated) that co-bundle with kinetochore microtubules (Mitchison, 2005; Oriola et al., 2018). The spindle continuously grows and elongates while the configuration of chromosomes gradually aligns to a plane that is equidistant from two poles (**Figure I.1C.c** metaphase I). Metaphase I typically ends ~2 hours after GVBD and the oocytes are ready for anaphase I where homologous chromosome pairs separate (**Figure I.1C.c**, anaphase I).

I.1.2.2 Spindle microtubule organization: molecular aspects

The metaphase spindle is a highly dynamic structure that keeps self-rebuilding. Our knowledge of spindle microtubule dynamics is mainly from spindles assembled in *Xenopus*

[4] In mitosis and some cases of meiosis, there is an extra class called astral microtubules that emanate away from spindle poles. In our studies, the metaphase spindles in intact *Xenopus* oocytes or oocyte extracts are anastral, as we will see in the subsequent chapters.

egg extracts, but the principles hold at both metaphase I and II in intact oocytes. If not specified, most studies described in this section are conducted in *Xenopus* egg extracts.

Microtubules are hollow tubes composed of spirally polymerized α/β-tubulin heterodimers. The asymmetry of the heterodimer leads to distinct biochemical characteristics at different ends of a microtubule: a fast-growing plus end (crowned by β-tubulin) and a slow-growing minus end (crowned by α-tubulin). The GDP- or GTP-bound β-tubulins at microtubule ends are the molecular switches of microtubule polymerization: A cap of GTP-bound tubulins favours growth (or rescue) while GDP-bound tubulins are prone to shrink rapidly (or catastrophe). That the microtubule ends stochastically switch between growth and rapid shrinkage is termed as dynamic instability (**Figure I.2A**, dynamic instability) (Brouhard and Rice, 2018).

Microtubule dynamic instability is harnessed within spindle apparatus; individual microtubules exhibit a cooperative movement to exert forces that arrange chromosomes and shape the bipolar structure. Sawin and Mitchison reported that, by using photoactive tubulins, locally activated tubulins move coherently from the spindle midzone to spindle poles (and then disappear) at a rate of 3 μm/min, a.k.a. microtubule poleward flux (Sawin and Mitchison, 1991). Spindle microtubule poleward flux is thought to consist of two different mechanisms: (i) Kinetochore microtubules undergo net polymerization at the spindle midzone (plus ends) and net depolymerization at spindle poles (minus ends) (Sawin and Mitchison, 1991). (ii) short, non-kinetochore microtubules slide towards poles by motor proteins; their minus ends are found to be relatively stable and the turnover rates are determined by the dynamic instability at their plus ends. Whereas the lifetime of kinetochore microtubules is about 5 minutes, the average lifetime of individual microtubules is only ~16 seconds (Needleman et al., 2010).

Figure I.2 Metaphase spindle assembly in *Xenopus* oocytes or oocyte extracts
A figure illustrates a metaphase I spindle of *Xenopus* oocytes and associated mechanisms in the thumbnail cartoons. MT stands for microtubule.
(A) Cartoons illustrate mechanisms involved in spindle microtubule dynamics and nucleation.
Dynamic instability: Microtubules are assembled by polymerizing α/β-tubulin heterodimers. Individual microtubule can switch between a growth (or rescue) state and a rapid shrinkage state (catastrophe). A GTP-bound tubulin cap is required for microtubule growth while GDP-bound tubulins at the microtubule end facilitate microtubule catastrophe.
Ran-GTP gradient: A Ran-GTP gradient is formed around the chromosome by the activity of RCC1(Regulator of chromosome condensation 1) locates at the chromosome converting Ran-GDP into Ran-GTP. Ran-GTP releases importin binding proteins that promote spindle assembly.
Aurora B activity: Aurora B is part of CPC (chromosome passenger complex) that primarily locates at the centromere. It phosphorylates proteins such as MCAK (mitotic centromere-associated kinesin) to stabilize microtubules near chromosomes.
(B) A schematic illustrates a metaphase I spindle. The spindle poles are where microtubule minus ends converge. Kinetochore microtubules are long microtubules that connect the kinetochores on the centromeres to the spindle poles. Short, non-kinetochore microtubules constitute the majority of spindle microtubules.
(C) Cartoons illustrate mechanisms involved in spindle pole formation and bipolarization.
Pole organization: Microtubule minus ends are sorted and focused with the help of dynein. NuMA is able to recruit dynein and crosslink microtubule minus end at the spindle pole.
Antiparallel crosslink: Antiparallel microtubules (mostly at the spindle midzone) are crosslinked by plus end motor protein kinesin-5 to keep a bidirectional configuration.
Kinetochore orientation: In meiosis II, Aurora B activity regulates kinetochore biorientation by phosphorylation of Ndc80 complex through a tension system (see main texts). In meiosis I, Aurora B activity helps to establish bipolarity through uncharacterized meiosis I-specific targets in *Xenopus* oocytes.
(D) Schematics illustrate the consequences if the mechanisms in **(C)** are undermined. At metaphase spindles, inhibition of dynein leads to an unfocused structure with bidirectional microtubules alignment while inhibition of kinesin-5 results in a monopolar structure (monoastral spindle). However, double inhibition of kinesin-5 and dynein makes a microtubule-focused structure with mixed ends at the focused directions. These phenotypes suggest the bipolar structure of spindles is closely associated with the balance of kinesin-5 and dynein activities.

Figure I.2 Metaphase spindle assembly in *Xenopus* oocytes or oocyte extracts

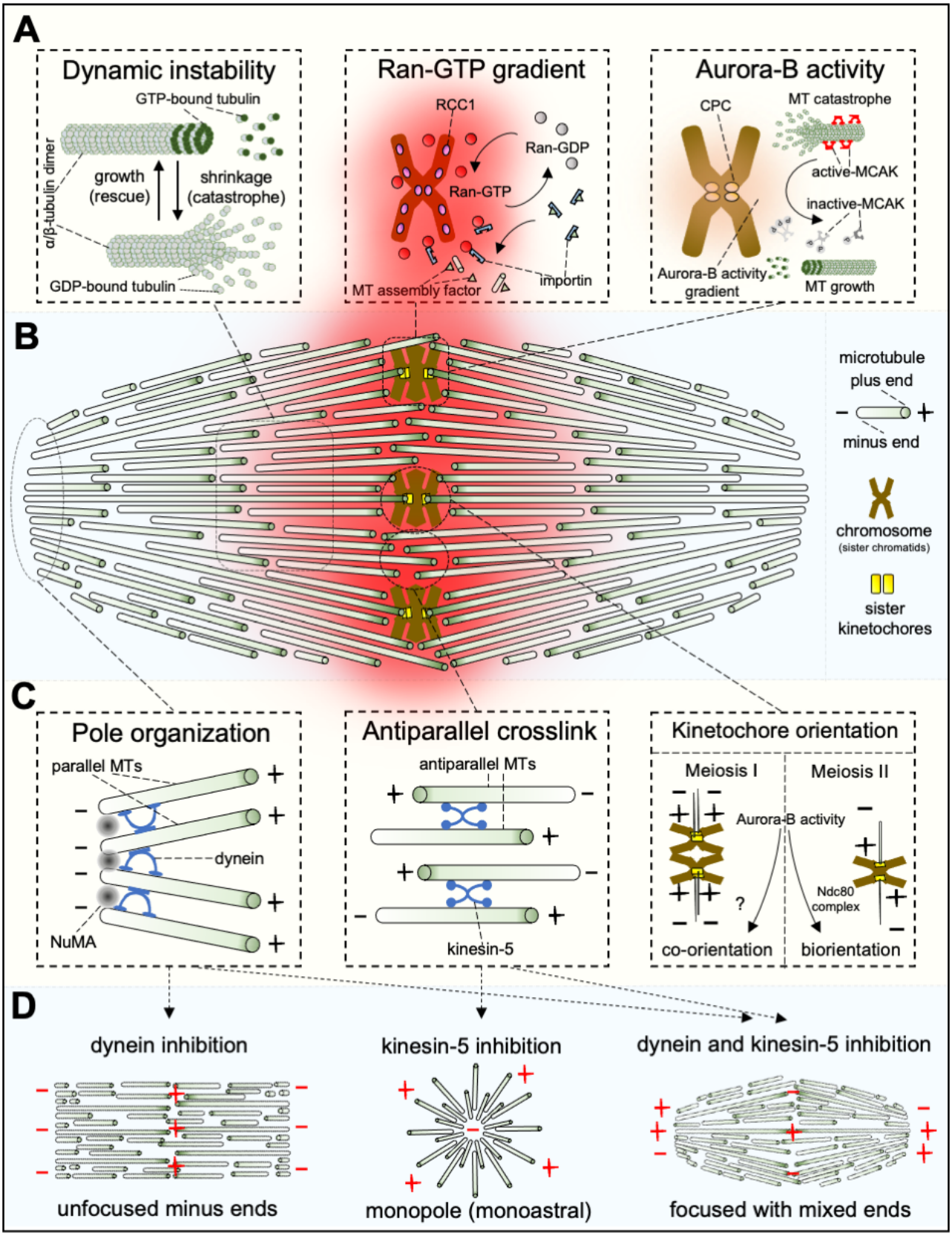

Given their highly dynamic and ever-renewing nature, how do spindle microtubules assemble and maintain around chromosomes, but not elsewhere in the oocyte cytoplasm? The prevailing view is that spatial gradients of microtubule nucleators are generated and extended from chromosomes, assembling microtubules *de novo* from α/β-tubulin subunits (*i.e.* microtubule nucleation) (Oriola et al., 2018). A classical experiment showed that adding plasmid DNA-coated beads (artificial chromosomes) into *Xenopus* egg extracts leads to bipolar spindle formation, suggesting an important role for DNA in the spatial control of spindle apparatus (Heald et al., 1996). Two chromosome-based signals turn out to be crucial to spindle assembly: Ran-GTP gradients and Aurora B activities (Fuller, 2010).

Ran (Ras-related nuclear protein) is a small nuclear G protein that can be bound to GDP (inactive form) or GTP (active form). Depletion of Ran-GTP distorts and destabilizes spindle microtubules (Kalab et al., 2002). Further investigation revealed that Ran-GDP is first recruited around the chromosomes by regulator of chromosome condensation 1 (RCC1, a protein that directly recognizes histone 2A and binds to nucleosomes) (Carazo-Salas et al., 1999; Halpin et al., 2011; Hondele and Ladurner, 2010). RCC1 converts Ran-GDP into Ran-GTP, resulting in an important reaction-diffusion gradient (a.k.a. Ran-GTP gradient) around chromosomes (**Figure I.2A**, Ran-GTP gradient). The Ran-GTP gradient attracts nucleocytoplasmic transport receptors — importins — that bind to the spindle assembly factors such as TPX2 (targeting protein for Xklp2) and NuMA (nuclear mitotic apparatus protein). These importin-binding molecules are released by Ran-GTP hydrolysis (**Figure I.2A**, Ran-GTP gradient). Consequently, downstream reactions for microtubule nucleation, polymerization and organization are initiated (Kalab and Heald, 2008). TPX2/Aurora A signaling is one of the best characterized Ran-GTP dependent pathway for spindle assembly.

TPX2 activity is inhibited when bound to importin. Ran-GTP-mediated hydrolysis releases TPX2 which recruits Aurora A serine/threonine kinase, promoting Aurora A autophosphorylation (Thr295 in *Xenopus laevis*) by inducing conformational change of its catalytic domain (Dodson and Bayliss, 2012; Eyers et al., 2003). The locally activated Aurora A in turn phosphorylates and thereby activates γ-tubulin ring complex, the major microtubule nucleator —— an anchor and template for α/β-tubulin dimer polymerization (Magnaghi-Jaulin et al., 2019; Pinyol et al., 2013). Aside from TPX2/Aurora A, tens of proteins related to spindle assembly have also been identified as Ran-GTP-dependent; characterizing molecular pathway and function of Ran-GTP regulating proteins is still an ongoing work (Alfaro-Aco et al., 2017; Helmke and Heald, 2014; Kapoor, 2017).

The second crucial signal originated from chromosomes for spindle assembly is Aurora B activity. This signal is generated by Aurora B serine/threonine kinase which is a part of the chromosome passenger complex (CPC) located at chromosome centromeres (**Figure I.2A**, Aurora B activity). Researchers have shown that, in the absence of Ran-GTP gradients, localized CPC activity can still induce spindle assembly in the vicinity of chromosomes, though the exact mechanisms are poorly characterized (Krenn and Musacchio, 2015; Maresca et al., 2009). Some reports suggested that Aurora B kinase stimulates microtubule assembly by phosphorylating and thereby deactivating microtubule catastrophe factors such as MCAK (mitotic centromere-associated kinesin) and Op18/Stathmin[5] (**Figure I.2A**, Aurora B activity) (Gupta et al., 2013; Kelly et al., 2007; Lan et al., 2004). MCAK, also known as kinesin-13, is

[5] Op18/Stathmin is a robust microtubule depolymerizer mainly acting on the minus-end (spindle pole). It can bind and destabilize nascent α/β-tubulin dimers (Gupta et al., 2013).

a motor protein that can target both microtubule plus ends and minus ends to induce depolymerization efficiently (Strothman et al., 2019). MCAK has multiple phosphorylation sites; a recent study showed that Aurora B kinase phosphorylation can reduce depolymerase activity of MCAK at graded levels (McHugh et al., 2019).

I.1.2.3 Meiotic spindle pole formation and bipolarization

In animal mitosis, spindle poles are organized by centrosome, an amorphous structure containing a pair of centrioles plus pericentriolar materials that promote spindle microtubule organization. The two centrioles separate to organize different poles, assuming the dominant microtubule organization centers (MTOCs) for microtubule anchoring (Prosser and Pelletier, 2017). Animal oocyte meiosis, however, lacks centrosome control: Meiotic spindle poles — the regions where microtubule minus ends are converged — are not organized by a single, predefined organelle (Ohkura, 2015). In mouse oocytes, tens of small MTOCs (>80) are clustering during spindle pole formation, which can be easily specified under optical microscopy (Schuh and Ellenberg, 2007). MTOCs of mouse oocytes contain pericentriolar material components of centrosomes, such as γ-tubulin ring complex, but lack of centriole cores (Clift and Schuh, 2015). On the other hand, the oocyte meiotic pole formation in some species (*e.g.* humans, *Xenopus*, *Drosophila* and *C. elegans*), where discrete MTOCs are not as distinct as those in mouse oocytes, is thought to largely rely on the activities of microtubule-associated proteins that can be classified into motor proteins or non-motor proteins (Bennabi et al., 2016). Studies in *Xenopus* egg extracts suggested that several motor proteins, dynein in particular, shape meiotic poles by sorting and focusing the microtubule minus ends (**Figure I.2C**, pole organization) (Heald et al., 1996; Walczak et al., 1998). Furthermore, the non-motor protein NuMA cross-links the parallel microtubules (in the same orientation), promoting the

bundling of microtubule minus ends in the polar region (**Figure I.2C**, pole organization) (Gehmlich et al., 2004; Merdes et al., 1996). Correspondingly, microinjection of dynein or NuMA antibody into *Xenopus* oocytes generates abnormal spindles (monopolar, multipolar, or scattered microtubules) at metaphase I (Becker et al., 2003).

In meiosis I of *Xenopus* oocytes, Shao *et al.* have shown the bidirectional sorting of Aurora A, as a MTOC marker, from multi-foci into a bipolar fashion, reminiscent of the transformation from the MTOC-TMA into a bipolar spindle (see **I.1.2.1**). However, the mechanism underlying this bidirectional sorting, *i.e.* meiotic spindle bipolarization, remains poorly understood. Some authors argue that the bipolar structure of the spindle may be determined by the relative balance of minus-end motor dynein that sorts microtubules at the spindle poles and plus-end motor kinesin-5 that cross-links the antiparallel microtubules at the spindle midzone (**Figure I.2C**, pole organization and antiparallel crosslink) (Oriola et al., 2018). This idea is illustrated in **Figure I.2D** and supported by a series of experiments. At the metaphase spindles assembled in *Xenopus* egg extracts, (i) inhibition of dynein activity (by adding excessive p50 subunits of dynamitin or p150 subunits of dynactin) leads to a unfocused, flag-like structure (**Figure I.2D**, dynein inhibition) (Brugues et al., 2012; Mitchison et al., 2005); (ii) inhibition of kinesin-5 (by adding small molecule inhibitor monastrol) results in a monopolar structure (or monoastral spindle) (**Figure I.2D**, kinesin-5 inhibition) (Brugues et al., 2012; Mitchison et al., 2005); (iii) surprisingly, inhibition of both dynein and kinesin-5 makes a bipolar structure, but the "poles" are converged by mixed ends rather than minus ends only (**Figure I.2D**, dynein and kinesin-5 inhibition) (Brugues et al., 2012; Mitchison et al., 2005). In addition to the action of motor proteins, many lines of evidence suggested that chromosome factors also contribute to spindle bipolarity. In meiosis II, kinetochore

microtubules that are bound to the same pair of sister chromatids align in an antiparallel manner (in opposite directions), due to the biorientation of the kinetochores on centromeres of sister chromatids (a.k.a. sister kinetochores) (**Figure I.2C**, kinetochore orientation). What controls the orientation of kinetochores? It is suggested that the chromosome passenger complex (CPC) associated with kinetochores is the major player; an tension system located at the CPC regulates the biorientation of sister kinetochores through the interaction of Aurora B with the Ndc80 complex — a protein complex that directly attaches microtubule plus ends to kinetochores (Welburn et al., 2010). Specifically, when kinetochores sense low tension (unidirectional pulling), Aurora B will become spatially close to the microtubule ends, hence Aurora B phosphorylates several microtubule-binding sites including the Ndc80 complex, leading to loss of the affinity of kinetochores to microtubules (unstable attachment). By contrast, kinetochores that sense high tension (bidirectional or antiparallel pulling) reduce phosphorylation by Aurora B, increasing the affinity of kinetochores to microtubules (stable attachment) (Welburn et al., 2010). In meiosis I, it is however the co-orientation of sister kinetochores that favors the antiparallel alignment of kinetochore microtubules and thereby overall spindle bipolarity (**Figure I.2C**, kinetochore orientation). The mechanism of sister kinetochore co-orientation at meiosis I of animal oocytes is largely unknown. In budding yeast, the kinetochore co-orientation is mediated by meiosis-I-specific monopolin complexes to bind sister kinetochores (Plowman et al., 2019); however, the monopolin equivalent has not been reported yet in animal oocytes. In *Xenopus* oocytes, Aurora B is found to regulate spindle bipolarity by stabilizing chromosome-associated microtubules in meiosis I, though the exact mechanism is not clear (Shao et al., 2012). This suggests Aurora B activity is important to establish bipolarity in both meiosis I and II (**Figure I.2C**, kinetochore orientation). Altogether,

it is likely the coordination of the motor proteins and chromosome factors that establishes the meiotic spindle bipolarity.

I.1.3 Anaphase I and polar body emission

I.1.3.1 Anaphase I spindles are characteristic of homologous chromosome separation and active depolymerization of microtubules

About 2 hours after GVBD, oocytes transition from metaphase I to anaphase I where homologous chromosomes separate (**Figure I.1C.c**, anaphase I). Anaphase I spindles in *Xenopus* oocytes share some common molecular mechanisms with those in mitotic cells. Cohesin (a ring-shaped protein complex) that wraps around the sister chromatids at chromosome arms are removed (but not cohesins at centromeres which are protected by a protein called shugoshin [6] in meiosis I), resulting in the separation of homologous chromosomes and loss-of-tension at the kinetochore microtubules (**Figure I.1C.d**) (Kudo et al., 2006; Maddox et al., 2003). Individual homologous chromosomes are pulled toward each pole by the shortening kinetochore microtubules (Shao et al., 2012). It is suggested that two main factors that account for the shortening of kinetochore microtubules during anaphase: (i) the pre-existing microtubule poleward flux caused by continuous depolymerization at the spindle poles (see **I.1.2.2**); (ii) the active microtubule depolymerization at kinetochores by the activation of microtubule catastrophe factors around centromeres (Maddox et al., 2003). Meanwhile, a few anti-parallel interpolar microtubules elongate, generating cooperative pushing force to separate the chromosome pairs (FitzHarris, 2012). At late anaphase I, a polar

[6] Protection of cohesin by shugoshin at centromeres in anaphase I is the most crucial difference from mitotic and meiosis II anaphase where the cohesins are completely removed (Ohkura, 2015).

body that protrudes from the oocyte surface comes into shape containing half of the homologous chromosomes, whereas the remaining spindle microtubules are reorganized into a thin and long shape that connects two sets of separated chromosomes. The transient structure (mostly consists of the reorganized spindle microtubules) that connects the oocyte and the polar body is called the midbody which is thought to be the signaling hub for cytokinesis regulation (Hu et al., 2012; Maddox et al., 2012). It usually takes about 15 minutes from the initiation of anaphase I to the completion of the first polar body emission (**Figure I.1C.c** anaphase I) (Zhang et al., 2008).

I.1.3.2 Molecular trigger of anaphase I onset

The molecular trigger of *Xenopus* oocyte anaphase I is largely unknown. In this section, we will first introduce the molecular trigger at canonical anaphase, and then compare it to that of *Xenopus* oocytes.

In mitosis and some cases of meiosis, the spindle assembly checkpoint (SAC) is thought to be the major mechanism that controls anaphase onset (Alfieri et al., 2016). During metaphase, the SAC surveillance mechanism determines the proper attachment of chromosomes to the poles to ensure the correct segregation of homologous chromosomes (in meiosis I) or sister chromatids (in meiosis II or mitosis) (Alfieri et al., 2016; Liu, 2012). The entity of SAC is an active signal generated at the kinetochore. The signal consists of a heterogeneous protein complex, *i.e.* mitotic checkpoint complex (MCC). MCC can bind to Cdc20, an activator subunit of the anaphase-promoting complex or cyclosome (APC/C) (Sudakin et al., 2001). Before proper alignment of all chromosomes, MCC deactivates APC/C by competitively binding Cdc20 and serving as a pseudo-substrate (Hwang et al., 1998; Kim et al., 1998). Once kinetochore microtubules are adequately attached to the chromosomes in a

bipolar fashion, the MCC is disassembled and Cdc20 is released to activate APC/C (Liu and Zhang, 2016; Pinsky and Biggins, 2005). APC/C is an E3 ubiquitin ligase that controls the degradation of several metaphase-maintaining proteins including cyclin B, leading to MPF inactivation (Chang et al., 2003; Chang et al., 2015). APC/C also leads to securin destruction in securin-separase complexes, resulting in separase release and activation. Separase then removes the cohesin at chromosome arms (meiotic anaphase I) or centromeres (meiotic anaphase II or mitotic anaphase), making it possible for kinetochore microtubules to pull chromosomes apart (Brar et al., 2006; Challa et al., 2019; Salic et al., 2004).

In *Xenopus* oocytes, APC/C activation (manifested by cytosolic Cdc20 levels) and cyclin B degradation occur immediately after GVBD but before spindle assembly (**Figure I.1C.b**) (Shao et al., 2013; Taieb et al., 2001), which is in sharp contrast to aforementioned canonical timing of APC/C activation and cyclin B degradation (during anaphase). Further investigation revealed that neither SAC nor APC/C is mandatory for meiosis I progression. First, SAC is missing in the whole meiosis. Complete disruption of spindle assembly by nocodazole does not prevent the cyclin B degradation nor chromosome separation (Shao et al., 2013) while in mitosis both events require proper kinetochore-microtubule attachment (Gorbsky, 2015). Although lack of SAC surveillance, meiosis in *Xenopus* oocytes is not error-prone, producing few aneuploidies (Liu et al., 2014). The substitute mechanism, if any, to assure chromosome fidelity is unknown. Second, APC/C appears to be dispensable in anaphase I. Inhibition of APC/C activity or cyclin B degradation does not prevent the completion of meiosis I manifested by polar body emission (Peter et al., 2001; Taieb et al., 2001). Overall, the initiation of anaphase I is much less restricted in *Xenopus* oocytes than that in mitosis (Shao et al., 2013).

I.1.3.3 Polar body emission

Polar body emission is a specialized form of cytokinesis, where the parent cell is asymmetrically divided into a robust daughter cell (the oocyte or the egg) with half the parental chromosomes (meiosis I) or chromatids (meiosis II), and a miniature cell (polar body) (Liu, 2012). The cytoplasmic separation processes involve: (1) the protrusion of plasma membrane with the chromosomes and a small pocket of cytoplasm, (2) constriction of the connection between the polar body and the oocyte and finally (3) severing (or abscission) of the connection (Maddox et al., 2012). During these processes, membrane-bound Rho Family GTPases such as RhoA and Cdc42 play a crucial role in regulating the cytoskeleton changes such as actin nucleation. The major distinction of polar body emission from mitotic cytokinesis is the establishment of emission sites and membrane protrusion, which is led by local Cdc42 activation. The separation machinery is however much like its mitotic counterpart: A RhoA contractile ring is assembled around the emission site (or division plane in mitosis) and then constricts the plasma membrane (Zhang et al., 2008).

In *Xenopus* oocytes, the morphogenesis and the molecular mechanism of polar body emission have been extensively studied in our laboratory (**Figure I.3A**) (Leblanc, 2014; Leblanc et al., 2011; Li et al., 2016; Liu, 2012; Ma et al., 2006; Zhang et al., 2008). Following anaphase onset, Cdc42 becomes activated inside the RhoA ring and creates an actin cap over the spindle pole bound to the plasma membrane (**Figure I.3A**) (Ma et al., 2006). These two distinct GTPases, Cdc42 and RhoA, colocalize with two categories of actin filaments: (1) Cdc42 with dynamic, branching F-actin nucleated by Arp2/3 complex (a protein complex that assembles actin nucleation core) and (2) RhoA with stable, unbranched F-actin (Leblanc et al., 2011; Zhang et al., 2008). Subsequently, activated Cdc42 promotes membrane protrusion

while the RhoA ring constricts the "neck" (or intercellular bridge) connecting two daughter cells (**Figure I.3A**) (Zhang et al., 2008). A bipolar spindle structure is necessary for Cdc42 activation, but not RhoA activation (Leblanc et al., 2011; Li et al., 2016). This suggests that spindle-based signaling ensures the coordination of membrane protrusion and chromosome separation.

The last step of polar body emission is abscission (**Figure I.3B**), a process that cuts and seals the plasma membrane that connects two daughter cells (Maddox et al., 2012). Unlike cytokinetic abscission in mitosis that has been studied and reviewed (Mierzwa and Gerlich, 2014), polar body abscission in oocyte meiosis is nearly unexplored in both timing and molecular mechanisms. It is suggested that polar body abscission should be generally similar to mitotic abscission except for some possible oocyte-specific mechanisms (Maddox et al., 2012). Polar body abscission can be interrupted by loading oocytes with Ca^{2+} chelator during anaphase, suggesting local Ca^{2+} transients are involved in the process (**Figure I.3B,** see figure legends) (Leblanc, 2014). A more detailed introduction and discussion in this regard are provided in **Chapter V. Snapshotting Ca^{2+} transients during polar body abscission**.

Figure I.3 Anaphase I and polar body emission in *Xenopus* oocytes
(A) A schematic illustrates the detailed progression of anaphase I and polar body emission. Times are from anaphase initiation.
~0 minutes: When anaphase initiates (chromosomes separate), the small GTPase Cdc42 is activated at the spindle-cortex contact site and circumvented by an active RhoA contractile ring. Note that spindle microtubules assume an astral shape in anaphase which increases the contact area (at the spindle-cortex interface), in contrast to anastral microtubules in metaphase.
~0–5 minutes: An active Cdc42 cap leads the membrane protrusion while the RhoA contractile ring constricts rapidly. Plasma membranes are stacked at the oocyte-polar-body interface where the RhoA contractile ring has swept (see **Figure V.5** for a more detailed topological demonstration of the stacked membranes).
~5–10 minutes: Cdc42 cap and RhoA contractile ring continues to action while a set of homologous chromosomes is located in the polar body.
~10–15 minutes: The RhoA contractile ring is closed, which marks the completion of polar body emission.
(B) A schematic illustrates the assessment of polar body abscission by fluorescence-labeled dextran.
Oocytes are subjected to water (top branch, control) or DB-BAPTA injection (bottom branch) 2-5 minutes after anaphase initiation. Both groups exhibit normal polar body emission. Fluorescence-labeled Dextran (Dextran Texas Red, 3000 MW, Invitrogen) is injected into the oocytes in both groups ~1 hour after anaphase initiation. The majority of control oocytes (73%, n=30) exhibit successful polar body abscission (no dextran filled) while most DB-BAPTA-injected oocytes (76%, n=21) fail abscission manifested by filled dextran (numbers are from Leblanc, 2014).

Figure I.3 Anaphase I and polar body emission in *Xenopus* oocytes

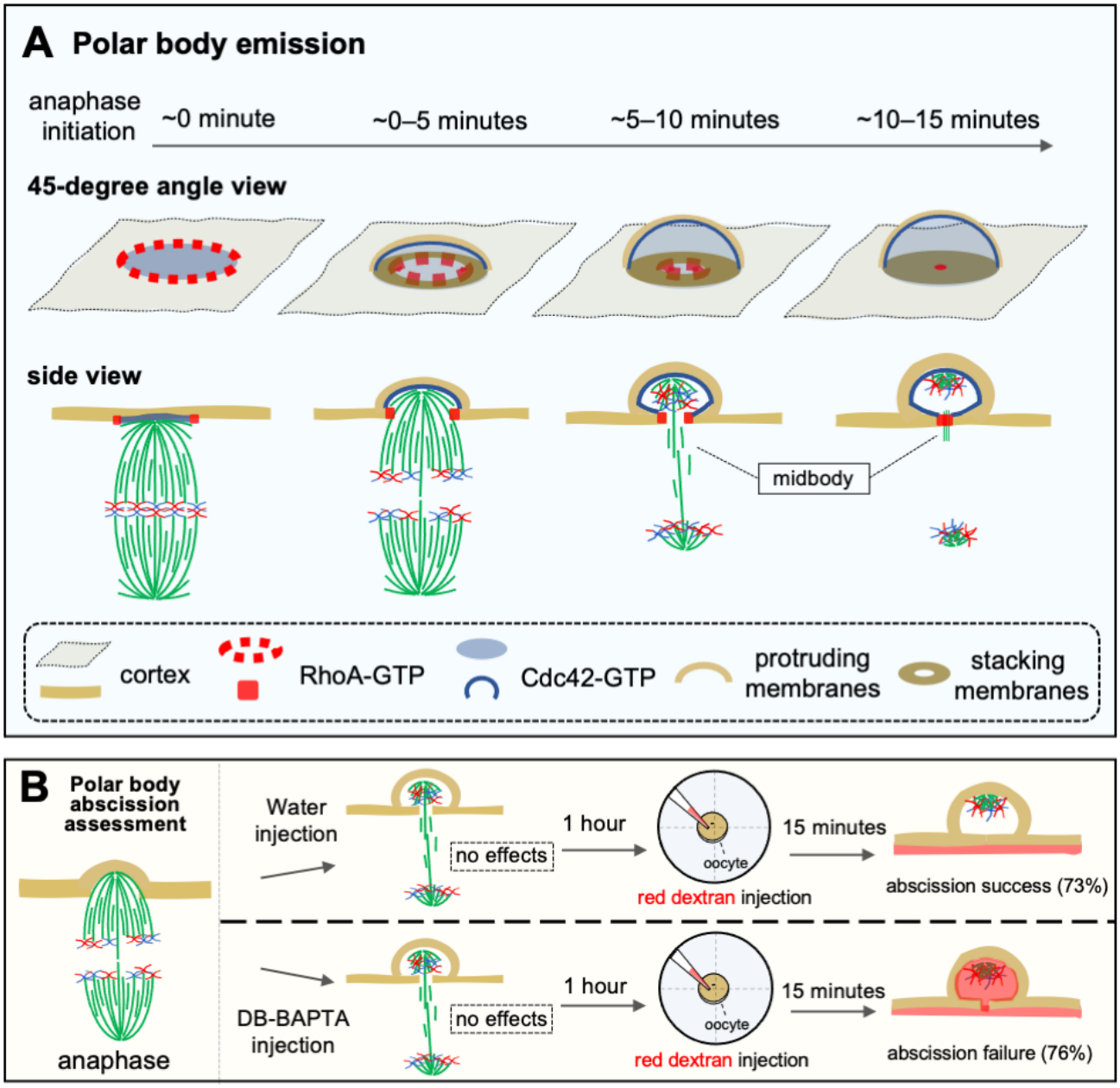

I.1.4 Metaphase II arrest and exit

I.1.4.1 Molecular mechanism of metaphase II arrest

The transition of meiosis I to meiosis II (or pro-metaphase II) takes about 20 minutes after the first polar body emission, without entering the interphase. About 2.5–3 hours after GVBD, the oocyte reaches metaphase II (**Figure I.1C.c**, metaphase II) (Ma et al., 2003). At this stage, the kinetochore microtubules attach to sister chromatids instead of homologous chromosomes. The metaphase II spindle microtubule dynamics are essentially the same as that in meiosis I (see **I.1.2.2**, and **Figure I.2**), except for a significantly reduced size (Leblanc et al., 2011). Meiosis II oocytes only have half the amount of DNA as meiosis I oocytes do; the reduced size of metaphase II spindles is likely the result of smaller RanGTP gradients and fewer spindle-assembly factors such as TPX2 (Helmke and Heald, 2014). Meiosis will arrest at metaphase II (until fertilization). At this stage, oocyte maturation concludes and the mature oocyte, a.k.a. the egg, is reproductively competent.

Metaphase II arrest is caused by a cytostatic factor (CSF) which was discovered in the early 1970s together with MPF (Masui and Markert, 1971). Unlike MPF (cyclin B/Cdc2), CSF lacks biochemical characterization or purification for a long time. Several pathways that inhibit APC/C activity are proposed to be CSF candidates, such as c-mos/MAPK and Emi-related protein 1 (Erp1, also known as Emi2) (Liu et al., 2007; Schmidt et al., 2006). c-mos/MAPK are present in cytoplasm since meiosis I and contribute to the maintenance of MPF activity (see **I.1.1**). Erp1, however, is synthesized shortly after meiosis I and phosphorylated (at Thr-336, Ser-342 and Ser-344 sites in *Xenopus laevis*) through the MAKP pathway. Subsequently,

Erp1 binds to the C-terminus destruction box[7] of APC/C-Cdc20 and blocks its activity that may otherwise degrade cyclin B (Inoue et al., 2007; Miller et al., 2006; Nishiyama et al., 2007). Induced by fertilization, global Ca^{2+} elevation is able to trigger degradation of Erp1, leading to exit from metaphase II (see next section) (Rauh et al., 2005). Collectively, it is suggested that the coordination of MPF activity and APC/C inactivation maintains metaphase II arrest (**Figure I.1C.b** and **Figure I.1C.c**, metaphase II) (Madgwick and Jones, 2007).

The knowledge of metaphase II arrest led to the application of CSF extracts (a.k.a. *Xenopus* egg extracts), a popular tool to study spindle assembly *in vitro*. CSF extracts are made from crushed *Xenopus* eggs that maintain metaphase characteristics. EGTA is routinely added into the preparation buffer to preserve CSF activity. The presence of EGTA in the extracts led to the common belief that calcium signaling is not required for spindle assembly.

I.1.4.2 Fertilization breaks metaphase II arrest by a sweeping Ca^{2+} wave

Sperm penetration, namely fertilization, breaks the metaphase II arrest. During *Xenopus* oocyte fertilization, sperm activates phospholipase Cγ (PLCγ) through the action of membrane-originated non-receptor tyrosine kinases (Src kinase family) [8]. PLCγ, in turn, catalyzes the breakdown of membrane phosphatidylinositol-4,5-bisphosphate (PIP_2) to increase cytosolic inositol-1,4,5-triphosphate (IP_3) (Stith, 2015). A single and large calcium wave is generated from the IP_3 receptors (IP_3Rs) on the endoplasmic reticulum (ER) in response to the elevation of IP_3 (Bugrim et al., 2003; Wagner et al., 2004). This wave traverses

[7] Destruction box is a short sequence (~10) of amino acid residue of APC/C that senses the ubiquitinated protein and signals subsequent proteolysis.

[8] This mechanism is specific to the fertilization of some aquatic or amphibian species such as *Xenopus laevis*. In mammalian oocyte-sperm fusion such as mouse, it is sperm-specific phospholipase C, *i.e.* PLCζ, introduced by sperm into mouse eggs, dominates IP_3 releasing (Stith, 2015).

the entire oocyte in about 4 minutes and induces a global biochemical response (Wagner et al., 2004). Meanwhile, the intracellular free Ca^{2+} concentration ($[Ca^{2+}]_i$) jumps from 200–300 nM to roughly 0.7–1.3 μM (Fontanilla and Nuccitelli, 1998; Nuccitelli et al., 1993; Wagner et al., 1998). Calmodulin, a highly conservative Ca^{2+}-binding protein, is activated by the elevated $[Ca^{2+}]_i$. Ca^{2+}-bound calmodulin activates calmodulin-dependent protein kinase II (CaMKII) through allosteric regulation that causes auto-phosphorylation of CaMKII. CaMKII and its downstream effector polo-like kinase 1 (Plk1) sequentially phosphorylate the $_{192}$RSST and $_{32}$DSGYSDS motifs of Erp1 (aforementioned CSF candidate, see **I.1.4.1**), which leads to the recognition and destruction of Erp1 by ubiquitin E3 ligase Skp1/Cul1/F-box complex (or $SCF^{\beta\text{-}TRCP}$ which primarily controls G_1/S and G_2/M transition in mitosis) (Hansen et al., 2006; Liu and Maller, 2005; Rauh et al., 2005). Without Erp1-dependent inhibition, APC/C-Cdc20 is activated, resulting in cyclin B degradation and thereby MPF inactivation. APC/C activity also destroys the cohesins around the centromeres of sister chromatids, the hallmark of anaphase II onset (see **I.1.3.2**). The second polar body emission is similar to the first polar body emission (see **I.1.3.3**) (Leblanc et al., 2011). After second polar body emission, one set of chromatids that remains in the egg is decondensed, forming a maternal pronucleus that is ready for fusion with the paternal genome. This concludes the oocyte meiosis and thereafter the embryo cell cycle initiates.

I.2 Calcium nanodomains in spindle regulation

I.2.1 Ca^{2+} signaling is required for oocyte maturation

In the previous section, we describe that the fertilization of eggs leads to global $[Ca^{2+}]_i$ elevation. But before fertilization (during oocyte maturation), the requirement of Ca^{2+}

signaling is contentious and inconsistent in the early years (Cork et al., 1987; Robinson, 1985; Wasserman et al., 1980). During the last two decades, by manipulating cytosolic Ca^{2+} before maturation entry (*i.e.* before GVBD), Machaca and his co-workers conducted a series of remarkable experiments to elucidate the significance of $[Ca^{2+}]_i$ during *Xenopus* oocyte maturation (Nader et al., 2013). Their findings could be summarized into two categories:

(1) Ca^{2+} signaling regulates both the entry and the completion of oocyte maturation. Sun and Machaca showed that the main meiotic drivers — the MPF/MAPK pathway (see **I.1.1**) – – can be negatively impacted by Ca^{2+}: Increasing cytosolic Ca^{2+} slows down MPF/MAPK activation while depletion of Ca^{2+} accelerates it by promoting c-mos mRNA transcription (Sun et al., 2008; Sun and Machaca, 2004). However, depletion of cytosolic Ca^{2+} intervenes with bipolar spindle formation and blocks polar body extrusion, suggesting Ca^{2+} signaling is crucial for proper spindle function (Sun et al., 2008; Sun and Machaca, 2004). In particular, the cytosolic mRNA and the protein level of Aurora A (a Ran-GTP effector and microtubule nucleator that is involved in spindle assembly, see **I.1.2.2**) is attenuated by Ca^{2+} deprivation (Sun et al., 2008).

(2) During oocyte maturation, the elements of Ca^{2+} signaling are being reorganized for reproductive competence. This includes (i) the sensitization of ER calcium releasing channels by ER remodeling and IP_3R clustering (El-Jouni et al., 2005; Sun et al., 2009; Sun et al., 2011) and (ii) inactivation of store-operated Ca^{2+} channels (uptake) at the plasma membrane by an internalization process (El-Jouni et al., 2008; Machaca and Haun, 2002). The authors argue that the clustering of Ca^{2+} release channels is for the readiness of fertilization (Ullah et al.,

2014) and the internalization of Ca^{2+} uptake channels is mainly prepared for embryogenesis (El-Jouni et al., 2008; Smyth et al., 2012; Yu et al., 2019)[9].

Despite their significant implications, previous studies were not able to address the exact role of Ca^{2+} signaling during oocyte maturation, as all the experimental interventions were conducted before GVBD and lacked spatiotemporal precision (Sun et al., 2008; Sun and Machaca, 2004). Besides, our understanding of Ca^{2+} dynamics during *Xenopus* oocyte maturation is still based on early results of microelectrode recording on plasma membranes or calcium dyes indicating global cytosolic Ca^{2+} concentration (Cork et al., 1987; Robinson, 1985); however, no local Ca^{2+} changes under physiological condition have been reported. Nevertheless, Ca^{2+} signaling is likely involved in several stages of oocyte maturation, as suggested by studies in mitosis such as nuclear envelope breakdown (Subramanian and Meyer, 1997), anaphase initiation (Groigno and Whitaker, 1998), cytokinesis (Webb and Miller, 2017). More direct clues are from the results of Ca^{2+} chelation at different timings during oocyte maturation (see **I.1.3.2, Figure I.3B** and the coming section).

I.2.2 Spindle collapse is caused by fast rather than slow Ca^{2+} chelators

Our interest in Ca^{2+} signaling for spindle assembly stems from our laboratory's previous studies on polar body emission in *Xenopus* oocytes, with particular focus on the membrane-bound GTPase Cdc42 and RhoA regulation (see **I.1.3.3 Polar body emission** for the brief review). Several studies implicated that calcium signaling might be involved in polar body

[9] In mitosis where fertilization and further embryo development do not exist, loss-of-function studies showed that extensive ER remodeling and temporary inactivation of external Ca^{2+} uptake are also required, otherwise mitotic catastrophe (mitosis-linked cell death) occurs. It seems that the adaption of Ca^{2+}-sensitive elements has a more conservative and universal role in general cell cycle progression, not just oocyte meiosis (Yu *et al.*, 2019).

emission at multiple steps (see **I.2.1**), we were therefore motivated to investigate the role of calcium by determining Ca^{2+}-dependent phenotypes following intracellular injection of Ca^{2+} chelators at different timings during oocyte maturation. In the previous section, we have introduced that the intervention of Ca^{2+} signaling during anaphase leads to abscission defects (see **I.1.3.3**); here we describe the intervention of Ca^{2+} signaling in metaphase oocytes (Li et al., 2016).

Specifically, the Ca^{2+} chelator DB-BAPTA (or BAPTA) was injected during meiosis I followed by timelapse imaging to determine the immediate effects of Ca^{2+} buffering. Most dramatically, when DB-BPATA was injected during prometaphase and metaphase, the spindle underwent rapid collapse, disappearing within ~4–6 minutes (**Figure I.4A**, BAPTA or DB-BAPTA intervention) (Li et al., 2016). Although this is consistent with the previous observation that DB-BAPTA interfered with polar body emission (Sun et al., 2008; Sun and Machaca, 2004), its dramatic effect challenges the conventional wisdom that spindle assembly is independent of Ca^{2+} signaling. Injection of the same or greater concentrations of EGTA was able to inhibit global $[Ca^{2+}]_i$ elevation by fertilization, but unexpectedly failed to induce spindle collapse or block first polar body emission (**Figure I.4**, EGTA intervention) (Li et al., 2016). Further experiments showed that loading oocytes with EGTA at an estimated intracellular concentration up to 10 mM, which reaches the limit of the stock solution, had no effects on spindle assembly while DB-BAPTA took effect as low as 0.38 mM (**Table I.1**). Such disparity cannot be explained by calcium affinities of the two chelators, since DB-BAPTA (disassociation rate K_d = 1.6 μM) has a much lower Ca^{2+} affinity than EGTA (K_d = 180 nM), whereas BAPTA (K_d = 220 nM) has a similar affinity with EGTA (**Table I.2**). However, the Ca^{2+}-binding rates of chelators, rather than the affinities, explain differential

sensitivity of spindle assembly to different chelators. BAPTA and DB-BAPTA have 40–400 times faster Ca^{2+} binding rates than that of EGTA depending on the working condition (**Table I.2**). The detailed implication of the EGTA/BAPTA test will be discussed in the next section.

It is worth noting that BAPTA and its derivatives unlikely to cause spindle disassembly via Ca^{2+}-independent mechanisms. First, increasing Ca^{2+} concentrations in the DB-BAPTA buffer progressively rescues the disruptive effect of DB-BAPTA on the spindles in *Xenopus* oocytes (Li et al., 2016). This argues against the possibility that microtubule depolymerization by BAPTA derivatives is induced by its Ca^{2+} chelation-independent action (Furuta et al., 2009; Saoudi et al., 2004). Second, N,N,N′,N′-tetrakis(2-pyridinylmethyl)-1,2-ethanediamine (TPEN, a high-affinity zinc chelator) injection into metaphase oocytes does not affect spindle assembly nor polar body emission (**Table I.1**), suggesting the rapid spindle collapse caused by BAPTA derivatives is irrelevant to the Zn^{2+}-dependent mechanisms that regulate oocyte maturation (Bernhardt et al., 2011; Kim et al., 2011; Sun et al., 2007).

Figure I.4 BAPTA/EGTA tests in understanding nanodomain Ca^{2+} coupling
(A) A schematic depicts differential effects of BAPTA and EGTA on spindle assembly in *Xenopus* oocytes. Metaphase I oocytes are subjected to different injections: water (top row), EGTA (middle row) and BAPTA/DB-BAPTA (bottom row).
In water-injected (or Ca^{2+}-unperturbed) oocytes (top row), the oocyte undergoes normal meiosis I and arrests at metaphase II. Following pseudo-fertilization (egg activation without fusion of maternal and paternal pronuclei) by a needle prick, a global Ca^{2+} wave is generated from the prick site (n = 11). The EGTA-injected oocyte (middle row) also undergoes normal meiosis I and arrests at metaphase II (n = 32). In contrast, the oocyte with BAPTA or DB-BAPTA intervention (bottom row) exhibits fast spindle collapse (n = 28). Oocytes in both chelator-treated groups cannot be activated by needle prick, and no global Ca^{2+} waves are observed. Whereas EGTA is able to inhibit global Ca^{2+} elevation, it fails to cause spindle disassembly. The striking contrast of the effects of fast chelator BAPTA and slow chelator EGTA suggests that spindle assembly is controlled by a highly localized Ca^{2+} signaling. The experimental data are from Li et al., 2016.
(B) A schematic depicts the fast neurotransmitter release in squid giant synapse, the well-studied paradigm of highly localized, or nanodomain Ca^{2+} signaling.
Graphs in the middle row illustrates a pair of sympathetic nerves in a giant cell lobe. During the experiment, two sharp micro-electrodes are connected to the pre-synapse and post-synapse respectively. The electrode connected to the pre-synapse loads the nerve with the indicative buffer (KCl, EGTA or BAPTA), and also injects currents to cause membrane depolarization or action potential. The electrode connected to the post-synapse records the voltage oscillation of the membranes in response to neurotransmitter release at the pre-synapse terminal.
In chelator-free condition (left column, pre-synapse loaded with KCl), a current of 100–200 nA initiates an action potential at the pre-synapse, which results in the opening of voltage-gated Ca^{2+} channels at the synapse terminal, thereby Ca^{2+} ion influx (this influx is indicated by a "shoulder" on the pre-synapse's voltage curve; see dashed circles at the top row). Subsequently, Ca^{2+} ions bind to the Ca^{2+} sensor on the vesicle containing neurotransmitters docked at the plasma membrane. The binding leads to vesicle exocytosis and then neurotransmitter release at the synapse terminal cleft. The neurotransmitter receptor at the post-synapse is thereby activated by its ligands, initiating an action potential at the post-synapse that can be recorded by the electrode. The neurotransmitter release can be gauged by the slope of the recorded voltage curve (*i.e.* ΔVotage/Δtime, the depolarization speed). In this chelator-free condition, the delay between influx of calcium and initiation of transmitter release is about 200 μs, suggesting a fast Ca^{2+} signal coupling.
In the presence of slow chelator EGTA (middle column, pre-synapse loaded with EGTA), the Ca^{2+} gradient around the voltage-gated Ca^{2+} channel has been sharpen. However, the action potential at the post-synapse is not affected, suggesting EGTA is ineffective in inhibition of neurotransmitter release.
In the presence of fast chelator BATPA or its derivatives (right column, pre-synapse loaded with BAPTA), the Ca^{2+} gradient around the voltage-gated Ca^{2+} channel has been greatly sharpened. The amplitude of the action potential at the post-synapse is significantly attenuated, suggesting BAPTA largely inhibits neurotransmitter release.
At the resting status (buffer/Ca^{2+} equilibrium), neurotransmitters are held in vesicles. A theoretical model suggests that the re-equilibrium time of BAPTA(10 mM)/Ca^{2+} around the channel mouth is about 3 μs, which is fast enough to prevent the Ca^{2+} ion to reach Ca^{2+} sensors at the vesicle. By contrast, it takes 1200 μs for EGTA(10 mM)/Ca^{2+} to re-equilibrium, which allows Ca^{2+} diffuses to the nearby vesicle sensor to activate exocytosis (<200 μs). Inside green dashed rectangle depicts a typical nanodomain Ca^{2+} coupling between a channel and a sensor. The coupling distance is about 100 nm and it takes about 10–15 μs for Ca^{2+} to travel through as estimated. The data of experiments are from Alder et al., 1991 and Llinas 1984.

Figure I.4 BAPTA/EGTA tests in understanding nanodomain Ca^{2+} coupling

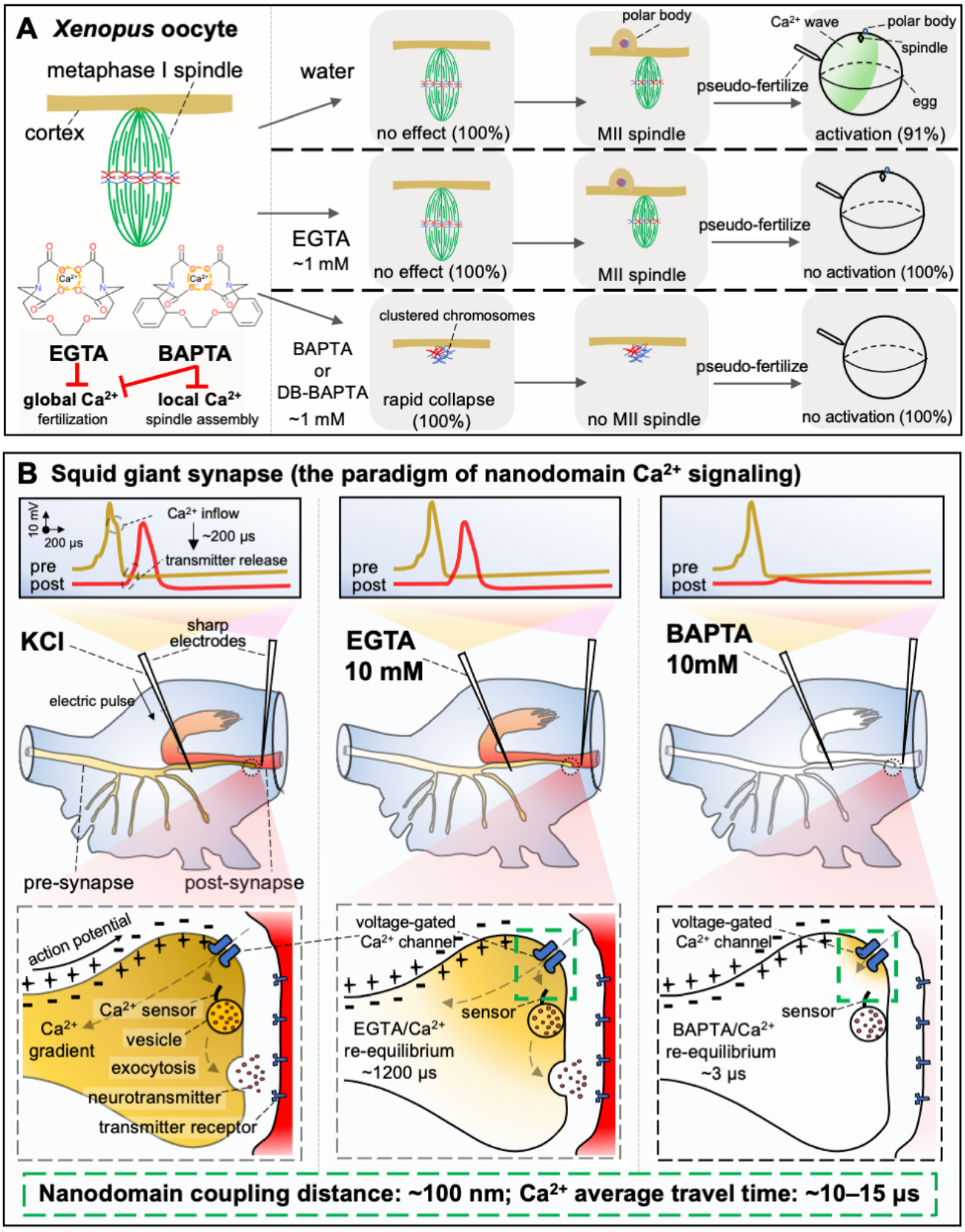

Table I.1 DB-BAPTA *vs.* EGTA *vs.* TPEN intervention with the 1st polar body emission

	0.19 mM	0.38 mM	0.75 mM	10 mM
DB-BAPTA	12/12(100%)	**11/20 (55%)**	**0/12(0%)**	-
EGTA	-	-	12/12(100%)	12/12(100%)
TPEN	-	-	10/10(100%)	-

Metaphase I oocytes are injected with listed buffers at the estimated intercellular concentrations shown in the table (considering oocyte cytosolic volume as 1000 nL). DB-BAPTA injection causes spindle collapse and inhibits the 1st polar body emission by 45% and 100% at a concentration of 0.38 mM and 0.75 mM, respectively. Control group (water injection, n = 12) is not listed but all oocytes emit the 1st polar body. EGTA and TPEN injection has no significant effects on spindle assembly nor the 1st polar body emission.

Table I.2 Kinetics of Ca^{2+} buffers

Buffer molecule	Affinity (K_d)*	Binding Rate (K_{on})	Reference
EGTA	200 nM	1.5×10^6 M^{-1} s^{-1}	(Adler et al., 1991)
	180 nM	**2.5×10^6 M^{-1} s^{-1}**	**(Naraghi and Neher, 1997)**
	70 nM	1.0×10^7 M^{-1} s^{-1}	(Nagerl et al., 2000)
BAPTA	160 nM	6.0×10^8 M^{-1} s^{-1}	(Adler et al., 1991)
	220 nM	**4.0×10^8 M^{-1} s^{-1}**	**(Naraghi and Neher, 1997)**
DB-BAPTA	1.6 μM	similar to BAPTA**	(Adler et al., 1991)
Calmodulin N-lobe	208 μM (tense***) 688 nM (relaxed)	7.7×10^8 M^{-1} s^{-1} 3.2×10^{10} M^{-1} s^{-1}	(Faas et al., 2011)
Calmodulin C-lobe	31 μM (tense) 260 nM (relaxed)	8.4×10^7 M^{-1} s^{-1} 2.5×10^7 M^{-1} s^{-1}	(Faas et al., 2011)

The affinity of EGTA and BAPTA are close under the physiological conditions but the binding rate of BAPTA and its derivatives are at least 40 times faster than EGTA, depending on the conditions (Adler et al., 1991; Naraghi and Neher, 1997; Nagerl et al, 2000). Throughout the thesis we will use the numbers in bold which are measured by the same author under the physiological condition.

Calmodulin is the fastest endogenous calcium buffer protein (Faas et al., 2011; Eggermann et al., 2011). It has two lobes, each of which has two Ca^{2+} binding sites. Its N-lobe exhibits the lower affinity but faster binding rate than those of C lobe. In the bulk solution, 1–10 μM of Ca^{2+} will be sufficient to cause binding to the C-lobe of calmodulin. 100 μM of Ca^{2+} is needed for the full occupation of N-lobe. The concentration determines to what extent calmodulin can be activated, and what downstream molecule can be regulated (Faas et al., 2011).

*Affinity is gauged by dissociation constant K_d. The bigger the K_d, the smaller the binding affinity. For a dissociation reaction $Ca^{2+} \cdot \text{Buffer} \rightleftharpoons Ca^{2+} + \text{Buffer}$, the dissociation constant K_d is defined as $K_d = \frac{[Ca^{2+}][\text{Buffer}]}{[Ca^{2+}\text{Buffer}]}$ or $K_d = \frac{K_{dissociation}}{K_{binding}} = \frac{K_{off}}{K_{on}}$. All the numbers in the table are obtained under the physiological pH (7.0–7.4) with different ion existence and strength in the solution. Both K_d and K_{on} of EGTA are more sensitive to the pH change due to its protonated status in the physiological condition. Internal pH of *Xenopus* oocyte is 7.43 ± 0.03 (mean ± S.D.) with a maximum elevation of 0.30 ± 0.03 after GVBD (Cicirelli et al., 1983).

**To our knowledge there is no report to determine the exact K_{on} for DB-BAPTA (Tymianski et al., 1994). Nonetheless, Adler *et al*. have shown that both DB-BAPTA and BAPTA inhibit the release of neurotransmitters. DB-BAPTA exhibits even higher buffer efficacy under the same condition. This indicates that DB-BAPTA has a similar, if not higher K_{on}, than that of BAPTA (Adler., 1991). Tsien also points out that, unlike EGTA, BAPTA nucleus is already fully ionized at physiological pH. Higher K_d in its derivatives results mainly from increase the K_{off}, with only modest change in K_{on} (Tien, 1999).

*** Calmodulin is a highly cooperative Ca^{2+} binding protein and it can shift between tense (low affinity) and relaxed states (high affinity). It has been suggested by an allosteric model, as well as experimental data, that the Ca^{2+}-unbounded calmodulin assumes the tense state (Stefan et al., 2008).

I.2.3 Understanding nanodomain Ca^{2+} coupling by EGTA/BAPTA tests

I.2.3.1 A lesson from squids

Although the disparate action of EGTA and BAPTA on spindles was only recently discovered (Li et al., 2016), it is not unfamiliar in other biological systems such as neurotransmitter release in squid giant synapses (Adler et al., 1991), fast mammalian synapses (Eggermann et al., 2011), Ca^{2+}-dependent ion channel inactivation in leukemic T lymphocytes (Zweifach and Lewis, 1995) and activation of pancreatic β-cells (Selway et al., 2012). Probing calcium nanodomain, or highly spatially restricted Ca^{2+} signaling, by EGTA/BAPTA tests (*i.e.* determining the buffering effect of BAPTA *vs.* EGTA) is a classical and powerful method that is still widely applied nowadays since its establishment in 1991 (Adler et al., 1991; Heine et al., 2020; Wang and Augustine, 2014). In this section, we digress from cell cycle and illustrate the studies of synaptic neurotransmission as the paradigm of "nanodomain Ca^{2+} signaling".

At a squid giant synapse, when an action potential arrives at the presynaptic terminal, local $[Ca^{2+}]_i$ increases as a result of Ca^{2+} inflow through voltage-gated Ca^{2+} channels. Consequently, Ca^{2+} binds to a Ca^{2+} sensor closest to the channel mouth, which triggers exocytosis of synaptic vesicles containing neurotransmitters (**Figure I.4B**, left column, see legend for detailed description). Remarkably, it takes only 200 μs from Ca^{2+} inflow to neurotransmitter release, suggesting that there is a tight coupling between the Ca^{2+} channel and Ca^{2+} sensor in space and time (Augustine et al., 1985; Llinas, 1984). This notion is further tested by BAPTA or EGTA intervention (**Figure I.4B**). Although BAPTA and EGTA have a

comparative affinity index —dissociation rates (K_d), their Ca^{2+}-binding rates (K_{on}) [10] differ by a factor of 40–400, depending on the working conditions (**Table I.2**) (Adler et al., 1991; Cicirelli et al., 1983; Eggermann et al., 2011; Nagerl et al., 2000; Naraghi and Neher, 1997). BAPTA and its derivatives are therefore considered as *fast* Ca^{2+} chelators whereas EGTA is *slow*. At the resting potential, pre-synapse preloaded with Ca^{2+} buffer reaches buffer/Ca^{2+} equilibrium. The action-potential-induced Ca^{2+} inflow can be considered as a small perturbation to an environment at equilibrium nearby Ca^{2+} channels. This environment is however incapable to respond to the local change instantaneously, which allows Ca^{2+} to travel for a short time (*i.e.* form a temporary gradient) before re-establishment of equilibrium, or re-equilibrium (also known as "chemical relaxation"). According to the relaxation kinetic model, the time (τ) for re-equilibrium is inversely correlated to the binding rate (K_{on}) and the sum of the concentration ([$Buffer_{total}$]) and the dissociation rate (K_d) of the loaded buffer: $\frac{1}{\tau} = K_{on} \cdot ([Buffer_{total}] + K_d)$ (Adler et al., 1991; Bernasconi, 1976). To block neurotransmitter release at the pre-synapse, the time to reach buffer/Ca^{2+} re-equilibrium should be shorter than the Ca^{2+} diffusion time from the source to the sensor (<200 µs by measurable data; ~10–15 µs estimated by the theoretical model). Since the dissociation rates of EGTA and BAPTA are close, the binding rates will become the determinative factor if the same buffer concentrations are applied. For a concrete example, at a buffer concentration of 10 mM, EGTA/Ca^{2+} takes about 1200 µs to reach re-equilibrium whereas BAPTA/Ca^{2+} takes 3 µs (Adler et al., 1991). Obviously, only BATPA is fast (3 µs) enough to intercept Ca^{2+} diffusion from Ca^{2+} channels

[10] There is a straight relation between K_{on} and K_d: $K_d = \frac{K_{off}}{K_{on}}$. See **Table I.2** legend.

at the presynaptic terminal to the sensors of synaptic vesicle exocytosis (<200 μs) (**Figure I.4B**).

The term *nanodomain* is coined to describe this tight sensor-to-source coupling domain (**Figure I.4B**, green dashed rectangle). Since Ca^{2+} diffusion forms a continuous gradient, the diameter of calcium nanodomain is not strictly defined. Some authors suggested 100 nm as a theoretical distance limit to distinguish from a looser coupling system "microdomain" that could be abolished by EGTA at the micro- or millimolar range (Eggermann et al., 2011). This number (100 nm) is based on theoretical calculation: When excess amount of Ca^{2+} buffer is present (compared to Ca^{2+} increase at channel mouth), distance can be estimated as $\lambda = \sqrt{\frac{D_{Ca}}{K_{on}[B]^0}}$, where D_{Ca} is the calcium diffusion rate, K_{on} is binding rate and $[B]^0$ is the free buffer concentration (Eggermann et al., 2011). Others suggested that the physiological constraint could serve as the limit, such as synaptic vesicle size (~20 nm) or the distance between a synaptic vesicle Ca^{2+} sensor and its closest Ca^{2+} channel (~150 nm) (Satzler et al., 2002). It is worth noting that outside the discipline of neuroscience, authors sometimes use the term "microdomain" to replace "nanodomain" without discrimination, although they refer to the same entity that can be distinguished by EGTA/BAPTA tests (Hogan et al., 2010; Mehta and Zhang, 2015). In some other reports, authors refer to a general submicron compartment as a "microdomain" without doing any test (Whitaker, 2006b). **Regardless of such confusion, we will use "nanodomain" to describe the EGTA-insensitive Ca^{2+}-coupling domains but won't emphasize the nuance of the terminologies. For cited references, we will respect the original use of the terms.**

As a rule of thumb, if the Ca^{2+}-coupling distance is long enough, both fast and slow chelators will be effective; if the Ca^{2+}-coupling distance is short at a nanoscale, only the fast chelator, at millimolar concentrations, will be able to abolish the signaling. The sensitivity to fast but not slow chelators is considered to be the defining feature of nanodomain coupling (Augustine et al., 2003; Bucurenciu et al., 2008; Eggermann et al., 2011; Neher, 1998; Stanley, 2016; Wang and Augustine, 2014).

I.2.3.2 A problem for visualization

Direct visualization of highly localized, or individual calcium nanodomain is challenging. First, the dimension of nanodomains is beyond the spatial resolution of conventional fluorescent microscopy or confocal microscopy (optimal x-y resolution ~200 nm, and in many cases much worse) (Schermelleh et al., 2010). Second, the coupling time is very fast (tens of microseconds), it may outpace the capture time of the camera or the response time of the Ca^{2+} indicator. Furthermore, the total amount of Ca^{2+} through a single channel is too small to be detected by conventional calcium probes. For instance, in fast synapses, it is estimated that only ~1000 Ca^{2+} molecules flow through a nanodomain-associated channel in an opening event (Augustine et al., 2003). The studies that reported successful detection of single channel activity always exploit sparse channels that are micrometers away from each other (Llinas et al., 1992; Parker and Smith, 2010; Tay et al., 2012). In particular, Tay *et al.* reported the use of total internal reflection fluorescence (TIRF) microscopy to measure signals generated by a genetically encoded Ca^{2+} sensor (TN-XL) fused to $Ca_V2.2$ Ca^{2+} channel (Tay et al., 2012). Their idea is to tether the sensor to Ca^{2+} channels, combined with super-resolution microscopy.

Another method is to buffer the system with high concentration EGTA, which will "sharpen"[11] signals at individual channels. A large Ca^{2+} transient spot (~1–2 μm in diameter) can be identified if channels are sparse enough (DiGregorio et al., 1999; Llinas et al., 1992).

I.2.4 Rationale for nanodomain Ca^{2+} signaling at spindles

The distinct effect of BAPTA *vs.* EGTA on spindle stability in *Xenopus* oocytes implicates the involvement of calcium nanodomains in regulating spindle function (Li et al., 2016). However, this implication does not necessitate the proximity between potential nanodomains and the spindle. There may there exist intermediate signal transduction mechanisms between the signaling source and the location where an effect can be gauged. Therefore, extra efforts are needed to figure out the precise location of calcium nanodomains that contribute to spindle assembly.

Emerging evidence suggests potential candidates for nanodomain molecules associated with spindles. First, the endoplasmic reticulum (ER) is the major Ca^{2+} storage of *Xenopus* oocytes, and its depletion by thapsigargin, an ER Ca^{2+} ATPase inhibitor, leads to spindle defects (Sun and Machaca, 2004). Previous studies showed that ER reorganizes its network during cell cycles, forming a tight contact with spindle microtubules in various systems including in *vitro Xenopus* egg extracts (Wang et al., 2013), HeLa cells (Smyth et al., 2012) and *Drosophila* embryos (Bergman et al., 2015; Parry et al., 2005). Of note, these reports investigate how dynamic microtubules direct the transformation of ER but do not further

[11] To be more precise, "sharpen" means, by using Ca^{2+} buffer, reducing the background signals to a concentration that falls into the lower part of the dynamic range of a Ca^{2+} indicator. This will make the image looks distinct around the channel mouth.

explore ER's biological significance in spindle formation and maintenance. Second, calmodulin is found to be closely associated with the spindle during *Xenopus* oocyte maturation (Li et al., 2016). Calmodulin is a calcium-binding messenger protein that mediates a variety of physiological processes, including multiple stages of cell cycle progression (Kahl and Means, 2003). It has been shown calmodulin participates in spindle MTOC formation in yeast and *Drosophila* embryos (Galletta et al., 2014; Sundberg et al., 1996). Calmodulin has two globular domains, *i.e.* N-lobe and C-lobe, each containing two Ca^{2+} binding motifs that possess distinct Ca^{2+} binding properties compared to those of the other lobe. Notably, the Ca^{2+} binding sites at its N-lobe exhibit low Ca^{2+} affinities but fast Ca^{2+} binding rates (see **Table I.2**) (Faas et al., 2011; Stefan et al., 2008). It implies that, as an endogenous calcium sensor, calmodulin has the potential to carry out Ca^{2+} signaling in nanodomains. Furthermore, IP_3R, the major Ca^{2+} channel of ER, has a calmodulin tethering domain that makes intimate cooperation possible (Taylor and Laude, 2002).

The ultimate test would be the direct visualization of Ca^{2+} signals at the spindle which is one of the main objectives in my thesis.

I.3 Probing cells with Ca^{2+} indicators

Calcium is a ubiquitous intracellular messenger responsible for nearly every aspect of cellular processes. Berridge *et al.* refer to this phenomenon as "calcium signaling toolkit" (Berridge et al., 2000). A natural question to ask: how Ca^{2+} concentration fluctuation regulates so many things without chaos? The secret is embedded in the flexibility and versatility of Ca^{2+} signaling coded in speed, amplitude and spatiotemporal pattern (Berridge et al., 2000). For extreme examples, Ca^{2+} concentration in subcellular compartments could differ by 1000 folds

between resting and stimulated status within the same location (*e.g.* mitochondria, jumping from ~100 nM to ~100 μM) or by 10,000 folds between two different locations at the same time (*e.g.* cytoplasm *vs.* ER lumen, ~100 nM vs. ~1 mM) (Suzuki et al., 2016). Calcium nanodomain is one such mechanism for highly precise control: Nanodomain Ca^{2+} channels can amplify a tiny Ca^{2+} influx (thousands of ions) into a highly localized Ca^{2+} signal at micro-molar to millimolar concentrations (100 μM to 1 mM), which can fully activate signaling molecules like calmodulin in a restricted region (see **Table I.2** legend) (Faas et al., 2011; Tadross et al., 2013). The versatility of Ca^{2+} in turn raises the demand for the diversity of Ca^{2+} indicators. There is no one-for-all Ca^{2+} probe that captures all signaling; rather, a Ca^{2+} probe is sometimes created just for one unique purpose. This is especially true for some genetically encoded calcium indicators (GECIs) that probe Ca^{2+} in subcellular compartments by connecting Ca^{2+} sensor to an organelle- or cytoskeleton-specific binding domain (Shigetomi et al., 2010a; Wu et al., 2014). In the following sections, major categories of calcium indicators and their applications in understanding Ca^{2+} events during cell cycles are briefly reviewed.

I.3.1 Bioluminescent Ca^{2+} indicators

The first practical calcium probe is *aequorin*, a chemiluminescent protein extracted from bioluminescent jellyfish half a century ago (Shimomura, 2005; Shimomura et al., 1962). Upon capturing Ca^{2+} ions, the chromophore of aequorin is oxidized by consuming a chemical cofactor coelenterazine, emitting blue light (~460 nm wavelength) (Inouye and Sasaki, 2006). In the early years, aequorin had been extensively applied to study Ca^{2+} events involved in cell cycles. Examples include Ca^{2+} transients during nuclear envelope breakdown in dividing sea urchin eggs (Browne et al., 1996), intracellular free Ca^{2+} oscillations in dividing *Xenopus* embryos (Grandin and Charbonneau, 1991; Keating et al., 1994) and intracellular Ca^{2+} increase

during fertilization of sea urchin eggs (Eisen and Reynolds, 1985). Aequorin can also be structurally modified and used to probe Ca^{2+} microdomains in subcellular compartments (Bonora et al., 2013). An example related to the aforementioned neurotransmitter releasing scenario (see **I.2.3**): Injecting presynaptic terminal of the giant squid synapse with n-aequorin-J, a low-sensitivity derivative of aequorins, enables the visualization of discrete Ca^{2+} hotspots that are attributed to the opening of a small number of plasma membrane Ca^{2+} channels (Llinas et al., 1992; Silver et al., 1994). However, despite the recent improvement, the associated challenges, including laborious preparation, the requirement of coelenterazine, low light emission, poor affordability and scarcity, limit the utility of aequorin and its derivatives (Bonora et al., 2013).

I.3.2 Small-molecule organic Ca^{2+} indicators

In the early 1980s, Roger Tsien and his colleagues designed and synthesized a series of small-molecule organic calcium indicators based on the BAPTA skeleton. The BAPTA skeleton has two additional benzene rings based on EGTA structure and the ring substituents are highly modulable for research (Tsien, 1999). This idea has proven a huge success: Modern chemical calcium probes from major providers are mostly the derivatives of BAPTA. These commercially available indicators can be employed to detect intracellular Ca^{2+} from lower than 50 nM to more than 50 μM. Some are conjugated with dextran (for dye compartmentalization) or acetoxymethyl moiety (AM, for membrane permeability) (Johnson and Spence, 2010; Paredes et al., 2008). A variety of user-friendly Ca^{2+} probes push the investigation of intracellular calcium signaling to an unprecedented level.

The research of anaphase onset considerably benefits from the application of organic calcium indicators. Early reports can be traced back to 1985, when Quin-2, the first ever organic dye for ratiometric imaging, was loaded into endosperm cells of the plant *Haemanthus*. By measuring the relative excitation of Quin-2 at 340 nm (Ca^{2+} bound) and 360 nm (Ca^{2+} free), Keith *et al.* demonstrated a local increase of Ca^{2+} at the anaphase spindle poles, which may account for the microtubule shortening at this stage (Keith et al., 1985). Similarly, Ca^{2+} elevation during the metaphase-anaphase transition was found in PtK1 (potorous tridactylus kidney-1) cells, with the help of an improved ratiometric indicator, Fura-2 (Poenie et al., 1986). These observations spark numerous investigations for dissecting calcium's role in regulating anaphase microtubule dynamics and chromatid separation. As a result, a key serine/threonine-specific kinase, CaMKII (Ca^{2+}/calmodulin-dependent protein kinase II), is identified to be the major molecular effector in response to anaphase Ca^{2+} release (See **I.1.4.2**) (Skelding et al., 2011).

The association rate K_d is a commonly used parameter to describe the affinity of an indicator binding to Ca^{2+}. For a specific calcium indicator, the suitable Ca^{2+} concentrations to be tested range from 0.1–10 times of indicator's K_d (Johnson and Spence, 2010). The resting Ca^{2+} concentrations in the cytosol of most cell types are around 100–200 nM (Clapham, 2007). With this principle, Whitaker and colleagues utilized Calcium Green-1 (K_d = 190 nM) to probe cytoplasmic calcium dynamics during cell cycles in embryos of sea urchins and *Drosophila* (Ciapa et al., 1994; Groigno and Whitaker, 1998; Parry et al., 2005; Torok et al., 1998; Whitaker, 2006b; Wilding et al., 1996). With the assistance of confocal microscopy, several IP_3-mediated Ca^{2+} events are resolved, including perinuclear signals at mitotic entry (Wilding et al., 1996) and spindle-based signals in anaphase (Groigno and Whitaker, 1998). Based on

the loss-of-function studies by Ca^{2+} chelators and channel inhibitors, the authors argued that localized calcium signaling are important in controlling cell cycles and further proposed the concept of ER-related "calcium microdomains" (calcium changes in very limited sub-micron dimensions) to describe such events (Whitaker, 2006b).

To investigate IP_3R-mediated Ca^{2+} signals, especially within the model of *Xenopus* oocytes, Ian Parker and colleagues have published a series of inspiring works by using chemical Ca^{2+} indicators (Oregon Green BAPTA-1, K_d = 170 nM; Fluo-4, K_d = 345 nM) together with photo-activatable IP_3 (caged-IP_3) and various calcium buffers. According to their characterization, the spatiotemporal patterns of IP_3R-mediated Ca^{2+} signals can be classified into "blip" (Ca^{2+} releasing of a single channel) or "puff" (Ca^{2+} releasing of a few clustered channels) or "wave" (Ca^{2+} releasing of channels propagates in continuous intracellular regions) (Dargan and Parker, 2003; Dargan et al., 2004; Demuro and Parker, 2015; Shuai et al., 2006; Swillens et al., 1999). All these signal patterns are ubiquitous features in vertebrate and mammalian cells (Dickinson et al., 2016; Smith et al., 2009; Swillens et al., 1999). The authors suggested that, in physiological conditions, these distinct patterns of Ca^{2+} signals can serve as basic units for localized signaling or building blocks for the propagation of global Ca^{2+} waves such as those in fertilization (see **I.1.4.2**) (Lock et al., 2019).

I.3.3 Genetically encoded Ca^{2+} indicators (GECIs)

The next leap of imaging intracellular Ca^{2+} comes with the introduction of genetically encoded Ca^{2+} indicators (GECIs). GECIs are intracellularly produced chimeric fluorescent

proteins by expression from plasmids or mRNA[12]. GECIs can precisely target specific intracellular micro-compartments. The idea was popularized by Roger Tsien and colleagues who also pioneered chemical calcium indicators (Miyawaki et al., 1997; Nakai et al., 2001). Not surprisingly, this approach becomes especially effective in imaging organellar calcium that is sometimes not achievable for chemical indicators (Suzuki et al., 2016). Over the last two decades, a diverse array of GECIs has been engineered to monitor the dynamics of various Ca^{2+} signaling pathways (Greenwald et al., 2018).

GFP-Calmodulin fusion protein (GCaMP) family is regarded as one of the most popular and successful types of GECIs so far (Yang et al., 2018). GCaMPs comprise a helical M13 fragment from myosin light chain kinase (M13, stabilizing unit) at the N-terminus, a circularly permutated EGFP (cpEGFP, reporting unit) and a calmodulin moiety (CaM, the Ca^{2+} sensing unit) at the C-terminus (Nakai et al., 2001). In a Ca^{2+}-free or dim state, the circular permutation of EGFP stabilizes the protonation form of its fluorophore at physiological pH[13], leading to largely decreased fluorescence. In Ca^{2+}-bound or bright state, CaM-Ca^{2+} "grips" the M13 helix, forming a condensed structure that intensively contacts with cpEGFP moiety; as a result of the conformational change, the fluorophore of cpEGFP becomes much less accessible to the solvent (*i.e.* water, the proton donor) and thereby restores its deprotonated form (bright state) (Akerboom et al., 2009; Wang et al., 2008). GCaMP3 is a remarkably advanced variation over the previous versions by introducing several point mutations near the EGFP fluorophore and

[12] Bioluminescent indicators (aequorin) can be literally categorized into GECIs, as some reviews do (Greenwald *et al.*, 2018). But in this section we focus on contemporary artificial architectures.
[13] The deprotonated form of cpEGFP fluorophore has an excitation peak at a wavelength of 475 nm, while its protonated form has an excitation peak at 395 nm that is hardly excited by the conventional GFP excitation laser (450-500 nm) (Wang *et al*, 2008).

the locations that favor protein folding. GCaMP3 exhibits largely improved baseline fluorescence and dynamic range; it also possesses better protein stability and photostability than the other contemporary GECIs (Tian et al., 2009). After GCaMP3, the improvements diverged into two branches, focusing on either speed like fast-GCaMP3 (GCaMP3f), fast-GCaMP6 (GCaMP6f) or brightness like GCaMP5G (Badura et al., 2014; Behera et al., 2013). Of equal importance, there are also GCaMP color variants. Zhao *et al.* developed a red-shifted sensor by replacing the cpEGFP domain of GCaMP3 with a circularly permuted version of mApple (a red fluorescent protein) and dubbed it as RGECO (Zhao et al., 2011).

GCaMPs tethered to subcellular targeting sequence have been extensively applied to revealing spatially compartmentalized Ca^{2+} signaling (microdomains or nanodomains) in various systems. For instance, to investigate Ca^{2+} channel behaviors on the plasma membrane of astrocytes, Shigetomi *et al.* generate Lck-GCaMPs by connecting GCaMP2 or GCaMP3 with the membrane-tethering domain of Lck (Lymphocyte-specific protein tyrosine kinase). Following neuron firing and transmembrane Ca^{2+} influxes, Lck-GCaMPs can visualize and characterize the spotty calcium microdomains that cannot be detected by cytosolic GCaMPs (Shigetomi et al., 2010a; Shigetomi et al., 2010b). In addition to the benefit of targeted effects, the authors suggested that the tethering domain greatly increases the Ca^{2+} sensitivity of GCaMP3 to ~4-fold of the cytosolic forms, which may also contribute to its capacity in detecting calcium microdomains (Shigetomi et al., 2010a). Another classical application is to probe the Ca^{2+} events in the junctional cleft, *i.e.* the gap between Ryanodine receptors (RyRs) and plasma membrane, of cardiomyocytes. By tethering GCaMPs to RyR-coupled proteins like FBKP12.6 or triadin-1/junctin, it becomes possible to detect the quaky nanodomain Ca^{2+}

release events, or so-called Ca^{2+} nanosparks, from a single junctional region in muscle cells (Despa et al., 2014; Shang et al., 2014).

On the other hand, the application of GECIs in resolving the precise spatiotemporal pattern of Ca^{2+} signaling during the cell cycle is just at the beginning page. During my Ph.D. study, I developed a microtubule-tethered GCaMP3 that reported spindle-based $[Ca^{2+}]_i$ (Tubecamp1 or TC1) in both mitosis and meiosis. Main results have been deposited in bioRxiv as a preprint (also as part of the results in **Chapter III** and **IV**) (Mo et al., 2018). Thereafter, Helassa *et al.* reported that a centrosome-based calcium signal during mitosis can be probed by actin-linked GCaMP6s in HeLa cells, which is consistent with our findings in HeLa cells (Helassa et al., 2019). We expect that the research of these topics will progress rapidly in the near future.

I.4 Hypothesis and objectives

Hypothesis: There exists highly localized Ca^{2+} signaling, or calcium nanodomains, that are in close proximity of the spindles. These calcium nanodomains are involved in spindle assembly and spindle microtubule stability.

Rationale: see **I.2.4 Rationale for nanodomain in Ca^{2+} signaling at spindles.**

Objective: (1) Identify local $[Ca^{2+}]_i$ associated with spindle assembly. Novel genetically encoded Ca^{2+} indicators will be constructed to probe the target subcellular compartment, the spindle apparatus (**Chapter III**).

(2) Explore molecular components of potential calcium nanodomains at spindles: Ca^{2+} store, channels, and signal receivers (effectors). *Xenopus* oocyte-based systems will be our main experimental models (**Chapter IV**).

(3) A range of calcium probes will be used to examine the spindle-associated events during oocyte maturation. This leads to the detection of a Ca^{2+} transient during polar body emission (**Chapter V)**.

Chapter II Methodology

II.1 *Xenopus laevis* handling and oocyte preparation

Mature *Xenopus laevis* females were purchased from Nasco Wisconsin and kept in the animal facility at Roger Guindon Hall (room temperature, regular day-night circle) of the University of Ottawa. The maintenance follows the guidelines established by the Animal Care and Veterinary Services (ACVS) that meets the standards of the Canadian Council on Animal Care (CCAC)[14].

3 to 10 days prior to oocyte collection, each frog was injected with 50 IU pregnant mare serum gonadotropin (PMSG, Sigma-Aldrich, G4527) to promote oogenesis and shorten the GVBD time when the oocytes were primed with 1μM progesterone (Sigma-Aldrich, P0130). On the experiment day, the ovarian lobes[15] were removed after anesthesia (in an ice bath) and sacrifice (by guillotine) of the frog. Stage VI oocytes (**Figure I.1A**) were then manually defolliculated by a pair of forceps under the dissecting microscope (Liu and Liu, 2006). Depending on the requirement of the follow-up experiments, oocytes were micro-injected with purified mRNA (cytoplasmic injection) or plasmid (nuclear injection) (see **II.3.1** for injection details) (Altafaj et al., 2006). It took at least 6 hours (generally overnight) for the mRNA-injected oocytes to reach proper expression (or 12 hours for nuclear injection).

[14] https://research.uottawa.ca/acvs/animal-care-veterinary-service , the guideline for animal care and maintenance.
[15] For each mature *Xenopus laevis* female, there are roughly 24 ovarian lobes (Jessus et al., 2020).

Oocytes were kept in OCM (oocyte culture medium; 60% Leibovitz's L-15 medium plus 40% distilled water, 0.4% BSA. L-15 medium powder was from Gibco, 41300039) at 18 °C. The defolliculated oocytes were generally used within 2-4 days, as recent research found that IP_3R desensitized overtime after oocytes removal from the ovary (Demuro and Parker, 2015).

II.2 Constructing genetically encoded calcium probes

To detect the spindle-based Ca^{2+}, we designed and constructed a series of genetically encoded calcium probes that target spindle microtubules. The idea was to connect a calcium sensor (GCaMP family, see **I.3.3** for the introduction) to a microtubule-binding domain (microtubule binding domain of ensconsin, EMTB) (Bulinski et al., 2001). The product was dubbed as *TubeCamp* or *TC.* We generated the prototype TC1 (EMTB-GCaMP3) and our collaborator Zachary Swider from Dr. William Bement's laboratory contributes several ratio-metric variations including TC4 (mCherry-EMTB-GCaMP3). Protocols for basic molecular biology experiments (agarose gel electrophoresis, DNA ligation, primer design, PCR, restriction cloning, etc.) were performed according to Addgene protocols (https://www.addgene.org/protocols/).

II.2.1 Tubecamp1（TC1, EMTB-GCaMP3）

TC1 is constructed by restriction digesting and ligating the GCaMP3 fragment and the EMTB fragment into a common vector. The entire GCaMP3 sequence (Addgene #22692) was excised using restriction enzyme BglII and NotI. The fragment was treated with Klenow to fill in 5' overhangs before being inserted it into the StuI site of pCS2+ vector (Addgene #2295) (Turner and Weintraub, 1994), resulting in the pCS2-GCaMP3 plasmid (Li et al., 2016). Next, the EMTB sequence (amino acids 18-282 of ensconsin, GenBank reference sequence X73882)

was cloned from the EMTB-mCherry plasmid (Addgene #26742) (von Dassow et al., 2009) using the following two primers (forward and reverse respectively): 5'-TAT GAA TTC ACC ATG GCA GTG CGA AGC GAA ACA-3' and 5'-TAT GAA TTC GAA GAG CCC TCA GGT GG -3'. The EMTB fragment was digested with EcoRI followed by inserting into pCS2+GCaMP3. To prevent the recircularization of the linearized vector and thereby improve the yield of the product containing the appropriate insert, the 5' end of the linearized vector was dephosphorylated by calf intestinal alkaline phosphatase (CIAP, Invitrogen) before the incorporation of fragments. The resultant plasmid, TubeCamp1 (pCS2-EMTB-GCaMP3) or TC1, expresses EMTB at the N-terminus followed by the original GCaMP3 coding sequence including its N-terminal poly-His tag (Tian et al., 2009). These cloning manipulations also created a seven-amino-acid insert (NSRDLAT) between EMTB and the initiating methionine of GCaMP3. The gist of plasmid design and working principle is illustrated in **Chapter III**, **Figure III.1**. Detailed TC1 vector map and engineering pipeline are presented in **Appendix**, **Figure S3** and **Figure S4**.

II.2.2 Tubecamp4 (TC4, mCherry-EMTB-GCaMP3)

TC4 is a construct based on TC1 using In-Fusion® cloning to combine the TC1 vector and an mCherry moiety (Raman and Martin, 2014). The idea of In-Fusion® cloning is to use an enzyme mixture to fuse DNA fragments by recognizing a 15-bp overlap at their ends; therefore the key step is to design primers such that the ends of the amplified insert have a 15-bp homology to the corresponding ends of the linearized vector[16]. The plasmid TubeCamp1

[16] https://www.takarabio.com/learning-centers/cloning/in-fusion-cloning-guide , In-Fusion® cloning protocol is the product of Takara Bio Group (Raman, 2014).

(pCS2-EMTB-GCaMP3) was linearized by inverse PCR using the following primers (5'- ATG GCA GTG CGA AGC GAA AC -3' and 5'- GGT GAA TTC GAA TCG ATG GGA TCC TG -3'). The complete reading frame for mCherry was amplified using the following PCR primers (5'- CGA TTC GAA TTC ACC GCC ACC ATG GTG AGC AAG -3' and 5'- GCT TCG CAC TGC CAT CTT GTA CAG CTC GTC CAT G -3'), resulting in a PCR product containing 15bp homology to the linearized EMTB-GCaMP3 plasmid on either side of the mCherry reading frame. These two products were combined by In-Fusion® cloning to generate mCherry-EMTB-GCaMP3, which contains an MAV insert between the mCherry and EMTB reading frames. The gist of plasmid design and working principle is illustrated in **Chapter V**, **Figure V.1A**. Detailed TC4 vector map and engineering pipeline is presented in **Appendix**, **Figure S3** and **Figure S4**.

II.2.3 Plasmid DNA and mRNA preparation

To produce stock plasmid DNA for further use, bacterial transformation and culture were performed using XL10-Gold® Ultracompetent Cells (Stratagene, cat. no. 200314). Heat shock, bacterial growth and streaking on an agar plate with 100 μg/ml ampicillin were carried out following the product's manual[17]. Then the bacteria from a single colony were further cultured in LB (Lysogeny broth) at optimal conditions (see manual). The plasmids were harvested and purified using QIAGEN plasmid PlusMidi Kit (Qiagen, cat. no. 12943). The purified plasmids were dissolved in distilled water and stored at 4 °C. All the details were following the kit's instructions[18].

[17] https://www.chem-agilent.com/pdf/strata/200314.pdf , for using XL10-Gold® Ultracompetent Cells.
[18] http://tiny.cc/plasmidmidi , for using QIAGEN plasmid PlusMidi Kit. The short URL is generated by tiny.cc.

A portion of the stock plasmids was linearized with NotI and transcribed *in vitro* using mMESSAGE mMACHINE™ SP6 Transcription Kit (Ambion, AM1340) following the manufacture's user guide[19]. Each reaction of 20 µL volume yields 15–25 µg of Capped RNAs (7-methyl guanosine cap structure — cap analog [$m^7G(5')ppp(5')G$] — at the 5' end, protecting RNA from exonuclease digesting) which mimic most eukaryotic mRNAs *in vivo*. The products were then purified and dissolved in nuclease-free water and stored at -80 °C for future use.

II.2.4 Nucleic acid verification

To confirm the size of the DNA/RNA product, agarose gel electrophoresis was performed followed by linearization using routine procedures (Green and Sambrook, 2019). To check the size of a specific insert sequence in the plasmid, PCR was performed to amplify the corresponding sequence using the primers described in **II.2.1** and **II.2.2**.

To validate the plasmid sequence at base-pair resolution, plasmid samples were sent to StemCore Laboratories (Ottawa Hospital Research Institute) for diagnosis[20]. The samples were sequenced by 3730 DNA Analyzer (Applied Biosystems), an automated Sanger sequencer, with the primers for the promoter region (SP6 for pCS2+ vector). The output files (~800–1000 bp) were aligned and compared with insert sequences by SnapGene 3.2.1 (GSL Biotech). The chromatogram of mismatched regions identified by SnapGene was double-checked by Chromas 2.6.2 (Technelysium Pry Ltd.).

[19] https://assets.thermofisher.com/TFS-Assets/LSG/manuals/cms_055516.pdf , manual for mMESSAGE mMACHINE™ SP6 Transcription Kit.
[20] http://www.ohri.ca/stemcore/LaboratoryServices/DNASequencing.aspx , protocol details of the DNA sequencing used in the facility.

II.3 Microinjection methods

II.3.1 Equipment and operations

Glass needles (Drummond, cat. no. 1-000-0300) for microinjection were pulled by P-97 micropipette puller (Sutter Instruments) using the manufacturer's recommended program for *Xenopus* oocyte microinjection[21]. This created a pipette (*i.e.* glass needle) which had a taper of ~10 mm and an opening tip of ~5 µm. We further cut 1/4 to 1/3 of the taper for more precise control of the injection volume. Injections were controlled and conducted with PLI-100 (on stage, Medical Systems Corp.) or PLI-100A (on the bench, Warner Instruments) pico-litter injector. The injection volume was adjusted by changing the injection time and pressure so that the needle expulsed 2.5–10 nL per injection. For mRNA injection, the needle was inserted into the oocyte equator for about 20-50 µm and a volume typically of 5–30 nL was injected. For nuclear injection, the needle was inserted into the middle of the animal sphere for about 20-50 µm and a volume typically of ~3–5 nL was injected. The oocyte equator and animal sphere are illustrated in **Figure I.1**.

II.3.2 Artificial egg activation

In response to sperm penetration, mature eggs arrested at metaphase II oocytes will resume meiosis with a global Ca^{2+} elevation. The penetration can be mimicked by an artificial prick, and the consequence — egg activation in the absence of paternal and maternal pronuclear fusion — is called parthenogenetic activation. We pricked the egg (in OR2 medium plus 1mM Ca^{2+} or OR2+ medium; the presence of Ca^{2+} is crucial in this case) with a glass

[21] https://www.sutter.com/PDFs/pipette_cookbook.pdf , chapter 9, for *Xenopus* oocyte injection.

needle (same as injection needle described in **II.3.1**) near the equator and then withdrew it as soon as possible. The success of activation can be assessed by (1) the deepening of pigmentation around the prick site and (2) the redistribution of the cortical pigment in the animal hemisphere *i.e.* cortical contraction (Sive et al., 2000). This contraction would become obvious in about 30 seconds after prick. If the oocyte had been activated, a global calcium elevation was started at the point of puncture and then swept the whole cortical region. We exploited this mechanism to evaluate the capacity of Ca^{2+} probes (Li et al., 2016).

II.4 Confocal microscopy systems and image presentation

Three major confocal systems were employed in this study. The choice of systems for an individual experiment was the trade-off among capability, imaging speed, resolution, convenience and cost. In general, for experiments that required UV photolysis and microinjection on the fly, we used an MRC-1024 laser scanning confocal imaging system (Bio-Rad Laboratories, Inc. Software: LaserSharp2000) with an electronic shutter (LAMBDA SC, Sutter Instrument) and an on-stage micro-injector (Tritech Research). For experiments that needed good resolution and fast imaging, we used Quorum spinning disk confocal system (Quorum Technologies Inc. Software: Metamorph) integrated with an EM-CCD camera. For experiments of fixed samples and some live cell images, we used the Zeiss LSM880 system (Carl Zeiss Inc. Software: Zen2 black version) with the Airyscan module for optimal visualization while the total capture time is compromised (Korobchevskaya et al., 2017). Airyscan microscopy improves the imaging power by utilizing the extra light that is normally rejected by pinholes. The extra light is collected by multiple detectors. Pixel reassignment (combing information from multiple detectors) and image deconvolution (using a computer

algorithm to correct the optical distort caused by filter and objective) was performed on Zen2 blue version (Sheppard et al., 2013; Weisshart, 2014).

To avoid confusion and redundancy, microscopy used for individual experiments would only be mentioned in the result section or figure legend when the information was considered important to the reasoning. The detailed microscopy methods used in all experiments are listed in the **Appendix** (**Microscopy in the results**, **Table S1**).

For thick specimens (intact *Xenopus* oocytes), confocal images were captured along the *z*-axis in a step-by-step fashion (**Figure II.1A**, top row). The images were further processed and analyzed by ImageJ-FIJI (Schindelin et al., 2012) or Volocity 6.3 (Quorum Technologies Inc.). For 3D-image presentations, we first reconstructed 3D volume by Volocity and then took snapshots at a proper perspective (**Figure II.1A**, bottom left). Typical examples (used throughout the whole thesis) of spindle presentations are shown in **Figure II.1A**, bottom right panel. Images were sometimes recorded as time series at fixed temporal intervals *i.e.* multifocal plane (4D) timelapse imaging (Li et al., 2016; Shao et al., 2012; Varjabedian et al., 2018; Zhang et al., 2008). All the manipulation and use of images conformed to the ethical guideline for scientific digital image processing (Cromey, 2010).

Figure II.1 Methods for image presentation, *in vitro* spindle assembly and UV-photolysis
(A) Schematics show image acquisition and presentation.
Top: Confocal images of a thick specimen (*e.g. Xenopus* oocyte) are acquired at a fixed *z*-step (ranging from 0.2 μm to 3 μm in our study). Each scan of a confocal plane is called a *z*-section.
Bottom left: *z*-stacked images (acquired confocal images) are reconstructed into a 3D object by software processing (Volocity 6.3), which allows 360-degree free rotation. The 3D object can be snapshotted and presented by perspective projection onto a 2D plane.
Bottom right: Shown confocal images are representative ones of the same spindle displayed by different approaches that are indicated by the corresponding texts and cartoons. Green: microtubule. Red: DNA.
(B) A flow chart exhibits basic steps for making *Xenopus* egg extracts and assembling spindles. Thumbnail cartoons illustrate specimens under a dissecting microscope. The 1st panel: Sperm nuclei droplets (5–10 nL for each) are made by using a tip-opening glass pipette under the mineral oil. 2nd panel: 200–300 nL oocyte cytoplasm is aspirated by a tip-opening glass pipette that punctures into the oocyte. 3rd panel: To make extract droplets (50–100 nL for each), oocyte cytoplasm is expelled out of the glass pipette onto sperm nuclei. 4th panel: It usually takes 30–60 minutes for bipolar spindle formation following the addition of extract onto nuclei. Confocal images show extract spindles that are labeled with microtubule marker (green) and chromosome marker (red).
(C) Schematics show the photolysis approaches of microscope setup (bottom left), and intracellular environment changes following UV exposure to Caged IP_3 (top left), diazo-2 (top right) and colcemid (mid-right).
Microscope setup: UV light is generated by a mercury light source through a bandpass filter (350 ± 50 nm). The exposure time is controlled by an electronic shutter that can be manipulated through a program. After reflection by a dichroic mirror, UV light reaches samples through the objective in the same optic path as the confocal laser. An inset on the upper-left corner shows an oocyte with the animal pole (spindle spot) attached to the glass surface right above the objective.
Uncaging IP_3: Upon UV flash, IP_3 is uncaged from NPE binding. IP_3 subsequently activates IP_3R and opens a channel mouth for Ca^{2+} releasing from ER lumen.
Uncaging BAPTA: Following UV illumination, diazo-2 is photolyzed into a BAPTA equivalent, which captures Ca^{2+} faster and has a much higher Ca^{2+} affinity than the unphotolyzed form.
Colcemid inactivation: Before photolysis, colcemid depolymerizes microtubules and inhibits spindle formation. After UV exposure, colcemid is inactivated and the spindle reforms.

Figure II.1 Methods for image presentation, *in vitro* spindle assembly and UV-photolysis

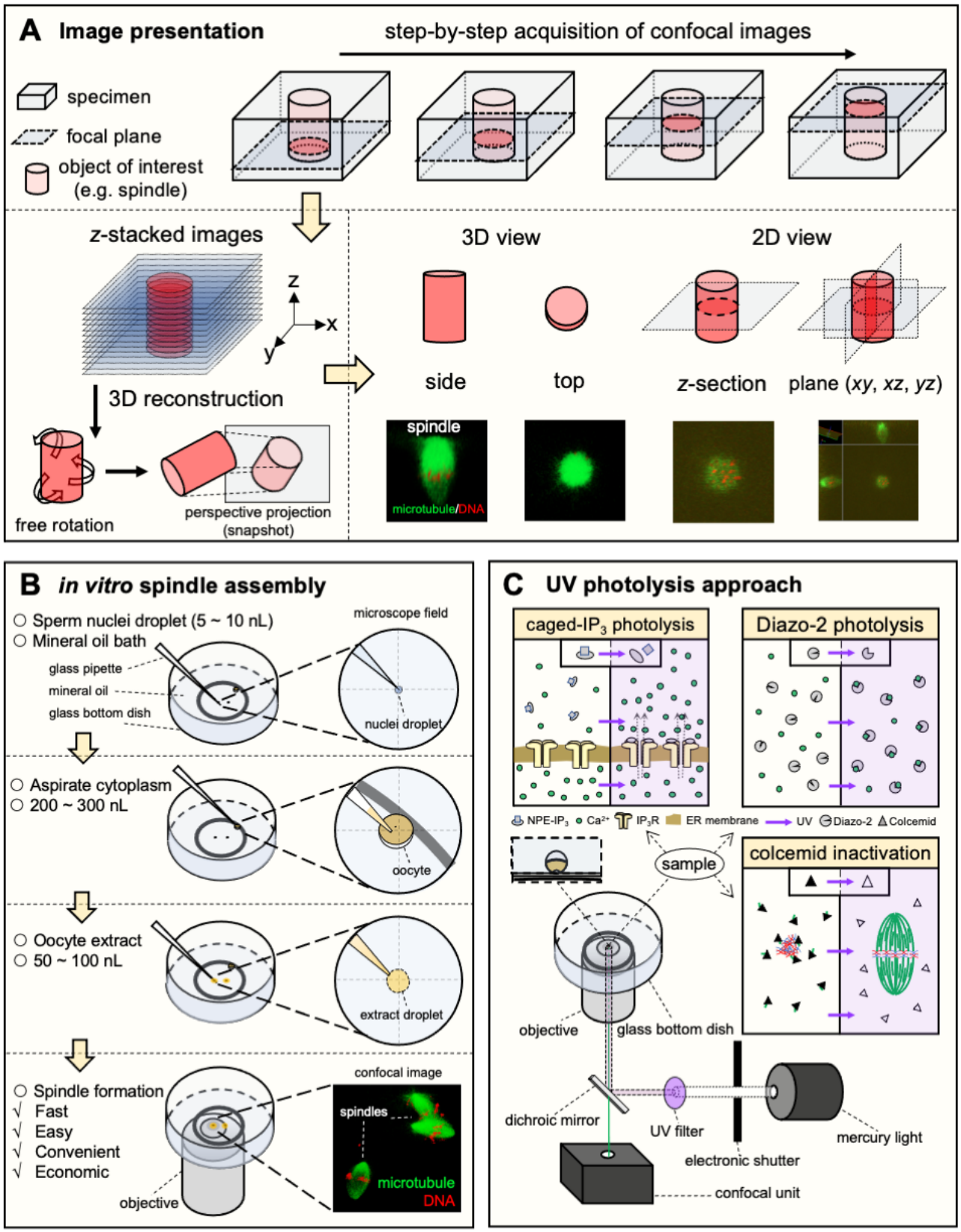

II.5 Imaging spindles in *Xenopus* oocytes

On the experiment day, oocytes cultured in OCM were primed with progesterone to trigger oocyte maturation (or prophase I resumption). It usually took 3–5 hours to reach the point of GVBD, manifested by the appearance of a white maturation spot on the animal pole. GVBD oocytes were individually transferred to fresh OR2 medium (82.5 mM NaCl, 2.5 mM KCl, 1.0 mM Na_2HPO_4, 3.8mM NaOH, 1.0 mM $MgCl_2$, 5 mM HEPES, pH 7.4) with 1mM $CaCl_2$. Most *Xenopus* oocytes completed meiosis I in 2 hours and reached metaphase II around 3 hours after GVBD (**Figure I.1C.c**). Our live images were captured within this time frame. *Xenopus* oocyte live imaging was performed under room temperature and no special atmosphere conditioning was required.

When an oocyte was ready for imaging, it would be placed upside-down (animal pole downwards) on a glass-bottom microwell dish (MatTek Corp., P35G-0-10-C or P35G-1-10-C, a cartoon illustration can be found in **Figure II.1C,** microscope setup). The white spot, where the spindle was located inside, was closely attached to the glass and observed through a 63x oil objective on an inverted microscope system. Since the spindle was perpendicular to the object lens, each scan represented a section along the z-axis (*i.e. z*-section, **Figure II.1A** top row). The animal sphere of the oocyte had moderate opacity, but the imaging depth was about 50 μm. This made the inner pole of the spindle dimmer than the outer pole contacted to the cortex (**Figure II.1A,** side view). To inspect the spatial details of the specimen during the experiments, the volume (*i.e.* 3D-image) was reconstructed from multiple sections by software (**Figure II.1A**, bottom left panel). In general, we obtained images in a step of 1–3 μm along the z-axis, or 0.2–1 μm if a higher resolution was preferred. The spindles were about 20–40 μm in longitude, hence 15–30 images were generated for lower resolution images and 50–100

for higher. Timelapse image series were collected at various time intervals, ranging from tens of seconds (*e.g.* anaphase) to several minutes (*e.g.* prometaphase to metaphase), depending on the stage of the meiosis.

II.6 Assembling spindles in cell extracts from a single oocyte

Spindle assembly *in vitro* has been extensively studied for decades but it requires heavy work and laborious preparation (Maresca and Heald, 2006). Here, a novel method that makes cytoplasmic extract from a *single* oocyte is described. This approach can significantly shorten the preparation time (from hours to minutes) and largely reduce the use of reagents. The essential steps are illustrated in **Figure II.1B**.

Demembrenated sperm nuclei (~ 500 nuclei/μL), as chromosome donors, were made and stored in -80 °C according to detailed protocol presented elsewhere (Hazel and Gatlin, 2018; Ohsumi et al., 2006). On the experiment day, the stored sperm nuclei were diluted with NPB buffer (nuclear preparation buffer; 1 mM EDTA, 15 mM HEPES, 0.5 mM spermidine, 0.2 mM spermine, 250 mM sucrose, pH 8.0). Hoechst 33342 (Invitrogen, H1399) was added to the final concentration of 1 μg/mL to label DNA. For the convenience of confocal imaging, a petri dish with a thin coverslip at the bottom was used as a container. With the assistance of a micro-injector and glass needle, NPB buffer containing sperm nuclei was made as droplets (**Figure II.1B**, the 1st panel) covered by mineral oil (Sigma-Aldrich, M8410). Mineral oil helped to maintain the shape of the droplet (due to surface tension) and prevented evaporation. Oocytes at metaphase II were prepared and placed onto the same dish for making cytoplasmic extracts. A glass pipette attached to the micro-injector with a tip-opening of ~30 μm was used to puncture into the oocyte from the animal hemisphere. Oocyte cytoplasm was then slowly

aspirated into the glass pipette by applying negative pressure (**Figure II.1B**, 2nd panel). Once the desired volume was collected (~200–300 nL), the cytoplasm would be expelled (by applying positive pressure) onto the sperm nuclei (~5–10 nL). Two paralleled cytoplasm droplets (~50–100 nL) were generally made from each oocyte (**Figure II.1B**, 3rd panel). Following cytoplasm addition onto nuclei, it usually took 30–60 minutes to form a bipolar spindle (**Figure II.1B**, 4th panel). If needed, chemicals were delivered by micro-injector, typically in a volume less than one-tenth of the droplets.

II.7 Photolysis experiments

In our study, three light-sensitive chemical compounds were used for targeted perturbation of a biological process: NPE-caged inositol 1,4,5-triphosphate (or caged IP_3), diazo-2 (or caged BAPTA), and colcemid. See below for details, and **Figure II.1C** for graphic illustration.

NPE-caged [22] inositol 1,4,5-triphosphate or "caged IP_3" (Invitrogen, I23580), is biologically inactive before photolysis (Ellis-Davies, 2007). The stock solution was prepared at 0.5 mM in water and stored at -20°C. On the experiment day, caged IP_3 was injected into the oocytes at a final concentration of 1–1.5 μM (20–30 nL of the stock) about 30 mins to 1 hour before UV exposure. UV illumination results in a rapid and highly localized release of free IP_3. It is usually used for generating a localized high concentration of Ca^{2+} through opening IP_3R channels on ER membrane (**Figure II.1C**, uncaging IP_3) (Smith et al., 2009).

[22] NPE stands for 1-(*ortho*-nitrophenyl)-ethyl, a caging chromophore that bonds IP_3 and greatly reduces the affinity of IP_3 to IP_3R. The bond can be broken by UV absorption (Ellis-Davies, 2007).

Diazo-2 (Invitrogen, D3034), or "caged BAPTA"[23], is a photoactive Ca^{2+} scavenger (Zucker, 2010). Stock solution was prepared at 2 mM in water and stored at -20°C. On the experiment day, caged IP_3 was injected into the oocytes at a final concentration of ~6 μM (30 nL of the stock for each oocyte) about 30 mins to 1 hour before UV exposure. Following UV excitation (wavelength of ~360 nm), it will be photolyzed from a weak chelator to a high-affinity BAPTA-equivalent (Diazon-2 photolyzed form, K_d = 73 nM) that can rapidly bind to cytosolic free Ca^{2+} (**Figure II.1C**, uncaging BAPTA) (Adams et al., 1989; Li et al., 2016). The higher Ca^{2+} affinity is likely due to an increase of K_{on} (see footnote).

Colcemid[24] (Sigma-Aldrich, D7385), also known as demecolcine, is a UV-labile chemical that depolymerizes microtubules hence blocking spindle formation during M-phase (Shao et al., 2013; Sluder, 1979). The stock solution was prepared at 50 mM in DMSO and stored at -20°C. On the experiment day, the solution was added into oocyte culture medium at a final concentration of 50 μM at the time of GVBD. 3 h after GVBD (when control oocytes were in metaphase II), the oocytes were transferred to colcemid-free OR2 medium and ready for UV excitation. Upon photolysis, it becomes ineffective and the bipolar spindle reforms (**Figure II.1C**, colcemid inactivation) (Shao et al., 2013).

For the implementation of photolysis in the MRC-1024 microscope system (**Figure II.1C**, bottom left), a mercury light source was set up in the system with a UV bandpass filter (Chroma 11000V3, 350/50 nm). During the experiment, the oocyte animal pole (where the

[23] "Diazo-2" is named after an extra electron-withdrawing diazoketone group that is bonded to the aromatic ring of BAPTA. The high K_{on} (compared to EGTA) and Ca^{2+} affinity of BATPA is much attributable to the negative charge of its aromatic rings (Tsien, 1999), which can be largely weaken by bonded diazoketone. The bond is photolyzable.

[24] Colcemid is a trademark. Its generic name is N-methyl-N-deacetyl-colchicine.

spindle spot located[25]) was exposed to UV excitation through the same 63x oil objective that was subjected to confocal laser scanning (Shao et al., 2013). UV exposure time was precisely controlled by an electronic shutter (LAMBDA SC, Sutter Instrument) via the manufacturer's program (LAMBDA SC utility and LAMDA TEST).

II.8 HeLa cell methods

HeLa cells were transfected via Lipofectamine (Invitrogen, 11668019) according to the manufacturer's instruction[26]. Transfection was carried out on glass-bottom dishes coated with poly-lysine. Transfection buffer consists of the following components for each 35 mm dish: 0.25 μg of mCherry-EMTB and 0.13 μg of TubeCamp (plasmids), 4 μL of Lipofectamine, 2 mL of OptiMEM medium (Gibco, 31985088) plus 5% fetal bovine serum (FBS). The incubator was conditioned to 37 °C and 5% CO_2 mixed with air. The cells (~90% confluence) were incubated in the transfection mixture for 6 hours followed by change into a fresh α-MEM medium (Gibco, 12561072) plus 5% FBS.

Transfected cells were imaged either directly in the transfection dishes the next day or were split into new glass-bottom dishes and imaged on subsequent days. Prior to imaging, Hoechst 33342 was added to 1 μg/mL to the cells for 5 minutes before changes into the dye-free medium. The live-cell imaging was performed in an air-conditioned chamber (37 °C and 5% CO_2).

[25] For the location of spindle spot, see **Figure I.1C**, from prometaphase to metaphase II, top row.
[26] http://tiny.cc/Lipofectromine , for Lipofectamine transfection protocol. The URL is shortened by tiny.cc.

II.9 Immunofluorescence protocol for *Xenopus oocytes*

In circumstances where live imaging was not convenient (*e.g.* no antibodies of interest or high-resolution images were required, etc.), immunofluorescence tests were performed. Generally speaking, compared with regular immunofluorescence methods, extra incubation times were implemented in each step since the large size of *Xenopus* oocytes hampers the penetration of antibodies (Becker and Gard, 2006). Our procedure described here was based on Becker's method with modification. After oocyte defolliculation (see **II.1**), collagenase (Sigma-Aldrich, C6885) digestion was conducted to remove the follicle cells around the oocytes (Liu and Liu, 2006). The oocytes were then kept at 18 °C overnight to recover from potential digestion damage. On the next day, oocytes were primed to resume meiosis and then fixed by 100% methanol (at least 4 hours, or overnight) at the desired stage. After being rinsed, the fixed samples were penetrated with TBST (1mM Tris-HCl, 15.5 mM NaCl, 0.1% Triton X-100, pH 7.4) for 2 hours. Primary antibodies were then applied with TBST plus 2% BSA and the samples were incubated for 24 to 48 hours at 4°C. The extra antibodies were washed off by TBST for 48 hours (buffer was changed every 8 hours). For dual fluorescence, the other primary antibodies would be applied after this step, and the washing step was repeated. Following the wash-out, the fluorescent conjugated second antibodies (in TBST + 2% BSA), together with Hoechst 33342 (1 μg in 200 uL), were incubated with samples for another 24 to 48 hours at 4°C. The second antibodies were washed out and the oocytes were ready for slide mounting. A rotary mixer was used in all the incubation and washing steps. Next, the oocytes were hemisected by a sharp scalpel and the animal halves were mounted on glass depression slides (with a thick cavity at the center, purchased from VWR, 470235-728) with the mounting

solution (Santa Cruz Biotech, sc-24941). Lastly, the samples were covered with thin coverslips (0.085 to 0.15 mm) and sealed by regular nail oil (transparent).

II.10 Other reagents

In this section, selected probes and reagents that are not covered in previous methods are listed.

II.10.1 Organic Ca^{2+} probes

Several solvable Ca^{2+} probes were used in this study: Oregon Green 488 BAPTA-2 or "OG-2", $K_d[Ca^{2+}]$ = 580 nM (Invitrogen, O6808). Oregon Green 488 BAPTA-6f or "OG-6f", $K_d[Ca^{2+}]$ = 3 μM (Invitrogen, O23990). We referred to Invitrogen's molecular probes handbook for detailed properties and applications (Johnson and Spence, 2010). The chemicals (salts) were dissolved in water (2–4 mM) and stored at -20°C. To minimize their potential interference with spindle physiology we injected the chemicals prior to the imaging as late as possible (usually ~30 minutes) at the final concentration of micromolar range (2.5–5 μM). This concentration is as ~1/100 as the IC_{50} value of causing spindle dysfunction (**Table I.1**).

II.10.2 Plasmids

Numerous plasmids were used to express fluorescent protein markers. The cloning, diagnosis and mRNA preparation methods were described in **II.2.3 – II.2.4**.

pCS2+ (Addgene #2295) is a backbone vector routinely used in our laboratory. Its CMV promotor can be primed by *Xenopus* oocytes for transcription.

pCS2-EMTB-3XGFP (Addgene #26741, expressing microtubule-binding domain of ensconsin as a microtubule marker), pCS2-EMTB-mCherry(Add gene #26742, expressing microtubule-binding domain of ensconsin as a microtubule marker), pCS2-eGFP-C2 (expressing C2 domain of PKCβ) and mCherry-α-tubulin (a microtubule marker) were gifts from William Bement (Kita et al., 2019; Miller and Bement, 2009; Yu and Bement, 2007).

CMV-NLS-RGECO (Addgene #32462) was a gift from Robert Campbell and the functional sequence was subcloned into pCS2+ vector in our laboratory. RGECO is a red-shifted variation of GCaMP3, whose fluorescence increases upon Ca^{2+} binding (see **I.3.3**) (Zhao et al., 2011).

pCS-H2B-EGFP and pCS-H2B-RFP was a gift from Aaron Straight and served as chromosome markers (expressing histone 2B).

sfGFP-ER-3 (Addgene #56482) was a gift from Michael Davidson. As an ER marker, it expresses calreticulin signal peptide plus KDEL ER retention signal peptide (Salo et al., 2019).

GFP-IP3R1-N was a gift from Katsuhiko Mikoshiba and served as an IP_3R marker. GFP-IP3R1-N was achieved by subcloning full-length IP_3R1 (mouse origin) fusing with the N-terminus of EGFP sequence into pcDNA3.1/Zeo+ (Zhang et al., 2003). *Xenopus* oocytes mainly express the type-1 IP_3R isoform (IP_3R1) (Kume et al., 1993; Parrington et al., 1998).

pCS2-Lck-mCherry was generated by inserting an Lck (or lymphocyte-specific protein tyrosine kinase) fragment into the pCS2+mCherry vector (Li et al., 2016; von Dassow et al., 2009). The “Lck fragment” refers to the N-terminal 26-amino-acid membrane-targeting sequence of Lck (Src tyrosine kinase). Lck fragments were achieved by PCR-amplifying the

Lck fragment sequence (26 amino acids at the N-terminus) of Lck-GCaMP3 plasmids (Addgene #26974) (Shigetomi et al., 2010b).

II.10.3 Primary Antibodies

For dual immunofluorescence, we used the combination of rabbit polyclonal plus mouse monoclonal primary antibodies (dilution range: 1:50–1:200). See **II.9** for a detailed procedure.

Rabbit polyclonal antibodies: IP3R-1 antibody (H80) (Santa Cruz, sc-28614) was for oocyte immunostaining. An anti-calmodulin antibody (Sigma-Aldrich, SAB4503194) was used to locate potential endogenous calcium sensors (Li et al., 2016). Anti-tubulin β (H-235) (Santa Cruz, sc-9104) or β-tubulin (DM1B, ICN) was used as the spindle microtubule marker.

Mouse/Rat monoclonal antibodies: 4C11, an antibody (rat) against IP_3 receptors, was a gift from Katsuhiko Mikoshiba (Kume et al., 1993). It was used for HeLa cell immunostaining. Anti-β-tubulin (Sigma-Aldrich, T5201, mouse source) was used as a spindle microtubule marker.

II.10.4 Chemicals and organelle probes

DB-BAPTA (K_d = 1.6 μM) and EGTA (K_d = 180 nM) was deployed as "typical" fast and slow Ca^{2+} chelators, respectively (Li et al., 2016). A program — MaxChelator — was used (Bers et al., 2010) [27] to calculate the ratio of Ca^{2+} buffers over $CaCl_2$ (EGTA : $CaCl_2$ = 4:1; DB-BAPTA : $CaCl_2$ = 10:1) to give the desired free Ca^{2+} concentration,∼140 nM (Busa and Nuccitelli, 1985). The calcium buffers used in oocyte-extract experiments were based on this

[27] https://somapp.ucdmc.ucdavis.edu/pharmacology/bers/maxchelator/index.html, developed by Chris Patton, Stanford.

consideration. During most experiments, we injected the buffer to a final concentration of ~1 mM (30 nL injection), if not specified.

S-trityl-l-cysteine or STLC (Tocris Bioscience, 2799-0707), a small molecular inhibitor of Eg5 (kinesin-5), is routinely used for generating monoastral spindles (Shao et al., 2013). The stock solution was prepared at 50 mM in DMSO and stored at -20°C. STLC (5–10 μM, final concentration) was added to OCM upon progesterone stimulation (See **II.1**) and presented throughout the whole experiment without wash-out.

N,N,N′,N′-tetrakis(2-pyridinylmethyl)-1,2-ethanediamine or TPEN (Sigma-Aldrich, P4413), a zinc-chelator, was dissolved in ethanol at 5 mg/ml and stored at -20°C. It was used for testing if zinc was involved with spindle physiology. Previous studies have shown egg activation requires zinc signaling (Duncan et al., 2016; Sun et al., 2007).

Tubulin protein, Rhodamine labeled (Cytoskeleton, Inc., TL590M) has a maximum excitation wavelength at 547 nm and resistant to UV photobleaching. It was used as the microtubule label and in some experiments where the other microtubule probes (e.g. mCherry-EMTB) might have potential fluorescence quenching problems. The chemical powder was dissolved in water to 5 mg/ml just before the experiment, and the solution was directly micro-injected into the oocytes or oocyte extracts.

Heparin (Sigma-Aldrich, H4784) is a classical IP_3R inhibitor. It was dissolved in water (for experiments in intact cells) or OR2 medium (for experiments in oocyte extracts) at a concentration of 10–50 mg/mL and stored at -20°C. On the experiment day, heparin stock solution was directly injected into the system at a final concentration of 200 μg/mL (in oocyte extracts) or 300 μg/mL (in intact oocytes).

GMPCPP or GpCpp (Jena Bioscience, NU-405S) is a non-hydrolysable GTP analog that prevents microtubule from depolymerization after binding to the tubulins (Hyman et al., 1992; Wehland and Sandoval, 1983). The stock was made in the water at a concentration of 10 mM and kept at -20°C. On the experiment day, GMPCPP was injected into the oocyte at a final concentration of 1 mM.

Triton X-100 (Sigma-Aldrich, X100) is a common non-ionic surfactant that was used for cell penetration and washing in our immunofluorescence protocols (see **II.9**). When used in low concentration, it is considered as a comparatively mild, non-denaturing detergent for lysing cellular membrane (van de Ven et al., 2009). To destroy the ER membrane while keeping the oocyte extract as viable as possible, a final concentration of 0.1% of Triton X-100 was made.

II.11 Statistics

Two-tailed Student's t-test was used to compare the statistical difference between experimental groups (**Figure III.2C, Figure III.4D, Figure III.6C, Figure IV.1A, Figure IV.2C, Figure IV.3C, Figure IV.4C, Figure IV.4B, Figure IV.5B, Figure V.2C**). For non-parametric tests (**Figure IV.4A, Figure S2A**), Fisher's exact test was used. For colocalization analysis (**Figure III.6D**), Manders' overlap coefficient was evaluated by the corresponding ImageJ plug-in (Manders et al., 1993). The threshold was set to the average value of a cytosolic region. For time-series experiments, data points at the same time were combined as mean values (**Figure IV.1B, Figure V.1B, Figure V.2B, Figure V.3B, Figure V.3C, Figure V.4C**) or representative curve from a single experiment was presented (**Figure III.2A', Figure III.3A', Figure III.5B**). A p-value less than 0.05 was considered to be significant (very

significant if <0.01) against the null hypothesis. All experiments were repeated at least 6 times if not specified. All acquired data were processed with Excel v16.35 (Microsoft Co.) or RStudio v1.2.5033 (RStudio, Inc.). Descriptive statistical data were analyzed and graphed by Prism v8.4 (GraphPad Software).

II.12 Artworks

Cartoons and schematics in this thesis are all original work by the author using Adobe illustrator v24.0.1 (Adobe Inc.), Adobe Photoshop v21.2.0 (Adobe Inc.), PowerPoint v16.35 (Microsoft Co.) or DeepDream (Developed by Alexander Mordvintsev). Chemical structures **(Figure I.4A)** are drawn using Chemdoodle Web Sketcher (iChemLabs, LLC.). Detailed vector maps and procedures are generated using SnapGene v5.2 (GSL Biotech) and edited by Photoshop and PowerPoint (**Figure S3** and **Figure S4**). Some molecule structure cartoons (elements in **Figure I.1B**) are inspired by the drawing from *Molecular Biology of the Cell* (sixth edition, Garland Science).

Chapter III Probing spindle-based Ca^{2+} signals

III.1 Introduction

The precise role of Ca^{2+} signaling in spindle assembly remains inconsistent and contentious for decades (Groigno and Whitaker, 1998; Keith et al., 1985; Kiehart, 1981; Marin, 2012; Whitaker, 2006b). A practical reason for this is the lack of evidence and approaches to show Ca^{2+} signals in an adequately spatiotemporal resolution. A previous report has shown the dramatic difference between the actions of EGTA and BAPTA on *Xenopus* oocyte spindles (Li et al., 2016). The result that only BAPTA is able to block spindle assembly could be explained by its fast Ca^{2+}-binding rate, disrupting the Ca^{2+} communication between its channels and sensors in a very short distance. The differential sensitivity of Ca^{2+} signaling to EGTA and BAPTA is well studied in other systems such as squid giant synapse, lymphocyte and pancreatic β-cell, suggesting a tight coupling between Ca^{2+} and its downstream effectors (Adler et al., 1991; Selway et al., 2012; Zweifach and Lewis, 1995). Therefore, BAPTA's action on spindles suggests a highly localized Ca^{2+} signaling, or calcium nanodomains, that contributes to spindle assembly and microtubule organization. However, previous studies failed to detect local $[Ca^{2+}]_i$ change at the spindle (Li et al., 2016).

One way to probe localized Ca^{2+} domains is using a targeted approach to engineer a genetically encoded Ca^{2+} indicator that fuses Ca^{2+} reporter to a region-specific marker. This targeted approach has proved to be a valuable tool for *in situ* monitoring of Ca^{2+} activities in many subcellular compartments (Despa et al., 2014; Luo et al., 2019; Luo and Hill, 2014; Tay et al., 2012); but it has been rarely reported in investigating spindle apparatus. In this chapter,

we attempt to probe the Ca^{2+} signal at spindles by constructing a novel Ca^{2+} probe, namely Tubecamp1 (TC1). We report the properties and behaviors of TC1, in combination with other reference probes, in various systems of spindle assembly.

III.2 Results

III.2.1 Constructing microtubule-tethered Ca^{2+} reporter TC1

To boost the local Ca^{2+} imaging capacity at the spindle region, we designed and engineered a plasmid encoding the microtubule-binding domain of ensconsin (EMTB) fused in frame with fluorescent calcium sensor GCaMP3. The detailed procedure has been described in **Methodology** (see **II.2.1**) and diagramed in **Figure III.1A, B** (see figure legends). The product, EMTB-GCaMP3, was dubbed Tubecamp1 (TC1). As the working principle for TC1 proteins, the EMTB unit binds to the microtubule while the local $[Ca^{2+}]_i$ elevation is indicated by the fluorescence change of the GCaMP3 unit (**Figure III.1C**). GCaMP3 is a circularly permutated variant of enhanced fluorescent protein (cpEGFP) flanked by a pair of molecular switches: the C-terminal calcium sensor calmodulin (CaM) and the N-terminal myosin light chain kinase M13 peptide (a CaM stabilizer) (**Figure III.1C**, left). On Ca^{2+} binding, CaM moiety interacts with the M13 subunit, triggering a conformational change of cpEGFP that leads to a significant increase of fluorescence intensity (**Figure III.1C**, right) (Tian et al., 2009).

Figure III.1 Schematic representation of TC1 production and working principle
(A) Schematics illustrate the design and engineering of Tubecamp1 or TC1. AA stands for amino acid. GBID stands for GenBank ID.
Upper: TC1 sequence comprises a microtubule-binding domain (AAs 18–282 of ensconsin, GBID: X73882) at N-terminus, an AA linker with a 6xHis-tag, a myosin light chain kinase or M13 peptide, a permutated EGFP moiety (AAs 149–238 at N-terminus and AAs 1–144 at C-terminus) with two point mutations (M153K and T203V), a CaM moiety with one point mutation (N60D) at C-terminus.
Lower: TC1-sequence-contained plasmid is generated by two-step of restriction cloning: GCaMP3 and EMTB sequences are inserted into pCS2+ vector in tandem.
(B) A schematic illustrates that TC1 mRNAs are transcribed *in vitro* from the linearized TC1 plasmid by sp6 polymerase. TC1 proteins are expressed in oocytes after mRNA injection.
(C) A cartoon illustrates the working principle of TC1. The probe reports microtubule-proximal $[Ca^{2+}]_i$ elevation. Ca^{2+}-bound CaM binds the M13 peptide (CaM stabilizer), leading to the change of the EGFP fluorophore that generates much more fluorescence (deprotonation of the fluorophore, see **I.3.3** for detailed explanation). On the other hand, the EMTB subunit can bind to the microtubule in an unbiased manner.

Figure III.1 Schematic representation of TC1 production and working principle

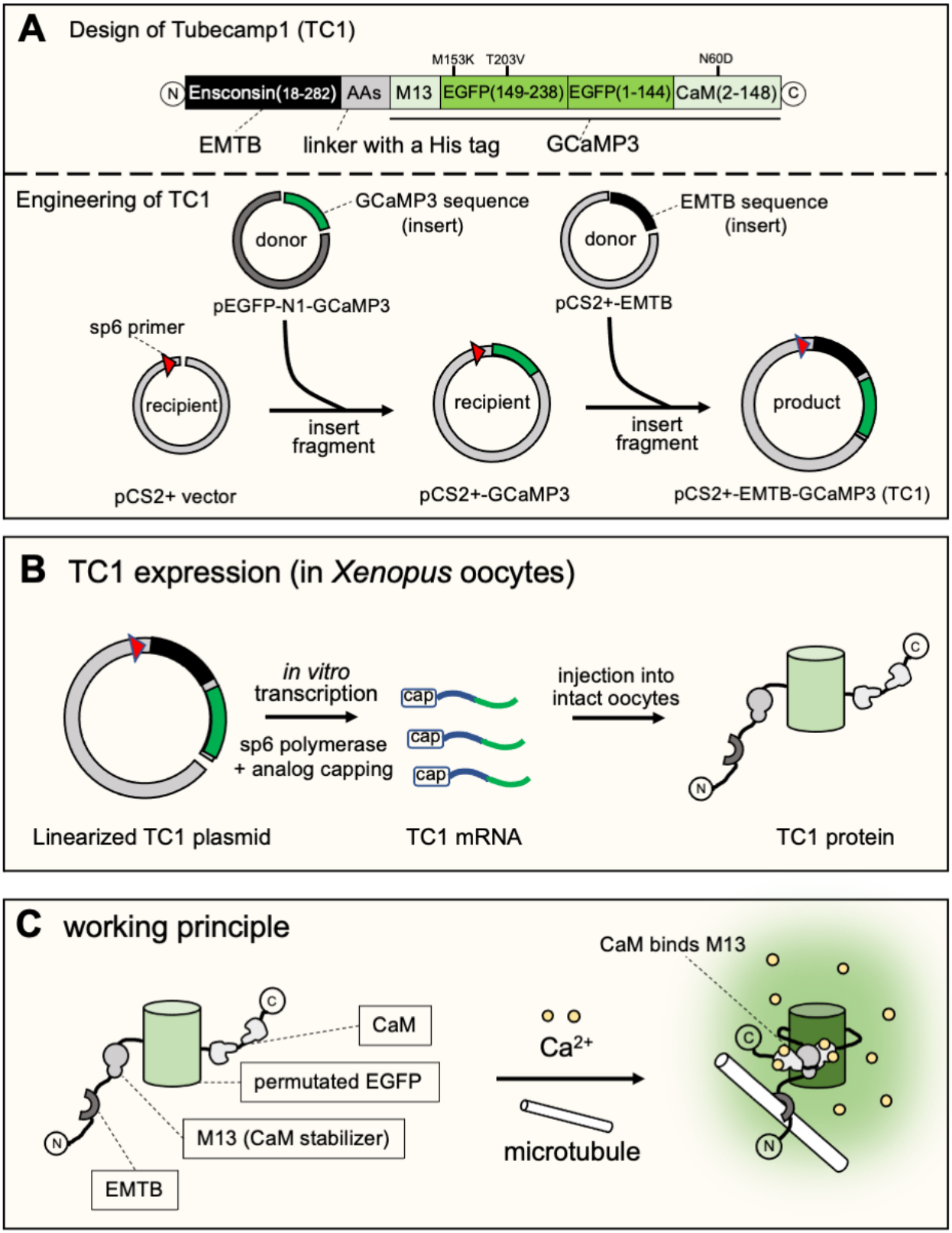

III.2.2 Testing TC1: $[Ca^{2+}]_i$ elevation during wound healing

As design verification, we tested TC1's function as a Ca^{2+} reporter and its capacity to bind microtubules by exploiting the well-studied wounding system in *Xenopu*s oocytes (Benink and Bement, 2005; Mandato and Bement, 2003; Varjabedian et al., 2018; Yu and Bement, 2007). Following oocyte wounding at the cortex, microtubules are transported to the wound, and a local $[Ca^{2+}]_i$ elevation plays a key role in regulating the healing process (Varjabedian et al., 2018).

We first expressed TC1 in *Xenopus* oocytes with RGECO, a popular Ca^{2+} reporter that is modified from GCaMP3 for red fluorescence (Zhao et al., 2011). Oocyte wounding was produced by a laser (**Figure III.2A**, the dashed circle indicates the laser focus) (Mandato and Bement, 2001). Before wounding, the oocyte cortex displayed low levels of both RGECO and TC1 fluorescence (**Figure III.2A**, -00:10, time in minute:second); immediately after wounding, both RGECO and TC1 fluorescence increased sharply in a large circular region (~30–35 μm in diameter) around the wound (**Figure III.2A**, 00:10). **Figure III.2A'** exhibited two line plots quantifying a region near wound (**Figure III.2A**, dashed square 2; **Figure III.2A'**, plot 2) and a region far from the wound (**Figure III.2A**, dashed square 1; **Figure III.2A'**, plot 1), respectively, over the recording course (290 seconds in total). While the global pattern of TC1 fluorescence paralleled that of RGECO in space and time (**Figure III.2A'**), the shape of the TC1 signal was distinctly filamentous (**Figure III.2A**). The difference can be explained by the microtubule-binding capacity of TC1, in contrast to RGECO which is a mobile probe without a targeted sequence.

Figure III.2 TC1 reports microtubule-proximal $[Ca^{2+}]_i$ during oocyte wound healing
(A) Representative time-series images (*xy*-plane view) of wounded *Xenopus* oocyte showing total $[Ca^{2+}]_i$ (RGECO; red) and microtubule-proximal $[Ca^{2+}]_i$ (TC1; green). Time in minute:second; sample wounded at 0 seconds. Dashed circle: laser-focused region. Small dashed squares: regions for fluorescence measurements (see **A'**). Scale bar: 25 μm.
(**A')** Fluorescence intensity plots of regions indicated as 1 and 2 in the first panel in A with 1 (top plot) distal to the wound and 2 (bottom plot) proximal to the wound. The temporal patterns of elevated $[Ca^{2+}]$ (RGECO; red) and TC1 (green) closely parallel each other.
(B) Representative time-series images of wounded *Xenopus* oocyte showing total microtubules (revealed by mCherry-EMTB; red) and microtubule-proximal $[Ca^{2+}]_I$ (TC1; green). The sample is wounded at 0 seconds. Prior to wounding (−00:04), cortical microtubules are labeled with mCherry-EMTB but not TC1. Shortly after wounding (00:04) microtubules within ~20 μm of the wound acquire green fluorescence; this fluorescence disappears as the wound heals. Time in minute:second. Dashed circle: laser-focused region. Solid rectangle: far-from-wound region for fluorescence measurement. Dashed rectangle: near-wound region for fluorescence measurement. Scale bar: 10 μm.
(B') Montage showing enlargement of a solid rectangle in the first frame of **(B)** at 4-second intervals. Wounding occurs between the 3rd and 4th panels and is accompanied by a local, microtubule-associated increase in green (TC1) but not red (mCherry-EMTB) fluorescence. The brackets and dashed lines above the montage indicate the corresponding measuring frames in **(B)**.
(C) Quantification of relative mCherry-EMTB and TC1 fluorescence on microtubules before (00:00) and after wounding (00:04) and within 10 μm or farther than 30 μm from the wound. Microtubules within 10 μm of wound undergo a significant increase in TC1 but not mCherry-EMTB fluorescence. Results are represented as: Mean ± S.D.; ** indicates $p < 0.0001$; n=11. NS: not statistically significant.

Figure 3.2 TC1 reports on microtubule-proximal $[Ca^{2+}]_i$ during wounding healing

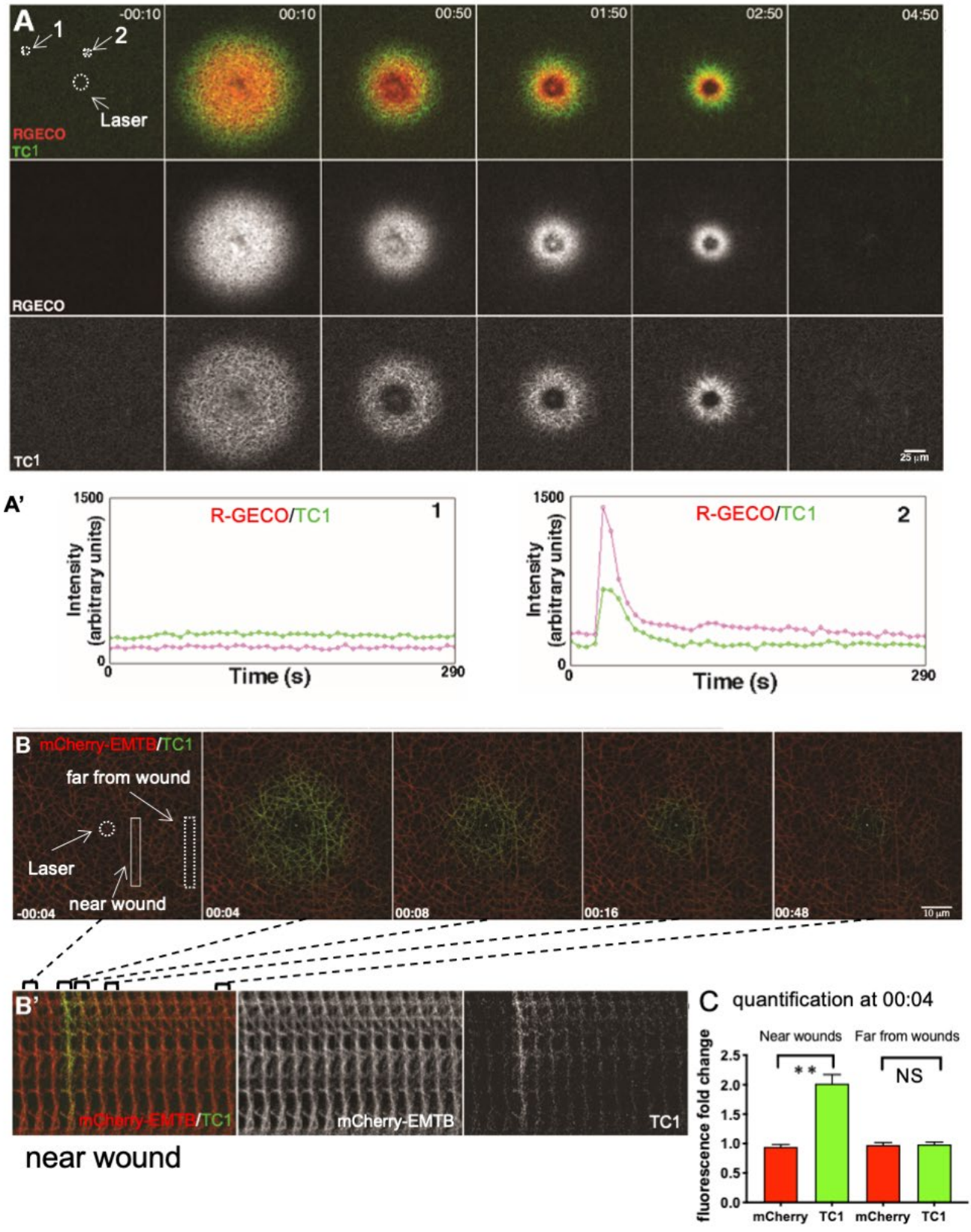

To further identify the filamentous structures detected by TC1, TC1 was expressed in combination with mCherry-EMTB (**Figure III.2B, B'**). mCherry-EMTB had the same targeted sequence as TC1 and was used as a microtubule marker in previous reports (Miller and Bement, 2009; Mooney et al., 2017; Uchida and Yajima, 2018). As expected, TC1 and mCherry-EMTB exhibited the same filamentous structures, meaning TC1 was indeed labeling microtubules (**Figure III.2B, B'**). Furthermore, in contrast to mCherry-EMTB which showed no fluorescence changes before and after wounding, the fluorescence of TC1 increased dramatically and transiently at microtubules in close vicinity (~10 μm) of the wound after laser damage (**Figure III.2B** a rectangular region for measurement, **Figure III.2B'** tiled rectangular regions from each time point, **Figure III.2C** quantification of fluorescence at rectangular region 4 seconds after laser wounding). These results showed that TC1 was capable to indicate microtubule-proximal $[Ca^{2+}]_i$ elevation.

III.2.3 Probing spindle-based Ca^{2+} signal by TC1 and OG-2 in *Xenopus* oocytes

III.2.3.1 TC1 reports distinct Ca^{2+} signal at the spindle poles

Having verified TC1's capacity to report microtubule-proximal $[Ca^{2+}]_i$ elevation, we next explored potential Ca^{2+} signals at the spindle during oocyte maturation.

TC1 was co-expressed with mCherry-EMTB in *Xenopus* oocytes. As shown in the previous section, mCherry-EMTB can serve as a reference for TC1 distribution since it labeled the same filamentous structures (microtubules) as TC1 (**Figure III.2B'**). Timelapse confocal microscopy was performed to observe TC1 signals change during oocyte maturation. At prometaphase I, TC1 fluorescence began to rise at the spindle microtubules close to the cortex (**Figure III.3A**, 00:36, time in hour:minute). As the spindle grew into bipolar shape, TC1

fluorescence was evident at the spindle pole and became most prominent at metaphase I, relative to that of mCherry-EMTB (**Figure III.3A**, 01:12, arrow). Consistent with the observations, fluorescence intensity profiles showed that TC1 signal was more concentrated at the pole than mCherry-EMTB signal, especially at metaphase and anaphase (**Figure III.3A**, bottom row, arrows). The increase of total TC1 fluorescence over time had a similar trend to that of mCherry-EMTB (**Figure III.3A'**). The different patterns between TC1 and the reference microtubule probe suggested highly localized Ca^{2+} at the spindle poles during *Xenopus* oocyte maturation.

Motivated by the distinct TC1 signal at spindle poles, we further examined oocytes expressing TC1 and mCherry-EMTB using LSM880 confocal system with Airyscan module (see **II.4** for detailed method). At an improved resolution, the TC1 signal exhibited a distinct ring shape at the spindle poles (**Figure III.3B**, top row). The projection of the polar *z*-stacks (*i.e. z*-projection) exhibited a clear ring-shaped structure (**Figure III.3B**, thumbnail). As a complementary approach, we imaged TC1-expressing oocytes which were injected with rhodamine-tubulin to label microtubules. Consistently, the metaphase spindle showed a distinct TC1 ring at the polar regions (**Figure III.3B**, bottom row). The ring-shaped signals at spindle poles agreed with the notion that, due to the lack of centrosomes, meiotic spindle poles had a broad shape compared with the more focused mitotic spindle poles (see **I.1.2.3**) (Bennabi et al., 2016). The different patterns between TC1 signals and microtubule probes, again, suggested highly localized $[Ca^{2+}]_i$ elevation at spindle poles.

Figure III.3 TC1 signals at spindles during oocyte maturation
(A) Representative confocal images of a *Xenopus* oocyte at indicated stages during oocyte maturation (*xz*-plane view). TC1 signal (green) is focused at spindle poles (arrows), compared to mCherry-EMTB (red). Time in hour:minute from image recording. Scale bar: 10 µm.
The 4th row (bottom row) exhibits the intensity profiles of the spindle at corresponding meiotic stages. Arrows indicate the prominent polar fluorescence as shown in the 1st row.
(A') Line plots depict the total fluorescence change of TC1 and mCherry-EMTB at the spindles during meiosis I.
(B) High-resolution confocal images (LSM880 with Airyscan module) of oocytes at metaphase, probed by TC1 (green) with the microtubule probe mCherry-EMTB (red, top row) or rhodamine-tubulin (red, bottom row). In both cases, TC1 exhibits distinct ring-shaped signals at spindle poles (arrows), compared to corresponding microtubule probes. The thumbnails exhibit *z*-projections of *z*-stacks at the polar regions (between the white dashed lines), which show distinct ring-shaped TC1 signal compared to mCherry-EMTB. Scale bar: 10 µm.

Figure III.3 TC1 signals at spindles during oocyte maturation

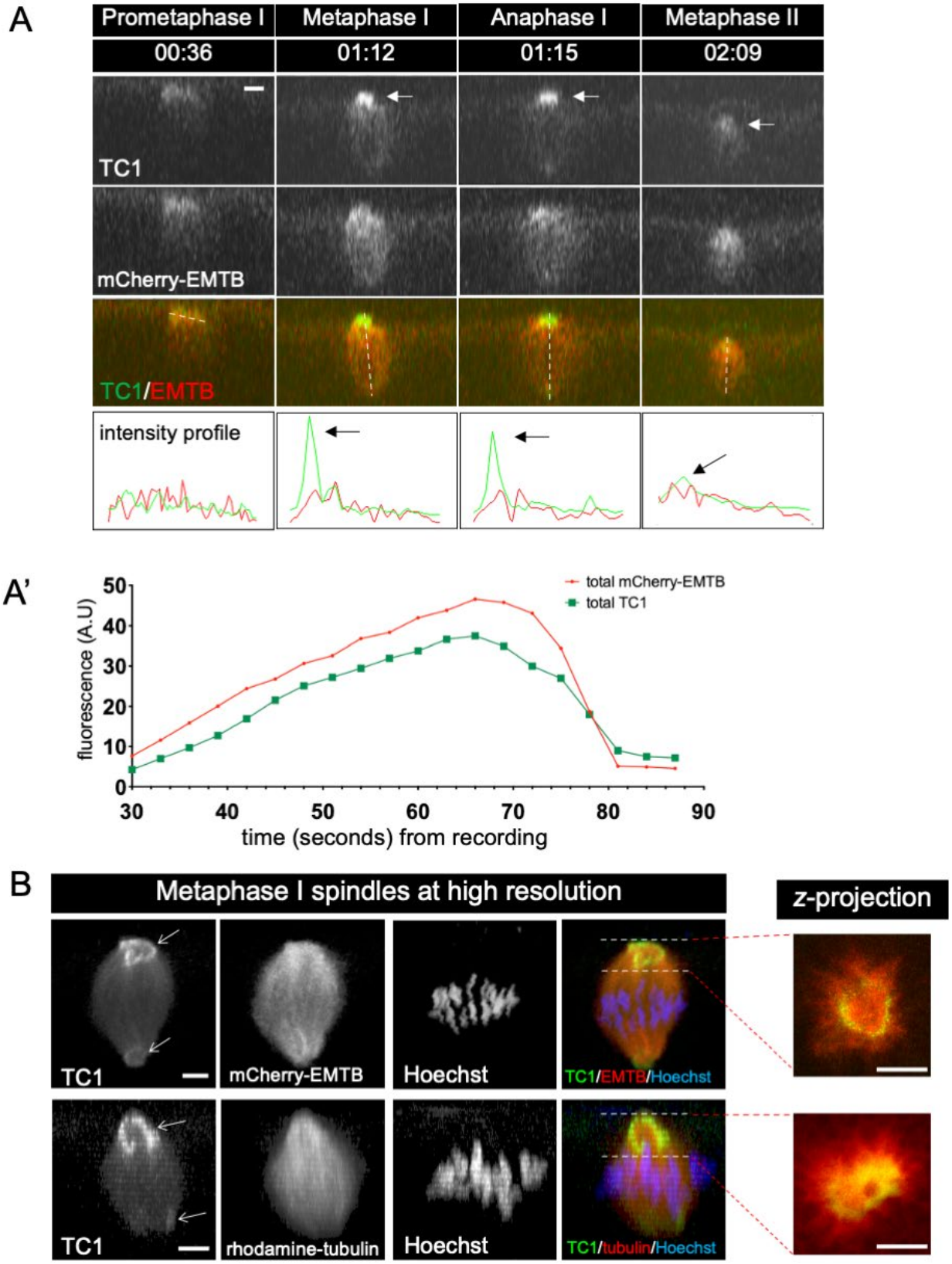

III.2.3.2 TC1 reports spindle-based $[Ca^{2+}]_i$ elevation during egg activation

During fertilization (sperm-egg fusion), a wave of global $[Ca^{2+}]_i$ elevation is triggered from the site where the sperm penetrates (see **I.1.4.2**) (Busa and Nuccitelli, 1985). $[Ca^{2+}]_i$ at wavefront could be raised from ~0.2 μM up to about ~1.3–2.0 μM (Wagner et al., 1998). This Ca^{2+} wave triggers a series of molecular reactions that break metaphase II arrest (see **I.1.4.2**).

We wondered how spindle labeled with TC1 would respond to the Ca^{2+} wave. To this end, oocytes expressing TC1 and H2B-RFP (a chromosome marker) were imaged after a needle prick, which mimicked sperm penetration (see **II.3.2** for detailed method) (Li et al., 2016). A Ca^{2+} wave was originated from the prick site and then propagated across the whole oocyte (**Figure III.4A**, schematic). When the equator band of an oocyte had been pricked, it took ~2 minutes for the Ca^{2+} wave to sweep through where the spindle was anchored to the animal pole. Before the arrival of the Ca^{2+} wave, the signal was only prominent at the pole (**Figure III.4B**, left panels; arrows), which was consistent with the detected TC1 signal at metaphase II spindle in **Figure III.3A**. A large increase of TC1 signal was observed at the time when the Ca^{2+} wave reached the spindle spot (**Figure III.4B,** right panels). The original pole-specific TC1 signal was overwhelmed by the increased TC1 signal at the whole spindle, in response to the dramatic elevation of local $[Ca^{2+}]_i$ (**Figure III.4C,** TC1-spindle). In contrast, no TC1 change was found in the polar body, consistent with the fact that Ca^{2+} elevation is only inside the oocyte during fertilization (**Figure III.4C**, TC1-pb).

Figure III.4 TC1 reports spindle-based $[Ca^{2+}]_i$ elevation during egg activation
(A) A cartoon series illustrates a Ca^{2+} wave sweeping across the whole MII oocyte (egg) after needle prick at the oocyte equator. Typically, it takes ~2 minutes for the Ca^{2+} wave to reach the spindle and ~4 minutes to reach the opposite side of the prick point.
(B) In a metaphase II oocyte expressing TC1 and RFP-H2B before (left) and 2 minutes after (right), a prick-induced Ca^{2+} wave reaches the spindle. Spindle-based TC1 signal dramatically increases in response to local $[Ca^{2+}]_i$ elevation. Arrows indicate prominent TC1 signals before Ca^{2+} wave arrival. pb: first polar body. Scale bar: 10 μm.
(C) Quantification for the fluorescence change when the Ca^{2+} wave arrives at the spindle. TC1 signal at the spindle (TC1-spindle) increases significantly compared to RFP-H2B or TC1 signal inside the polar body (TC1-pb). Mean ± S.D.; ** indicates $p < 0.01$; n=4

Figure III.4 TC1 reports spindle-based $[Ca^{2+}]_i$ elevation during egg activation

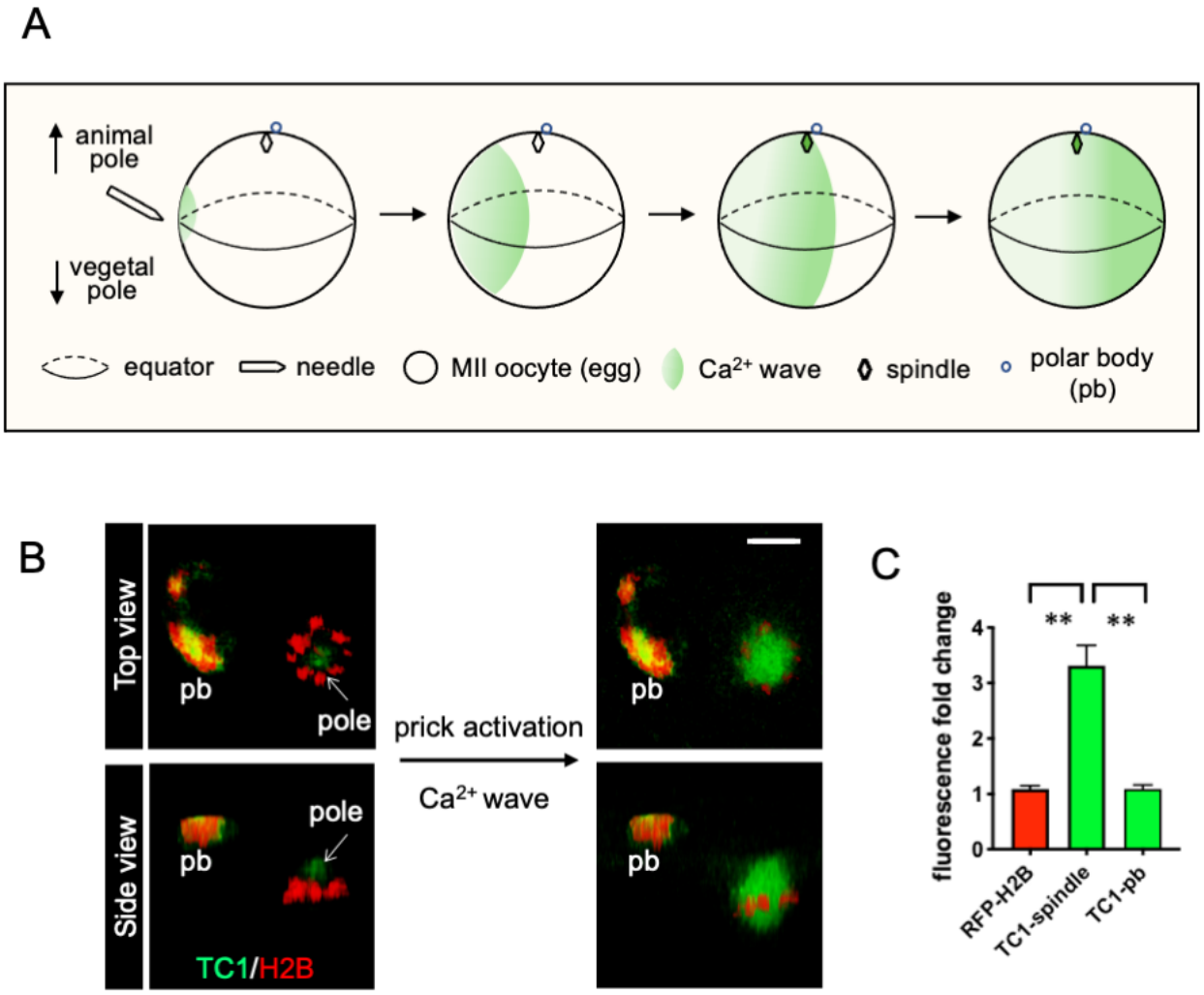

III.2.3.3 OG-2 reports diffuse Ca^{2+} signal at the spindle

To compare with the TC1, mobile Ca^{2+} indicators were used to detect spindle-based Ca^{2+} signals in *Xenopus* oocytes. The oocytes were imaged with Oregon green 488 BAPTA-2 (OG-2, K_d= 580 nM, the detail is described in **II.10.1**). OG-2 signal significantly increased at the spindle assembly site in a time course similar to that of TC1: OG-2 signal gradually appeared and accumulated in early meiosis (**Figure III.5A,** 00:00–00:15, time in hour:minute); the signal became most prominent at the metaphase and anaphase (**Figure III.5A,** 00:57–01:00, the arrows indicate chromosomes); disappears after completion of cytokinesis (**Figure III.5A,** 01:09, the arrow indicates polar body). Consistent with the observation, **Figure III.5B** exhibits the quantitative fluorescence change of OG-2 at the spindle during oocyte maturation.

Overall, the mobile OG-2 reports a diffuse Ca^{2+} signal at the spindle, compared to the restricted, spindle pole-associated Ca^{2+} signal detected by TC1. The diffuse pattern of OG-2 at the spindle is consistent with the previous report using mobile probes to detect spindle-based Ca^{2+} signal during mitosis of *Drosophila* embryos (Parry et al., 2005). The difference between OG-2 and TC1 signals also highlights the strategy to tether a Ca^{2+} sensor onto a microtubules-binding domain.

Figure III.5 OG-2 signals during oocyte maturation
(A) Confocal time series of an oocyte at the indicated stages, probed by OG-2 (green) and RFP-H2B (red). Time (hour:minute) is relative to the start of live cell imaging (00:00). $[Ca^{2+}]_i$ increase was seen only at the spindle assembly site, not elsewhere in the entire oocyte cortex. pb: first polar body. chr: chromosomes. Scale bar: 20 μm.
(B) A line plot indicates the fluorescence change of OG-2 at the spindle region during the oocyte maturation. Dashed squares indicate where the measurements are taken. The Roman number indicates the corresponding stages in **(A)**.

Figure III.5 Probing $[Ca^{2+}]_i$ at the spindle by OG-2 during oocyte maturation

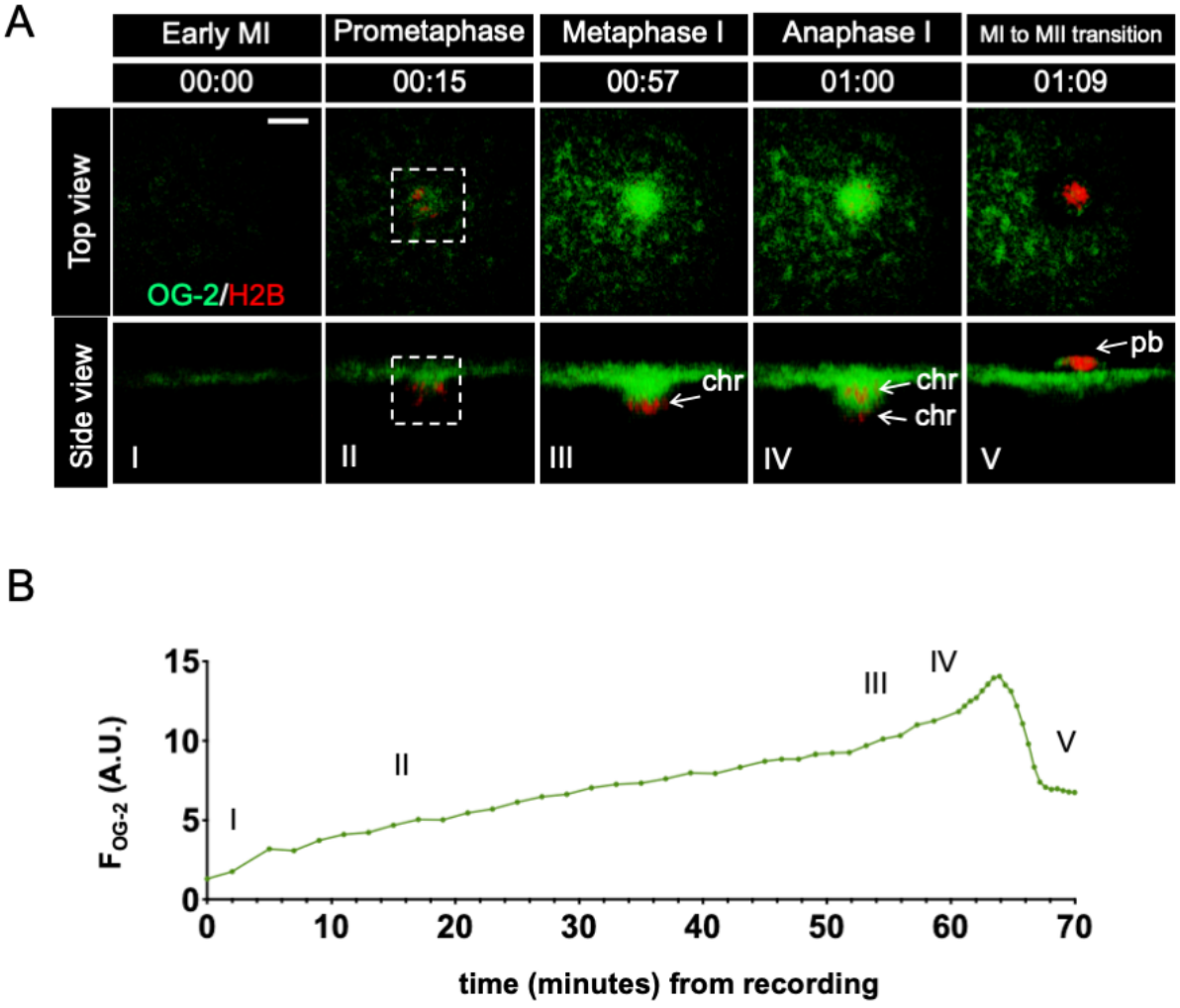

III.2.4 TC1 reports distinct Ca^{2+} signals at monoastral poles

The ring-shaped TC1 signals at spindle poles shown in the last section (**III.2.3, Figure III.3**) were reminiscent of the ring-like pole in STLC-induced monoastral spindles (Shao et al., 2013). STLC is a kinesin-5 (or Eg5) inhibitor. Kinesin-5 plays a crucial role in spindle pole segregation (bipolarization) by cross-linking the antiparallel (oriented in opposite direction) microtubules that support the bipolar structure (Eckerdt et al., 2008). In *Xenopus* oocyte extracts, blocking kinesin-5 activity inhibits bipolar spindle formation but does not disrupt the microtubule organization at monoastral poles, nor the microtubule-associated proteins (Kapoor et al., 2000). Similar phenotypes are found in intact *Xenopus* oocytes incubated with STLC, where the poles concentrated on the ring-shaped monoastral pole. (**Figure III.6A**, schematic) (Shao et al., 2013).

Based on our observation in **Figure III.3** (ring-shaped TC1 signals at bipolar spindle poles), we hypothesized that TC1-expressing oocytes incubated with STLC would also exhibit a prominent ring-shaped signal at monoastral poles. To test this hypothesis, *Xenopus* oocytes expressing TC1 and mCherry-EMTB were incubated with 5–10 μM STLC and subjected to confocal imaging. Before imaging, UV-sensitive caged-IP_3 was loaded for later TC1-binding and TC1/mCherry-EMTB colocalization analysis. Before UV exposure, as expected, TC1 exhibited a distinct ring-shaped signal on the inner periphery of the monoastral spindle, *i.e.* monoastral pole, compared to mCherry-EMTB (**Figure III.6B**, upper row). This TC1 pattern at kinesin-5-inhibited spindles further supported local $[Ca^{2+}]_i$ elevation at meiotic spindle poles.

Figure III.6 TC1 signals at monoastral spindles
(A) A schematic depicts STLC induced change of a spindle from the bipolar shape into monoaster. Left: Kinesin-5 activity supports bipolarity by cross-linking the antiparallel microtubules. Right: After inhibiting kinesin-5 by STLC, the bipolar spindle collapse into a monoastral spindle. However, the monopole can still organize microtubules.
(B) Live confocal images of a monoastral spindle before (upper row) and immediately after (lower row) UV uncaging of IP_3 (top view). Before UV exposure, the TC1 (green) signal is distinct at the monoastral pole, compared to mCherry-EMTB (red). After exposure, the pole-specific TC1 signal is overwhelmed by local $[Ca^{2+}]_i$ elevation. Scale bar: 5 µm.
(C) Quantification for TC1 responding to IP_3-induced $[Ca^{2+}]_i$ elevation at monoastral spindles. Left: In the presence of caged-IP_3 (as in **B**), TC1 fluorescence, but not mCherry-EMTB, significantly increases upon UV exposure. Results are mean ± SD. ** indicates $p<0.0001$; n=9. NS: not statistically significant.
Right: In the absence of caged-IP_3, TC1 fluorescence slightly decreases compared to mCherry-EMTB upon UV exposure. Results are mean ± SD. n=9.
(D) Colocalization analysis of TC1 and mCherry-EMTB before and after UV exposure. Upon UV exposure, (left) Manders' colocalization coefficients M1 (percentage of TC1 overlapping mCherry-EMTB) increase significantly while (right) M2 (percentage mCherry-EMTB of overlapping TC1) stays the same. Since Ca^{2+} saturated TC1 reflects probe distribution, high M1 (0.85) and M2 (0.89) value after UV exposure suggests that TC1 and mCherry-EMTB are highly colocalized at monoastral spindles. Mean ± S.D; ** indicates $p<0.0001$; n=9. NS: not statistically significant.

Figure III.6 TC1 signals at monoastral spindles

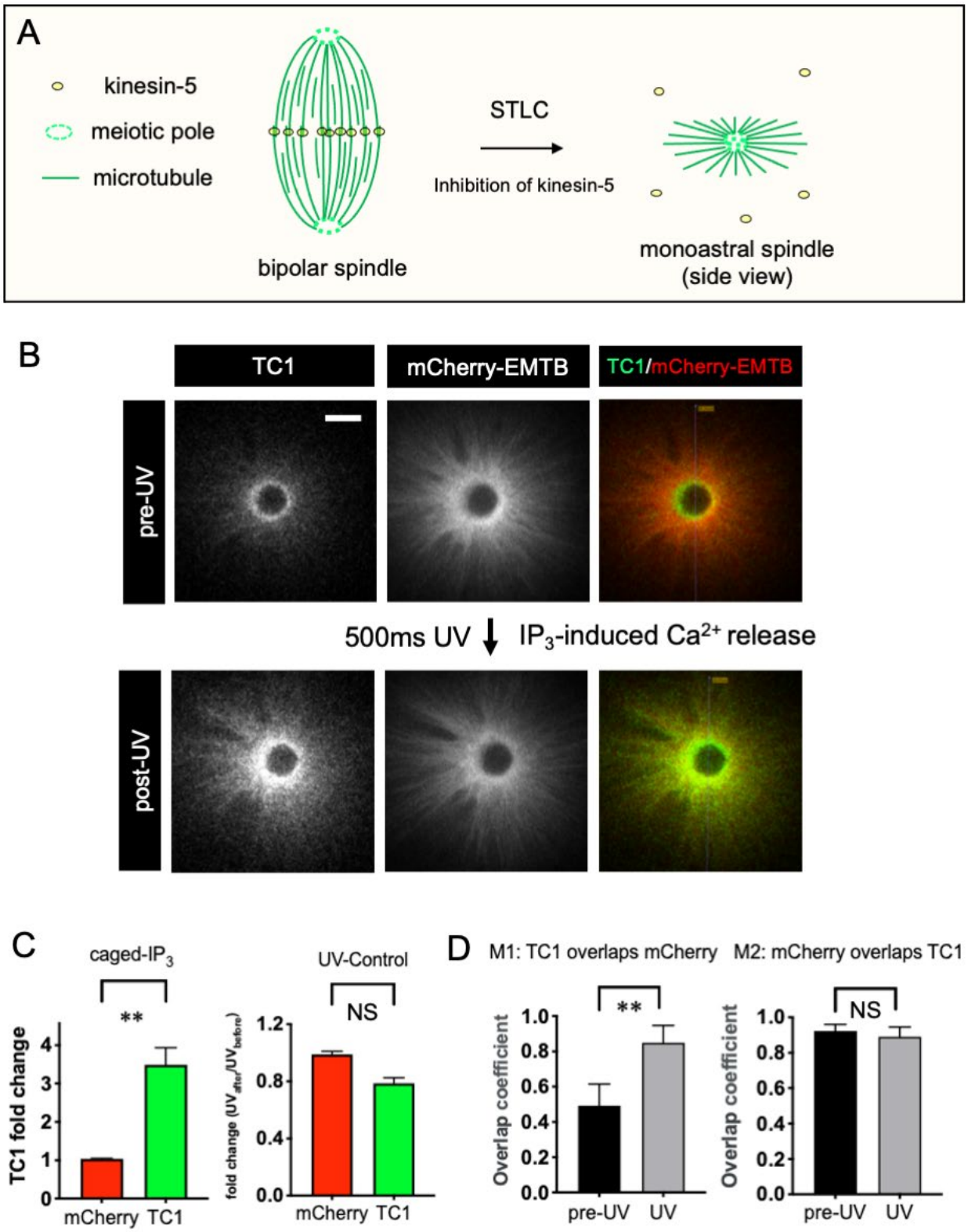

Next, we performed a quantitative analysis to evaluate TC1 distribution at monoastral spindles. We first analyzed TC1-binding on monoastral spindles. Upon 500 ms of UV exposure, the TC1 signal increased immediately at the whole monoastral spindle, (**Figure III.6B**, bottom row), indicating local $[Ca^{2+}]_i$ elevation as a result of IP_3R opening (Dargan and Parker, 2003). Quantitative analysis showed that TC1 signal increased to ~3.5 folds of the pre-UV status, while mCherry-EMTB stayed unchanged (**Figure III.6C**, left bar plot). As a negative control, in the absence of caged-IP_3, TC1 signal slightly decreased in response to UV exposure (**Figure III.6C**, right bar plot), suggesting that the increase of TC1 signal was not caused by UV stimulus. Taken together, these data suggested that TC1 probes were bound to the whole monoastral spindle, and responded to $[Ca^{2+}]_i$ elevation.

The distinction of TC1 signal at poles shown by **Figure III.6B** (pre-UV) was dependent on the assumption that mCherry-EMTB and TC1 probes had similar distribution on monoastral spindles. To evaluate this assumption, Manders' colocalization coefficients were analyzed (Manders et al., 1993). Upon UV exposure, M1 (the percentage of TC1 overlapping mCherry-EMTB) increased significantly from 0.49 to 0.85 (**Figure III.6D**, left panel) while M2 (the percentage of mCherry-EMTB overlapping TC1) kept highly correlated (~0.9) (**Figure III.6D**, right panel). The Ca^{2+}-saturated TC1 signals reflected the distribution of TC1 probes. Therefore, M1 and M2 values after UV exposure suggested that mCherry-EMTB and TC1 probes were highly colocalized at monoastral spindles.

III.2.5 TC1 reports distinct Ca^{2+} signals at spindle poles in oocyte extracts

Xenopus oocyte extract system is a powerful tool for studying spindle assembly and the underlying molecular mechanisms (Hannak and Heald, 2006; Heald et al., 1997). We developed a novel micro-aspiration method by mixing sperm nuclei (*i.e.* demembrenated

spermatozoa) with cytoplasmic droplets from individual *Xenopus* oocytes. This approach significantly reduced the labor and time required to set up the assays (from hours to minutes) and increased versatility regarding probe expression and the cell cycle stage of the system. The detailed protocol is described in **II.6** and an illustration of procedures is presented in **Figure II.1B**.

To examine spindle-based Ca^{2+} signal in cell-free system, we imaged the mixture of sperm nuclei (with Hoechst dye) and cell extracts from *Xenopus* oocytes expressing TC1 and mCherry-EMTB. Shortly after oocyte cytoplasm was added onto sperm droplets, microtubules emanated around the sperm chromosomes. The TC1 signal was initially not distinct at any specific location (**Figure III.7A**, 00:00, time in hour:minute). However, compared to mCherry-EMTB, its signal gradually became brighter at nascent poles (**Figure III.7A**, 00:28) and more distinct at the two poles at metaphase spindle (bipolar spindle) (**Figure III.7A**, 00:58). As a complemental approach, we imaged the bipolar spindle assembled in cell extracts from *Xenopus* oocytes injected with rhodamine-labeled tubulin (another microtubule probe) and expressing TC1. Again, TC1 signal was found distinct at the spindle poles compared to rhodamine-labeled tubulin (**Fig. 3.7B**). Consistently, the line-scan fluorescence profile along the spindle long axis exhibited a steeper signal peak of TC1 at the poles compared to the microtubule probe (**Fig. 3.7B,** fluorescence profile). These results suggested highly localized $[Ca^{2+}]_i$ elevation at spindle poles in *Xenopus* oocyte extracts. They also suggested that the role of localized Ca^{2+} signaling for spindle assembly might not be restricted to meiosis, since the spindles formed in cell-free systems involve post-meiotic sperm nuclei are sometimes considered to be mitotic spindles (Hannak and Heald, 2006; Heald and Khodjakov, 2015).

Figure III.7 TC1 signals during spindle assembly in cell extracts
(A) Confocal time series of a bipolar spindle formation in the cell extract. Time (hr:min) is from the beginning of imaging, a few minutes after the addition of demembrenated sperm nuclei. Initially (00:00), the TC1 signal (green) is not prominent compared to mCherry-EMTB (red). Later, TC1 signals are concentrated at spindle poles. Arrows indicate the spindle poles. Scale bar: 10 μm.
(B) A representative bipolar spindle assembled in extracts derived from an oocyte expressing TC1 (green) and injected with rhodamine-tubulin (red). The fluorescence profile in the 4th panel is the measurement of TC1 and tubulin signal across the dashed line in the 3rd panel. Arrows indicate the distinct TC signals at spindle poles. Scale bar: 10 μm.

Figure III.7 TC1 signals during spindle assembly in cell extracts

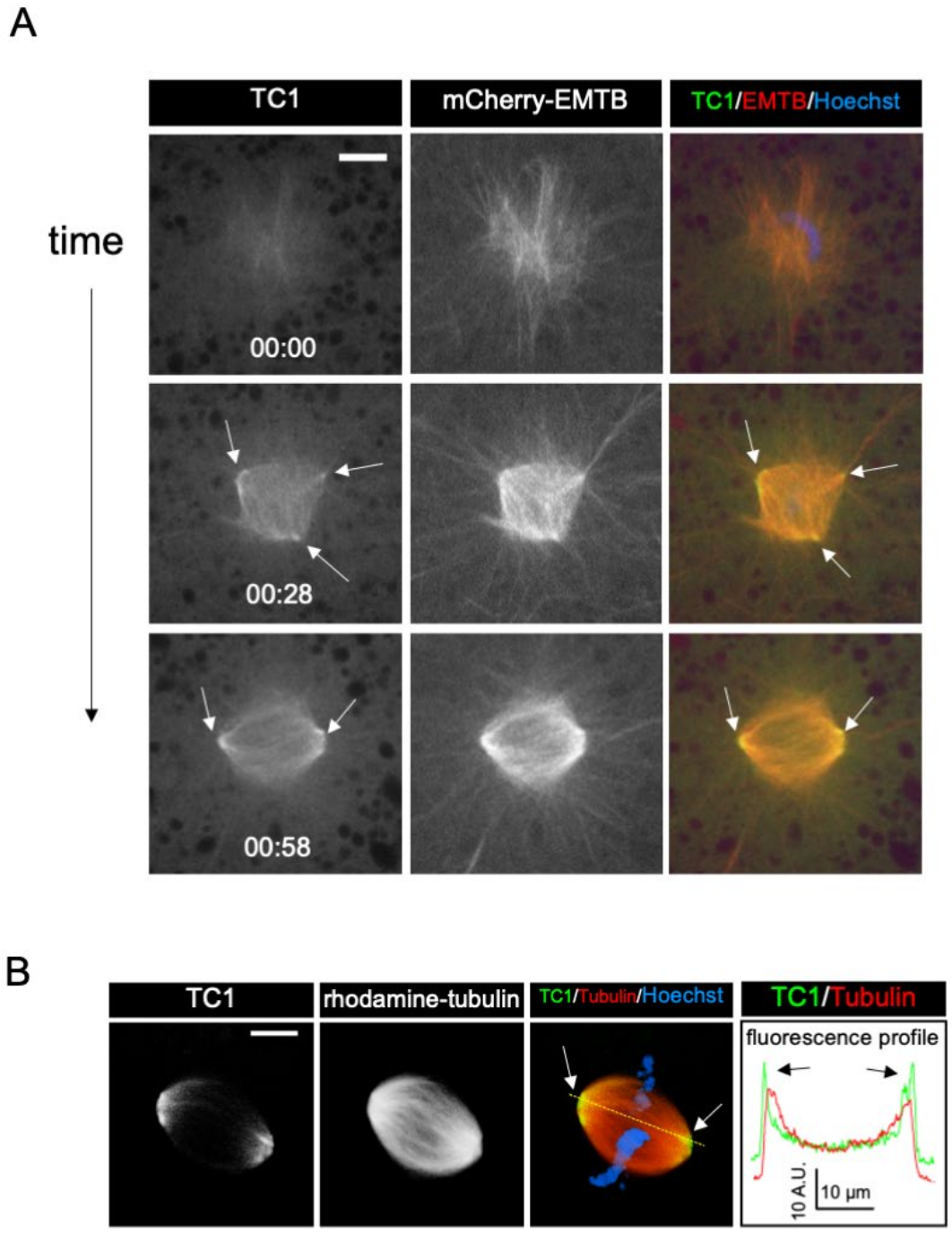

III.2.6 TC1 reports distinct Ca^{2+} signals at spindle poles in HeLa cells

Given the evidence in the cell-free system, we speculated that there existed spindle-based Ca^{2+} signal in mitotic cells of higher animals. To test this idea, we imaged HeLa cells expressing TC1 with mCherry-EMTB (**Figure III.8A**) or mCherry-α-tubulin (**Figure III.8B**).

In interphase cells, TC1 showed relatively even distribution throughout the cytoplasm (**Figure III.8A**, interphase). In particular, TC1 showed no increased signal, compared to mCherry-EMTB at centrosome where microtubules were abundant (**Figure III.8A**, interphase, arrows). This TC1 pattern suggested that there was no specific microtubule-proximal $[Ca^{2+}]_i$ elevation in interphase cells. In contrast, in mitotic cells, prominent TC1 signals were found at the spindle poles (**Figure III.8A**), compared to mCherry-EMTB. As a complemental approach, HeLa cells expressing TC1 together with mCherry-α-tubulin (another microtubule probe) were also imaged (**Figure III.8B**). Similarly, distinct TC1 signals were found at the metaphase spindle poles compared to mCherry-α-tubulin (**Figure III.8B**, arrows). The linescan profile was in line with the observation, showing dramatic peaks of TC1 signals at the poles (**Figure III.8B**, intensity profile, arrows). The observation of distinct TC1 signals at spindle poles (**Figure III.8**) was consistent with the notion that spindle-based Ca^{2+} signals existed in mammalian cells, and further suggested the involvement of localized Ca^{2+} signaling for spindle assembly and organization in HeLa cells.

Figure III.8 TC1 signals in HeLa cells
(A) Confocal images of HeLa cells at the indicated stages of mitosis. Interphase (arrow: centrosome), and the TC1 signal is concentrated at the spindle poles during mitosis. Scale bar: 5 μm.
(B) A typical metaphase HeLa cell expressing TC1 (green) and mCherry-α-tubulin (red) in the presence of Hoechst dye (blue). The profile in the 4th panel reflects the fluorescence fluctuation along the dashed line in the 3rd panel. Arrows indicate the distinct TC1 signals at spindle poles. Scale bar: 10 μm.

Figure III.8 TC1 signals in Hela cells

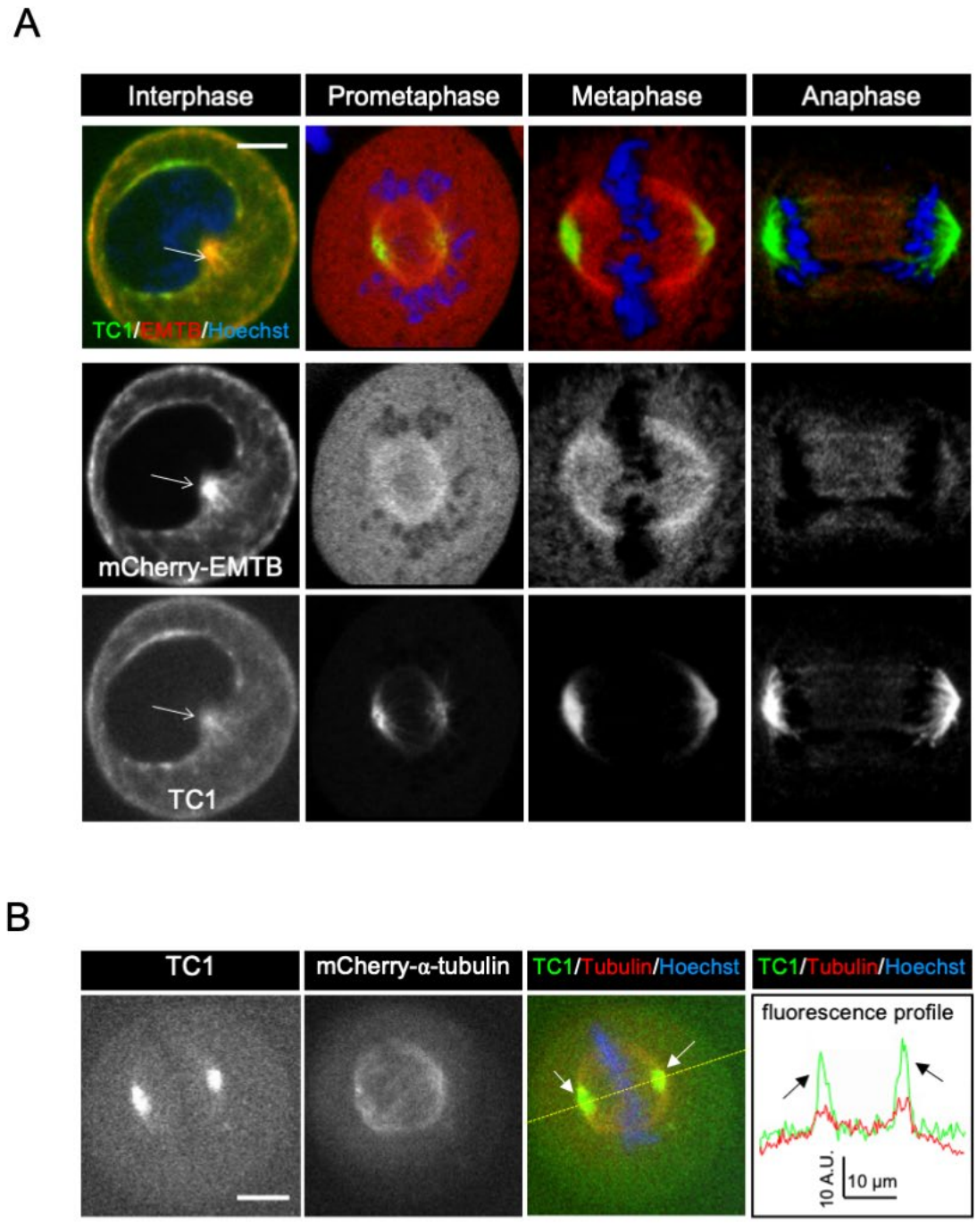

III.3 Discussion

III.3.1 Recap of the results

In this chapter, we described the construction of a novel genetically encoded Ca^{2+} probe, TC1 (**III.2.1**), and applied it to detect spindle-based Ca^{2+} signals (**III.2.3**–**III.2.6**). We showed that TC1 was able to report microtubule-proximal $[Ca^{2+}]_i$ increase in various well-studied events characteristic of global/local $[Ca^{2+}]_i$ elevation: **III.2.2** oocyte wound healing, **III.2.3.2** egg activation, **III.2.4** IP_3-induced Ca^{2+} release. The timelapse images captured during *Xenopus* oocyte maturation revealed a gradual increase of Ca^{2+} signal at the spindles (**III.2.3.1**). Notably, the TC1 signals at spindle poles were distinct from the reference microtubule probes (**III.2.3.1** TC1 *vs.* mCherry-EMTB/rhodamine-tubulin at the spindles), suggesting localized $[Ca^{2+}]_i$ elevation at spindle poles. In contrast, the mobile probe OG-2 failed to distinguish pole-specific $[Ca^{2+}]_i$ elevation (**III.2.3.3)**, emphasizing the importance of the targeted approach to probe Ca^{2+} at cellular organelles. The pole-specific TC1 signal was further confirmed at monoastral spindles (**III.2.4** oocytes incubated with STLC), extract spindles (**III.2.5** cell extracts mixed with sperm nuclei) and mitotic spindles in HeLa cells (**III.2.6** cell cycle of HeLa cells), suggesting that $[Ca^{2+}]_i$ elevation at spindle poles is featured in both mitosis and meiosis. Collectively, our findings support the notion that highly localized Ca^{2+} signaling is involved in spindle assembly (Li et al., 2016).

III.3.2 Pole-specific TC1 signals suggest that localized Ca^{2+} signaling is spatiotemporally correlated to spindle assembly in meiosis and mitosis

The results presented in this chapter are significant in several aspects. First of all, the detection of local $[Ca^{2+}]_i$ elevation in spindle assembly helps bridge the gap that was left by the previous studies: No local Ca^{2+} signals were identified during oocyte maturation despite

the clear importance of Ca^{2+} regulation (El-Jouni et al., 2005; Sun et al., 2008; Sun and Machaca, 2004). Specifically, Sun *et al.* have shown that Ca^{2+} deprivation of *Xenopus* oocytes before GVBD, by either BAPTA injection, extended Ca^{2+}-free medium incubation or Ca^{2+}-ATPase inhibitor treatment (ER Ca^{2+}-store depletion), leads to spindle abnormality and failure of cytokinesis (Sun et al., 2008; Sun and Machaca, 2004). In contrast to their argument that the defects are the consequence of the global Ca^{2+} deprivation, our data suggested that direct Ca^{2+} signaling, albeit in a highly spatiotemporally restricted fashion, is required for spindle assembly and function.

Furthermore, the observation of spindle pole-associated $[Ca^{2+}]_i$ elevation in cell-free systems and HeLa cells extends the research interest to mitosis. In fact, Groigno and Whitaker have noticed that the inhibition of Ca^{2+} signaling, by either heparin (a Ca^{2+} channel inhibitor) or DB-BAPTA, reduces spindle size in sea urchin embryos (Groigno and Whitaker, 1998). Similar reduction of spindle size by BAPTA-AM is also found in HeLa cell (Xu et al., 2003). The main themes in previous work, however, are mainly focused on anaphase initiation such as chromosome segregation (Groigno and Whitaker, 1998) or spindle checkpoint (Xu et al., 2003). Their efforts are more closely related to elucidate early observations of $[Ca^{2+}]_i$ elevation during anaphase (Keith et al., 1985; Poenie et al., 1986). A recent paper reports a centrosome-localized Ca^{2+} signal during mitosis in HeLa cells (Helassa et al., 2019). In this study, the authors used GCaMP fused with β-actin. Since the mitotic spindle poles are intimately associated with actin cytoskeleton (Farina et al., 2016; Inoue et al., 2019). Likely, the $[Ca^{2+}]_i$ elevation detected by Helassa *et al.* is the same as that detected by TC1 in HeLa cells.

III.3.3 Relations between pole-specific $[Ca^{2+}]_i$ elevation and calcium nanodomains

How does the pole-specific Ca^{2+} elevation detected by TC1 related to the potential calcium nanodomains? Nanodomain Ca^{2+} signaling relies on the high concentration of Ca^{2+} gradient around opening channel mouths. Hence, records of single channel activities (*e.g.* a single Ca^{2+} blip and a subsequent transient gradient) would directly report the calcium nanodomains at spindles. However, despite the overall elevated $[Ca^{2+}]_i$ at the poles, we were unable to identify *individual* Ca^{2+} transient events in our best attempts with fast imaging technique (see footnote [28]). Our observation that BAPTA causes rapid microtubule depolymerization suggests that calcium nanodomains are required for microtubule polymerization and/or stability (see **I.2.2** or Li *et al.*, 2016). Given the high density of microtubules at spindle poles, it is possible that numerous calcium nanodomains are "crowded" at spindle poles. This is also supported by the identification of Ca^{2+} channels — IP_3Rs which are dense at the spindle poles (see **IV.2.3.1**). To distinguish individual Ca^{2+} transient events, the distance between nearby nanodomains should be at least exceeding diffraction limit of the fluorescent method (~200 nm). In fact, the previous reports that succeeded in visualizing individual nanodomain Ca^{2+} transients all dealt with very sparse (micrometers away) single channels (Demuro and Parker, 2006; Llinas et al., 1992; Parker and Smith, 2010; Tay et al., 2012), which might not be applicable in the case of spindle poles. We suggest that the distinct TC1 signals at the poles reflect the average local $[Ca^{2+}]_i$ elevation due to numerous Ca^{2+} releasing events close to the potential nanodomains.

[28] To image evanescent Ca^{2+} transient of individual channels, spinning disk microscopy with EM-CCD (See **II.4)** was employed with modest compromise of resolution. We focused on a small polar region rather than the whole spindle at a temporal interval as short as 16.7 ms (i.e. 60 Hz or frames per second). However, apart from random signal noise at pixel level, individual Ca^{2+} transient could not be convincingly identified.

The spindle-based Ca^{2+} signal detected by TC1, together with loss of function study with the intervention of BAPTA (Li et al., 2016), suggests the presence of calcium nanodomains at or near the spindle poles. The pending interest is to explore the molecular entities of these potential calcium nanodomains and their roles. We will further explore these questions in the next chapter.

III.3.4 Limitations

The major concern in any Ca^{2+} detection study is that the Ca^{2+} indicators might interfere with the normal cellular physiology because of their ability to buffer intracellular Ca^{2+}. Multiple studies have reported unexpected side-effects of GCaMPs, ranging from the single cell to the whole organism level (Rose et al., 2014; Tian et al., 2009; Yang et al., 2018). The cause of GCaMPs' cytotoxicity is not fully understood. Some authors argue that the over-accumulation of CaM moieties perturbs the ubiquitous Ca^{2+}/calmodulin signaling pathways as well as calmodulin-regulated ion-channel function (Rose et al., 2014; Yang et al., 2018). In particular, the accumulation of GCaMPs in nuclei may be responsible for aberrant Ca^{2+} dynamics in some studies (Akerboom et al., 2012; Chen et al., 2013; Tian et al., 2009). In our studies when TC1 was probably over-expressed (*i.e.* signal was exceedingly strong), we occasionally observed lagging chromosomes in anaphase and improper cytokinesis in *Xenopus* oocytes. Interestingly, this defect was usually accompanied by non-specific interpolar TC1 signals in metaphase. These observations, in line with reported off-target effects, suggest that over-expression of TC1 might affect cellular health in the system to a certain extent.

Another concern is the possibility of biased accumulation of TC1 probes towards spindle poles. Even though TC1 and mCherry-EMTB have the same microtubule-binding domains,

the extra CaM unit of TC1 may contribute to the biased binding of spindle poles, compared to mCherry-EMTB. Especially since we have shown that calmodulins are preferentially bound to the spindle poles (**Figure IV.5A**). However, GCaMP3 exhibits no specific binding in *Xenopus* oocytes despite having the same CaM moiety (Li et al., 2016). Nonetheless, we cannot rule out the possibility that the CaM moiety in the context of a microtubule targeting sequence (EMTB) contributes to a biased binding to the spindle poles, which may partially explain the dramatic TC1 signal at the spindle poles. Prompted by this concern, we developed several ratiometric TC derivatives with an extra mCherry unit (a reference unit) to correct the potential bias. Although these ratiometric probes exhibited compromised Ca^{2+} sensitivity, they led to the discovery in **Chapter V. Snapshotting Ca^{2+} transients during polar body emission**.

Chapter IV Exploring calcium nanodomains at spindles

IV.1 Introduction

Pole-specific $[Ca^{2+}]_i$ elevation (**Chapter III**) suggests highly localized Ca^{2+} signaling, *i.e.* calcium nanodomains, at the spindles. Calcium nanodomains are based on the tight coupling of Ca^{2+} channels (source) and Ca^{2+} sensors. The coupling distance is generally thought to be below 100 nm (Eggermann et al., 2011; Hogan, 2015). This architecture is energy-efficiency that maximizes local signaling capacity while minimizing global Ca^{2+} load that may otherwise cause chaos (Tadross et al., 2013). A classical approach to probe nanodomains is to load cells with chelators of distinct Ca^{2+} binding rates, *i.e.* BAPTA *vs.* EGTA, to buffer local *vs.* global Ca^{2+} increase. Only the fast chelator BAPTA will be quick enough to disrupt the signal transduction within the miniature regimes (Adler et al., 1991; Selway et al., 2012; Zweifach and Lewis, 1995). By using this approach, a previous study has suggested that calcium nanodomains are involved in the spindle assembly of *Xenopus* oocytes (Li et al., 2016). In this chapter, we further explored the significance of calcium nanodomains for spindle assembly in the cell-free system as well as monoastral spindles in oocytes.

Another closely associated goal is to dissect the molecular components of potential nanodomains at spindles. To this end, the first question is what can be the source of localized $[Ca^{2+}]_i$ elevation. The Ca^{2+} source must be intracellular since the store-operated calcium entry for Ca^{2+} influx on the plasma membrane is being inactivated during oocyte maturation (Machaca and Haun, 2000). The endoplasmic reticulum (ER) is a likely candidate. ER or its specialized sub-compartments are the major Ca^{2+} reservoir of *Xenopus* oocytes. Previous

studies have shown that ER undergoes a substantial transformation during both mitosis and meiosis (Carlton et al., 2020; FitzHarris et al., 2007; Sun et al., 2011). Unlike interphase ER characteristic of tubular network with highly convolved cisternae[29], M-phase ER primarily comprises extended and loose cisternae with much less abundant tubules (Lu et al., 2009). Despite the fact that ER network is excluded from most of the spindle region, a fraction of ER cisternae accumulates at the spindle poles while ER tubules that emanated from polar ER cisternae are found to be closely aligned with spindle microtubules (Bergman et al., 2015; Lu et al., 2009). However, whether ER has any role in spindle formation and maintenance remains largely unexplored.

In *Xenopus* oocytes, IP_3Rs are the dominant Ca^{2+} release channels on ER membranes (Parys et al., 1992). *Xenopus* oocytes, as well as mammalian oocytes, almost exclusively express the type-1 IP_3R isoform (IP_3R1) (Kume et al., 1993; Parrington et al., 1998). During oocyte maturation, IP_3-dependent Ca^{2+} release becomes sensitized due to the phosphorylation and aggregation of IP_3R clusters as a part of ER remodeling (Sun et al., 2009; Sun et al., 2011; Terasaki et al., 2001). By MPF/MAPK activities, three residues of IP_3R1 (Thr-931, Thr-1136, and Ser-1145) are specifically phosphorylated, which may account for maturation-related IP_3R functions (Sun et al., 2009). The transformation of ER and IP_3Rs is thought to be essential for reproductive competence of a mature oocyte because the resultant IP_3R clusters form the "building blocks" for the propagation of Ca^{2+} wave that promotes fertilization (Kume et al., 1993; Schwarz and Blower, 2016; Sun et al., 2011). On the other hand, the adaption of ER and

[29] In some literature, cisternae are referred to as "sheets" (Wang et al., 2013) or "patches" (Sun et al., 2011), but they are all the same subcellular entities — flattened ER membrane disks.

IP_3R during oocyte maturation may also play a role in spindle functions. Interestingly, Sun *et al.* have shown that depletion of ER Ca^{2+} store by tharpsigargin, a non-competitive inhibitor of the ER Ca^{2+} ATPase, causes spindle defects (Sun et al., 2008; Sun and Machaca, 2004). These data suggested that IP_3Rs play an important role in spindle functions since insufficient channel release of Ca^{2+} is the direct consequence of Ca^{2+} store depletion. $[Ca^{2+}]_i$ gradients around the channel mouths are essential for highly localized Ca^{2+} signaling, or calcium nanodomains. It is thus attempting to investigate IP_3Rs' distribution and their possible roles in the context of spindle assembly.

To sum up the goals in this chapter: (1) We will apply BAPTA/EGTA tests to investigate the significance of calcium nanodomains in spindle assembly of various *Xenopus* oocyte-based systems. (2) Once the functional significance is established, we seek to dissect the molecular components of the calcium nanodomains at spindles (source, channels, sensors).

IV.2 Results

IV.2.1 Calcium nanodomains are required for spindle assembly in *Xenopus* oocyte-based systems

IV.2.1.1 DB-BAPTA causes rapid collapse of spindles in Xenopus oocyte extracts

In **III.2.5, Figure III.7**, we have shown pole-specific Ca^{2+} signal at the spindles assembled in oocyte extracts. We wonder if calcium nanodomains play any role in this system. To investigate this, bipolar spindles were assembled in cytoplasmic extracts aspirated from *Xenopus* oocytes expressing EMTB-GFP (microtubule marker, green) and H2B-RFP (chromosome marker, red), supplemented with demembrenated spermatozoa (see **II.6** for extract preparation method and **II.10.2** for plasmid information). We added fast chelator DB-

BAPTA (K_d = 1.6 μM, low affinity) or slow chelator EGTA (K_d = 180 nM, high affinity) into the cytoplasmic extracts. The spindles exposed to 1 mM EGTA persisted for more than an hour (**Figure IV.1A**, top row, time in hour:minute). In contrast, those exposed to 1 mM DB-BAPTA disassembled within minutes (**Figure IV.1A**, bottom row), as indicated by shortening the polar distance and dramatic decrease of microtubule abundance (**Figure IV.1A**, bar plot), similar to the phenotypes observed in intact oocytes (Li et al., 2016). These results suggested that calcium nanodomains are required for spindle assembly in *Xenopus* oocyte extracts.

Figure IV.1 BAPTA's intervention in *Xenopus* oocyte-based systems
(A) Confocal series of bipolar spindles formed in extracts treated with 1 mM EGTA (top row) or 1 mM DB-BAPTA (bottom row). DB-BAPTA, but not EGTA, causes spindle dissolution. Chromosomes are labeled with H2B-RFP (red); microtubules are labeled with EMTB-GFP (green). Scale bar = 20 μm.
The bar plot summarizes the relative microtubule abundance 10 minutes after injection. Means ± SD; ** indicates $p < 0.01$; n = 4 (EGTA), n = 8 (DB-BAPTA).
(B) Confocal series of monoastral spindles subjected to UV exposure (top view). The oocytes expressing TC1 (green) were injected with rhodamine-tubulin (red; microtubule marker) before imaging. Time in minute:second. Scale bar = 20 μm.
Diazo-2 series (oocytes injected with Diazo-2): Following UV exposure, TC1 and tubulin signal gradually diminish in parallel.
Control series: Following UV exposure, both TC1 and tubulin signals persist except for a short period of TC1 decrease (UV photobleaching).
The line plots summarize relative fluorescence (circle) at the indicated time points. The purple strip depicts the UV-exposure period. Means ± SEM; green lines: TC1; red lines: rhodamine-tubulin. N = 9 (Diazo-2 & control groups).
(C) Confocal images of colcemid-treated oocytes expose to UV illumination (side view). Following UV exposure (inactivation of colcemid) in the presence of EGTA, the spindle reforms (left panels); in the presence of BAPTA (photolysis of diazo-2), the spindle does not reform (right panels). Green: H2B-GFP, chromosome marker; red; rhodamine-tubulin, microtubule marker. Time in hour:minute. Scale bar = 20 μm.

Figure IV.1 BAPTA's intervention in *Xenopus* oocyte-based systems

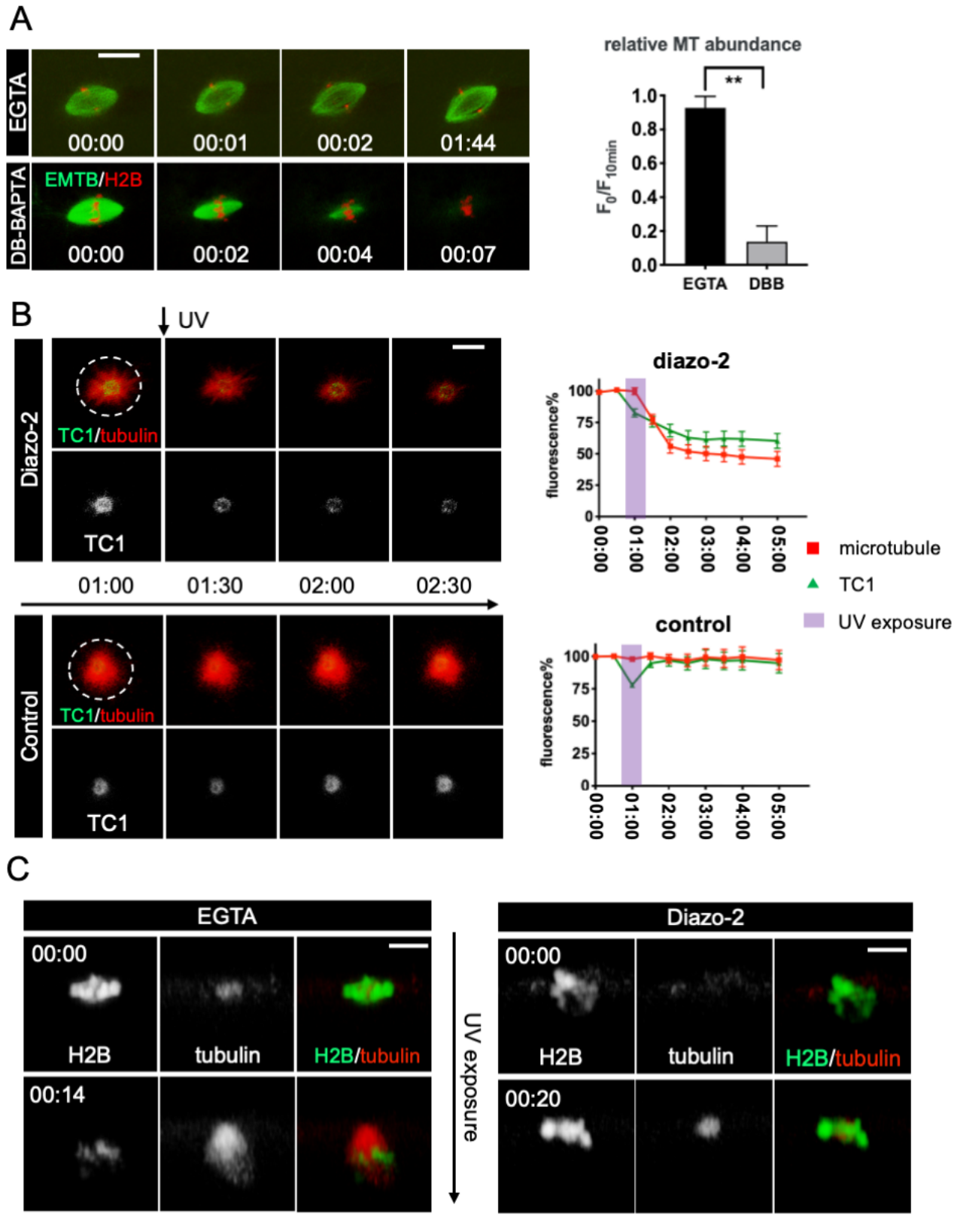

IV.2.1.2 BAPTA causes fast depolymerization of monoastral spindles

STLC is a kinesin-5 inhibitor that can induce monoastral spindles (Eckerdt et al., 2008; Shao et al., 2013). A previous study showed that inhibition of kinesin-5 blocks the formation of spindle bipolarity but not microtubule organization at monopoles (Kapoor et al., 2000). In **III.2.4** we have shown pole-specific Ca^{2+} signal at STLC-induced monoastral spindles, suggesting highly localized Ca^{2+} signaling in spindle microtubule organization. We wonder if BAPTA disrupts calcium nanodomains and microtubule organization at monoastral spindles.

To generate monoastral spindles, oocytes expressing TC1 (microtubule-associated Ca^{2+} reporter) were incubated with 5–10 μM STLC. Prior to the experiment, oocytes were injected with rhodamine-tubulin and UV-sensitive diazo-2 (caged-BAPTA). During imaging experiments, the oocytes animal where the spindle resides was exposed to UV for 30 seconds to induce local BAPTA release. Upon photolysis, the releasing BATPA caused a fast diminishing of spindle microtubules indicated by rhodamine-tubulin (**Figure IV.1B**, diazo-2 series). Quantitative analysis of the fluorescence (**Figure IV.1B**, circle) over time exhibits that the decrease of TC1 signals was in parallel with the decrease of microtubules (**Figure IV.1B**, top-line plots). In contrast, neither the microtubule nor TC1 signal in the control group altered significantly, except for a brief drop of TC1 signal during the UV exposure, consistent with the effect of photobleaching (**Figure IV.1B**, control series and the line plot). Besides, BAPTA releasing also caused the deterioration of the ring-shaped monopole (**Figure IV.1B**, diazo-2 series, TC1). These data suggested that calcium nanodomains are required for pole stability and microtubule organization in monoastral spindles.

IV.2.1.3 BAPTA attenuates the growth of spindle microtubules and inhibits bipolar formation in intact oocytes

Spindle microtubules are polymerized α/β-tubulin heterodimers (see **I.1.2.2**). Colcemid is a UV-labile microtubule poison that binds to tubulins and blocks the polymerization of microtubules, resulting in spindle dissolution (Banerjee and Bhattacharyya, 1979; Rieder and Palazzo, 1992). Colcemid is routinely used in inducing metaphase arrest while its effects on spindle microtubules are reversible. Upon UV-exposure, colcemid is inactivated which leads to the regrowth of microtubules and reformation of bipolar spindles (Shao et al., 2013).

We wonder if calcium nanodomains play any role in the regrowth of microtubules and the reformation of bipolar spindles following colcemid inactivation. *Xenopus* oocytes labeled with H2B-GFP (chromosome marker, green) and rhodamine-tubulin (microtubule marker, red) were incubated with 50 μM colcemid from GVBD. Oocytes at metaphase I were examined in the presence of EGTA or diazo-2. Metaphase I spindles were first found disassembled in both groups (by colcemid, as expected), and then the oocytes were exposed to UV illumination leading to colcemid inactivation (**Figure IV.1C**, 00:00, time in hour:minute, EGTA and Diazo-2 groups). In the presence of EGTA, the slow chelator, microtubules regrew and a bipolar spindle reformed (**Figure IV.1C**, EGTA, 00:00–00:14). But in the presence of diazo-2, which released BAPTA by the same UV exposure for inactivating colcemid, no bipolar spindles were observed despite the regrowth of a small bundle of microtubule asters (**Figure IV.1C**, diazo-2, 00:00–00:20). These results suggested that calcium nanodomains are required for promoting spindle microtubule growth and bipolar spindle formation.

IV.2.2 Evidence of ER's role in maintaining spindle integrity

IV.2.2.1 Spindles assembled in extracts are in close contact with ER

Having shown the calcium nanodomains were required in extract spindles (**IV.2.1.1, Figure IV.1**), we further investigated the distribution of potential Ca^{2+} stores in relation to the spindles. To label ER and microtubules, sfGFP-ER and mCherry-EMTB were expressed in *Xenopus* oocytes. SfGFP-ER is a super-folded GFP tagged with a calreticulin-KDEL ER retention sequence to protect itself from being secreted out of ER lumen (Salo et al., 2019). Cytoplasmic extracts were made directly from individual oocytes and mixed with demembrenated spermatozoa (DNA stained with Hoechst dye). Before spindle formation, ER exhibited a tubular network with highly convolved cisternae (**Figure IV.2A**, 00:00, time in hour:minute, arrows indicate convolved cisternae). No specific relationships were observed between the ER network and the individual microtubules found in these extracts (**Figure IV.2A**, 00:00). Microtubules were first organized around the sperm nuclei while the highly convolved ER cisternae gradually loosen themselves around the nascent spindle (**Figure IV.2A**, 00:06). At the time when bipolar spindle formed, ER network was reorganized into loose and extended cisternae that concentrated at spindle poles (**Figure IV.2A**, 01:00, arrowheads), but not inside the non-polar region. ER tubules radiated from the polar cisternae and a few of which were in close proximity to spindle microtubule bundles (**Figure IV.2A**, 01:00, arrows). Overall, spindle microtubules were tightly "coated" with ER membrane (**Figure IV.2A**, 01:00), in contrast to the random distribution of non-spindle microtubules (**Figure IV.2A**, 00:00). These observations are consistent with previous reports that ER network encloses the spindle region and a fraction of ER cisternae accumulate at the spindle poles (Bergman et al., 2015; Karabasheva and Smyth, 2019; Lu et al., 2009; Wang et al., 2013;

Whitaker, 2006b). Our data also suggested that the pole-specific $[Ca^{2+}]_i$ elevation detected by TC1 (**III.2.5, Figure III.7**) was likely attributable to the ER cisternae that concentrate at the spindle poles.

IV.2.2.2 Disruption of ER is accompanied by spindle disassembly

Given the close contact between ER membranes and spindle microtubules, we wondered what would happen to spindles if their associated ER membranes were disrupted. Triton X-100 is a widely used surfactant that dissolved membranes into micelles (Koley and Bard, 2010). We injected Triton X-100 (final concentration of 0.1%, v/v) into oocyte extracts that had assembled bipolar spindles, followed by live imaging. Upon Triton injection, ER cisternae shrank rapidly and became fragmented (**Figure IV.2B**, time in minute:second). The disassembly of spindles was in parallel with disruption of the ER network, both in space and time (**Figure IV.2B** and **Figure IV.2C**, bar plot summary for fluorescence change). This result is consistent with the involvement of ER in spindle assembly/maintenance.

Figure IV.2 ER membranes are associated with spindle microtubules
(A) Bipolar spindle formation in oocyte extracts shown by confocal images. Microtubules (red; mCherry-EMTB) are polymerized around the sperm nuclei/chromosomes (blue; Hoechst) and then organized into a bipolar spindle. Meanwhile, ER membranes (green; ER-sfGFP) surrounding spindle microtubules gradually transform and accumulate at spindle poles. Arrows at 00:00 indicate the highly convolved cisternae, which loosen and extend themselves over time. Arrowheads at 01:00 indicate the microtubules concentrated at spindle poles. Arrows at 01:00 show some ER tubules radiated from polar cisternae. Time in hour:minute. Scale bar = 5 μm.
(B) Triton X-100's treatment on extract spindle shown by confocal timelapse images. Triton X-100 (0.1%, v/v) shatters ER membranes (green; ER-sfGFP) and spindle microtubules (red; mCherry-EMTB) simultaneously. Time in minute:seccond. Scale bar = 10 μm.
(C) A bar plot summarizes the relative fluorescence change of microtubule (EMTB) or ER probes before and after 10-minute Triton X-100 treatment in **(B)**. Results are mean ± SD. ** and ## indicate $p<0.01$ 10-minute *vs.* 0-minute in corresponding groups; n=5.

Figure IV.2 ER membranes are associated with spindle microtubules

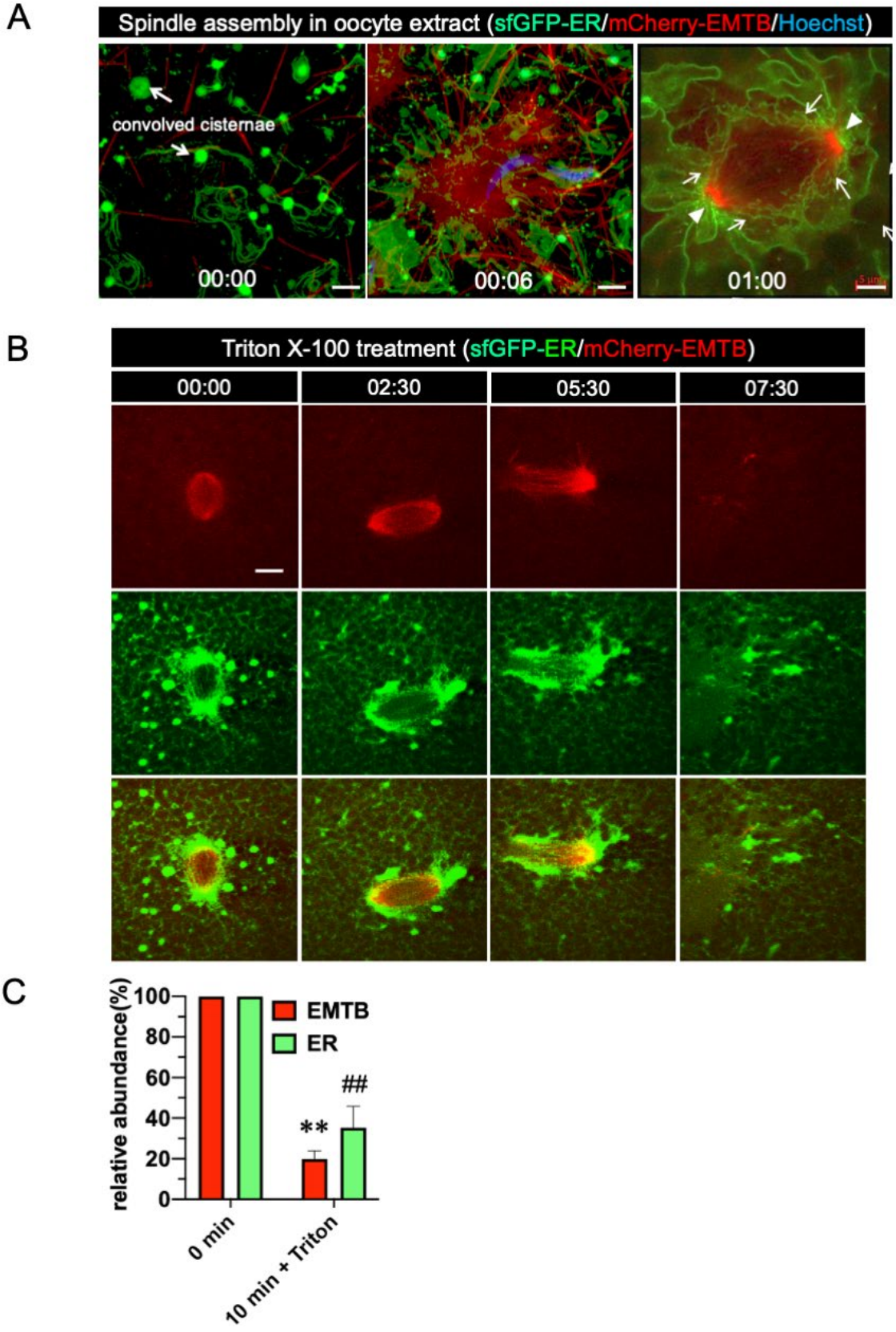

IV.2.3 IP_3Rs are required for spindle function

IV.2.3.1 IP_3Rs are concentrated at spindle poles

Since IP_3Rs are the dominant Ca^{2+} releasing channels of ER in *Xenopus* oocytes (Parys et al., 1992), they are the likely channel candidates that cause local $[Ca^{2+}]_i$ elevation at the spindles. We first examined the distribution of IP_3Rs at the spindles assembled in cell extracts expressing full-length EGFP-IP_3R1 (see **II.10.2** for plasmid information) and microtubule marker mCherry-EMTB. Using live-cell imaging, IP_3Rs were found to be concentrated at the spindle poles (**Figure IV.3A**, arrows), reminiscent of the ER distribution in **Figure IV.2A**. Next, immunofluorescence was performed to examine the distribution of IP_3Rs at the spindle region of intact oocytes (see **II.9** for staining method). Methanol-fixed oocytes were stained with anti-IP3R1 rabbit polyclonal and anti-β-tubulin mouse monoclonal antibodies (see **II.10.3** for detailed antibody information). The IP_3Rs were accumulated at the poles of bipolar spindles (**Figure IV.3B**, top row, single *z*-section focused at one pole) and STLC-induced monoastral spindles (**Figure IV.3B**, bottom row). At a closer look, the typical size of an IP_3R particle is about 250–400 nm in diameter (**Figure IV.3B**, inset), suggesting the clustering of IP_3Rs (a single IP_3R is about 30 nm in diameter) (Shuai et al., 2006). At the spindle region where tubulin fibers are relatively sparse, puncta IP_3R1 signals could be specified on the microtubules (tubulin signal) (**Figure IV.3B**, "beads on a string"), reminiscent of a recent report that showed that IP3R1 motion is directed along microtubules (Thillaiappan et al., 2017). Taken together, these results were consistent with the previous observation that ER membranes were closely contacted with spindle microtubules and concentrated at the poles (**Figure IV.2A**), suggesting that IP_3Rs are responsible for the Ca^{2+} release from the ER-associated with spindles.

Figure IV.3 Spindles are associated with functional IP_3Rs
(A) A representative bipolar spindle assembled in the oocyte extract expressing EGFP-IP_3R (green), mCherry-EMTB (red; microtubule marker) and in the presence of Hoechst (blue; DNA marker). Arrows: IP_3Rs accumulate at spindle poles. Scale bar = 10 μm.
(B) Immunofluorescence images of IP_3R1 distribution in bipolar spindles (a *z*-section focused at one pole), STLC-induced monopolar spindles (bottom row). Oocytes are fixed and stained with anti-β-tubulin (green), anti-IP_3R1 (red) antibodies and Hoechst dye (blue). IP_3R1 signals are associated with spindle microtubules (tubulin signals) and particularly concentrated at spindle poles. The inset shows typical sizes of fluorescent spots. Scale bar = 10 μm (general) and 1 μm (inset and "beads on a string").
The right panel shows a beads-on-a-string pattern of IP_3R1 signals on microtubules (β-tubulin). Scale bar = 1 μm.
(C) Spindle-based $[Ca^{2+}]_i$ increase upon IP_3 releasing. Oocytes injected with OG-2 and caged IP_3 are imaged 1hour after GVBD. A schematic on the leftmost depicts two focal planes where measurements are taken. Red circles denote the measurement taken at the spindle or a measurement taken at the cortex region directly above the spindle. Similarly, black circles denote the measurement taken at the cytosol or the region at the cortex directly above the cytosol. Every oocyte has two measurements taken, with one at the spindle plane and the other at the cortex plane. Each measurement is taken in separate UV-exposure attempts with an interval of more than 5 minutes for the re-sensitization of IP_3Rs.
Heatmaps indicate $[Ca^{2+}]_i$ distribution before and after 500ms UV exposure at the cortex plane (top row) or the spindle plane (bottom row). Dashed circles in images represent areas of fluorescence measuring as described above. Scale bar = 20 μm.
The ratios of the bar plot summarizes the change of $[Ca^{2+}]_i$ at the spindle plane compared to that at the cortex plane following UV exposure. $\text{Ratio}_{\text{spindle plane}} = \frac{\Delta F_{\text{spindle}}}{\Delta F_{\text{cytosol}}} = \frac{\Delta F_{\text{red circle}}}{\Delta F_{\text{black circle}}}$; $\text{Ratio}_{\text{cortex plane}} = \frac{\Delta F_{\text{cortex-above-spindle}}}{\Delta F_{\text{cortex-above-cytosol}}} = \frac{\Delta F_{\text{red circle}}}{\Delta F_{\text{black circle}}}$. Means ± S.E.M.; ** indicates $p < 0.01$ *vs.* cortex plane; n = 14.
IP_3R are known to be enriched at the cortex. However, the much greater increase of fluorescence at the spindle region indicates the enriched presence of functional IP_3Rs at the spindle (red circle) than nearby cytoplasm (black circle).

Figure IV.3 Spindles are associated with functional IP_3Rs

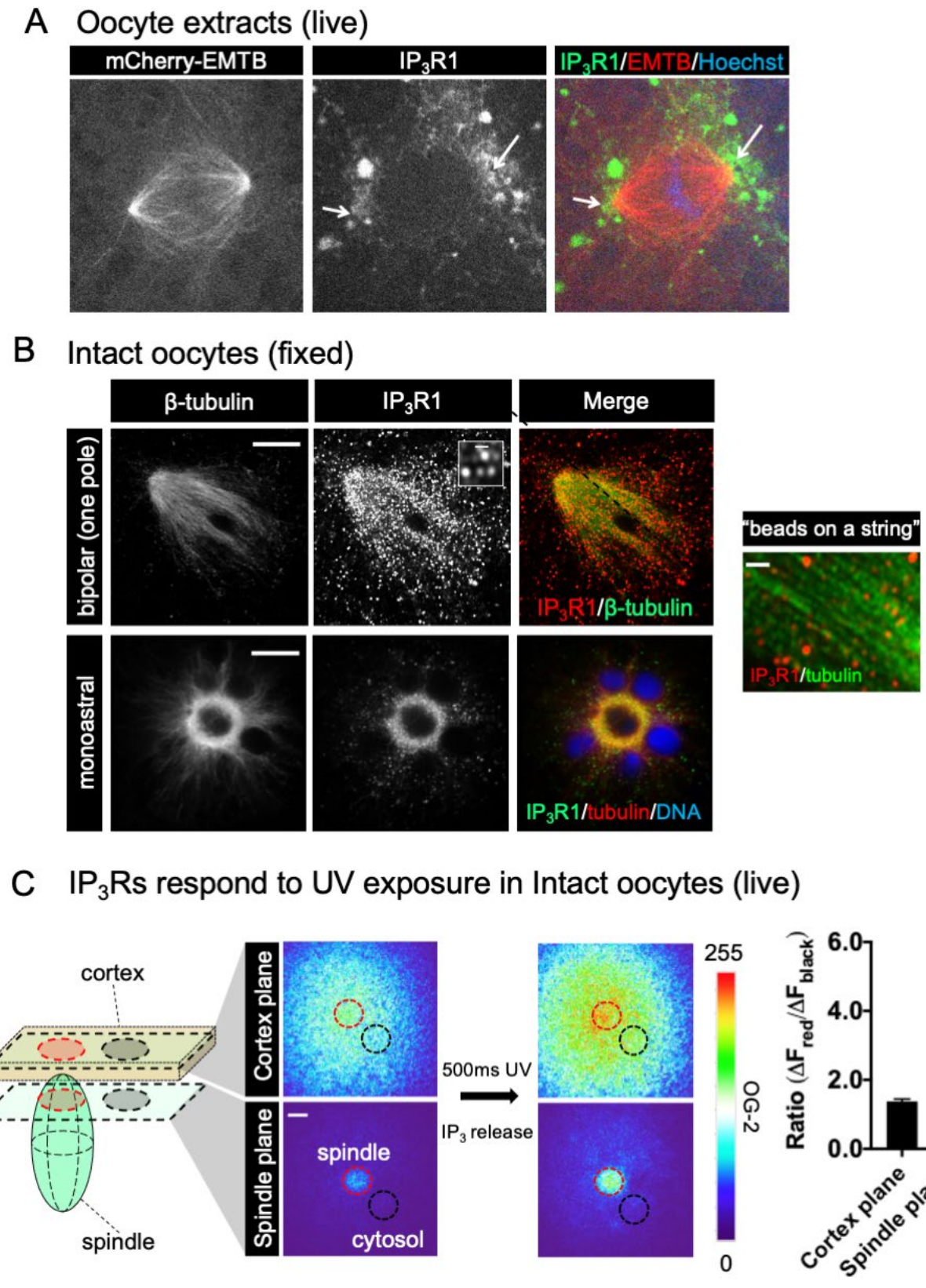

IV.2.3.2 Spindle-associated IP$_3$Rs are responsible for Ca^{2+} release

To demonstrate the Ca^{2+} releasing capability of the spindle-associated IP$_3$Rs, we injected oocytes with OG-2 (a mobile Ca^{2+} indicator) and caged-IP$_3$ (see **II.7** for uncaging protocol), as well as a chromosome probe to mark cell cycle stage and spindle location (chromosomes are not presented in figures). We imaged metaphase oocytes, focusing on a plane about 10μm away from the cortex (**Figure IV.3C** schematic). Before UV exposure, the OG-2 signal was more intense at the spindle than the surrounding cytosol (**Figure IV.3C**, left column, also shown in **III.2.2.3, Figure III.5C)**. Immediately after UV photolysis (IP$_3$ uncaging), OG-2 signal in the spindle region increased dramatically (**Figure IV.3C**, spindle plane), suggesting local $[Ca^{2+}]_i$ elevation due to the opening of IP$_3$Rs.

Since Ca^{2+} could be released from the cortex where IP$_3$Rs are enriched (El-Jouni et al., 2005), quantitative analysis was performed to evaluate the Ca^{2+} from the cortex source and the spindle source. OG-2 signals were measured at the spindle region and a nearby cytosolic region of the same size as a reference (**Figure IV.3C**, spindle plane, dashed circles). Measurements were also taken in separate UV-exposure attempts at the cortex regions (**Figure IV.3C**, cortex plane, dashed circles) directly above the corresponding regions at the spindle plane (**Figure IV.3C** schematic). We calculated the ratio of increased signals at the two circled regions of the same plane (*e.g.* $\text{ratio}_{\text{spindle plane}} = \frac{\Delta F_{\text{spindle}}}{\Delta F_{\text{cytosol}}} = \frac{\Delta F_{\text{red circle}}}{\Delta F_{\text{black circle}}}$, ΔF is the increased signal following UV illumination); if the $[Ca^{2+}]_i$ elevation at the spindle is only caused by Ca^{2+} flow from the cortex, the ratio of increased signals at two planes should be identical. However, the ratio of increased signals at the spindle plane was significantly higher than that of the corresponding regions at the cortex plane (**Figure IV.3C**, bar plot). This result suggested that

there existed spindle-based Ca^{2+} release, consistent with the enrichment of functional IP_3Rs at the spindle.

IV.2.3.3 IP_3R inhibitor causes spindle collapse

To test the function of IP_3R in spindle assembly, we injected heparin, an IP_3R antagonist, into intact oocytes (**Figure IV.4A**) or oocyte extracts (**Figure IV.4B**). Metaphase I oocytes injected with increasing concentrations of heparin showed that polar body emission was significantly inhibited at the concentration of 330 μg/mL (**Figure IV.4A**, bar plot). Confocal imaging was then performed to examine the detailed process. Spindles in the control group (injected with water) persisted through metaphase I and succeeded in polar body emission (**Figure IV.4A,** top series) while the spindles in the heparin group (330 μg/mL, final concentration.) shrank and detached from the cortex within 20 minutes after injection (**Figure IV.4A** bottom series). In cell extract, heparin treatment (200 μg/mL, final concentration) caused the loss of microtubules (~80%) and spindle disassembly within 20 minutes (**Figure IV.4B** bottom series, and the bar plot), a time course similar to that of injection in intact oocytes. For comparison, Groigno *et al.* injected heparin in sea urchin early embryos at a final concentration of 150–200 μg/mL, where they found spindle sizes are reduced by ~30% and chromosome separation during cytokinesis is hindered (Groigno and Whitaker, 1998). These data suggested that IP_3Rs are required for spindle assembly, consistent with the results that functional IP_3Rs are intimately associated with spindles (**Figure IV.3A**, **IV.3B**, **IV.3C**).

Figure IV.4 Heparin intervention causes spindle collapse

(A) Confocal images show a representative metaphase oocyte before (00:00) and at the indicated time after microinjection of water (top row) or heparin (bottom row, final concentration is 330 μg/mL). The spindle in the control group persists through metaphase and the oocyte succeeds in polar body emission (top row, arrow) while the spindle in the heparin group disappears within 20 minutes after injection (bottom row). Spindle microtubules labeled with GFP-EMTB (green); chromosomes with H2B-RFP (red). Time in hour:minute. Scale bar = 20 μm.

The bar plot exhibits the percentage of oocytes emitting polar bodies at the different concentrations of heparin injection. Only 330 μg/mL group shows a significant difference compared to control (** indicates $p < 0.01$). NS: not statistically significant. Numbers for control, 33 μg/mL, 110 μg/mL and 330 μg/mL are 7, 7, 9 and 10 respectively.

(B) Confocal images show control (OR2 medium; top row) and heparin-treated (200 μg/mL; bottom row) extract spindles. Heparin injection causes spindle disassembly in the treatment group. Microtubules are labeled with EMTB-GFP (green); chromosomes labeled with H2B-RFP (red). n = 10. Time in hour:minute. Scale bar = 20 μm.

Right: A bar plot summarizes the relative spindle microtubule abundance of 20 minutes after heparin injection (% before injection). Means ± S.D.; ** indicates $p < 0.01$ *vs.* control; n = 10.

Figure IV.4 Heparin intervention causes spindle collapse

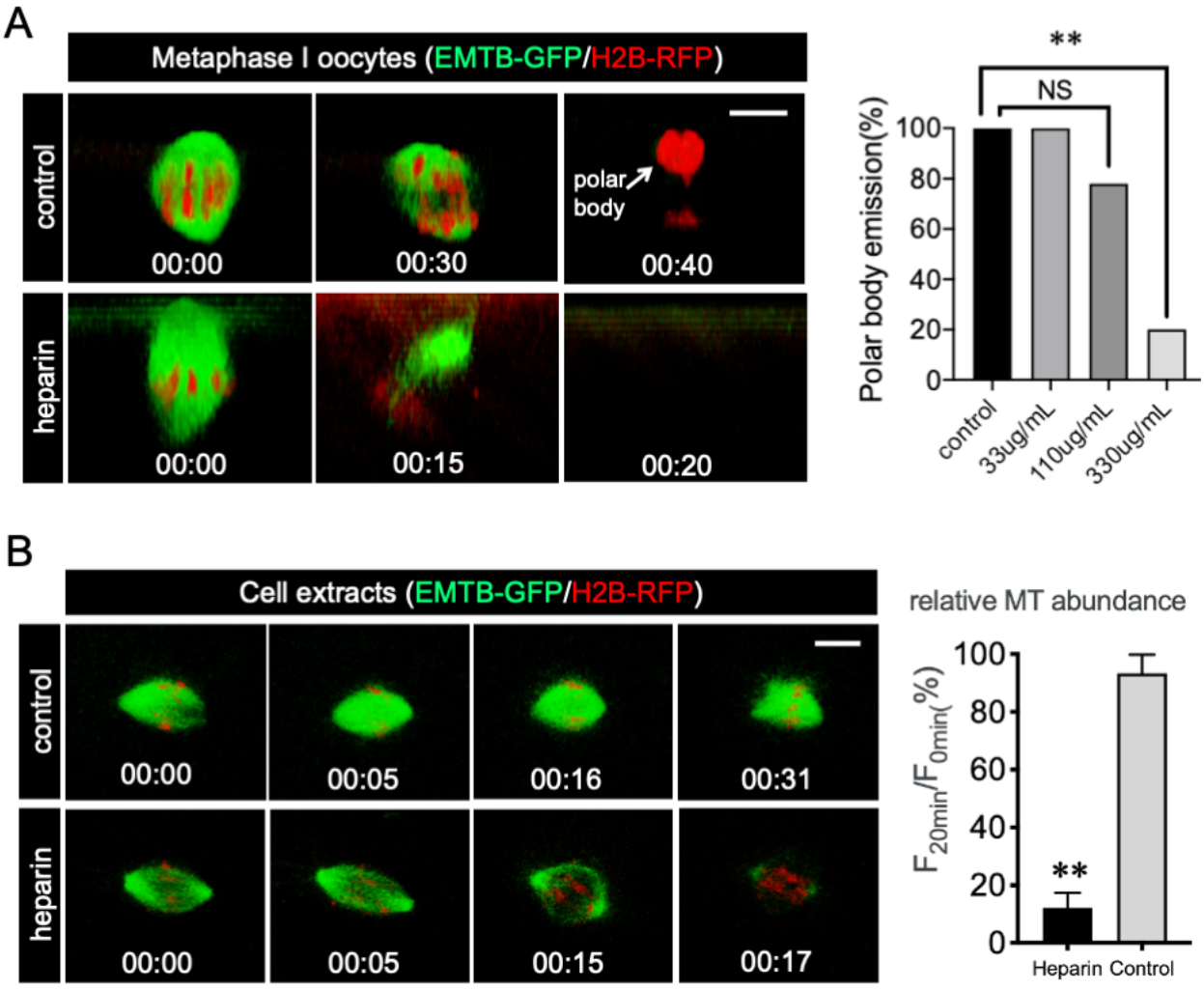

IV.2.4 Potential targets of nanodomain Ca^{2+} signaling

IV.2.4.1 Calmodulin is associated with Xenopus oocyte spindles

Calmodulin is a common calcium-binding messenger that can regulate a variety of target proteins. Calmodulin is known to bind IP_3Rs and functions to regulate IP_3R channel activity and/or as a Ca^{2+} sensor downstream of IP_3Rs (Kasri et al., 2006; Tang et al., 2001). Previous studies have shown that calmodulins are intimately associated with spindles, and involved in regulating microtubule assembly, organization and pole formation (Li et al., 2016; Moisoi et al., 2002; Schoborg et al., 2015; van der Voet et al., 2009; Xu et al., 2012). To investigate the distribution of calmodulins at the spindles of *Xenopus* oocytes, we stained methanol-fixed metaphase I oocytes with anti-calmodulin and anti-β-tubulin antibodies and performed immunofluorescent assays (see **II.9** for immunostaining method, **II.10.3** for antibody information). Bipolar spindles and STLC-induced monoastral spindles were imaged with LSM880 Airyscan microscopy (**Figure IV.5A**, bottom row). High-resolution imaging showed a pattern of polar accumulation, similar to that of IP_3Rs (**Figure IV.3B**).

Figure IV.5 Potential targets of Ca^{2+} nanodomain signaling
(A) Immunofluorescence images of calmodulin distribution in the bipolar spindle (top row, a z-section focused at one pole) and STLC-induced monopolar spindle (lower). Oocytes are stained with anti-β-tubulin, anti-calmodulin antibodies and Hoechst dye. Calmodulin signals are associated with spindle microtubules (tubulin signals) and particularly concentrated at spindle poles. The inset shows typical sizes of fluorescent spots. Scale bar = 10 μm (general) and 1 μm (inset).
(B) GMPCPP protects spindle microtubules from DB-BAPTA intervention. Control oocytes and GMPCPP-injected (1mM) oocytes before (00:00) and after injection of DB-BAPTA (00:12; 2.5mM final concentration). Green: microtubules; red: chromosomes. Scale bar = 20 μm. Time in hour:minute.
The bar plot summarizes the relative microtubule abundance 12 minutes after DB-BAPTA injection. Means ± S.D.; ** indicates $p < 0.01$; n= 5.

Figure IV.5 Potential targets of nanodomain Ca^{2+} signaling

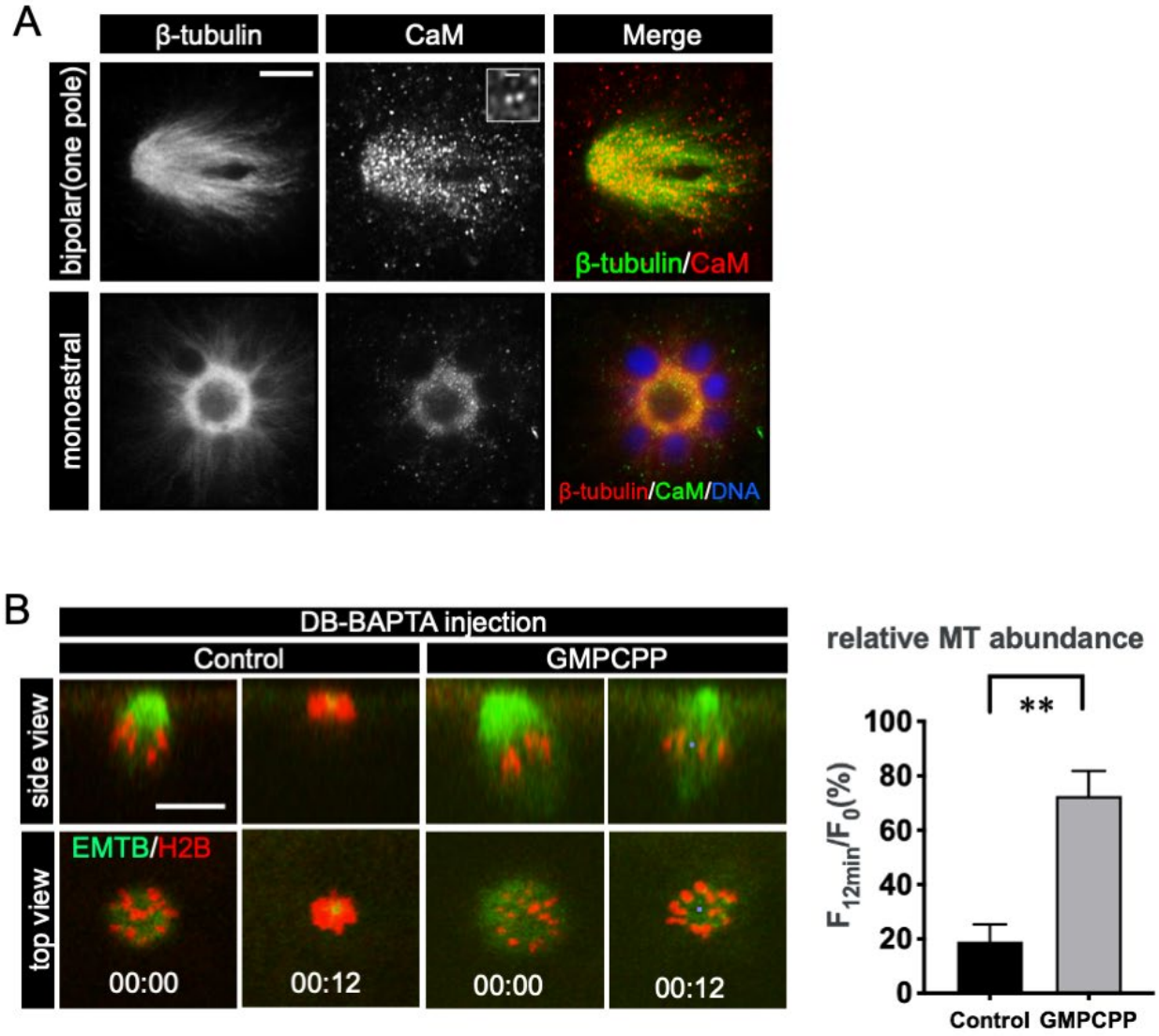

IV.2.4.2 Calcium nanodomain protects spindle microtubules by attenuating GTP-hydrolysis dependent depolymerization

The rapid spindle collapse caused by BAPTA (**IV.2.1** and Li et al., 2016) is reminiscent of nocodazole-treated oocytes where nocodazole disrupts most spindle microtubules in ~4 minutes (Shao et al., 2013). Nocodazole is thought to cause microtubule depolymerization by generating GDP-bound β-tubulins at microtubules (Vasquez et al., 1997). Microtubules can dynamically switch between growth and shrinkage (a.k.a. catastrophe). The "switches" are β-tubulins bound with GTP or GDP (see **I.1.2.2**). The GTP-bound β-tubulins are an essential factor for microtubule polymerization while, upon GTP hydrolysis, the resulting GDP-β-tubulins are much more prone to depolymerization leading to microtubule shrinkage (Desai and Mitchison, 1997).

Inspired by the similar phenotypes of nocodazole- or BAPTA-treated oocytes, we wonder if nanodomain Ca^{2+} signaling functions to prevent GTP hydrolysis-dependent catastrophe. To examine this possibility, we tested the effect of BAPTA on spindles assembled in the presence of non-hydrolyzable GTP analog, GMPCPP (see **II.10.4** for detailed information). A previous report showed that GMPCPP-tubulin exhibited a similar polymerization rate to that of GTP-tubulin while high resistance to depolymerization (depolymerization rate of GMPCPP is 5,000 times slower than GDP-tubulin) (Hyman et al., 1992). Partial incorporation of GMPCPP can also consistently rescue depolymerizing microtubules from catastrophe (Tropini et al., 2012). During experiments, oocytes expressing microtubule (EMTB-GFP, green) and chromosome probes (H2B-RFP, red) were injected with

water (control) or GMPCPP (1 mM, final concentration)[30]. Control oocytes with a bipolar spindle (**Figure IV.5B**, control, 00:00) were injected with DB-BAPTA which caused fast microtubule depolymerization and chromosome clustering (**Figure IV.5B**, control, 00:12). In contrast, the bipolar spindle formed in the presence of GMPCPP (**Figure IV.5B**, GMPCPP, 00:00) showed significant resistance to DB-BAPTA (**Figure IV.5B**, GMPCPP, 00:12). These results suggested that the rapid collapse of spindles by fast Ca^{2+} chelators was at least partially attributed to the increase of GDP-tubulin mediated depolymerization. In other words, spindle-associated calcium nanodomains help stabilize spindle microtubules by preventing rapid shrinkage of microtubules, *i.e.* microtubule catastrophe.

IV.3 Discussion

IV.3.1 Recap of the results

In this chapter, we explored potential calcium nanodomains at spindles. By using EGTA/BAPTA tests, the significance of calcium nanodomains was first elaborated at spindles assembled in cell extracts, monoastral spindles and spindle bipolarization in intact oocytes (**IV.2.1**). Then we dissected the molecular components of potential Ca^{2+} source for calcium nanodomains at the spindle (**IV.2.2-IV.2.3**). ER membranes were found to be in close contact with spindles and concentrated at spindle poles in oocyte extracts (**IV.2.2.1**). Consistently, the dominant Ca^{2+} releasing channel IP_3Rs were associated with spindles, especially polar regions (**IV.2.3.1**). Similar IP_3R patterns were found at the spindles in intact oocytes (**IV.2.3.1**). The

[30] Too much GMPCPP will hamper normal microtubule dynamics that ensure proper spindle functions. We injected increasing concentrations of GMPCPP and found that at 1 mM or below, GMPCPP did not affect spindle assembly or polar body emission.

IP_3Rs at the spindles were indeed functional, supported by experiments of IP_3-induced Ca^{2+} release (**IV.2.3.2**) and inhibitor intervention (**IV.2.3.3**). The identities of downstream targets remained unclear, but calmodulin appears to be a promising candidate as a calcium sensor in the spindle-based nanodomains (**IV.2.4.1**). Spindle microtubules were protected by nanodomain Ca^{2+} signaling through a GTP-hydrolysis dependent pathway (**IV.2.4.2**). Altogether, these results demonstrate the distribution of Ca^{2+} stores (ER) and channels (IP_3Rs) associated with spindle apparatus, and their functional links to spindle organization and maintenance.

IV.3.2 ER-IP_3R based Ca^{2+} signaling at spindles

Microtubules and ER have long been considered to be highly interdependent structures (Lee et al., 1989; Terasaki et al., 1986). During the cell cycle, microtubule-associated proteins at the spindle play a crucial role in ER dynamics. In our study, we observed the ER remodeling accompanied bipolar spindle formation: Highly convolved ER membranes gradually loosened themselves and accumulated at spindle poles (**Figure IV.2**). This observation is consistent with previous reports that dynein, the microtubule minus-end motor, accounts for the partitioning and aggregation of ER at spindle poles or MTOCs (Niclas et al., 1996; Wang et al., 2013). On the other hand, Ca^{2+} signals in dividing *Drosophila* embryos have suggested that ER compartmentalizes spindle apparatus during the cell cycle and delivers highly localized Ca^{2+} for proper spindle functions (Parry et al., 2005; Whitaker, 2006b). Previous studies for calcium's role in spindle functions, however, are mainly focused on local Ca^{2+} regulation in anaphase and cytokinesis (Chang and Meng, 1995; Groigno and Whitaker, 1998). Li *et al.* provide the first compelling evidence that highly localized Ca^{2+}, or calcium nanodomain, can be functionally associated with spindle assembly (Li et al., 2016). Our studies

in various *Xenopus* oocyte-based systems provide further evidence and link the source of Ca^{2+} to the spatiotemporally intimate ER and IP_3R channels (**Figure IV.2–IV.4**). The distribution pattern of ER and IP_3R also strongly support the detection of pole-specific $[Ca^{2+}]_i$ elevation (**Chapter III**). Interestingly, apart from the accumulation of IP_3Rs at the spindle poles (minus ends of microtubules), our high-resolution images also show a "beads-on-a-string" pattern of IP_3Rs (**Figure IV.3B,** IP_3R puncta on tubulin strings). This result is consistent with the recent reports that microtubules and motor proteins direct the movement of mobile IP_3Rs (mobile within ER membranes), where similar patterns of IP_3R puncta on tubulin string are observed (Geyer et al., 2015; Thillaiappan et al., 2017). Our study of IP_3R's role in spindle regulation, together with previous reports on microtubule directing IP_3R clustering, suggests that there is a profound interplay between IP_3R function and spindle microtubule organization.

The sizes of IP_3R "particles" (**Figure IV.3B**, ~250–400 nm) suggest the clustering of IP_3Rs associated with the spindle. This is consistent with the previous report that IP_3R clusters are being reshaped during *Xenopus* oocyte maturation in response to major M-phase drivers such as MPF (El-Jouni et al., 2005; Sun et al., 2011). It is estimated a typical IP_3R is about 30 nm in diameter and can be packed into a "crown-like" cluster (consists of ~30–60 individual receptors) ranging from less than 300 nm to 800 nm in lateral extent (Shuai et al., 2006). In a classical paper, Dargan *et al.* reported that, in *Xenopus* oocytes, intra-IP_3R-cluster Ca^{2+} communication can be interfered with by fast chelator BAPTA but is much more resistant to slow chelator EGTA intervention (Dargan and Parker, 2003). Similarly, Ca^{2+} binding proteins of different kinetics can fine-tune local Ca^{2+} events induced by IP_3, implicating an endogenous localized regulating mechanism (Dargan et al., 2004). These reports implicate that, in our study, the calcium nanodomains for spindle assembly are likely within the IP_3R cluster.

Calmodulin is considered as a "prototype" Ca^{2+} sensor in nanodomain source-to-sensor coupling (Tadross et al., 2008). But its role in spindle nanodomains is much less clear. Previous reports have shown calmodulin is enriched at spindles in both mitosis and meiosis (Li et al., 2016; Moisoi et al., 2002). Our results also showed that, in high-resolution imaging, calmodulins exhibited a similar pattern as IP_3Rs at the spindle (**Figure IV.5A**). Calmodulin can regulate IP_3R activity by direct binding in a Ca^{2+} dependent manner (Hirota et al., 1999). Calmodulin has four Ca^{2+} binding sites and can be activated to different extents depending on Ca^{2+} occupation. *In vitro* study suggested that full activation of calmodulin requires 10–100 μM local $[Ca^{2+}]_i$ (Faas et al., 2011). This high $[Ca^{2+}]_i$ can only be reached nearby Ca^{2+} channel mouths, including those of IP_3Rs (Rudiger et al., 2010; Tadross et al., 2013). Faas *et al.* report that calmodulin is the fastest endogenous calcium buffer protein (CBP) and is able to intercept Ca^{2+} released from the Ca^{2+} channel mouth before any other CBP has a chance (Faas et al., 2011). As estimated, it takes only ~12.5 μs for the N-lobe of calmodulin to be fully bound by Ca^{2+} at 50 nm away from the channel mouth (Faas et al., 2011). This response time is close to the time required for BAPTA/Ca^{2+}'s equilibrium (~3 μs) at the distance of 100 nm, but much faster than that of EGTA/Ca^{2+} (~1.2 ms) (see **I.2.3.1**) (Adler et al., 1991), suggesting only BAPTA but not EGTA can inhibit the full activation of calmodulin. Given the distribution of calmodulin at spindles, we suggest that calmodulin is a promising candidate as a nanodomain Ca^{2+} sensor at the spindle. However, further evidence, especially loss-of-function studies, are required to elucidate the exact role of calmodulin in nanodomain Ca^{2+} signaling.

The end effectors — the molecules that directly bind and regulate microtubules — of nanodomain Ca^{2+} signaling is unclear. Our data showed that incorporation of GMPCPP reduced the effect of DB-BAPTA's intervention on spindles (**Figure IV.5B**), suggesting

calcium nanodomain's role in protecting microtubule from rapid depolymerization, *i.e.* microtubule catastrophe. We thus speculate that nanodomain Ca^{2+} signaling may function through deactivating (or preventing from activation) catastrophe factors, such as MCAK (kinesin-13) and Kif18A (kinesin-8) (Gardner et al., 2011). To unravel the molecular pathway of nanodomain Ca^{2+} signaling at spindle apparatus remains to be our future goal.

IV.3.3 Limitations

Current results fall short of reagent specificity in loss-of-function studies. Heparin is a competitive IP_3R antagonist but also widely uses as an anticoagulant. As an IP_3R inhibitor, it should be used with caution due to its non-specific binding and side effects (Taylor and Tovey, 2010). A more specific inhibitory assay is to use peptides that bind to IP_3R's N-terminal "suppressor domain". This binding will block the conformational change that is essential to activate IP_3R (Sun et al., 2013). Alternatively, the ligand IP_3 can be targeted and "trapped" by high-affinity binding peptides that are based on the IP_3-binding domain of IP_3Rs (Yoshikawa et al., 1999). While production and purification of peptides can be laborious, a recently developed method based on rapid protein degradation in live cells, dubbed "Trim-Away", is easily applicable and has successful implementations in mouse oocytes (Clift et al., 2017; Clift et al., 2018). The key player TRIM21, which recognizes Fc domain and binds to immunoglobulin G, A, and M, can ubiquitinate antibody-bound pathogens; within minutes (reported half-lives: 10–20 minutes), the tagged proteins will be degraded rapidly by endogenous proteasomes (Clift et al., 2018). The combined application of TRIM21 and IP_3R specific antibodies (Kume et al., 1993) is a promising approach to study IP_3R's role in spindle functions.

In our study, Triton X-100 was used to examine the correlation between ER and spindle integrity. However, ER's function as Ca^{2+} stores cannot be fully explained by indiscriminate disruption of membrane structures. For example, the Golgi apparatus, another membrane-based system, has also been shown to regulate spindle assembly (Wei et al., 2015; Zhang et al., 2011). Besides this, there are also controversial reports regarding the requirement of membranes in spindle assembly. Groen *et al.* report that bipolar spindles can be assembled in the processed extracts that do not contain visible membranes probed by the lipophilic membrane dye, FM4-64 (Groen et al., 2011). In other reports, evidence suggested membranes are required for spindle pole formation, motor protein actions and spindle compartmentalization with biochemical properties that favor the nucleation/growth of microtubules (Liu and Zheng, 2009; Poirier et al., 2010; Schweizer et al., 2015). Further experiments, especially loss-of-function in intracellular settings, are needed to address these controversies.

Chapter V Ca^{2+} transients during polar body emission

V.1 Introduction

In animal mitotic cells, cytokinesis occurs when chromosomes separate, initiated by the formation of an actomyosin contractile ring at the plasma membrane at the division plane. Subsequently, the actomyosin contractile ring constricts and furrows the cell into two parts connected by an intercellular bridge filled with reorganized spindle microtubules known as the midbody. The middle part of the bridge is a protein-rich structure called centralspindlin functioning as a transient signaling hub (Hu et al., 2012). Recent midbody interactome studies in HeLa cells revealed that nearly 3000 proteins are associated with the midbody, suggesting a complicated and robust role of the midbody in regulating cytokinesis (Capalbo et al., 2019). Abscission is the last step of cytokinesis that completes the separation of daughter cells. During the last decade, emerging evidence suggests that ESCRT-III (endosomal sorting complex required for transport-III), an evolutionary-conserved protein filament across archaea and eukaryotes, likely drives the abscission by constricting and splitting the plasma membrane at both sides of the midbody (Goliand et al., 2018; Tarrason Risa et al., 2020). Recruitment and assembly of ESCRT-III at the intercellular bridge require activities of membrane vesicle-fusion machinery such as SNARE (soluble N-ethylmaleimide sensitive factor attachment protein receptor) and Rab GTPases; the exact pathway is however poorly understood and remains one of the most important questions in cytokinesis (Fremont and Echard, 2018; Pollard, 2017).

A special kind of cytokinesis, called polar body emission, happens in animal oocyte meiosis. Oocyte meiosis consists of two rounds of asymmetric division (meiosis I and meiosis II), producing two polar bodies and a larger haploid oocyte. In *Xenopus* oocytes, anaphase initiates with the separation of homologous chromosomes and the membrane protrusion at the cortex where the spindle apparatus contacts. During membrane protrusion, a ring-shaped RhoA activity zone (or RhoA contractile ring) that overlaps the actomyosin contractile ring is formed. The RhoA contractile ring gradually constricts from mid-anaphase (2–5 minutes after anaphase initiation). Polar body emission is considered to be accomplished within ~15 minutes after anaphase initiation, indicated by the complete closure of RhoA contractile ring (Ma et al., 2006; Zhang et al., 2008). The timing of polar body abscission and the associated mechanisms are entirely unclear. Due to the asymmetric nature of cytokinesis in oocyte meiosis, it is suggested the activities required for polar body abscission are specifically presented or enriched in the polar body (Maddox et al., 2012). More detailed background (morphology changes, molecular mechanisms) has been introduced in **I.1.3.3 polar body emission**.

A large body of research has suggested that Ca^{2+} signaling plays important roles in multiple steps of cytokinetic regulation in somatic cells, especially in regulating contractile ring and cleavage furrow (Atilla-Gokcumen et al., 2010; Li et al., 2008). In *Xenopus* oocytes or oocytes of any higher animal species, the role of Ca^{2+} signaling in regulating cytokinesis, if any, is much less clear than in somatic cells (Liu, 2012; Marin, 2012). For instance, in *Xenopus* embryonic cells, calcium waves along the cleavage furrows are well-characterized, and the inhibition of which affects cell divisions (Muto et al., 1996). In contrast, in *Xenopus* oocyte maturation (*i.e.* meiosis I to metaphase II arrest), no Ca^{2+} transients have been identified to be associated with cytokinetic regulation. On the other hand, Sun *et al.* have shown deprivation

of Ca^{2+} before GVBD inhibits polar body emission, suggesting Ca^{2+} signaling is crucial in this process (Sun et al., 2008; Sun and Machaca, 2004). The failure to complete polar body emission can be attributed to spindle dysfunction or cytokinesis failure or both. Indeed, injecting Ca^{2+} chelator DB-BAPTA into oocytes at metaphase or anaphase onsets causes spindle collapse and complete block of polar body protrusion (Li et al., 2016), while injecting DB-BAPTA at mid-anaphase does not stop membrane protrusion nor actomyosin ring contraction, but blocks polar body abscission (**Figure I.3B**) (Leblanc, 2014). In previous chapters we have demonstrated the spindle-based Ca^{2+} that contributes to spindle functions; in this chapter, our goal is to reveal the Ca^{2+} signal that is potentially involved in polar body emission.

V.2 Results

V.2.1 Constructing TC4: a ratiometric Ca^{2+} reporter based on TC1

During polar body emission, spindle apparatus and plasma membranes undergo rapid and dramatic remodeling in space and time (Li et al., 2016; Zhang et al., 2008). To eliminate potential reporting bias of Ca^{2+} probes, we engineered a TC1 derivative that connected a red fluorescent protein (mCherry) to the N-terminus of TC1 (see **III.2.1** or **Figure III.1** for TC1 description). The resultant plasmid (mCherry-EMTB-GCaMP3) was dubbed Tubecamp4 or TC4. The detailed protocol was described in **II.2.2**. A schematic of construct design and working principle is shown in **Figure V.1A**. TC-mCherry stands for the mCherry unit of TC4 while TC-GCaMP3 stands for the GCaMP3 unit. In a TC4 expressing system, the TC-mCherry signal constitutively indicates the total amount of TC4 binding to microtubules while the TC-GCaMP3 signal reflects microtubule-proximal $[Ca^{2+}]_i$. Hence microtubule-proximal $[Ca^{2+}]_i$

elevation can be fairly measured by the elevated ratio of TC-GCaMP3 to TC-mCherry, regardless of any possible uneven distribution of the probe.

Figure V.1 TC4: a ratiometric Ca^{2+} reporter
(A) Upper: A diagram shows the design of TC4. TC4 is a TC1 derivative in which an N-terminus mCherry moiety has been added. Specifically, TC4 comprises an mCherry moiety at N-terminus, a linker with three amino acids (AAs), a microtubule-binding domain consisted of AAs 18–282 of ensconsin, a linker with a 6xHis tag, a myosin light chain kinase or M13 peptide, a permutated EGFP moiety (AAs 149–238 at N-terminus and AAs 1–144 at C-terminus) with two point mutations (M153K and T203V), a CaM moiety at C-terminus. The linkers within GCaMP3 moiety (M13-cpEGFP-CaM) are omitted in the diagram.
Lower: A cartoon illustrates the working principle of TC4. Upon Ca^{2+} binding, the GCaMP3 domain is circulated by the interaction of M13 peptide (CaM stabilizer) and CaM-Ca^{2+}. This leads to the change of EGFP fluorophore that generates much more fluorescence. Meanwhile, the fluorescence of mCherry unit stays unchanged. The calculated ratio of TC-GCaMP3 to TC-mCherry reflects the Ca^{2+} concentration corrected for potentially biased probe distribution.
(B) (Series) Selective still frames of a timelapse series show the change of TC4 subunits — TC-mCherry and TC-GCaMP3 following 2 seconds of UV exposure. The object in the dashed circle is a cross-section of the metaphase spindle. Oocytes were injected with caged IP_3 before imaging. Upon Ca^{2+} release by UV exposure (shown by an arrow in the plot), TC-GCaMP3 signal transiently arises while TC-mCherry stays the same. Scale bar = 20 μm. Time in minute:second.
The line plot summarizes the ratio change of fluorescence (TC-GCaMP3/TC-mCherry) inside the dashed circle over the recording time course. Mean ± S.E.M; n = 10.

Figure V.1 TC4: a ratiometric Ca^{2+} reporter

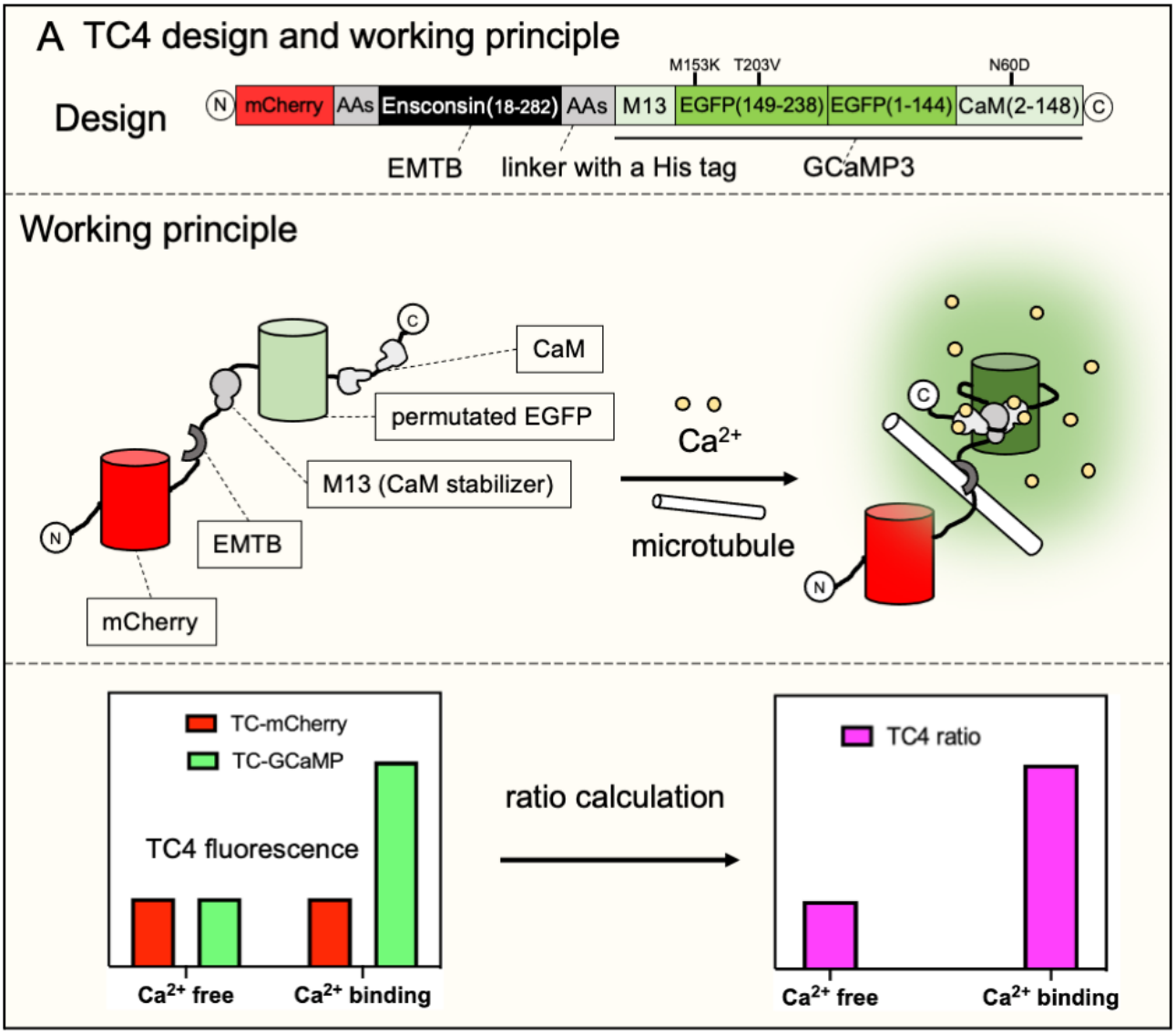

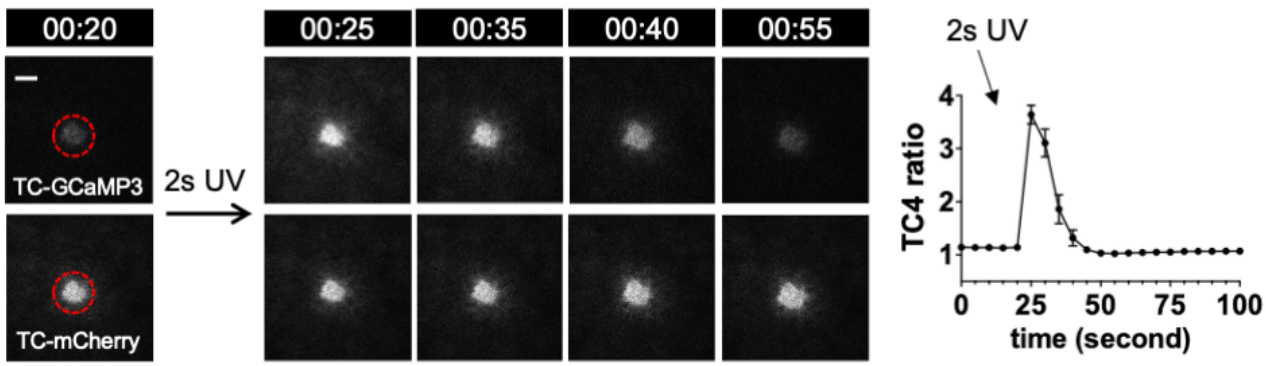

Figure V.1B demonstrates the measurement of microtubule-proximal $[Ca^{2+}]_i$ increase indicated by TC4. Oocytes expressing TC4 were injected with caged-IP_3 and then subjected to UV exposure. Images were taken at a plane 10–20 μm away from the cortex of metaphase I oocytes. Following UV exposure (IP_3 release), TC-GCaMP3 signal increased while TC-mCherry signal remained unchanged (**Figure V.1B,** confocal time series). The change of ratio at the spindle region reflects the change of spindle-based $[Ca^{2+}]_i$ (**Figure V.1B,** line plot). These data showed that TC4 was working as designed to report $[Ca^{2+}]_i$ elevation ratiometrically.

V.2.2 TC4 reports transient $[Ca^{2+}]_i$ elevation during polar body emission

Next, we employed TC4 to investigate the potential $[Ca^{2+}]_i$ change during polar body emission. In *Xenopus* oocytes, a previous study has shown that the majority (~73%) of intercellular bridges are closed within 60 minutes of anaphase onset, by using dextran conjugated dye to check the connection of polar bodies with oocytes (**Figure I.3B**). When the oocytes were injected with Ca^{2+} chelator 2-5 minutes after anaphase onset (*i.e.* mid-anaphase), neither membrane protrusion nor contractile ring constriction of the polar body was affected, but abscission fell to ~24% from ~73% (Leblanc, 2014). This suggested Ca^{2+} signaling plays a crucial role in polar body abscission.

To detect the potential Ca^{2+} signal during polar body abscission, TC4-expressing oocytes were subjected to timelapse confocal imaging (1-minute interval) after anaphase initiation (*i.e.* chromosome separation). A dramatic rise of TC-GCaMP3 signal was detected following the protrusion of the polar body (**Figure V.2A**, 12:00 and 13:00, time in minute:second from anaphase initiation). The elevated TC-GCaMP3 signal was first seen both in the polar body and the oocyte but later only in the polar body and midbody (arrow) before receding (**Figure**

V.2A). On average, the TC-GCaMP3 signal peaked ~13 minutes after anaphase initiation and lasted ~2 minutes (**Figure V.2B**). The timing and duration of TC-GCaMP3 signals overlap with the closure of the contractile ring indicated by RhoA-GTP signals (Zhang et al., 2008), suggesting that the detected Ca^{2+} signals were involved in polar body abscission. In addition, a significant increase of TC-mCherry signal towards midbody was observed during the transient $[Ca^{2+}]_i$ elevation (**Figure V.2A**, dashed squares, **Figure V.2C** for quantification). It suggested microtubule migration towards the emission site where membrane remodeling is active. This is reminiscent of the cytoskeleton dynamics during wound healing of *Xenopus* oocytes, whereby transport of microtubule with F-actin is pulled to wound borders via actomyosin-based contraction (Mandato and Bement, 2003), triggered by Ca^{2+} transient (Yu and Bement, 2007).

Figure V.2 TC4 reports transient local $[Ca^{2+}]_i$ elevation
(A) TC4 signals during polar body emission in *Xenopus* oocytes. Shown are selective still frames of a confocal timelapse series (minute:second). A transient $[Ca^{2+}]_i$ elevation is peaked around 13 minutes following anaphase initiation. Green: TC-GCaMP3; Red: TC-mCherry; Blue: Hoechst (DNA). White arrows indicate the midbody. Time in minute:second. Scale bar: 10μm.
(B) A line plot summarizes the fluorescence ratio change of TC4 subunits (TC-GCaMP3/TC-mCherry) during anaphase. Means ± S.E.M.; n=9.
(C) A bar plot summarizes the relative microtubule abundance near the midbody before and after the locally transient $[Ca^{2+}]_i$ elevation. A dashed directional line (fainted white) indicates the gradual increase of microtubules. This is reminiscent of the cytoskeleton dynamics during oocyte wound healing (Yu et al., 2007; Davenport et al., 2016; also shown in **Chapter III, Figure III.2**), suggesting the involvement of protein kinase Cβ activities. Dashed squares depict the regions of fluorescence measurement. Fluorescence before Ca^{2+} transient is normalized to 1. Means ± S.E.M.; n=9. ** indicates $p < 0.01$ *vs.* before transient; n= 9.

Figure V.2 TC4 reports transient local $[Ca^{2+}]_i$ elevation

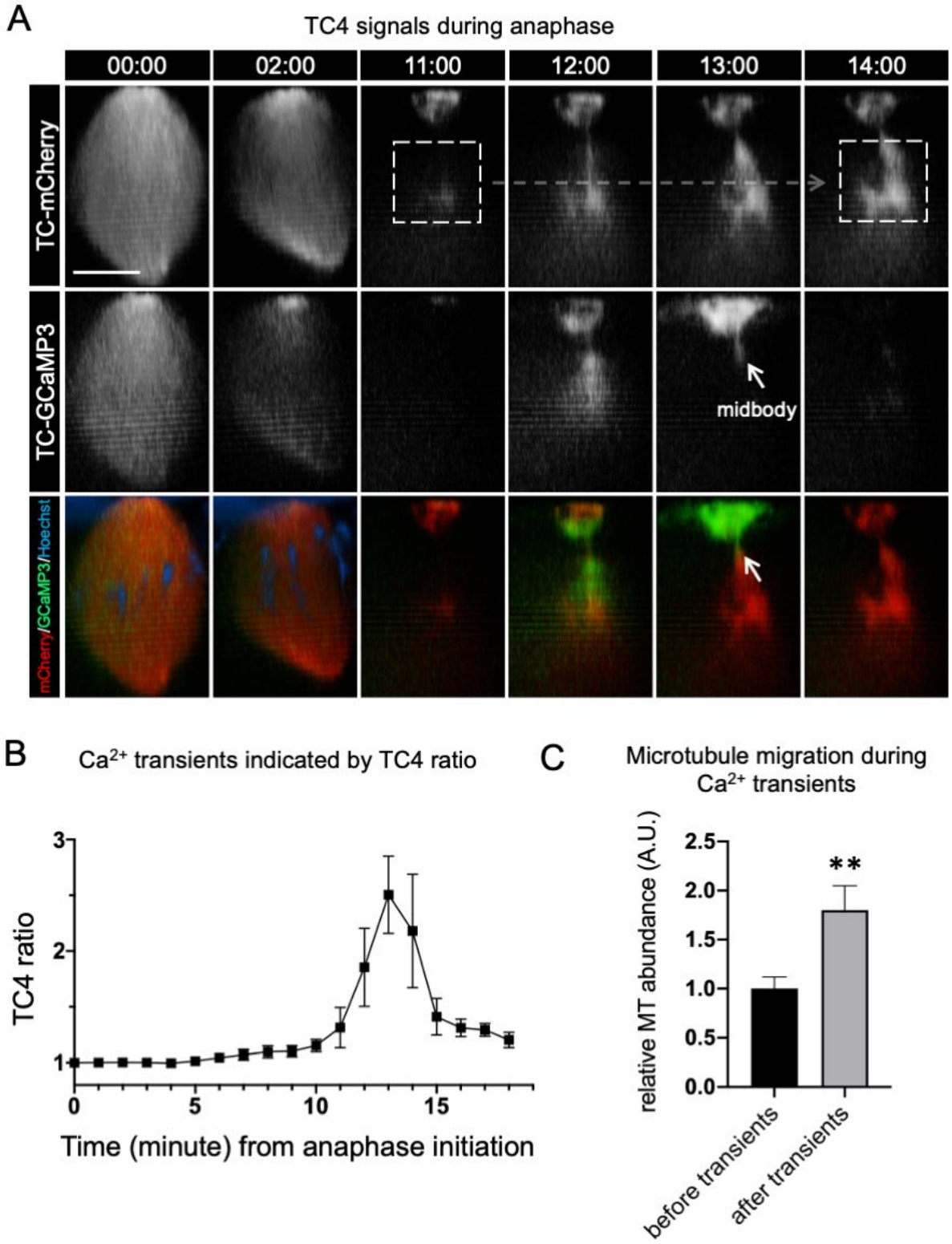

V.2.3 OG-2 and OG-6f report asymmetric Ca^{2+} transient during polar body emission

The distinct patterns of TC-GCaMP3 signals associated with microtubules shown in **Figure V.2A** implied the Ca^{2+} transient might be asymmetric and more intense at the polar body. To further explore the cytoplasmic Ca^{2+} fluctuation, we employed a mobile Ca^{2+} indicator, Oregon green 488 BAPTA-2 or OG-2 (K_d = 580 nM, See **II.10.1** for the detailed application of OG-2 and OG-6f). As expected, OG-2-indicated Ca^{2+} transient inside polar body exhibited the same time course as that detected by TC4 (**Figure V.3A**), suggesting the cytoplasmic change of Ca^{2+} inside the polar body was the same as that associated with microtubule. Next, we focused on a plane where both the oocyte cortex and polar body presented (**Figure V.3B,** schematic). The images and line plots in **Figure V.3B** and **Figure V.3C** (OG-6f) were recorded from ~11–12 minutes after anaphase initiation. Timelapse images at 3-second intervals showed that the transient $[Ca^{2+}]_i$ elevation was restricted to the polar body but largely absent nearby oocyte cortex (**Figure V.3B**, image series). Fluorescence quantification confirmed this observation and further revealed that the receding of the Ca^{2+} transient at the polar body was slow in contrast to the abrupt rising (**Figure V.3B**, line plot). This asymmetric Ca^{2+} transient during polar body emission was further tested by Oregon green 488 BAPTA-6f or OG-6f (K_d = 3 μM). It also showed a steeply rising signal and its spatial distribution was similar to those of OG-2 (**Figure V.3C**). Collectively, these results clearly suggested that during polar body emission the Ca^{2+} transient was preferentially active at the polar body but not the oocyte.

Figure V.3 Asymmetric $[Ca^{2+}]_i$ rise during polar body emission

(A) Shown are selective frames of a confocal time series (side view at 0:00, top view after 4:00) indicating OG-2 fluctuation during polar body emission. A transient rise of OG-2 signal is identified ~12–13 minutes after anaphase initiation. Time in minute:second from anaphase initiation. Scale bar = 20 μm.

(B) Imaging a horizontal cross-section (*xy*-plane view) across polar body and oocyte cortex by OG-2 during the transient rise of $[Ca^{2+}]_i$.

Top series: Selective frames (heatmaps) represent the uneven rise of OG-2 signal during polar body emission across the focal plane. Time in minute:second from recording. Scale bar = 10 μm. The line plot summarizes the fluorescence quantification of OG-2 at the polar body region (red) and cortex (black). Means ± S.E.M.; n =8.

The left schematic shows the focal plane for imaging (red dashed line). The focal plane includes the oocyte cortex and the polar body.

(C) Selective frames (heatmaps) represent the uneven rise of the OG-6f signal during polar body emission across the focal plane. Time in minute:second from recording. Scale bar = 10 μm. The line plot summarizes the fluorescence quantification of OG-6f at the polar body region (red) and cortex (black). Means ± S.E.M.; n = 10.

Figure V.3 Asymmetric $[Ca^{2+}]_i$ rise during polar body emission

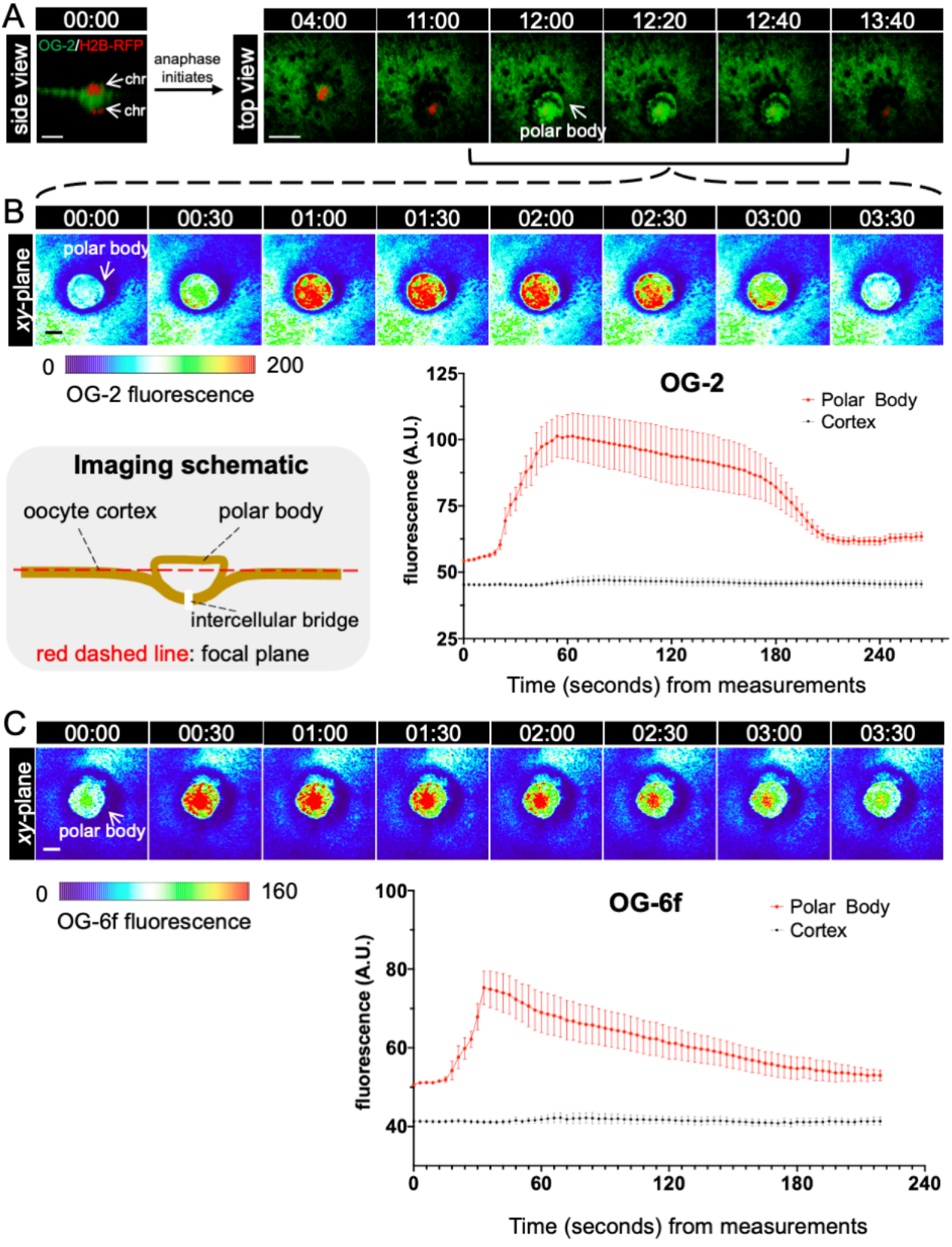

V.2.4 Transient accumulation of PKCβ C2 at the intercellular bridge

Results in **V.2.2** and **V.2.3** showed that the Ca^{2+} transient at the end of polar body emission was probably associated with membrane remodeling to separate the polar body from the oocyte. We next explored the spatiotemporal correlation between the Ca^{2+} transient and membrane dynamics. Protein kinase Cβ (PKCβ) activation is commonly engaged in membrane dynamics such as sealing, splitting, exocytosis and fusion. The initial step of these processes is the recruitment of PKCβ to membranes. The recruitment is triggered by local Ca^{2+} release, since Ca^{2+} binding leads to an increase of affinity of the PKCβ C2 domain for membrane lipids (Davenport et al., 2016; Yu and Bement, 2007).

To investigate the PKCβ C2 distribution during Ca^{2+} transient, Ca^{2+}-sensitive eGFP-PKCβ-C2 (C2 domain of PKCβ tagged with eGFP) and lipophilic Lck-mCherry (membrane targeting sequence of Lck tagged with mCherry) were expressed in oocytes (see **II.10.2** for plasmid information). Timelapse imaging was performed ~12 minutes after anaphase I initiation and recorded for ~3–4 minutes. Before the occurrence of Ca^{2+} transient, only the background eGFP-PKCβ-C2 signal was observed (**Figure V.4A** *xy*-plane view or **Figure V.4A'** *xz*-plane view, 00:00–00:25, time in minute:second). During the Ca^{2+} transient, eGFP-PKCβ-C2 rapidly concentrated on the intercellular bridge where the polar body connected to the oocyte; in contrast, Lck-mCherry stayed relatively static (**Figure V.4A**, **A',** 00:50–01:15). In addition, a temporary decrease of the eGFP-PKCβ-C2 signal was only seen at the polar body but not the oocyte (**Figure V.4A'**, *xz*-plane view). This can be explained by the relocation of eGFP-PKCβ-C2 in the polar body, due to the Ca^{2+}-binding that increases the lipophilicity of the PKCβ C2 domain. The fluorescence quantification indicates that the eGFP-PKCβ-C2 signal increased at the intercellular bridge (**Figure V.4B**) in a time course similar to that of the

Ca^{2+} transient shown in **Figure V.2** and **Figure V.3**. The schematic in **Figure V.4C** depicts a transient rise of eGFP-PKCβ-C2 and that cytosolic eGFP-PKCβ-C2 of the polar body is temporarily "drained" to the bridge membrane (reflecting what happened in **Figure V.4A'**, 00:50). This result suggested a Ca^{2+}-dependent PKCβ activity on the bridge membrane (Davenport et al., 2016; Yu and Bement, 2007). The spatial distribution of eGFP-PKCβ-C2 signals also suggested that the cytokinetic abscission only occurred at the polar body's side, not at the oocyte's.

Figure V.4 Transient recruitment of PKCβ C2 at the intercellular bridge
(A)&(A') Representative frames of *xy*- **(A)** and *xz*-plane **(A')** view during the rise of eGFP-PKCβ-C2 signals (green). The eGFP-PKCβ-C2 signal concentrates on the bridge membrane (indicated by Lck-mCherry, red) where the polar body is connected to the oocyte. eGFP-PKCβ-C2 signal **(A')** at 00:50 shows the probe in the polar body cytosol are temporally "drained" to the neck. Time in minute:second. Scale bar: 20 μm.
(B) A line plot summarizes the fluorescence change of eGFP-PKCβ-C2 during polar body emission. Means ± S.E.M.; n = 6.
(C) A schematic depicts the redistribution of eGFP-PKCβ-C2 inside the polar body during the arise. The 1st row: Before the occurrence of Ca^{2+} transient, eGFP-C2 is evenly distributed inside the polar body and nearby cortex. 2nd row: During Ca^{2+} transient, eGFP-PKCβ-C2 accumulates at the intercellular bridge where membranes are thick since the C2 domain of PKCβ assumes a lipophilic conformation upon Ca^{2+} binding. 3rd row and 4th row: The Ca^{2+} transient recedes, and the bridge is gradually closed.

Figure V.4 Transient recruitment of PKCβ C2 at the intercellular bridge

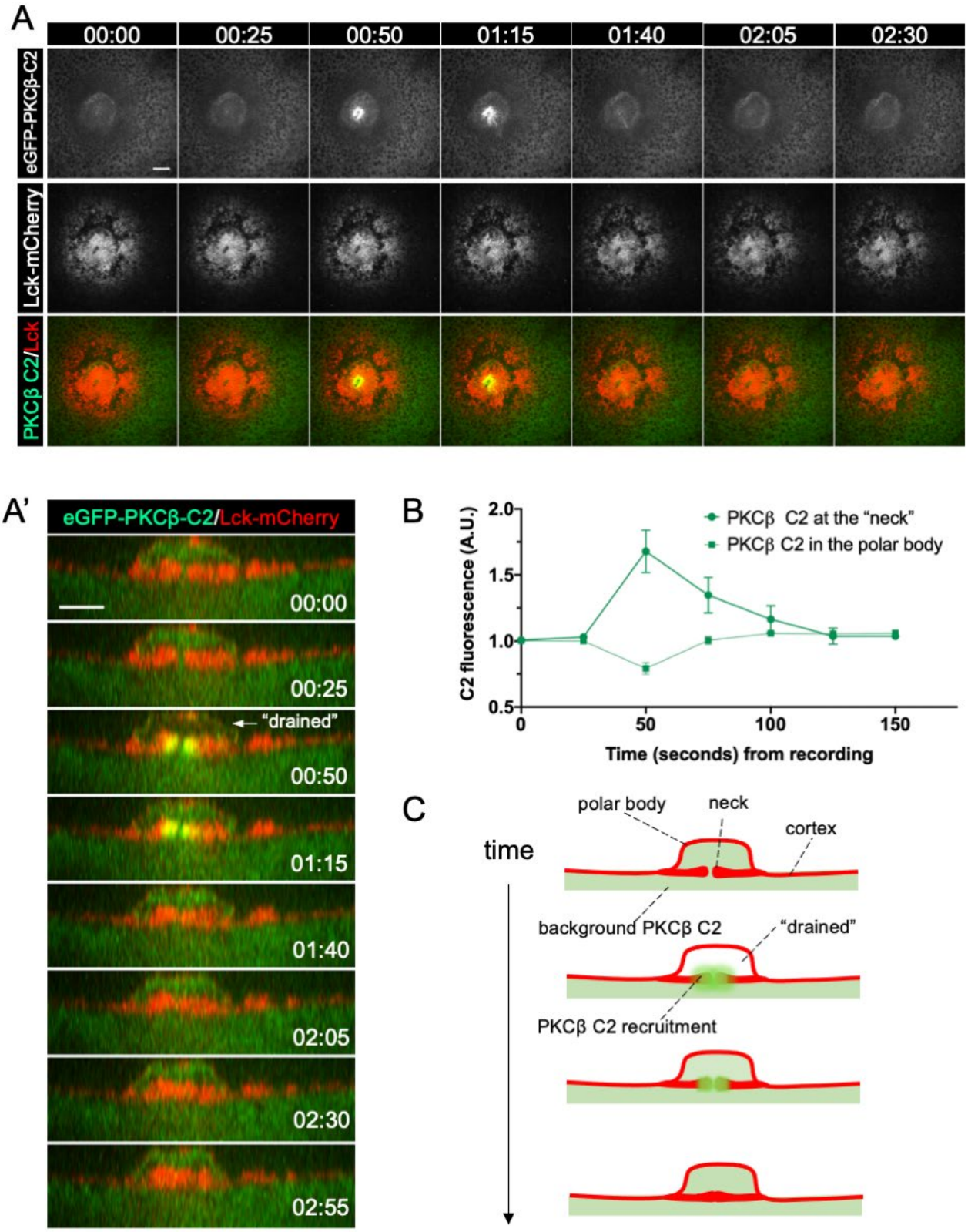

V.3 Discussion

V.3.1 Recap of the results

In this chapter, we constructed a ratiometric probe TC4 to detect Ca^{2+} signal during polar body emission of *Xenopus* oocyte (**V.2.1**). A transient $[Ca^{2+}]_i$ elevation was identified to be peaked ~13 minutes after anaphase initiation and lasted for about 2 minutes (**V.2.2**). The Ca^{2+} transient was preferentially active in the polar body, revealed by mobile dye OG-2 and OG-6f (**V.2.3**). Triggered by the $[Ca^{2+}]_i$ elevation, transient accumulation of PKCβ C2 domain was found at the intercellular bridge, suggesting PKCβ's role in regulating polar body abscission (**V.2.4**). Collectively, we identified a Ca^{2+} transient during polar body emission that was potentially involved in membrane dynamics.

V.3.2 A local Ca^{2+} transient is associated with polar body abscission

We propose that the detected Ca^{2+} transient was associated with polar body abscission for the following reasons: (1) The detected Ca^{2+} transient was temporally correlated to the completion of polar body emission. The timing and duration of Ca^{2+} transients detected by all Ca^{2+} probes (**Figure V.2–V.4**) were concurrent with the closure of the contractile ring (Zhang et al., 2008). (2) The detected transient was spatially correlated to the site where polar body abscission occurred. Images from TC4-expressing oocytes showed that $[Ca^{2+}]_i$ elevation was found at midbody (**Figure V.2A**, arrow), the cytokinesis signaling hub. In addition, the Ca^{2+}-sensitive PKCβ C2 domain transiently accumulated at the intercellular bridge, where the abscission site was located. (3) Ca^{2+} signaling is required for polar body abscission. A previous study has shown that injection of DB-BAPTA at the mid-anaphase (2–5 minutes after anaphase initiation) does not affect polar body extrusion or contractile ring constriction, but inhibits

polar body abscission (Leblanc, 2014). Altogether, these data suggest that a Ca^{2+} transient regulates polar body abscission, probably as a molecular trigger.

What can be the molecular target of the detected Ca^{2+} transient? The detailed molecular mechanism of polar body abscission remains unexplored (Maddox et al., 2012). Inspired by the recent studies of mitotic cytokinesis, the most promising candidate is Endosomal Sorting Complex Required for Transport (ESCRT) machinery, an evolutionary conserved membrane "scissor" that is universal in archaea and eukaryotes (Christ et al., 2017; Gatta and Carlton, 2019; McCullough et al., 2018). Previous reports have shown that at the end of cytokinesis, ESCRT-III, a distinct subtype of ESCRT, transiently forms helical filaments at the intercellular bridge and then constricts the membrane as the "final cut" (**Figure V.5C** & **D**) (Henne et al., 2013; Teis et al., 2008). In higher animal cells, local Ca^{2+} increase can activate Ca^{2+}-sensitive recruiters which in turn assemble ESCRT-III for membrane fusion and scission (Scheffer et al., 2014; Skowyra et al., 2018). Ca^{2+}-triggering PKCβ activity is possibly involved in the cytokinetic abscission since it is a crucial kinase responsible for many downstream reactions including local actin assembly and membrane fusion (Davenport et al., 2016; Yu and Bement, 2007). Despite their functional relevance, how PKCβ activity and the assembly of ESCRT machinery are related has not yet been explored. In the future, it will be interesting to investigate the connection between Ca^{2+} signaling and ESCRT-III activation during polar body emission.

Figure V.5 Schematic representation of polar body abscission (theory)
(A) Polar body emission in anaphase oocytes. **B**–**D** illustrate the possible mechanisms involved in polar body abscission, the last step of polar body emission.
(B) A cartoon illustrates a polar body being emitted where the geometry of plasma membranes and important cytokinetic machinery are shown. A layer of the vitelline membrane (a thick transparent membrane that consists mostly of protein fibers for supporting oocytes, also called *zona pellucida* in mammals) tightly coats the oocyte and the protruding polar body such that the plasma membrane (shown by phospholipid bilayers) at the oocyte-polar-body interface are closely contacted. A contractile ring constricts "the neck" (or intercellular bridge) and generates a force inducing local invagination of the oocyte cortex. The midbody is a transient structure that connects the oocyte and the polar body. It mostly consists of reorganized spindle microtubules and microtubule-associated proteins, serving as a signaling center for cytokinetic regulation.
(C) Shown is a possible outcome of polar body abscission supported by our data. ESCRT families, as the potential abscission effectors, form transient spiral filaments that coil around the conical part of plasma membranes induced by contractile ring constriction. The abscission effectors cut only one end of the intercellular bridge at the polar body's side, which is potentially caused by Ca^{2+} transients preferentially active in the polar body. After the asymmetrical abscission, the midbody remnant stays inside the oocyte and is attached to the cortex, functioning as a signaling structure that is important for metaphase II spindle assembly and embryogenesis.
(D) Shown is an *unlikely* outcome of polar body abscission: the abscission effectors are assembled at the two ends of the intercellular bridge and make symmetrical cuts. Thereafter, the midbody is deposed in the extracellular space (a common scheme in somatic cells).

Figure V.5 Schematic representation of polar body abscission (theory)

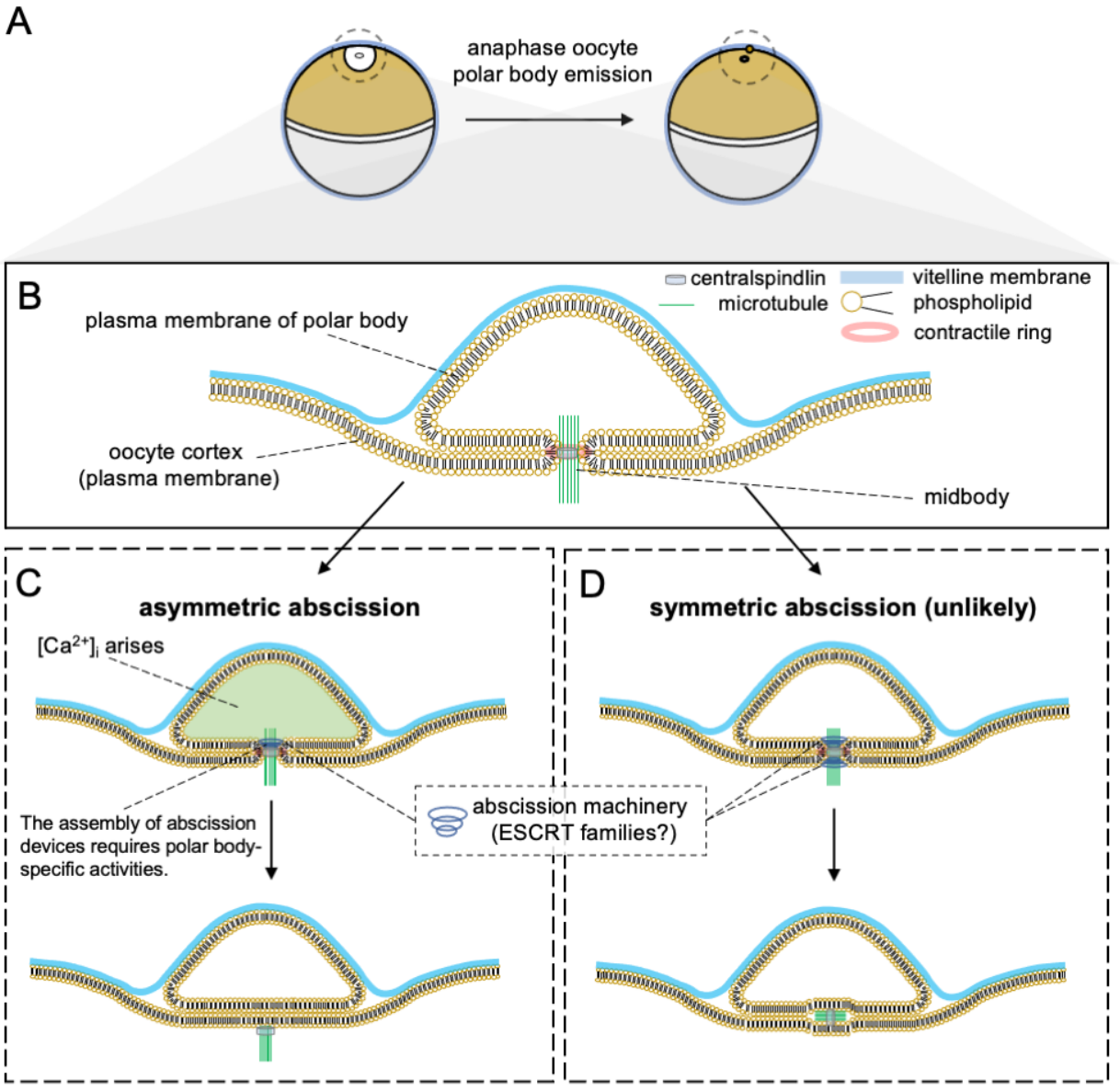

Our data also showed that the Ca^{2+} transient during polar body emission was preferentially active at the one side of the intercellular bridge (**Figure V.2–V.4**), suggesting the abscission only occurred in the polar body, a.k.a. asymmetric abscission. This asymmetric abscission likely leaves the midbody (so-called midbody remnant) in the oocyte (**Figure V.5C**). By contrast, during cytokinesis of most mitotic cells, the abscission is symmetric and the midbody is disposed of by both daughter cells (Dionne et al., 2015); this is an unlikely outcome of polar body abscission (**Figure V.5D**). Indeed, results from previous reports in *Xenopus* oocytes suggested that midbodies remain inside oocytes after polar body emission, consistent with the notion of asymmetric abscission (Ma et al., 2006; Zhang et al., 2008). Interestingly, a recent study showed that in ascidian oocytes, the midbody remnant from meiosis I directs the tethering of the metaphase II spindle and the location for second polar body emission (McDougall et al., 2019). Recent reports also suggest midbodies can persist in certain progenitor cells and function as membrane-bound signal organelles that manage cell polarity, stemness and proliferation (Peterman et al., 2019; Peterman and Prekeris, 2019). We therefore propose that asymmetric Ca^{2+} transients have an important role in maintaining the midbody that contributes to spindle function in meiosis II oocytes or dividing embryos. Future investigations will involve molecular mechanisms underlying asymmetric Ca^{2+} transients and the formation of midbody remnants.

V.3.3 Limitations

In the current study, the ratiometric probe TC4 was used as an unbiased Ca^{2+} indicator to identify the calcium transient during abscission. However, when compared to the original GCaMP3 (mobile Ca^{2+} reporter) or TC1 in **Chapter III**, the dynamic range of the GCaMP3 subunit was significantly compromised. The fluorescence elevation of GCaMPs following

Ca^{2+}-binding depends on the proper conformational change of Ca^{2+}-sensing and stabilizing units, *i.e.* circularizing the M13-CaM duo (see **I.3.3**). Therefore, any extra sequence that extends the M13 or CaM domain may introduce hindrance to the circularization. It is thus not surprising that TC1 (EMTB-GCAMP3) was about half the brightness of its red-shifted equivalent RGECO (**III.2.2**, **Figure III.2A'**), and TC1's derivative TC4 (mCherry-EMTB-GCaMP3) showed a further decline: It takes more than 4-fold UV-responsive Ca^{2+} release (from caged IP_3) for TC4 to reach a similar signal response as TC1 (*e.g.* compare **Figure V.1B** with **Figure III.6B**, 2 seconds vs. 500 milliseconds of UV exposure to reach ~3 to 4-fold fluorescence increase; it is estimated that uncaged IP_3 is linearly correlated with UV-exposure time.) (Callamaras and Parker, 1998). The compromised reporting sensitivity and dynamic range may restrict the application of TC4 to detect a wider range of Ca^{2+} events. Preliminary imaging experiments suggested that TC4 failed to detect the prominent spindle pole Ca^{2+} signal in metaphase oocytes (*e.g.* **Figure V.2A**). Further experiments are required to investigate this discrepancy.

Another concern is that the condition for polar body abscission is still not fully understood. According to the abscission assessment by dextran dye (**Figure I.3B**), 73% of the oocytes completed the abscission within 60 minutes following anaphase initiation (Leblanc, 2014). Similarly, the endpoint of imaging individual oocytes was set to ~20–30 minutes after anaphase initiation and the calcium transient was detected in ~60% percent of the oocytes (27/45; OG-2, OG-6f and TC4 were counted). The relatively low detection rates of abscission and Ca^{2+} transients might be explained by the compromised extracellular environment (all oocytes underwent *in vitro* maturation).

Chapter VI Conclusions and outlook

VI.1 Key discoveries

In this project, we aimed to dissect Ca^{2+} signals and potential Ca^{2+} nanodomains associated with spindle assembly. In **Chapter III**, we describe the work in generating a novel Ca^{2+} probe dubbed TC1 by tethering a microtubule-binding domain to a Ca^{2+} biosensor GCaMP3. By using this probe, a pole-specific $[Ca^{2+}]_i$ elevation was identified at spindles in various systems including intact *Xenopus* oocytes, STLC-incubated oocytes, cell extracts and HeLa cells. In **Chapter IV**, we investigated the function and molecular components of calcium nanodomains at spindles in *Xenopus* oocyte-based systems. BAPTA/EGTA tests showed that calcium nanodomains were important for the assembly of extract spindles and monoastral spindles and bipolar spindles in intact oocytes. ER and IP_3Rs, as the Ca^{2+} store and channels, were found to be in tight contact with spindles and concentrated at the poles. Taken together, we propose that the accumulation of ER and IP_3Rs caused the pole-specific $[Ca^{2+}]_i$ elevation. This pole-specific $[Ca^{2+}]_i$ elevation reflects the overall distribution of calcium nanodomains rather than individual transients. In other words, the detected Ca^{2+} signals reflect a balance between Ca^{2+} releasing through IP_3Rs into the spindle region and its subsequent buffering, diffusion, removal by ER pumps; their underpinning, nanodomain Ca^{2+} signaling, plays an important role in spindle regulation. We propose that the spindle-associated TC1 signal is the long searched local Ca^{2+} signal that accounts for spindle assembly and maintenance during *Xenopus* oocyte maturation (Li et al., 2016; Sun et al., 2008; Sun and Machaca, 2004).

In **Chapter V**, we identified a local Ca^{2+} transient during polar body emission by several Ca^{2+} reporters including a novel ratiometric probe TC4 and mobile probes OG-2, OG-6f and Ca^{2+}-sensitive eGFP-PKCβ-C2. The spatiotemporal pattern of the Ca^{2+} transient revealed by these dyes suggests that the elevation of $[Ca^{2+}]$ is primarily inside the polar body and triggers the abscission of the polar body.

Overall, the detection of spindle- and cytokinesis-associated Ca^{2+} signals expand our knowledge of Ca^{2+} signaling during oocyte maturation. Our findings are consistent with the previous assumption that multiple steps of localized Ca^{2+} signaling lead to successful polar body emission (Liu, 2012). The $[Ca^{2+}]_i$ elevation preferentially at the polar body is likely the previously speculative but uncharacterized activities that account for polar body abscission and midbody retention in oocytes (Maddox et al., 2012).

More generally, our results in HeLa cells and cell extracts suggest that spindle-associated Ca^{2+} signaling is a common mechanism in both mitosis and meiosis. Identifying the downstream target molecules and signaling cascade remains to be our future goal. Besides, how this localized Ca^{2+} signaling interacts with upstream cell cycle drivers is also an interesting research subject. Research on spindle-associated ER-IP_3R may open a new avenue for understanding the spatiotemporal signal transduction in cell division.

In addition, our novel constructs of TC families contribute to the toolkit for investigating Ca^{2+} signaling in microtubule physiology. Apart from regulation of spindle apparatus, TC families can also be applied to research of subcellular cargo transporting (Franker and Hoogenraad, 2013), wound healing (Nakamura et al., 2018), cytokinetic microtubule

reorganization (Eno et al., 2018), ER-microtubule communication (Grigoriev et al., 2008) and any other cellular process involving microtubules and local Ca^{2+} regulation.

VI.2 Implications in disease pathology and translational medicine

Aside from basic research, our data also provide new angles to tackle existing medical challenges.

Because Ca^{2+} signaling is involved in multi-steps of reproductive cell development, it has long been recognized as a crucial regulator of fertilization and embryo development (Whitaker, 2006a). Infertility and birth defects are common reproductive problems for human. It is estimated 15% of couples experience some kind of infertility (Thoma et al., 2013) and 6% of newborn babies have birth defects worldwide (Christianson et al., 2006). The poor quality of oocytes or spermatozoa is one of the major causes of these issues (Hoshino, 2018; Kovac et al., 2013; Liu, 2016). Ca^{2+} deficiency can be detrimental to these reproductive cells; understanding how the dysregulation of Ca^{2+} signaling affects infertility and birth defects, either in humans or animals, has received increasing recognition (Beigi Harchegani et al., 2019; Haverfield et al., 2016). Our study of calcium nanodomains at *Xenopus* oocyte spindles provides fresh insights into how calcium signaling affects spindle fitness in oocytes. Oocyte aneuploidy (*i.e.* incorrect chromosome number) is the direct clinical consequence of spindle dysfunction, which is prevalent in reproductively aged women (age > 35 years). Studies showed old mice (age > 1year) have reduced Ca^{2+} replenishing ability (Haverfield et al., 2016), thus it is attempting to suggest there exists similar, if not more serious, conditions in aged human oocytes. The results and the non-invasive tools achieved in our study can help to

investigate the pathology of infertility that is caused by impaired calcium homeostasis in aging oocytes.

The study of calcium nanodomains in dividing cells may also inspire novel cancer therapies. Growing reports show that cancer cells exhibit abnormal Ca^{2+} homeostasis that is adaptive for carcinogenesis, tumor progression and metastasis. Through mutation, cancer cells alter their Ca^{2+} signaling network to raise division rate and mobility while escaping from immune supervision and apoptosis (Kondratskyi et al., 2013). Targeting Ca^{2+} signaling has become an emerging research topic for cancer therapies. In fact, many Ca^{2+} channel inhibitors have been in the process of cancer drug R&D (Cui et al., 2017). In our study, we showed a pole-specific Ca^{2+} signal during mitosis of HeLa cells, the cell line derived from cervical tumors. In addition, using *Xenopus* oocyte as a model of asymmetric cell division — a feature of cancer stem cell theory (Shahriyari and Komarova, 2013), we also showed IP_3Rs were associated to spindle function and the corresponding inhibitors were able to interrupt the normal cell cycle progression. Noticeably in previous studies, several IP_3R blockers, such as Xestospongin, 2-APB and heparin, have shown the capacity to suppress cell proliferation of various cancer types (Cardenas et al., 2016; Ponert et al., 2018; Qu et al., 2018). It will be interesting to see whether the interference of spindle calcium nanodomain contributes to the anti-cancer pharmacology of these chemicals.

And last, we'd like to discuss the medical opportunities that the research of Ca^{2+} in cytokinetic abscission may provide. Viruses exploit the environment of host cells to live and replicate. Enveloped viruses, such as Ebolavirus (EBOV) and HIV-1 (Human Immunodeficiency Virus-1), release their progenies from host cell via budding, a process hijacking the cellular machinery that accounts for cytokinetic abscission. Remarkably, viral

budding shares many common mechanisms with asymmetric cytokinesis of daughter cells (McDonald and Martin-Serrano, 2009; Votteler and Sundquist, 2013). Research works showed that the host Ca^{2+} signal mediated by store-operated calcium channels (STIM1/ORAI1) is essential for the final step of virus releasing like EBOV; accordingly, pharmacological interventions of the channel signaling can inhibit the infection (Han et al., 2015). Therefore, Ca^{2+} channel inhibitors are proposed to be broad-spectrum antiviral candidates for enveloped viruses (Chen et al., 2019). In January 2020, World Health Organization (WHO) declared that the outbreak constitutes a Public Health Emergency of International Concern (PHEIC) for COVID-19 (Coronavirus Disease-2019), a disease caused by an enveloped RNA virus SARS-CoV-2 (Severe Acute Respiratory Syndrome-related CoronaVirus-2). Since then, COVID-19 has become a significant health and economic concern for most human beings in the world. A recent study suggested that SARS-CoV-2 has a unique PPxY Late (L) domain motif that can recruit and regulate abscission machinery to enhance virus budding and spreading, which may explain why it's more contagious than SARS-CoV-1 (Maaroufi, 2020). This offers a potential target for therapeutic intervention by Ca^{2+} channel inhibitors through blocking budding and spreading. Interestingly, *Xenopus* oocytes have been used to study virus activation and replication, such as HIV-1 and Poliovirus, and possible intervention (Braddock et al., 1994; Gamarnik and Andino, 1996). Inspired by current work on Ca^{2+}'s role in cytokinetic abscission, it will be appealing to exploit the *Xenopus*-oocyte system further for the research of virus-budding mechanisms and possible drug interventions.

Bibliography

Adams, S.R., Kao, J., and Tsien, R.Y. (1989). Biologically Useful Chelators That Take Up Ca2+ Upon Illumination. J Am Chem Soc *111*, 1.

Adler, E.M., Augustine, G.J., Duffy, S.N., and Charlton, M.P. (1991). Alien intracellular calcium chelators attenuate neurotransmitter release at the squid giant synapse. J Neurosci *11*, 1496-1507.

Akerboom, J., Chen, T.W., Wardill, T.J., Tian, L., Marvin, J.S., Mutlu, S., Calderon, N.C., Esposti, F., Borghuis, B.G., Sun, X.R.*, et al.* (2012). Optimization of a GCaMP calcium indicator for neural activity imaging. J Neurosci *32*, 13819-13840.

Akerboom, J., Rivera, J.D., Guilbe, M.M., Malave, E.C., Hernandez, H.H., Tian, L., Hires, S.A., Marvin, J.S., Looger, L.L., and Schreiter, E.R. (2009). Crystal structures of the GCaMP calcium sensor reveal the mechanism of fluorescence signal change and aid rational design. The Journal of biological chemistry *284*, 6455-6464.

Alfaro-Aco, R., Thawani, A., and Petry, S. (2017). Structural analysis of the role of TPX2 in branching microtubule nucleation. The Journal of cell biology *216*, 983-997.

Alfieri, C., Chang, L., Zhang, Z., Yang, J., Maslen, S., Skehel, M., and Barford, D. (2016). Molecular basis of APC/C regulation by the spindle assembly checkpoint. Nature *536*, 431-436.

Altafaj, X., Joux, N., Ronjat, M., and De Waard, M. (2006). Oocyte expression with injection of purified T7 RNA polymerase. Methods in molecular biology *322*, 55-67.

Asp, L., Kartberg, F., Fernandez-Rodriguez, J., Smedh, M., Elsner, M., Laporte, F., Barcena, M., Jansen, K.A., Valentijn, J.A., Koster, A.J.*, et al.* (2009). Early stages of Golgi vesicle and tubule formation require diacylglycerol. Mol Biol Cell *20*, 780-790.

Atilla-Gokcumen, G.E., Castoreno, A.B., Sasse, S., and Eggert, U.S. (2010). Making the cut: the chemical biology of cytokinesis. ACS Chem Biol *5*, 79-90.

Augustine, G.J., Charlton, M.P., and Smith, S.J. (1985). Calcium entry and transmitter release at voltage-clamped nerve terminals of squid. J Physiol *367*, 163-181.

Augustine, G.J., Santamaria, F., and Tanaka, K. (2003). Local Calcium Signaling in Neurons. Neuron *40*, 331-346.

Badura, A., Sun, X.R., Giovannucci, A., Lynch, L.A., and Wang, S.S. (2014). Fast calcium sensor proteins for monitoring neural activity. Neurophotonics *1*, 025008.

Banerjee, A.C., and Bhattacharyya, B. (1979). Colcemid and colchicine binding to tubulin. Similarity and dissimilarity. FEBS Lett *99*, 333-336.

Bayaa, M., Booth, R.A., Sheng, Y., and Liu, X.J. (2000). The classical progesterone receptor mediates Xenopus oocyte maturation through a nongenomic mechanism. Proc Natl Acad Sci U S A *97*, 12607-12612.

Becker, B.E., and Gard, D.L. (2006). Visualization of the cytoskeleton in Xenopus oocytes and eggs by confocal immunofluorescence microscopy. Methods in molecular biology *322*, 69-86.

Becker, B.E., Romney, S.J., and Gard, D.L. (2003). XMAP215, XKCM1, NuMA, and cytoplasmic dynein are required for the assembly and organization of the transient microtubule array during the maturation of Xenopus oocytes. Dev Biol *261*, 488-505.

Behera, S., Krebs, M., Loro, G., Schumacher, K., Costa, A., and Kudla, J. (2013). Ca2+ imaging in plants using genetically encoded Yellow Cameleon Ca2+ indicators. Cold Spring Harb Protoc *2013*, 700-703.

Beigi Harchegani, A., Irandoost, A., Mirnamniha, M., Rahmani, H., Tahmasbpour, E., and Shahriary, A. (2019). Possible Mechanisms for The Effects of Calcium Deficiency on Male Infertility. Int J Fertil Steril *12*, 267-272.

Benink, H.A., and Bement, W.M. (2005). Concentric zones of active RhoA and Cdc42 around single cell wounds. The Journal of cell biology *168*, 429-439.

Bennabi, I., Terret, M.E., and Verlhac, M.H. (2016). Meiotic spindle assembly and chromosome segregation in oocytes. The Journal of cell biology *215*, 611-619.

Bergman, Z.J., McLaurin, J.D., Eritano, A.S., Johnson, B.M., Sims, A.Q., and Riggs, B. (2015). Spatial reorganization of the endoplasmic reticulum during mitosis relies on mitotic kinase cyclin A in the early Drosophila embryo. PLoS One *10*, e0117859.

Bernasconi, C.F. (1976). Chapter 1 - Basic Principles. In Relaxation Kinetics, C.F. Bernasconi, ed. (Academic Press), pp. 3-10.

Bernhardt, M.L., Kim, A.M., O'Halloran, T.V., and Woodruff, T.K. (2011). Zinc requirement during meiosis I-meiosis II transition in mouse oocytes is independent of the MOS-MAPK pathway. Biology of reproduction *84*, 526-536.

Berridge, M.J., Lipp, P., and Bootman, M.D. (2000). The versatility and universality of calcium signalling. Nat Rev Mol Cell Biol *1*, 11-21.

Bers, D.M., Patton, C.W., and Nuccitelli, R. (2010). A practical guide to the preparation of Ca(2+) buffers. Methods Cell Biol *99*, 1-26.

Bertagnolo, V., Benedusi, M., Brugnoli, F., Lanuti, P., Marchisio, M., Querzoli, P., and Capitani, S. (2007). Phospholipase C-beta 2 promotes mitosis and migration of human breast cancer-derived cells. Carcinogenesis *28*, 1638-1645.

Bonora, M., Giorgi, C., Bononi, A., Marchi, S., Patergnani, S., Rimessi, A., Rizzuto, R., and Pinton, P. (2013). Subcellular calcium measurements in mammalian cells using jellyfish photoprotein aequorin-based probes. Nat Protoc *8*, 2105-2118.

Braddock, M., Cannon, P., Muckenthaler, M., Kingsman, A.J., and Kingsman, S.M. (1994). Inhibition of human immunodeficiency virus type 1 Tat-dependent activation of translation in Xenopus oocytes by the benzodiazepine Ro24-7429 requires trans-activation response element loop sequences. J Virol *68*, 25-33.

Brar, G.A., Kiburz, B.M., Zhang, Y., Kim, J.E., White, F., and Amon, A. (2006). Rec8 phosphorylation and recombination promote the step-wise loss of cohesins in meiosis. Nature *441*, 532-536.

Brouhard, G.J., and Rice, L.M. (2018). Microtubule dynamics: an interplay of biochemistry and mechanics. Nat Rev Mol Cell Biol *19*, 451-463.

Browne, C.L., Creton, R., Karplus, E., Mohler, P.J., Palazzo, R.E., and Miller, A.L. (1996). Analysis of the calcium transient at NEB during the first cell cycle in dividing sea urchin eggs. Biol Bull *191*, 5-16.

Brugues, J., Nuzzo, V., Mazur, E., and Needleman, D.J. (2012). Nucleation and transport organize microtubules in metaphase spindles. Cell *149*, 554-564.

Bucurenciu, I., Kulik, A., Schwaller, B., Frotscher, M., and Jonas, P. (2008). Nanodomain Coupling between Ca2+ Channels and Ca2+ Sensors Promotes Fast and Efficient Transmitter Release at a Cortical GABAergic Synapse. Neuron *57*, 536-545.

Bugrim, A., Fontanilla, R., Eutenier, B.B., Keizer, J., and Nuccitelli, R. (2003). Sperm initiate a Ca2+ wave in frog eggs that is more similar to Ca2+ waves initiated by IP3 than by Ca2+. Biophysical journal *84*, 1580-1590.

Bulinski, J.C., Odde, D.J., Howell, B.J., Salmon, T.D., and Waterman-Storer, C.M. (2001). Rapid dynamics of the microtubule binding of ensconsin in vivo. Journal of cell science *114*, 3885-3897.

Busa, W.B., and Nuccitelli, R. (1985). An elevated free cytosolic Ca2+ wave follows fertilization in eggs of the frog, Xenopus laevis. The Journal of cell biology *100*, 1325-1329.

Callamaras, N., and Parker, I. (1998). Caged inositol 1,4,5-trisphosphate for studying release of Ca2+ from intracellular stores. In Methods in Enzymology (Academic Press), pp. 380-403.

Carazo-Salas, R.E., Guarguaglini, G., Gruss, O.J., Segref, A., Karsenti, E., and Mattaj, I.W. (1999). Generation of GTP-bound Ran by RCC1 is required for chromatin-induced mitotic spindle formation. Nature *400*, 178-181.

Cardenas, C., Muller, M., McNeal, A., Lovy, A., Jana, F., Bustos, G., Urra, F., Smith, N., Molgo, J., Diehl, J.A.*, et al.* (2016). Selective Vulnerability of Cancer Cells by Inhibition of Ca(2+) Transfer from Endoplasmic Reticulum to Mitochondria. Cell Rep *15*, 219-220.

Carlton, J.G., Jones, H., and Eggert, U.S. (2020). Membrane and organelle dynamics during cell division. Nat Rev Mol Cell Biol *21*, 151-166.

Challa, K., Fajish, V.G., Shinohara, M., Klein, F., Gasser, S.M., and Shinohara, A. (2019). Meiosis-specific prophase-like pathway controls cleavage-independent release of cohesin by Wapl phosphorylation. PLoS Genet *15*, e1007851.

Chang, D.C., and Meng, C. (1995). A localized elevation of cytosolic free calcium is associated with cytokinesis in the zebrafish embryo. The Journal of cell biology *131*, 1539-1545.

Chang, D.C., Xu, N., and Luo, K.Q. (2003). Degradation of cyclin B is required for the onset of anaphase in Mammalian cells. The Journal of biological chemistry *278*, 37865-37873.

Chang, L., Zhang, Z., Yang, J., McLaughlin, S.H., and Barford, D. (2015). Atomic structure of the APC/C and its mechanism of protein ubiquitination. Nature *522*, 450-454.

Chen, T.W., Wardill, T.J., Sun, Y., Pulver, S.R., Renninger, S.L., Baohan, A., Schreiter, E.R., Kerr, R.A., Orger, M.B., Jayaraman, V.*, et al.* (2013). Ultrasensitive fluorescent proteins for imaging neuronal activity. Nature *499*, 295-300.

Chen, X., Cao, R., and Zhong, W. (2019). Host Calcium Channels and Pumps in Viral Infections. Cells *9*.

Chenevert, J., Roca, M., Besnardeau, L., Ruggiero, A., Nabi, D., McDougall, A., Copley, R.R., Christians, E., and Castagnetti, S. (2020). The Spindle Assembly Checkpoint Functions during Early Development in Non-Chordate Embryos. Cells *9*.

Christ, L., Raiborg, C., Wenzel, E.M., Campsteijn, C., and Stenmark, H. (2017). Cellular Functions and Molecular Mechanisms of the ESCRT Membrane-Scission Machinery. Trends Biochem Sci *42*, 42-56.

Christianson, A., Howson, C.P., and Modell, B. (2006). Global report on birth defects. March of Dimes, 10.

Ciapa, B., Pesando, D., Wilding, M., and Whitaker, M. (1994). Cell-cycle calcium transients driven by cyclic changes in inositol trisphosphate levels. Nature *368*, 875-878.

Cicirelli, M.F., Robinson, K.R., and Smith, L.D. (1983). Internal pH of Xenopus oocytes: a study of the mechanism and role of pH changes during meiotic maturation. Dev Biol *100*, 133-146.

Clapham, D.E. (2007). Calcium signaling. Cell *131*, 1047-1058.

Clift, D., McEwan, W.A., Labzin, L.I., Konieczny, V., Mogessie, B., James, L.C., and Schuh, M. (2017). A Method for the Acute and Rapid Degradation of Endogenous Proteins. Cell *171*, 1692-1706 e1618.

Clift, D., and Schuh, M. (2015). A three-step MTOC fragmentation mechanism facilitates bipolar spindle assembly in mouse oocytes. Nat Commun *6*, 7217.

Clift, D., So, C., McEwan, W.A., James, L.C., and Schuh, M. (2018). Acute and rapid degradation of endogenous proteins by Trim-Away. Nat Protoc *13*, 2149-2175.

Cork, R.J., Cicirelli, M.F., and Robinson, K.R. (1987). A rise in cytosolic calcium is not necessary for maturation of Xenopus laevis oocytes. Dev Biol *121*, 41-47.

Courtois, A., Schuh, M., Ellenberg, J., and Hiiragi, T. (2012). The transition from meiotic to mitotic spindle assembly is gradual during early mammalian development. The Journal of cell biology *198*, 357-370.

Cromey, D.W. (2010). Avoiding twisted pixels: ethical guidelines for the appropriate use and manipulation of scientific digital images. Sci Eng Ethics *16*, 639-667.

Cui, C., Merritt, R., Fu, L., and Pan, Z. (2017). Targeting calcium signaling in cancer therapy. Acta Pharm Sin B *7*, 3-17.

Dargan, S.L., and Parker, I. (2003). Buffer kinetics shape the spatiotemporal patterns of IP3-evoked Ca2+ signals. J Physiol *553*, 775-788.

Dargan, S.L., Schwaller, B., and Parker, I. (2004). Spatiotemporal patterning of IP3-mediated Ca2+ signals in Xenopus oocytes by Ca2+-binding proteins. J Physiol *556*, 447-461.

Davenport, N.R., Sonnemann, K.J., Eliceiri, K.W., and Bement, W.M. (2016). Membrane dynamics during cellular wound repair. Mol Biol Cell *27*, 2272-2285.

de Moor, C.H., and Richter, J.D. (1999). Cytoplasmic polyadenylation elements mediate masking and unmasking of cyclin B1 mRNA. EMBO J *18*, 2294-2303.

Demuro, A., and Parker, I. (2006). Imaging single-channel calcium microdomains. Cell Calcium *40*, 413-422.

Demuro, A., and Parker, I. (2015). Picomolar sensitivity to inositol trisphosphate in Xenopus oocytes. Cell Calcium *58*, 511-517.

Deng, J., Lang, S., Wylie, C., and Hammes, S.R. (2008). The Xenopus laevis isoform of G protein-coupled receptor 3 (GPR3) is a constitutively active cell surface receptor that participates in maintaining meiotic arrest in X. laevis oocytes. Molecular endocrinology *22*, 1853-1865.

Desai, A., and Mitchison, T.J. (1997). Microtubule polymerization dynamics. Annu Rev Cell Dev Biol *13*, 83-117.

Despa, S., Shui, B., Bossuyt, J., Lang, D., Kotlikoff, M.I., and Bers, D.M. (2014). Junctional cleft [Ca(2)(+)]i measurements using novel cleft-targeted Ca(2)(+) sensors. Circ Res *115*, 339-347.

Dickinson, G.D., Ellefsen, K.L., Dawson, S.P., Pearson, J.E., and Parker, I. (2016). Hindered cytoplasmic diffusion of inositol trisphosphate restricts its cellular range of action. Sci Signal *9*, ra108.

DiGregorio, D.A., Peskoff, A., and Vergara, J.L. (1999). Measurement of Action Potential-Induced Presynaptic Calcium Domains at a Cultured Neuromuscular Junction. The Journal of Neuroscience *19*, 7846.

Dionne, L.K., Wang, X.J., and Prekeris, R. (2015). Midbody: from cellular junk to regulator of cell polarity and cell fate. Curr Opin Cell Biol *35*, 51-58.

Dodson, C.A., and Bayliss, R. (2012). Activation of Aurora-A kinase by protein partner binding and phosphorylation are independent and synergistic. The Journal of biological chemistry *287*, 1150-1157.

Duncan, F.E., Que, E.L., Zhang, N., Feinberg, E.C., O'Halloran, T.V., and Woodruff, T.K. (2016). The zinc spark is an inorganic signature of human egg activation. Sci Rep *6*, 24737.

Dupre, A., Buffin, E., Roustan, C., Nairn, A.C., Jessus, C., and Haccard, O. (2013). The phosphorylation of ARPP19 by Greatwall renders the auto-amplification of MPF independently of PKA in Xenopus oocytes. Journal of cell science *126*, 3916-3926.

Eckerdt, F., Eyers, P.A., Lewellyn, A.L., Prigent, C., and Maller, J.L. (2008). Spindle pole regulation by a discrete Eg5-interacting domain in TPX2. Current biology : CB *18*, 519-525.

Eggermann, E., Bucurenciu, I., Goswami, S.P., and Jonas, P. (2011). Nanodomain coupling between Ca^{2+} channels and sensors of exocytosis at fast mammalian synapses. Nature reviews Neuroscience *13*, 7-21.

Eisen, A., and Reynolds, G.T. (1985). Source and sinks for the calcium released during fertilization of single sea urchin eggs. The Journal of cell biology *100*, 1522-1527.

El-Jouni, W., Haun, S., and Machaca, K. (2008). Internalization of plasma membrane Ca2+-ATPase during Xenopus oocyte maturation. Dev Biol *324*, 99-107.

El-Jouni, W., Jang, B., Haun, S., and Machaca, K. (2005). Calcium signaling differentiation during Xenopus oocyte maturation. Dev Biol *288*, 514-525.

Ellis-Davies, G.C. (2007). Caged compounds: photorelease technology for control of cellular chemistry and physiology. Nat Methods *4*, 619-628.

Eyers, P.A., Erikson, E., Chen, L.G., and Maller, J.L. (2003). A novel mechanism for activation of the protein kinase Aurora A. Current biology : CB *13*, 691-697.

Faas, G.C., Raghavachari, S., Lisman, J.E., and Mody, I. (2011). Calmodulin as a direct detector of Ca2+ signals. Nat Neurosci *14*, 301-304.

Farina, F., Gaillard, J., Guerin, C., Coute, Y., Sillibourne, J., Blanchoin, L., and Thery, M. (2016). The centrosome is an actin-organizing centre. Nat Cell Biol *18*, 65-75.

Ferrell, J.E., Jr. (1999). Xenopus oocyte maturation: new lessons from a good egg. Bioessays *21*, 833-842.

Ferrell, J.E., Jr., and Machleder, E.M. (1998). The biochemical basis of an all-or-none cell fate switch in Xenopus oocytes. Science *280*, 895-898.

Field, C.M., Pelletier, J.F., and Mitchison, T.J. (2017). Xenopus extract approaches to studying microtubule organization and signaling in cytokinesis. Methods Cell Biol *137*, 395-435.

FitzHarris, G. (2012). Anaphase B precedes anaphase A in the mouse egg. Current biology : CB *22*, 437-444.

FitzHarris, G., Larman, M., Richards, C., and Carroll, J. (2005). An increase in [Ca2+]i is sufficient but not necessary for driving mitosis in early mouse embryos. Journal of cell science *118*, 4563-4575.

FitzHarris, G., Marangos, P., and Carroll, J. (2007). Changes in endoplasmic reticulum structure during mouse oocyte maturation are controlled by the cytoskeleton and cytoplasmic dynein. Dev Biol *305*, 133-144.

Fontanilla, R.A., and Nuccitelli, R. (1998). Characterization of the sperm-induced calcium wave in Xenopus eggs using confocal microscopy. Biophysical journal *75*, 2079-2087.

Fuller, B.G. (2010). Self-organization of intracellular gradients during mitosis. Cell Div *5*, 5.

Furuta, A., Tanaka, M., Omata, W., Nagasawa, M., Kojima, I., and Shibata, H. (2009). Microtubule disruption with BAPTA and dimethyl BAPTA by a calcium chelation-independent mechanism in 3T3-L1 adipocytes. Endocrine journal *56*, 235-243.

Gache, V., Waridel, P., Winter, C., Juhem, A., Schroeder, M., Shevchenko, A., and Popov, A.V. (2010). Xenopus meiotic microtubule-associated interactome. PLoS One *5*, e9248.

Galletta, B.J., Guillen, R.X., Fagerstrom, C.J., Brownlee, C.W., Lerit, D.A., Megraw, T.L., Rogers, G.C., and Rusan, N.M. (2014). Drosophila pericentrin requires interaction with calmodulin for its function at centrosomes and neuronal basal bodies but not at sperm basal bodies. Mol Biol Cell *25*, 2682-2694.

Gamarnik, A.V., and Andino, R. (1996). Replication of poliovirus in Xenopus oocytes requires two human factors. EMBO J *15*, 5988-5998.

Gard, D.L. (1992). Microtubule organization during maturation of Xenopus oocytes: assembly and rotation of the meiotic spindles. Dev Biol *151*, 516-530.

Gard, D.L., Cha, B.J., and Roeder, A.D. (1995). F-actin is required for spindle anchoring and rotation in Xenopus oocytes: a re-examination of the effects of cytochalasin B on oocyte maturation. Zygote *3*, 17-26.

Gardner, M.K., Zanic, M., Gell, C., Bormuth, V., and Howard, J. (2011). Depolymerizing kinesins Kip3 and MCAK shape cellular microtubule architecture by differential control of catastrophe. Cell *147*, 1092-1103.

Gatta, A.T., and Carlton, J.G. (2019). The ESCRT-machinery: closing holes and expanding roles. Curr Opin Cell Biol *59*, 121-132.

Gehmlich, K., Haren, L., and Merdes, A. (2004). Cyclin B degradation leads to NuMA release from dynein/dynactin and from spindle poles. EMBO Rep *5*, 97-103.

Gerhold, A.R., Poupart, V., Labbe, J.C., and Maddox, P.S. (2018). Spindle assembly checkpoint strength is linked to cell fate in the Caenorhabditis elegans embryo. Mol Biol Cell *29*, 1435-1448.

Geyer, M., Huang, F., Sun, Y., Vogel, S.M., Malik, A.B., Taylor, C.W., and Komarova, Y.A. (2015). Microtubule-Associated Protein EB3 Regulates IP3 Receptor Clustering and Ca(2+) Signaling in Endothelial Cells. Cell Rep *12*, 79-89.

Good, M.C., and Heald, R. (2018). Preparation of Cellular Extracts from Xenopus Eggs and Embryos. Cold Spring Harb Protoc *2018*.

Gorbsky, G.J. (2015). The spindle checkpoint and chromosome segregation in meiosis. FEBS J *282*, 2471-2487.

Grandin, N., and Charbonneau, M. (1991). Intracellular free calcium oscillates during cell division of Xenopus embryos. The Journal of cell biology *112*, 711-718.

Green, M.R., and Sambrook, J. (2019). Agarose Gel Electrophoresis. Cold Spring Harb Protoc *2019*.

Greenwald, E.C., Mehta, S., and Zhang, J. (2018). Genetically Encoded Fluorescent Biosensors Illuminate the Spatiotemporal Regulation of Signaling Networks. Chem Rev *118*, 11707-11794.

Groen, A.C., Coughlin, M., and Mitchison, T.J. (2011). Microtubule assembly in meiotic extract requires glycogen. Mol Biol Cell *22*, 3139-3151.

Groigno, L., and Whitaker, M. (1998). An anaphase calcium signal controls chromosome disjunction in early sea urchin embryos. Cell *92*, 193-204.

Guizzunti, G., and Seemann, J. (2016). Mitotic Golgi disassembly is required for bipolar spindle formation and mitotic progression. Proc Natl Acad Sci U S A *113*, E6590-E6599.

Gupta, K.K., Li, C., Duan, A., Alberico, E.O., Kim, O.V., Alber, M.S., and Goodson, H.V. (2013). Mechanism for the catastrophe-promoting activity of the microtubule destabilizer Op18/stathmin. Proc Natl Acad Sci U S A *110*, 20449-20454.

Haccard, O., and Jessus, C. (2006). Redundant pathways for Cdc2 activation in Xenopus oocyte: either cyclin B or Mos synthesis. EMBO Rep *7*, 321-325.

Halpin, D., Kalab, P., Wang, J., Weis, K., and Heald, R. (2011). Mitotic spindle assembly around RCC1-coated beads in Xenopus egg extracts. PLoS Biol *9*, e1001225.

Han, Z., Madara, J.J., Herbert, A., Prugar, L.I., Ruthel, G., Lu, J., Liu, Y., Liu, W., Liu, X., Wrobel, J.E*., et al.* (2015). Calcium Regulation of Hemorrhagic Fever Virus Budding: Mechanistic Implications for Host-Oriented Therapeutic Intervention. PLoS Pathog *11*, e1005220.

Hannak, E., and Heald, R. (2006). Investigating mitotic spindle assembly and function in vitro using Xenopus laevis egg extracts. Nat Protoc *1*, 2305-2314.

Hansen, D.V., Tung, J.J., and Jackson, P.K. (2006). CaMKII and polo-like kinase 1 sequentially phosphorylate the cytostatic factor Emi2/XErp1 to trigger its destruction and meiotic exit. Proc Natl Acad Sci U S A *103*, 608-613.

Haverfield, J., Nakagawa, S., Love, D., Tsichlaki, E., Nomikos, M., Lai, F.A., Swann, K., and FitzHarris, G. (2016). Ca2+ dynamics in oocytes from naturally-aged mice. Scientific Reports *6*, 19357.

Hazel, J.W., and Gatlin, J.C. (2018). Isolation and Demembranation of Xenopus Sperm Nuclei. Cold Spring Harb Protoc *2018*.

Heald, R., and Khodjakov, A. (2015). Thirty years of search and capture: The complex simplicity of mitotic spindle assembly. The Journal of cell biology *211*, 1103-1111.

Heald, R., Tournebize, R., Blank, T., Sandaltzopoulos, R., Becker, P., Hyman, A., and Karsenti, E. (1996). Self-organization of microtubules into bipolar spindles around artificial chromosomes in Xenopus egg extracts. Nature *382*, 420-425.

Heald, R., Tournebize, R., Habermann, A., Karsenti, E., and Hyman, A. (1997). Spindle assembly in Xenopus egg extracts: respective roles of centrosomes and microtubule self-organization. The Journal of cell biology *138*, 615-628.

Heine, M., Heck, J., Ciuraszkiewicz, A., and Bikbaev, A. (2020). Dynamic compartmentalization of calcium channel signalling in neurons. Neuropharmacology *169*, 107556.

Helassa, N., Nugues, C., Rajamanoharan, D., Burgoyne, R.D., and Haynes, L.P. (2019). A centrosome-localized calcium signal is essential for mammalian cell mitosis. FASEB journal : official publication of the Federation of American Societies for Experimental Biology *33*, 14602-14610.

Helmke, K.J., and Heald, R. (2014). TPX2 levels modulate meiotic spindle size and architecture in Xenopus egg extracts. The Journal of cell biology *206*, 385-393.

Henne, W.M., Stenmark, H., and Emr, S.D. (2013). Molecular mechanisms of the membrane sculpting ESCRT pathway. Cold Spring Harb Perspect Biol *5*.

Hirota, J., Michikawa, T., Natsume, T., Furuichi, T., and Mikoshiba, K. (1999). Calmodulin inhibits inositol 1,4,5-trisphosphate-induced calcium release through the purified and reconstituted inositol 1,4,5-trisphosphate receptor type 1. FEBS Lett *456*, 322-326.

Hogan, P.G. (2015). The STIM1-ORAI1 microdomain. Cell Calcium *58*, 357-367.

Hogan, P.G., Lewis, R.S., and Rao, A. (2010). Molecular basis of calcium signaling in lymphocytes: STIM and ORAI. Annu Rev Immunol *28*, 491-533.

Hondele, M., and Ladurner, A. (2010). A mitotic beacon reveals its nucleosome anchor. Mol Cell *39*, 829-830.

Hoshino, Y. (2018). Updating the markers for oocyte quality evaluation: intracellular temperature as a new index. Reprod Med Biol *17*, 434-441.

Hu, C.K., Coughlin, M., and Mitchison, T.J. (2012). Midbody assembly and its regulation during cytokinesis. Mol Biol Cell *23*, 1024-1034.

Huang, C.Y., and Ferrell, J.E., Jr. (1996). Dependence of Mos-induced Cdc2 activation on MAP kinase function in a cell-free system. EMBO J *15*, 2169-2173.

Humeau, J., Bravo-San Pedro, J.M., Vitale, I., Nunez, L., Villalobos, C., Kroemer, G., and Senovilla, L. (2018). Calcium signaling and cell cycle: Progression or death. Cell Calcium *70*, 3-15.

Hutchins, J.R., Toyoda, Y., Hegemann, B., Poser, I., Heriche, J.K., Sykora, M.M., Augsburg, M., Hudecz, O., Buschhorn, B.A., Bulkescher, J.*, et al.* (2010). Systematic analysis of human protein complexes identifies chromosome segregation proteins. Science *328*, 593-599.

Hwang, L.H., Lau, L.F., Smith, D.L., Mistrot, C.A., Hardwick, K.G., Hwang, E.S., Amon, A., and Murray, A.W. (1998). Budding yeast Cdc20: a target of the spindle checkpoint. Science *279*, 1041-1044.

Hyman, A.A., Salser, S., Drechsel, D.N., Unwin, N., and Mitchison, T.J. (1992). Role of GTP hydrolysis in microtubule dynamics: information from a slowly hydrolyzable analogue, GMPCPP. Mol Biol Cell *3*, 1155-1167.

Inoue, D., Obino, D., Pineau, J., Farina, F., Gaillard, J., Guerin, C., Blanchoin, L., Lennon-Dumenil, A.M., and Thery, M. (2019). Actin filaments regulate microtubule growth at the centrosome. EMBO J *38*.

Inoue, D., Ohe, M., Kanemori, Y., Nobui, T., and Sagata, N. (2007). A direct link of the Mos-MAPK pathway to Erp1/Emi2 in meiotic arrest of Xenopus laevis eggs. Nature *446*, 1100-1104.

Inouye, S., and Sasaki, S. (2006). Blue fluorescent protein from the calcium-sensitive photoprotein aequorin: catalytic properties for the oxidation of coelenterazine as an oxygenase. FEBS Lett *580*, 1977-1982.

Jessus, C., Munro, C., and Houliston, E. (2020). Managing the Oocyte Meiotic Arrest-Lessons from Frogs and Jellyfish. Cells *9*.

Johnson, I., and Spence, M. (2010). Indicators for Ca2+, Mg2+, Zn2+ and other metal ions. In Molecular Probes Handbook (Thermofisher), pp. 829-882.

Josefsberg Ben-Yehoshua, L., Lewellyn, A.L., Thomas, P., and Maller, J.L. (2007). The role of Xenopus membrane progesterone receptor beta in mediating the effect of progesterone on oocyte maturation. Molecular endocrinology *21*, 664-673.

Kadamur, G., and Ross, E.M. (2013). Mammalian phospholipase C. Annu Rev Physiol *75*, 127-154.

Kahl, C.R., and Means, A.R. (2003). Regulation of cell cycle progression by calcium/calmodulin-dependent pathways. Endocr Rev *24*, 719-736.

Kalab, P., and Heald, R. (2008). The RanGTP gradient - a GPS for the mitotic spindle. Journal of cell science *121*, 1577-1586.

Kalab, P., Weis, K., and Heald, R. (2002). Visualization of a Ran-GTP gradient in interphase and mitotic Xenopus egg extracts. Science *295*, 2452-2456.

Kapoor, T.M. (2017). Metaphase Spindle Assembly. Biology (Basel) *6*.

Kapoor, T.M., Mayer, T.U., Coughlin, M.L., and Mitchison, T.J. (2000). Probing spindle assembly mechanisms with monastrol, a small molecule inhibitor of the mitotic kinesin, Eg5. The Journal of cell biology *150*, 975-988.

Karabasheva, D., and Smyth, J.T. (2019). A novel, dynein-independent mechanism focuses the endoplasmic reticulum around spindle poles in dividing Drosophila spermatocytes. Sci Rep *9*, 12456.

Karaiskou, A., Jessus, C., Brassac, T., and Ozon, R. (1999). Phosphatase 2A and polo kinase, two antagonistic regulators of cdc25 activation and MPF auto-amplification. Journal of cell science *112 (Pt 21)*, 3747-3756.

Kasri, N.N., Torok, K., Galione, A., Garnham, C., Callewaert, G., Missiaen, L., Parys, J.B., and De Smedt, H. (2006). Endogenously bound calmodulin is essential for the function of the inositol 1,4,5-trisphosphate receptor. The Journal of biological chemistry *281*, 8332-8338.

Keating, T.J., Cork, R.J., and Robinson, K.R. (1994). Intracellular free calcium oscillations in normal and cleavage-blocked embryos and artificially activated eggs of Xenopus laevis. Journal of cell science *107 (Pt 8)*, 2229-2237.

Keith, C.H., Ratan, R., Maxfield, F.R., Bajer, A., and Shelanski, M.L. (1985). Local cytoplasmic calcium gradients in living mitotic cells. Nature *316*, 848-850.

Kelly, A.E., Sampath, S.C., Maniar, T.A., Woo, E.M., Chait, B.T., and Funabiki, H. (2007). Chromosomal enrichment and activation of the aurora B pathway are coupled to spatially regulate spindle assembly. Developmental cell *12*, 31-43.

Kiehart, D.P. (1981). Studies on the in vivo sensitivity of spindle microtubules to calcium ions and evidence for a vesicular calcium-sequestering system. The Journal of cell biology *88*, 604-617.

Kim, A.M., Bernhardt, M.L., Kong, B.Y., Ahn, R.W., Vogt, S., Woodruff, T.K., and O'Halloran, T.V. (2011). Zinc sparks are triggered by fertilization and facilitate cell cycle resumption in mammalian eggs. ACS Chem Biol *6*, 716-723.

Kim, S.H., Lin, D.P., Matsumoto, S., Kitazono, A., and Matsumoto, T. (1998). Fission yeast Slp1: an effector of the Mad2-dependent spindle checkpoint. Science *279*, 1045-1047.

Kirschner, M., and Mitchison, T. (1986). Beyond self-assembly: from microtubules to morphogenesis. Cell *45*, 329-342.

Kita, A.M., Swider, Z.T., Erofeev, I., Halloran, M.C., Goryachev, A.B., and Bement, W.M. (2019). Spindle-F-actin interactions in mitotic spindles in an intact vertebrate epithelium. Mol Biol Cell *30*, 1645-1654.

Koley, D., and Bard, A.J. (2010). Triton X-100 concentration effects on membrane permeability of a single HeLa cell by scanning electrochemical microscopy (SECM). Proc Natl Acad Sci U S A *107*, 16783-16787.

Kondratskyi, A., Yassine, M., Kondratska, K., Skryma, R., Slomianny, C., and Prevarskaya, N. (2013). Calcium-permeable ion channels in control of autophagy and cancer. Front Physiol *4*, 272.

Korobchevskaya, K., Lagerholm, B.C., Colin-York, H., and Fritzsche, M. (2017). Exploring the Potential of Airyscan Microscopy for Live Cell Imaging. *4*, 41.

Kosako, H., Gotoh, Y., and Nishida, E. (1994). Requirement for the MAP kinase kinase/MAP kinase cascade in Xenopus oocyte maturation. EMBO J *13*, 2131-2138.

Koshland, D.E., Jr. (2002). Special essay. The seven pillars of life. Science *295*, 2215-2216.

Kotak, S., Busso, C., and Gonczy, P. (2014). NuMA interacts with phosphoinositides and links the mitotic spindle with the plasma membrane. EMBO J *33*, 1815-1830.

Kovac, J.R., Pastuszak, A.W., and Lamb, D.J. (2013). The use of genomics, proteomics, and metabolomics in identifying biomarkers of male infertility. Fertil Steril *99*, 998-1007.

Krenn, V., and Musacchio, A. (2015). The Aurora B Kinase in Chromosome Bi-Orientation and Spindle Checkpoint Signaling. Front Oncol *5*, 225.

Kudo, N.R., Wassmann, K., Anger, M., Schuh, M., Wirth, K.G., Xu, H., Helmhart, W., Kudo, H., McKay, M., Maro, B.*, et al.* (2006). Resolution of chiasmata in oocytes requires separase-mediated proteolysis. Cell *126*, 135-146.

Kume, S., Muto, A., Aruga, J., Nakagawa, T., Michikawa, T., Furuichi, T., Nakade, S., Okano, H., and Mikoshiba, K. (1993). The Xenopus IP3 receptor: structure, function, and localization in oocytes and eggs. Cell *73*, 555-570.

Lan, W., Zhang, X., Kline-Smith, S.L., Rosasco, S.E., Barrett-Wilt, G.A., Shabanowitz, J., Hunt, D.F., Walczak, C.E., and Stukenberg, P.T. (2004). Aurora B phosphorylates centromeric MCAK and regulates its localization and microtubule depolymerization activity. Current biology : CB *14*, 273-286.

Lane, S., and Kauppi, L. (2019). Meiotic spindle assembly checkpoint and aneuploidy in males versus females. Cell Mol Life Sci *76*, 1135-1150.

Leblanc, J. (2014). Calcium Signaling during Polar Body Emission in the Xenopus laevis Oocyte. In Department of Biochemistry, Microbiology, and Immunology (University of Ottawa), pp. 144.

Leblanc, J., Zhang, X., McKee, D., Wang, Z.B., Li, R., Ma, C., Sun, Q.Y., and Liu, X.J. (2011). The small GTPase Cdc42 promotes membrane protrusion during polar body emission via ARP2-nucleated actin polymerization. Molecular human reproduction *17*, 305-316.

Lee, C., Ferguson, M., and Chen, L.B. (1989). Construction of the endoplasmic reticulum. The Journal of cell biology *109*, 2045-2055.

Lee, K.Y., Davies, T., and Mishima, M. (2012). Cytokinesis microtubule organisers at a glance. Journal of cell science *125*, 3495-3500.

Li, R., Leblanc, J., He, K., and Liu, X.J. (2016). Spindle function in Xenopus oocytes involves possible nanodomain calcium signaling. Mol Biol Cell *27*, 3273-3283.

Li, W.M., Webb, S.E., Chan, C.M., and Miller, A.L. (2008). Multiple roles of the furrow deepening Ca2+ transient during cytokinesis in zebrafish embryos. Dev Biol *316*, 228-248.

Lin-Moshier, Y., and Marchant, J.S. (2013). The Xenopus oocyte: a single-cell model for studying Ca2+ signaling. Cold Spring Harb Protoc *2013*.

Liu, D., Mo, G., Tao, Y., Wang, H., and Liu, X.J. (2017). Putrescine supplementation during in vitro maturation of aged mouse oocytes improves the quality of blastocysts. Reprod Fertil Dev *29*, 1392-1400.

Liu, D., Shao, H., Wang, H., and Liu, X.J. (2014). Meiosis I in Xenopus oocytes is not error-prone despite lacking spindle assembly checkpoint. Cell cycle *13*, 1602-1606.

Liu, J., Grimison, B., and Maller, J.L. (2007). New insight into metaphase arrest by cytostatic factor: from establishment to release. Oncogene *26*, 1286-1289.

Liu, J., and Maller, J.L. (2005). Calcium elevation at fertilization coordinates phosphorylation of XErp1/Emi2 by Plx1 and CaMK II to release metaphase arrest by cytostatic factor. Current biology : CB *15*, 1458-1468.

Liu, S.T., and Zhang, H. (2016). The mitotic checkpoint complex (MCC): looking back and forth after 15 years. AIMS Mol Sci *3*, 597-634.

Liu, X.J. (2012). Polar body emission. Cytoskeleton *69*, 670-685.

Liu, X.J. (2016). Targeting oocyte maturation to improve fertility in older women. Cell and tissue research *363*, 57-68.

Liu, X.S., and Liu, X.J. (2006). Oocyte isolation and enucleation. Methods in molecular biology *322*, 31-41.

Liu, X.S., Ma, C., Hamam, A.W., and Liu, X.J. (2005). Transcription-dependent and transcription-independent functions of the classical progesterone receptor in Xenopus ovaries. Dev Biol *283*, 180-190.

Liu, Z., and Zheng, Y. (2009). A requirement for epsin in mitotic membrane and spindle organization. The Journal of cell biology *186*, 473-480.

Llinas, R., Sugimori, M., and Silver, R.B. (1992). Microdomains of high calcium concentration in a presynaptic terminal. Science *256*, 677-679.

Llinas, R.R. (1984). The Squid Giant Synapse. In Current Topics in Membranes and Transport, A. Kleinzeller, ed. (Academic Press), pp. 519-546.

Lock, J.T., Smith, I.F., and Parker, I. (2019). Spatial-temporal patterning of Ca(2+) signals by the subcellular distribution of IP3 and IP3 receptors. Seminars in cell & developmental biology.

Lu, L., Ladinsky, M.S., and Kirchhausen, T. (2009). Cisternal organization of the endoplasmic reticulum during mitosis. Mol Biol Cell *20*, 3471-3480.

Luo, C., Wang, H., Liu, Q., He, W., Yuan, L., and Xu, P. (2019). A genetically encoded ratiometric calcium sensor enables quantitative measurement of the local calcium microdomain in the endoplasmic reticulum. Biophysics Reports *5*, 31-42.

Luo, X., and Hill, J.A. (2014). Ca(2)(+) in the cleft: fast and fluorescent. Circ Res *115*, 326-328.

Ma, C., Benink, H.A., Cheng, D., Montplaisir, V., Wang, L., Xi, Y., Zheng, P.P., Bement, W.M., and Liu, X.J. (2006). Cdc42 activation couples spindle positioning to first polar body formation in oocyte maturation. Current biology : CB *16*, 214-220.

Ma, C., Cummings, C., and Liu, X.J. (2003). Biphasic activation of Aurora-A kinase during the meiosis I- meiosis II transition in Xenopus oocytes. Molecular and cellular biology *23*, 1703-1716.

Maaroufi, H. (2020). SARS-CoV-2 Encodes a PPxY Late Domain Motif that is Known to Enhance Budding and Spread in Enveloped RNA Viruses. bioRxiv, 2020.2004.2020.052217.

Machaca, K., and Haun, S. (2000). Store-operated calcium entry inactivates at the germinal vesicle breakdown stage of Xenopus meiosis. The Journal of biological chemistry *275*, 38710-38715.

Machaca, K., and Haun, S. (2002). Induction of maturation-promoting factor during Xenopus oocyte maturation uncouples Ca(2+) store depletion from store-operated Ca(2+) entry. The Journal of cell biology *156*, 75-85.

Maddox, A.S., Azoury, J., and Dumont, J. (2012). Polar body cytokinesis. Cytoskeleton *69*, 855-868.

Maddox, P., Straight, A., Coughlin, P., Mitchison, T.J., and Salmon, E.D. (2003). Direct observation of microtubule dynamics at kinetochores in Xenopus extract spindles: implications for spindle mechanics. The Journal of cell biology *162*, 377-382.

Madgwick, S., and Jones, K.T. (2007). How eggs arrest at metaphase II: MPF stabilisation plus APC/C inhibition equals Cytostatic Factor. Cell Div *2*, 4.

Magnaghi-Jaulin, L., Eot-Houllier, G., Gallaud, E., and Giet, R. (2019). Aurora A Protein Kinase: To the Centrosome and Beyond. Biomolecules *9*.

Mandato, C.A., and Bement, W.M. (2001). Contraction and polymerization cooperate to assemble and close actomyosin rings around Xenopus oocyte wounds. The Journal of cell biology *154*, 785-797.

Mandato, C.A., and Bement, W.M. (2003). Actomyosin transports microtubules and microtubules control actomyosin recruitment during Xenopus oocyte wound healing. Current biology : CB *13*, 1096-1105.

Manders, E.M.M., Verbeek, F.J., and Aten, J.A. (1993). Measurement of co-localization of objects in dual-colour confocal images. *169*, 375-382.

Maresca, T.J., Groen, A.C., Gatlin, J.C., Ohi, R., Mitchison, T.J., and Salmon, E.D. (2009). Spindle assembly in the absence of a RanGTP gradient requires localized CPC activity. Current biology : CB *19*, 1210-1215.

Maresca, T.J., and Heald, R. (2006). Methods for studying spindle assembly and chromosome condensation in Xenopus egg extracts. Methods in molecular biology *322*, 459-474.

Marin, M. (2012). Calcium signaling in Xenopus oocyte. Adv Exp Med Biol *740*, 1073-1094.

Masui, Y., and Markert, C.L. (1971). Cytoplasmic control of nuclear behavior during meiotic maturation of frog oocytes. J Exp Zool *177*, 129-145.

Matsu-Ura, T., Shirakawa, H., Suzuki, K.G.N., Miyamoto, A., Sugiura, K., Michikawa, T., Kusumi, A., and Mikoshiba, K. (2019). Dual-FRET imaging of IP3 and Ca(2+) revealed Ca(2+)-induced IP3 production maintains long lasting Ca(2+) oscillations in fertilized mouse eggs. Sci Rep *9*, 4829.

McCullough, J., Frost, A., and Sundquist, W.I. (2018). Structures, Functions, and Dynamics of ESCRT-III/Vps4 Membrane Remodeling and Fission Complexes. Annu Rev Cell Dev Biol *34*, 85-109.

McDonald, B., and Martin-Serrano, J. (2009). No strings attached: the ESCRT machinery in viral budding and cytokinesis. Journal of cell science *122*, 2167-2177.

McDougall, A., Hebras, C., Pruliere, G., Burgess, D., Costache, V., Dumollard, R., and Chenevert, J. (2019). Role of midbody remnant in meiosis II creating tethered polar bodies. hal-02115684.

McHugh, T., Zou, J., Volkov, V.A., Bertin, A., Talapatra, S.K., Rappsilber, J., Dogterom, M., and Welburn, J.P.I. (2019). The depolymerase activity of MCAK shows a graded response to Aurora B kinase phosphorylation through allosteric regulation. Journal of cell science *132*.

Mehta, S., and Zhang, J. (2015). Dynamic visualization of calcium-dependent signaling in cellular microdomains. Cell Calcium *58*, 333-341.

Mendez, R., Hake, L.E., Andresson, T., Littlepage, L.E., Ruderman, J.V., and Richter, J.D. (2000). Phosphorylation of CPE binding factor by Eg2 regulates translation of c-mos mRNA. Nature *404*, 302-307.

Merdes, A., Ramyar, K., Vechio, J.D., and Cleveland, D.W. (1996). A complex of NuMA and cytoplasmic dynein is essential for mitotic spindle assembly. Cell *87*, 447-458.

Mierzwa, B., and Gerlich, D.W. (2014). Cytokinetic abscission: molecular mechanisms and temporal control. Developmental cell *31*, 525-538.

Miller, A.L., and Bement, W.M. (2009). Regulation of cytokinesis by Rho GTPase flux. Nat Cell Biol *11*, 71-77.

Miller, J.J., Summers, M.K., Hansen, D.V., Nachury, M.V., Lehman, N.L., Loktev, A., and Jackson, P.K. (2006). Emi1 stably binds and inhibits the anaphase-promoting complex/cyclosome as a pseudosubstrate inhibitor. Genes Dev *20*, 2410-2420.

Mitchison, T.J. (2005). Mechanism and function of poleward flux in Xenopus extract meiotic spindles. Philos Trans R Soc Lond B Biol Sci *360*, 623-629.

Mitchison, T.J., Maddox, P., Gaetz, J., Groen, A., Shirasu, M., Desai, A., Salmon, E.D., and Kapoor, T.M. (2005). Roles of polymerization dynamics, opposed motors, and a tensile element in governing the length of Xenopus extract meiotic spindles. Mol Biol Cell *16*, 3064-3076.

Miyawaki, A., Llopis, J., Heim, R., McCaffery, J.M., Adams, J.A., Ikura, M., and Tsien, R.Y. (1997). Fluorescent indicators for Ca2+ based on green fluorescent proteins and calmodulin. Nature *388*, 882-887.

Mo, G., Li, R., Swider, Z., Tao, Y., Mikoshiba, K., Bement, W.M., and Liu, X.J. (2018). Calcium nanodomains in spindles. bioRxiv, 404715.

Moisoi, N., Erent, M., Whyte, S., Martin, S., and Bayley, P.M. (2002). Calmodulin-containing substructures of the centrosomal matrix released by microtubule perturbation. Journal of cell science *115*, 2367-2379.

Mooney, P., Sulerud, T., Pelletier, J.F., Dilsaver, M.R., Tomschik, M., Geisler, C., and Gatlin, J.C. (2017). Tau-based fluorescent protein fusions to visualize microtubules. Cytoskeleton *74*, 221-232.

Musacchio, A., and Desai, A. (2017). A Molecular View of Kinetochore Assembly and Function. Biology (Basel) *6*.

Muto, A., Kume, S., Inoue, T., Okano, H., and Mikoshiba, K. (1996). Calcium waves along the cleavage furrows in cleavage-stage Xenopus embryos and its inhibition by heparin. The Journal of cell biology *135*, 181-190.

Nader, N., Kulkarni, R.P., Dib, M., and Machaca, K. (2013). How to make a good egg!: The need for remodeling of oocyte Ca(2+) signaling to mediate the egg-to-embryo transition. Cell Calcium *53*, 41-54.

Nagaoka, S.I., Hassold, T.J., and Hunt, P.A. (2012). Human aneuploidy: mechanisms and new insights into an age-old problem. Nat Rev Genet *13*, 493-504.

Nagerl, U.V., Novo, D., Mody, I., and Vergara, J.L. (2000). Binding kinetics of calbindin-D(28k) determined by flash photolysis of caged Ca(2+). Biophysical journal *79*, 3009-3018.

Nakai, J., Ohkura, M., and Imoto, K. (2001). A high signal-to-noise Ca(2+) probe composed of a single green fluorescent protein. Nat Biotechnol *19*, 137-141.

Naraghi, M., and Neher, E. (1997). Linearized buffered Ca2+ diffusion in microdomains and its implications for calculation of [Ca2+] at the mouth of a calcium channel. J Neurosci *17*, 6961-6973.

Nebreda, A.R., Gannon, J.V., and Hunt, T. (1995). Newly synthesized protein(s) must associate with p34cdc2 to activate MAP kinase and MPF during progesterone-induced maturation of Xenopus oocytes. EMBO J *14*, 5597-5607.

Needleman, D.J., Groen, A., Ohi, R., Maresca, T., Mirny, L., and Mitchison, T. (2010). Fast microtubule dynamics in meiotic spindles measured by single molecule imaging: evidence that the spindle environment does not stabilize microtubules. Mol Biol Cell *21*, 323-333.

Neher, E. (1998). Usefulness and limitations of linear approximations to the understanding of Ca++ signals. Cell Calcium *24*, 345-357.

Niclas, J., Allan, V.J., and Vale, R.D. (1996). Cell cycle regulation of dynein association with membranes modulates microtubule-based organelle transport. The Journal of cell biology *133*, 585-593.

Nishiyama, T., Ohsumi, K., and Kishimoto, T. (2007). Phosphorylation of Erp1 by p90rsk is required for cytostatic factor arrest in Xenopus laevis eggs. Nature *446*, 1096-1099.

Nuccitelli, R., Yim, D.L., and Smart, T. (1993). The sperm-induced Ca2+ wave following fertilization of the Xenopus egg requires the production of Ins(1, 4, 5)P3. Dev Biol *158*, 200-212.

Ohkura, H. (2015). Meiosis: an overview of key differences from mitosis. Cold Spring Harb Perspect Biol *7*.

Ohsumi, K., Yamamoto, T.M., and Iwabuchi, M. (2006). Oocyte extracts for the study of meiotic M-M transition. Methods in molecular biology *322*, 445-458.

Oriola, D., Needleman, D.J., and Brugues, J. (2018). The Physics of the Metaphase Spindle. Annu Rev Biophys *47*, 655-673.

Paredes, R.M., Etzler, J.C., Watts, L.T., Zheng, W., and Lechleiter, J.D. (2008). Chemical calcium indicators. Methods *46*, 143-151.

Parker, I., and Smith, I.F. (2010). Recording single-channel activity of inositol trisphosphate receptors in intact cells with a microscope, not a patch clamp. The Journal of general physiology *136*, 119-127.

Parrington, J., Brind, S., De Smedt, H., Gangeswaran, R., Lai, F.A., Wojcikiewicz, R., and Carroll, J. (1998). Expression of inositol 1,4,5-trisphosphate receptors in mouse oocytes and early embryos: the type I isoform is upregulated in oocytes and downregulated after fertilization. Dev Biol *203*, 451-461.

Parry, H., McDougall, A., and Whitaker, M. (2005). Microdomains bounded by endoplasmic reticulum segregate cell cycle calcium transients in syncytial Drosophila embryos. The Journal of cell biology *171*, 47-59.

Parys, J.B., Sernett, S.W., DeLisle, S., Snyder, P.M., Welsh, M.J., and Campbell, K.P. (1992). Isolation, characterization, and localization of the inositol 1,4,5-trisphosphate receptor protein in Xenopus laevis oocytes. The Journal of biological chemistry *267*, 18776-18782.

Peter, M., Castro, A., Lorca, T., Le Peuch, C., Magnaghi-Jaulin, L., Doree, M., and Labbe, J.C. (2001). The APC is dispensable for first meiotic anaphase in Xenopus oocytes. Nat Cell Biol *3*, 83-87.

Peterman, E., Gibieza, P., Schafer, J., Skeberdis, V.A., Kaupinis, A., Valius, M., Heiligenstein, X., Hurbain, I., Raposo, G., and Prekeris, R. (2019). The post-abscission midbody is an intracellular signaling organelle that regulates cell proliferation. Nat Commun *10*, 3181.

Peterman, E., and Prekeris, R. (2019). The postmitotic midbody: Regulating polarity, stemness, and proliferation. Journal of Cell Biology *218*, 3903-3911.

Phengchat, R., Takata, H., Uchiyama, S., and Fukui, K. (2017). Calcium depletion destabilises kinetochore fibres by the removal of CENP-F from the kinetochore. Sci Rep *7*, 7335.

Pinsky, B.A., and Biggins, S. (2005). The spindle checkpoint: tension versus attachment. Trends Cell Biol *15*, 486-493.

Pinyol, R., Scrofani, J., and Vernos, I. (2013). The role of NEDD1 phosphorylation by Aurora A in chromosomal microtubule nucleation and spindle function. Current biology : CB *23*, 143-149.

Plowman, R., Singh, N., Tromer, E.C., Payan, A., Duro, E., Spanos, C., Rappsilber, J., Snel, B., Kops, G., Corbett, K.D.*, et al.* (2019). The molecular basis of monopolin recruitment to the kinetochore. Chromosoma *128*, 331-354.

Poenie, M., Alderton, J., Steinhardt, R., and Tsien, R. (1986). Calcium rises abruptly and briefly throughout the cell at the onset of anaphase. Science *233*, 886-889.

Poirier, C.C., Zheng, Y., and Iglesias, P.A. (2010). Mitotic membrane helps to focus and stabilize the mitotic spindle. Biophysical journal *99*, 3182-3190.

Pollard, T.D. (2017). Nine unanswered questions about cytokinesis. The Journal of cell biology *216*, 3007-3016.

Ponert, J.M., Schwarz, S., Haschemi, R., Muller, J., Potzsch, B., Bendas, G., and Schlesinger, M. (2018). The mechanisms how heparin affects the tumor cell induced VEGF and chemokine release from platelets to attenuate the early metastatic niche formation. PLoS One *13*, e0191303.

Popova, J.S., Greene, A.K., Wang, J., and Rasenick, M.M. (2002). Phosphatidylinositol 4,5-bisphosphate modifies tubulin participation in phospholipase Cbeta1 signaling. J Neurosci *22*, 1668-1678.

Potapova, T., and Gorbsky, G.J. (2017). The Consequences of Chromosome Segregation Errors in Mitosis and Meiosis. Biology (Basel) *6*.

Prosser, S.L., and Pelletier, L. (2017). Mitotic spindle assembly in animal cells: a fine balancing act. Nat Rev Mol Cell Biol *18*, 187-201.

Qu, Y.Q., Gordillo-Martinez, F., Law, B.Y.K., Han, Y., Wu, A., Zeng, W., Lam, W.K., Ho, C., Mok, S.W.F., He, H.Q.*, et al.* (2018). 2-Aminoethoxydiphenylborane sensitizes anti-tumor effect of bortezomib via suppression of calcium-mediated autophagy. Cell Death Dis *9*, 361.

Raman, M., and Martin, K. (2014). One solution for cloning and mutagenesis: In-Fusion® HD Cloning Plus. Nature Methods *11*, iii-v.

Rasar, M.A., and Hammes, S.R. (2006). The physiology of the Xenopus laevis ovary. Methods in molecular biology *322*, 17-30.

Rauh, N.R., Schmidt, A., Bormann, J., Nigg, E.A., and Mayer, T.U. (2005). Calcium triggers exit from meiosis II by targeting the APC/C inhibitor XErp1 for degradation. Nature *437*, 1048-1052.

Reber, S., Over, S., Kronja, I., and Gruss, O.J. (2008). CaM kinase II initiates meiotic spindle depolymerization independently of APC/C activation. The Journal of cell biology *183*, 1007-1017.

Rieder, C.L., and Palazzo, R.E. (1992). Colcemid and the mitotic cycle. Journal of cell science *102 (Pt 3)*, 387-392.

Rios-Cardona, D., Ricardo-Gonzalez, R.R., Chawla, A., and Ferrell, J.E., Jr. (2008). A role for GPRx, a novel GPR3/6/12-related G-protein coupled receptor, in the maintenance of meiotic arrest in Xenopus laevis oocytes. Dev Biol *317*, 380-388.

Robinson, K.R. (1985). Maturation of Xenopus oocytes is not accompanied by electrode-detectable calcium changes. Dev Biol *109*, 504-508.

Rose, T., Goltstein, P.M., Portugues, R., and Griesbeck, O. (2014). Putting a finishing touch on GECIs. Front Mol Neurosci *7*, 88.

Rudiger, S., Nagaiah, C., Warnecke, G., and Shuai, J.W. (2010). Calcium domains around single and clustered IP3 receptors and their modulation by buffers. Biophysical journal *99*, 3-12.

Salic, A., Waters, J.C., and Mitchison, T.J. (2004). Vertebrate shugoshin links sister centromere cohesion and kinetochore microtubule stability in mitosis. Cell *118*, 567-578.

Salo, V.T., Li, S., Vihinen, H., Holtta-Vuori, M., Szkalisity, A., Horvath, P., Belevich, I., Peranen, J., Thiele, C., Somerharju, P.*, et al.* (2019). Seipin Facilitates Triglyceride Flow to Lipid Droplet and Counteracts Droplet Ripening via Endoplasmic Reticulum Contact. Developmental cell *50*, 478-493 e479.

Saoudi, Y., Rousseau, B., Doussiere, J., Charrasse, S., Gauthier-Rouviere, C., Morin, N., Sautet-Laugier, C., Denarier, E., Scaife, R., Mioskowski, C.*, et al.* (2004). Calcium-independent cytoskeleton disassembly induced by BAPTA. Eur J Biochem *271*, 3255-3264.

Satzler, K., Sohl Lf Fau - Bollmann, J.H., Bollmann Jh Fau - Borst, J.G.G., Borst Jg Fau - Frotscher, M., Frotscher M Fau - Sakmann, B., Sakmann B Fau - Lubke, J.H.R., and Lubke, J.H. (2002). Three-dimensional reconstruction of a calyx of Held and its postsynaptic principal neuron in the medial nucleus of the trapezoid body.

Sauer, G., Korner, R., Hanisch, A., Ries, A., Nigg, E.A., and Sillje, H.H. (2005). Proteome analysis of the human mitotic spindle. Mol Cell Proteomics *4*, 35-43.

Sawin, K.E., and Mitchison, T.J. (1991). Poleward microtubule flux mitotic spindles assembled in vitro. The Journal of cell biology *112*, 941-954.

Scheffer, L.L., Sreetama, S.C., Sharma, N., Medikayala, S., Brown, K.J., Defour, A., and Jaiswal, J.K. (2014). Mechanism of Ca(2)(+)-triggered ESCRT assembly and regulation of cell membrane repair. Nat Commun *5*, 5646.

Schermelleh, L., Heintzmann, R., and Leonhardt, H. (2010). A guide to super-resolution fluorescence microscopy. The Journal of cell biology *190*, 165.

Schindelin, J., Arganda-Carreras, I., Frise, E., Kaynig, V., Longair, M., Pietzsch, T., Preibisch, S., Rueden, C., Saalfeld, S., Schmid, B.*, et al.* (2012). Fiji: an open-source platform for biological-image analysis. Nat Methods *9*, 676-682.

Schmidt, A., Rauh, N.R., Nigg, E.A., and Mayer, T.U. (2006). Cytostatic factor: an activity that puts the cell cycle on hold. Journal of cell science *119*, 1213-1218.

Schoborg, T., Zajac, A.L., Fagerstrom, C.J., Guillen, R.X., and Rusan, N.M. (2015). An Asp-CaM complex is required for centrosome-pole cohesion and centrosome inheritance in neural stem cells. The Journal of cell biology *211*, 987-998.

Schuh, M., and Ellenberg, J. (2007). Self-organization of MTOCs replaces centrosome function during acentrosomal spindle assembly in live mouse oocytes. Cell *130*, 484-498.

Schwarz, D.S., and Blower, M.D. (2016). The endoplasmic reticulum: structure, function and response to cellular signaling. Cell Mol Life Sci *73*, 79-94.

Schweizer, N., Pawar, N., Weiss, M., and Maiato, H. (2015). An organelle-exclusion envelope assists mitosis and underlies distinct molecular crowding in the spindle region. The Journal of cell biology *210*, 695-704.

Selway, J., Rigatti, R., Storey, N., Lu, J., Willars, G.B., and Herbert, T.P. (2012). Evidence that Ca2+ within the microdomain of the L-type voltage gated Ca2+ channel activates ERK in MIN6 cells in response to glucagon-like peptide-1. PLoS One *7*, e33004.

Shahriyari, L., and Komarova, N.L. (2013). Symmetric vs. asymmetric stem cell divisions: an adaptation against cancer? PLoS One *8*, e76195.

Shang, W., Lu, F., Sun, T., Xu, J., Li, L.L., Wang, Y., Wang, G., Chen, L., Wang, X., Cannell, M.B.*, et al.* (2014). Imaging Ca2+ nanosparks in heart with a new targeted biosensor. Circ Res *114*, 412-420.

Shao, H., Li, R., Ma, C., Chen, E., and Liu, X.J. (2013). Xenopus oocyte meiosis lacks spindle assembly checkpoint control. The Journal of cell biology *201*, 191-200.

Shao, H., Ma, C., Zhang, X., Li, R., Miller, A.L., Bement, W.M., and Liu, X.J. (2012). Aurora B regulates spindle bipolarity in meiosis in vertebrate oocytes. Cell cycle *11*, 2672-2680.

Sheng, Y., Tiberi, M., Booth, R.A., Ma, C., and Liu, X.J. (2001). Regulation of Xenopus oocyte meiosis arrest by G protein betagamma subunits. Current biology : CB *11*, 405-416.

Sheppard, C.J., Mehta, S.B., and Heintzmann, R. (2013). Superresolution by image scanning microscopy using pixel reassignment. Opt Lett *38*, 2889-2892.

Shibuya, E.K., Morris, J., Rapp, U.R., and Ruderman, J.V. (1996). Activation of the Xenopus oocyte mitogen-activated protein kinase pathway by Mos is independent of Raf. Cell Growth Differ *7*, 235-241.

Shigetomi, E., Kracun, S., and Khakh, B.S. (2010a). Monitoring astrocyte calcium microdomains with improved membrane targeted GCaMP reporters. Neuron Glia Biol *6*, 183-191.

Shigetomi, E., Kracun, S., Sofroniew, M.V., and Khakh, B.S. (2010b). A genetically targeted optical sensor to monitor calcium signals in astrocyte processes. Nat Neurosci *13*, 759-766.

Shimomura, O. (2005). The discovery of aequorin and green fluorescent protein. J Microsc *217*, 1-15.

Shimomura, O., Johnson, F.H., and Saiga, Y. (1962). Extraction, purification and properties of aequorin, a bioluminescent protein from the luminous hydromedusan, Aequorea. J Cell Comp Physiol *59*, 223-239.

Shuai, J., Rose, H.J., and Parker, I. (2006). The number and spatial distribution of IP3 receptors underlying calcium puffs in Xenopus oocytes. Biophysical journal *91*, 4033-4044.

Silver, R.B., Sugimori, M., Lang, E.J., and Llinas, R. (1994). Time-resolved imaging of Ca(2+)-dependent aequorin luminescence of microdomains and QEDs in synaptic preterminals. Biol Bull *187*, 293-299.

Simonetti, G., Bruno, S., Padella, A., Tenti, E., and Martinelli, G. (2019). Aneuploidy: Cancer strength or vulnerability? Int J Cancer *144*, 8-25.

Sive, H.L., Grainger, R.M., and Harland, R.M. (2000). Early Development of Xenopus laevis: A Laboratory Manual, (Cold Spring Harbor, NY: Cold Spring Harbor Laboratory Press).

Skelding, K.A., Rostas, J.A., and Verrills, N.M. (2011). Controlling the cell cycle: the role of calcium/calmodulin-stimulated protein kinases I and II. Cell cycle *10*, 631-639.

Skowyra, M.L., Schlesinger, P.H., Naismith, T.V., and Hanson, P.I. (2018). Triggered recruitment of ESCRT machinery promotes endolysosomal repair. Science *360*.

Sluder, G. (1979). Role of spindle microtubules in the control of cell cycle timing. The Journal of cell biology *80*, 674-691.

Smith, I.F., Wiltgen, S.M., and Parker, I. (2009). Localization of puff sites adjacent to the plasma membrane: functional and spatial characterization of Ca2+ signaling in SH-SY5Y cells utilizing membrane-permeant caged IP3. Cell Calcium *45*, 65-76.

Smyth, J.T., Beg, A.M., Wu, S., Putney, J.W., Jr., and Rusan, N.M. (2012). Phosphoregulation of STIM1 leads to exclusion of the endoplasmic reticulum from the mitotic spindle. Current biology : CB *22*, 1487-1493.

Stanley, E.F. (2016). The Nanophysiology of Fast Transmitter Release. Trends in Neurosciences *39*, 183-197.

Stauffer, T.P., Ahn, S., and Meyer, T. (1998). Receptor-induced transient reduction in plasma membrane PtdIns(4,5)P2 concentration monitored in living cells. Current biology : CB *8*, 343-346.

Stefan, M.I., Edelstein, S.J., and Le Novere, N. (2008). An allosteric model of calmodulin explains differential activation of PP2B and CaMKII. Proc Natl Acad Sci U S A *105*, 10768-10773.

Stith, B.J. (2015). Phospholipase C and D regulation of Src, calcium release and membrane fusion during Xenopus laevis development. Dev Biol *401*, 188-205.

Strothman, C., Farmer, V., Arpag, G., Rodgers, N., Podolski, M., Norris, S., Ohi, R., and Zanic, M. (2019). Microtubule minus-end stability is dictated by the tubulin off-rate. The Journal of cell biology *218*, 2841-2853.

Stumpff, J., Ghule, P.N., Shimamura, A., Stein, J.L., and Greenblatt, M. (2014). Spindle microtubule dysfunction and cancer predisposition. Journal of cellular physiology *229*, 1881-1883.

Subramanian, K., and Meyer, T. (1997). Calcium-induced restructuring of nuclear envelope and endoplasmic reticulum calcium stores. Cell *89*, 963-971.

Sudakin, V., Chan, G.K., and Yen, T.J. (2001). Checkpoint inhibition of the APC/C in HeLa cells is mediated by a complex of BUBR1, BUB3, CDC20, and MAD2. The Journal of cell biology *154*, 925-936.

Sun, L., Chai, Y., Hannigan, R., Bhogaraju, V.K., and Machaca, K. (2007). Zinc regulates the ability of Cdc25C to activate MPF/cdk1. Journal of cellular physiology *213*, 98-104.

Sun, L., Haun, S., Jones, R.C., Edmondson, R.D., and Machaca, K. (2009). Kinase-dependent regulation of inositol 1,4,5-trisphosphate-dependent Ca2+ release during oocyte maturation. The Journal of biological chemistry *284*, 20184-20196.

Sun, L., Hodeify, R., Haun, S., Charlesworth, A., MacNicol, A.M., Ponnappan, S., Ponnappan, U., Prigent, C., and Machaca, K. (2008). Ca2+ homeostasis regulates Xenopus oocyte maturation. Biology of reproduction *78*, 726-735.

Sun, L., and Machaca, K. (2004). Ca(2+)(cyt) negatively regulates the initiation of oocyte maturation. The Journal of cell biology *165*, 63-75.

Sun, L., Yu, F., Ullah, A., Hubrack, S., Daalis, A., Jung, P., and Machaca, K. (2011). Endoplasmic reticulum remodeling tunes IP(3)-dependent Ca(2)+ release sensitivity. PLoS One *6*, e27928.

Sun, Y., Rossi, A.M., Rahman, T., and Taylor, C.W. (2013). Activation of IP3 receptors requires an endogenous 1-8-14 calmodulin-binding motif. Biochem J *449*, 39-49.

Sundberg, H.A., Goetsch, L., Byers, B., and Davis, T.N. (1996). Role of calmodulin and Spc110p interaction in the proper assembly of spindle pole body compenents. The Journal of cell biology *133*, 111-124.

Suzuki, J., Kanemaru, K., and Iino, M. (2016). Genetically Encoded Fluorescent Indicators for Organellar Calcium Imaging. Biophysical journal *111*, 1119-1131.

Swillens, S., Dupont, G., Combettes, L., and Champeil, P. (1999). From calcium blips to calcium puffs: theoretical analysis of the requirements for interchannel communication. Proc Natl Acad Sci U S A *96*, 13750-13755.

Tadross, M.R., Dick, I.E., and Yue, D.T. (2008). Mechanism of local and global Ca2+ sensing by calmodulin in complex with a Ca2+ channel. Cell *133*, 1228-1240.

Tadross, M.R., Tsien, R.W., and Yue, D.T. (2013). Ca2+ channel nanodomains boost local Ca2+ amplitude. Proc Natl Acad Sci U S A *110*, 15794-15799.

Taieb, F.E., Gross, S.D., Lewellyn, A.L., and Maller, J.L. (2001). Activation of the anaphase-promoting complex and degradation of cyclin B is not required for progression from Meiosis I to II in Xenopus oocytes. Current biology : CB *11*, 508-513.

Takenawa, T., and Itoh, T. (2001). Phosphoinositides, key molecules for regulation of actin cytoskeletal organization and membrane traffic from the plasma membrane. Biochimica et biophysica acta *1533*, 190-206.

Tang, J., Lin, Y., Zhang, Z., Tikunova, S., Birnbaumer, L., and Zhu, M.X. (2001). Identification of common binding sites for calmodulin and inositol 1,4,5-trisphosphate

receptors on the carboxyl termini of trp channels. The Journal of biological chemistry *276*, 21303-21310.

Tay, L.H., Dick, I.E., Yang, W., Mank, M., Griesbeck, O., and Yue, D.T. (2012). Nanodomain Ca(2)(+) of Ca(2)(+) channels detected by a tethered genetically encoded Ca(2)(+) sensor. Nat Commun *3*, 778.

Taylor, C.W., and Laude, A.J. (2002). IP3 receptors and their regulation by calmodulin and cytosolic Ca2+. Cell Calcium *32*, 321-334.

Taylor, C.W., and Tovey, S.C. (2010). IP(3) receptors: toward understanding their activation. Cold Spring Harb Perspect Biol *2*, a004010.

Teis, D., Saksena, S., and Emr, S.D. (2008). Ordered assembly of the ESCRT-III complex on endosomes is required to sequester cargo during MVB formation. Developmental cell *15*, 578-589.

Terasaki, M., Chen, L.B., and Fujiwara, K. (1986). Microtubules and the endoplasmic reticulum are highly interdependent structures. The Journal of cell biology *103*, 1557-1568.

Terasaki, M., Runft, L.L., and Hand, A.R. (2001). Changes in organization of the endoplasmic reticulum during Xenopus oocyte maturation and activation. Mol Biol Cell *12*, 1103-1116.

Thillaiappan, N.B., Chavda, A.P., Tovey, S.C., Prole, D.L., and Taylor, C.W. (2017). Ca(2+) signals initiate at immobile IP3 receptors adjacent to ER-plasma membrane junctions. Nat Commun *8*, 1505.

Thoma, M.E., McLain, A.C., Louis, J.F., King, R.B., Trumble, A.C., Sundaram, R., and Buck Louis, G.M. (2013). Prevalence of infertility in the United States as estimated by the current duration approach and a traditional constructed approach. Fertil Steril *99*, 1324-1331 e1321.

Tian, L., Hires, S.A., Mao, T., Huber, D., Chiappe, M.E., Chalasani, S.H., Petreanu, L., Akerboom, J., McKinney, S.A., Schreiter, E.R.*, et al.* (2009). Imaging neural activity in worms, flies and mice with improved GCaMP calcium indicators. Nat Methods *6*, 875-881.

Tombes, R.M., and Borisy, G.G. (1989). Intracellular free calcium and mitosis in mammalian cells: anaphase onset is calcium modulated, but is not triggered by a brief transient. The Journal of cell biology *109*, 627-636.

Torok, K., Wilding, M., Groigno, L., Patel, R., and Whitaker, M. (1998). Imaging the spatial dynamics of calmodulin activation during mitosis. Current biology : CB *8*, 692-699.

Tropini, C., Roth, E.A., Zanic, M., Gardner, M.K., and Howard, J. (2012). Islands containing slowly hydrolyzable GTP analogs promote microtubule rescues. PLoS One *7*, e30103.

Tsien, R.Y. (1999). Monitoring cell calcium. In Calcium as a cellular regulator, E. Carafoli, and C.B. Klee, eds. (New York: Oxford University Press), pp. 28-54.

Turner, D.L., and Weintraub, H. (1994). Expression of achaete-scute homolog 3 in Xenopus embryos converts ectodermal cells to a neural fate. Genes Dev *8*, 1434-1447.

Uchida, A., and Yajima, M. (2018). An optogenetic approach to control protein localization during embryogenesis of the sea urchin. Dev Biol *441*, 19-30.

Ullah, A., Jung, P., Ullah, G., and Machaca, K. (2014). The role of IP3 receptor channel clustering in Ca2+ wave propagation during oocyte maturation. Prog Mol Biol Transl Sci *123*, 83-101.

van de Ven, A.L., Adler-Storthz, K., and Richards-Kortum, R. (2009). Delivery of optical contrast agents using Triton-X100, part 1: reversible permeabilization of live cells for intracellular labeling. J Biomed Opt *14*, 021012.

van der Voet, M., Berends, C.W., Perreault, A., Nguyen-Ngoc, T., Gonczy, P., Vidal, M., Boxem, M., and van den Heuvel, S. (2009). NuMA-related LIN-5, ASPM-1, calmodulin and dynein promote meiotic spindle rotation independently of cortical LIN-5/GPR/Galpha. Nat Cell Biol *11*, 269-277.

Varjabedian, A., Kita, A., and Bement, W. (2018). Living Xenopus oocytes, eggs, and embryos as models for cell division. Methods Cell Biol *144*, 259-285.

Vasquez, R.J., Howell, B., Yvon, A.M., Wadsworth, P., and Cassimeris, L. (1997). Nanomolar concentrations of nocodazole alter microtubule dynamic instability in vivo and in vitro. Mol Biol Cell *8*, 973-985.

Vazquez-Diez, C., Paim, L.M.G., and FitzHarris, G. (2019). Cell-Size-Independent Spindle Checkpoint Failure Underlies Chromosome Segregation Error in Mouse Embryos. Current biology : CB *29*, 865-873 e863.

von Dassow, G., Verbrugghe, K.J., Miller, A.L., Sider, J.R., and Bement, W.M. (2009). Action at a distance during cytokinesis. The Journal of cell biology *187*, 831-845.

Votteler, J., and Sundquist, W.I. (2013). Virus budding and the ESCRT pathway. Cell Host Microbe *14*, 232-241.

Wagner, J., Fall, C.P., Hong, F., Sims, C.E., Allbritton, N.L., Fontanilla, R.A., Moraru, II, Loew, L.M., and Nuccitelli, R. (2004). A wave of IP3 production accompanies the fertilization Ca2+ wave in the egg of the frog, Xenopus laevis: theoretical and experimental support. Cell Calcium *35*, 433-447.

Wagner, J., Li, Y.X., Pearson, J., and Keizer, J. (1998). Simulation of the fertilization Ca2+ wave in Xenopus laevis eggs. Biophysical journal *75*, 2088-2097.

Walczak, C.E., Vernos, I., Mitchison, T.J., Karsenti, E., and Heald, R. (1998). A model for the proposed roles of different microtubule-based motor proteins in establishing spindle bipolarity. Current biology : CB *8*, 903-913.

Wang, J., and Liu, X.J. (2004). Progesterone inhibits protein kinase A (PKA) in Xenopus oocytes: demonstration of endogenous PKA activities using an expressed substrate. Journal of cell science *117*, 5107-5116.

Wang, L.Y., and Augustine, G.J. (2014). Presynaptic nanodomains: a tale of two synapses. Front Cell Neurosci *8*, 455.

Wang, Q., Shui, B., Kotlikoff, M.I., and Sondermann, H. (2008). Structural basis for calcium sensing by GCaMP2. Structure *16*, 1817-1827.

Wang, S., Romano, F.B., Field, C.M., Mitchison, T.J., and Rapoport, T.A. (2013). Multiple mechanisms determine ER network morphology during the cell cycle in Xenopus egg extracts. The Journal of cell biology *203*, 801-814.

Wasserman, W.J., Pinto, L.H., O'Connor, C.M., and Smith, L.D. (1980). Progesterone induces a rapid increase in [Ca2+]in of Xenopus laevis oocytes. Proc Natl Acad Sci U S A *77*, 1534-1536.

Webb, S.E., and Miller, A.L. (2017). Ca(2+) Signalling and Membrane Dynamics During Cytokinesis in Animal Cells. Adv Exp Med Biol *981*, 389-412.

Wehland, J., and Sandoval, I.V. (1983). Cells injected with guanosine 5'-[alpha, beta-methylene]triphosphate, an alpha, beta-nonhydrolyzable analog of GTP, show anomalous patterns of tubulin polymerization affecting cell translocation, intracellular movement, and the organization of Golgi elements. Proc Natl Acad Sci U S A *80*, 1938-1941.

Wei, J.H., Zhang, Z.C., Wynn, R.M., and Seemann, J. (2015). GM130 Regulates Golgi-Derived Spindle Assembly by Activating TPX2 and Capturing Microtubules. Cell *162*, 287-299.

Weisenberg, R.C. (1972). Microtubule formation in vitro in solutions containing low calcium concentrations. Science *177*, 1104-1105.

Weisshart, K. (2014). The Basic Principle of Airyscanning.

Welburn, J.P., Vleugel, M., Liu, D., Yates, J.R., 3rd, Lampson, M.A., Fukagawa, T., and Cheeseman, I.M. (2010). Aurora B phosphorylates spatially distinct targets to differentially regulate the kinetochore-microtubule interface. Mol Cell *38*, 383-392.

Whitaker, M. (2006a). Calcium at fertilization and in early development. Physiol Rev *86*, 25-88.

Whitaker, M. (2006b). Calcium microdomains and cell cycle control. Cell Calcium *40*, 585-592.

Wilding, M., Wright, E.M., Patel, R., Ellis-Davies, G., and Whitaker, M. (1996). Local perinuclear calcium signals associated with mitosis-entry in early sea urchin embryos. The Journal of cell biology *135*, 191-199.

Wolff, J. (2009). Plasma membrane tubulin. Biochimica et biophysica acta *1788*, 1415-1433.

Wu, J., Prole, D.L., Shen, Y., Lin, Z., Gnanasekaran, A., Liu, Y., Chen, L., Zhou, H., Chen, S.R., Usachev, Y.M., *et al.* (2014). Red fluorescent genetically encoded Ca2+ indicators for use in mitochondria and endoplasmic reticulum. Biochem J *464*, 13-22.

Wuhr, M., Freeman, R.M., Jr., Presler, M., Horb, M.E., Peshkin, L., Gygi, S., and Kirschner, M.W. (2014). Deep proteomics of the Xenopus laevis egg using an mRNA-derived reference database. Current biology : CB *24*, 1467-1475.

Xu, N., Luo, K.Q., and Chang, D.C. (2003). Ca2+ signal blockers can inhibit M/A transition in mammalian cells by interfering with the spindle checkpoint. Biochem Biophys Res Commun *306*, 737-745.

Xu, X.L., Ma, W., Zhu, Y.B., Wang, C., Wang, B.Y., An, N., An, L., Liu, Y., Wu, Z.H., and Tian, J.H. (2012). The microtubule-associated protein ASPM regulates spindle assembly and meiotic progression in mouse oocytes. PLoS One *7*, e49303.

Yamagishi, Y., and Abe, H. (2015). Reorganization of actin filaments by ADF/cofilin is involved in formation of microtubule structures during Xenopus oocyte maturation. Mol Biol Cell *26*, 4387-4400.

Yamagishi, Y., and Abe, H. (2018). Actin assembly mediated by a nucleation promoting factor WASH is involved in MTOC-TMA formation during Xenopus oocyte maturation. Cytoskeleton *75*, 131-143.

Yamashita, M., Mita, K., Yoshida, N., and Kondo, T. (2000). Molecular mechanisms of the initiation of oocyte maturation: general and species-specific aspects. Prog Cell Cycle Res *4*, 115-129.

Yang, Y., Liu, N., He, Y., Liu, Y., Ge, L., Zou, L., Song, S., Xiong, W., and Liu, X. (2018). Improved calcium sensor GCaMP-X overcomes the calcium channel perturbations induced by the calmodulin in GCaMP. Nat Commun *9*, 1504.

Yoshikawa, F., Uchiyama, T., Iwasaki, H., Tomomori-Satoh, C., Tanaka, T., Furuichi, T., and Mikoshiba, K. (1999). High efficient expression of the functional ligand binding site of the inositol 1,4,5-triphosphate receptor in Escherichia coli. Biochem Biophys Res Commun *257*, 792-797.

Yu, F., Hubrack, S.Z., Chakraborty, S., Sun, L., Alcantara-Adap, E., Kulkarni, R., Billing, A.M., Graumann, J., Taylor, C.W., and Machaca, K. (2019). Remodeling of ER-plasma membrane contact sites but not STIM1 phosphorylation inhibits Ca(2+) influx in mitosis. Proc Natl Acad Sci U S A *116*, 10392-10401.

Yu, H.Y., and Bement, W.M. (2007). Control of local actin assembly by membrane fusion-dependent compartment mixing. Nat Cell Biol *9*, 149-159.

Zhang, C.H., Wang, Z.B., Quan, S., Huang, X., Tong, J.S., Ma, J.Y., Guo, L., Wei, Y.C., Ouyang, Y.C., Hou, Y.*, et al.* (2011). GM130, a cis-Golgi protein, regulates meiotic spindle assembly and asymmetric division in mouse oocyte. Cell cycle *10*, 1861-1870.

Zhang, S., Mizutani, A., Hisatsune, C., Higo, T., Bannai, H., Nakayama, T., Hattori, M., and Mikoshiba, K. (2003). Protein 4.1N is required for translocation of inositol 1,4,5-trisphosphate receptor type 1 to the basolateral membrane domain in polarized Madin-Darby canine kidney cells. The Journal of biological chemistry *278*, 4048-4056.

Zhang, X., Ma, C., Miller, A.L., Katbi, H.A., Bement, W.M., and Liu, X.J. (2008). Polar body emission requires a RhoA contractile ring and Cdc42-mediated membrane protrusion. Developmental cell *15*, 386-400.

Zhao, Y., Araki, S., Wu, J., Teramoto, T., Chang, Y.F., Nakano, M., Abdelfattah, A.S., Fujiwara, M., Ishihara, T., Nagai, T.*, et al.* (2011). An expanded palette of genetically encoded Ca(2)(+) indicators. Science *333*, 1888-1891.

Zucker, R. (2010). Photorelease techniques for raising or lowering intracellular Ca(2+). Methods Cell Biol *99*, 27-66.

Zweifach, A., and Lewis, R.S. (1995). Rapid inactivation of depletion-activated calcium current (ICRAC) due to local calcium feedback. The Journal of general physiology *105*, 209-226.

Appendix

Homologous chromosome disjunction does not require Ca^{2+} signaling in *Xenopus* oocytes

To avoid ambiguity, we'd like to clarify that the "chromosome disjunction" in the subtitle refers to the cohesin degradation leading to homologous chromosome separation (meiosis I) or sister chromatid separation (meiosis II or mitosis**)**. Some literature uses the same term "chromosome disjunction" to describe a process during which the chromosomes are pulled apart to different daughter cells by spindle microtubules. In the presence of strict spindle assembly checkpoint (SAC) (see **I.1.3.2**), these two events (cohesin degradation and chromosomes being pulled apart) are tightly coupled because cohesin degradation requires proper alignment of spindle microtubules; however, they can be independent events in the absence of SAC control such as in fish/frog oocytes and embryos (Chenevert et al., 2020). As shown by Shao *et al.*, the complete disruption of spindle microtubules by nocodazole inhibits the 1st polar body emission but does not block the homologous chromosome disjunction indicated by the release of homologous chromosomes from cohesin-mediated conjugation at recombinant crossovers (Shao et al., 2013).

In 1998, Groigno and Whitaker reported that Ca^{2+} signaling triggers metaphase-anaphase transition and chromosome disjunction in early sea urchin embryos (Groigno and Whitaker, 1998). Specifically, a global Ca^{2+} transient is detected at the anaphase of the first embryotic cycle; Ca^{2+} chelator (DB-BAPTA) and Ca^{2+} channel inhibitor (heparin) intervention prevent the chromosome segregation manifested by the reduction of spindle pole-to-pole distance and the increase of chromosome areas. The authors suggested that the SAC-associated Ca^{2+} signaling regulates APC/C activation and hence triggers chromosome segregation (Groigno

and Whitaker, 1998). Later in 2003 consistent with the findings in sea urchin embryos, Xu *et al.* reported that in HeLa cells and PtK2 cells (a cell line from the human kidney), BAPTA-AM and heparin inhibit cyclin B degradation and maintain the activity of securin and Mad2 (a molecular component of the mitotic checkpoint complex which is introduced in **I.1.3.2**), thereby blocking the cohesin cleavage and metaphase-anaphase transition (Xu et al., 2003). Interestingly, both studies found that Ca^{2+} signal blockers cause spindle microtubule depolymerization measured by significantly reduced spindle sizes (30%–50%). Recently, Phengchat *et al.* reported that, in HeLa cells and U2OS cells (a cell line originated from human sarcoma), Ca^{2+} depletion destabilizes kinetochore microtubules through disrupting the crucial kinetochore component — centromere protein F (CENP-F). The authors found that BAPTA and its derivatives, but not the other Ca^{2+} signal blockers, interfere with tubulin polymerization. They however concluded that Ca^{2+} depletion has no direct effects on microtubule depolymerization but rather through affecting kinetochore functions to destabilize the spindle (we explained this by nanodomain calcium signaling; the authors have different reasonings which will be soon discussed) (Phengchat et al., 2017). All these studies suggested Ca^{2+} signaling plays a role in chromosome disjunction by turning off the SAC regulation and thereby triggering APC/C activation and cohesin degradation. It is thus interesting to investigate whether a similar mechanism regulates chromosome disjunction during *Xenopus* oocyte maturation.

To examine the possibility that homologous chromosome disjunction requires Ca^{2+} signaling in *Xenopus* oocytes, we performed karyotype analysis at meiosis I and the putative timing of pro-metaphase II (115–145 minutes after GVBD) under different conditions including DB-BAPTA treatment. The karyotyping technique for *Xenopus* oocytes was

developed in our laboratory as reported before (Shao et al., 2013). Briefly, the oocytes were first incubated with cytochalasin B for 5–10 minutes to remove the spindle microtubules. And then a small portion of the oocyte cytoplasm containing chromosomes (a.k.a. the "mini cell") was excised by a pair of fine forceps. Obtaining the mini cell is the key step for applying the conventional method of chromosome spreading. Thereafter, the mini cell was transferred onto a glass slide pre-wet with the fixative solution and stained with anti-Aurora-B antibodies (as the centromere marker) and Sytox orange (as the DNA marker; Invitrogen, S11368). The chromosomes were spread out naturally overnight in a humid environment (Shao et al., 2013).

Figure S1 exhibits the representative results of oocyte karyotyping. The left image shows the bivalents (conjugated pairs of homologous chromosomes) from metaphase I oocyte; chromosome recombination and two pairs of sister centromeres [31] can be identified in individual bivalents (an example is shown in the dashed shape). The middle image, karyotyping for an unperturbed metaphase II oocyte, exhibits no bivalents but dyads (pairs of sister chromatids); no crossovers can be found and only one pair of sister centromeres can be identified in individual dyads (an example is shown in the dashed shape). The karyotyping on the right is from a metaphase II oocyte that was injected with DB-BAPTA during metaphase I. Although that the chromosomes are relaxed and convoluted obscures the recognition of bivalents or dyads, multiple isolated sister centromeres that are distant from any other sister centromeres can be identified (indicated by distant Aurora B foci, shown by arrows and the inset), suggesting that DB-BAPTA injection, or the blockage of Ca^{2+} signaling, does not prevent the homologous chromosome separation from crossovers which is preceded by

[31] Sister centromeres are a pair of centromeres located at the sister chromatids that are wrapped by cohesin.

cohesin degradation. This result is consistent with the aforementioned report that nocodazole-mediated microtubule disruption does not prevent the bivalent-to-dyad transition; *Xenopus* oocytes lack the SAC control (Shao et al., 2013). We therefore conclude that homologous chromosome disjunction does not require Ca^{2+} signaling in *Xenopus* oocytes.

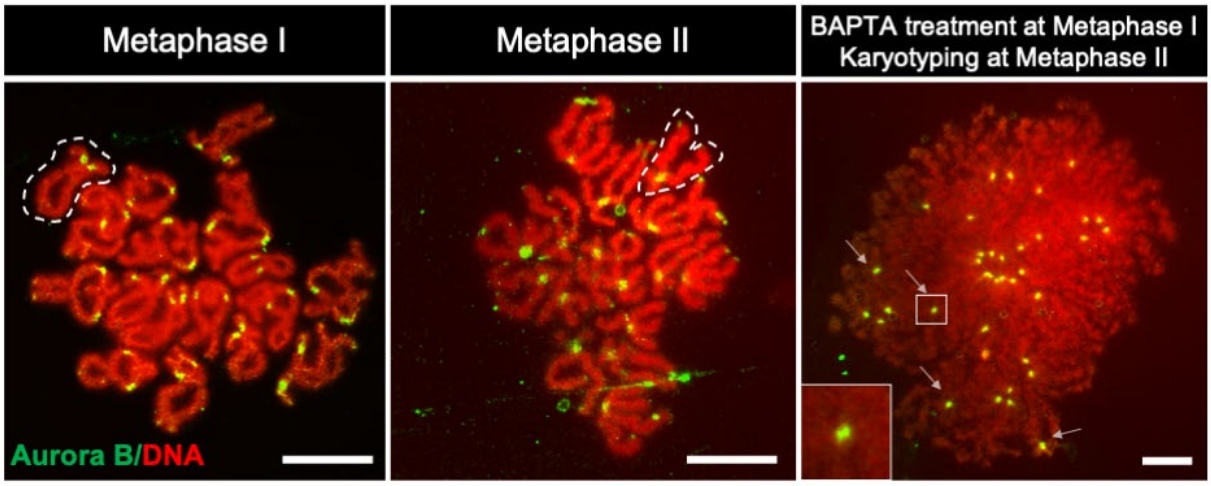

Figure S1 Karyotyping *Xenopus* oocytes after DB-BAPTA treatment
Representative images show *Xenopus* karyotyping under different conditions. DNA is labeled with Sytox orange while centromeres are indicated by Aurora B immunofluorescence. Scale bar = 10 μm.
Left shows the chromosome spread from metaphase I oocyte in which only bivalents can be identified. Each bivalent has clear crossovers indicating homologous recombination. The dumbbell-shaped Aurora B signal (inspected by zooming in the scope) indicates a pair of sister centromeres; each bivalent has two pairs of sister centromeres. A typical example is given inside the dashed shape.
Middle shows the chromosome spread from a metaphase II oocyte in which only dyads can be identified. Each dyad has only one pair of sister centromeres. The absence of crossovers also suggests that the homologous chromosomes have been separated. A typical example is given inside the dashed shape.
Right shows the chromosome spread from a metaphase II oocyte which was injected with DB-BAPTA during metaphase I. The chromosomes are more relaxed compared to those from the control oocyte (the middle image). Multiple isolated sister centromeres (inset and arrows) that are distant from any other centromeres can be identified, suggesting a successful separation of homologous chromosomes. This result further suggests the disjunction of homologous chromosomes in *Xenopus* oocytes does not require Ca^{2+} signaling.
Courtesy of Ms. Ruizhen Li for performing the experiments and providing the images.

Is the absence of the Ca^{2+}-dependent regulation of chromosome disjunction *Xenopus* oocyte-specific? Probably not. It is now widely believed that the SAC is relaxed or even absent in most animal oocytes and early embryos (Chenevert et al., 2020; Gerhold et al., 2018; Lane and Kauppi, 2019; Vazquez-Diez et al., 2019). Moreover, studies in early mouse embryos suggested that the transition from meiotic spindle assembly to mitotic spindle assembly is gradual; early embryos still rely on meiosis-like pathways to assemble and regulate spindles like those in oocytes (see **I.1.2.3,** for example, centrosome-independent spindle assembly) (Courtois et al., 2012). In hindsight, the failure of chromosome separation into two daughter cells by blocking anaphase Ca^{2+} signals in sea urchin embryos (1-cell stage or zygote) does not necessarily suggest a correlation between Ca^{2+} signaling and the SAC deactivation (Groigno and Whitaker, 1998). In our opinion, cohesin degradation in sea urchin embryos might still occur following Ca^{2+} signal blockage; karyotype analysis should be performed to determine whether or not Ca^{2+} signaling affects chromosome disjunction through a SAC-dependent mechanism. In somatic cell lines, however, it is likely the correlation between Ca^{2+} signaling and chromosome disjunction does exist, as the authors directly examine the SAC-associated molecules following the inhibition of Ca^{2+} signaling (Phengchat et al., 2017; Xu et al., 2003).

Despite the species/cell-line discrepancy regarding Ca^{2+}'s role in chromosome disjunction, it seems that the requirement of highly restricted Ca^{2+} signaling for spindle assembly is more universal, as all these studies reported the reduction of spindle microtubules by BAPTA intervention (Groigno and Whitaker, 1998; Phengchat et al., 2017; Xu et al., 2003) but not EGTA (Groigno and Whitaker, 1998; Phengchat et al., 2017).

Engagement of PLC-PIP_2-DAG pathway in spindle regulation

Given the regulatory role of IP_3R in spindle assembly, it is interesting to investigate how the action of IP_3R coordinates with the progression of oocyte maturation in *Xenopus* oocytes. The answer may be related to the signaling pathway of secondary messenger IP_3, the ligand of IP_3R (Dickinson et al., 2016). IP_3 is mainly produced by membrane-bound phospholipase C (PLC), a popular target for G-protein-coupled receptors (Kadamur and Ross, 2013). PLC hydrolyzes the membrane-bound phosphatidylinositol 4,5-bisphosphate (PIP_2), releasing IP_3 and diacylglycerol (DAG). Several PLC isoforms have been reported to be associated with egg activation (see **I.1.4.2**), mitotic G_2/M-phase progression (Bertagnolo et al., 2007) and actin/tubulin cytoskeleton organization (Popova et al., 2002; Takenawa and Itoh, 2001), but its role in spindle assembly is less clear. To examine the involvement of PLC in spindle regulation, we incubated oocytes with increasing concentrations of the PLC inhibitor U73122 (Sigma-Aldrich, U6756) and its non-active analogue U73433 (Sigma-Aldrich, U6881) as control. At a concentration of 100 μM, we found that U73122 but not U73433 caused spindle abnormality and inhibition of the 1st polar body emission (**Figure S2A**), suggesting a role of PLC-dependent mechanism in spindle regulation.

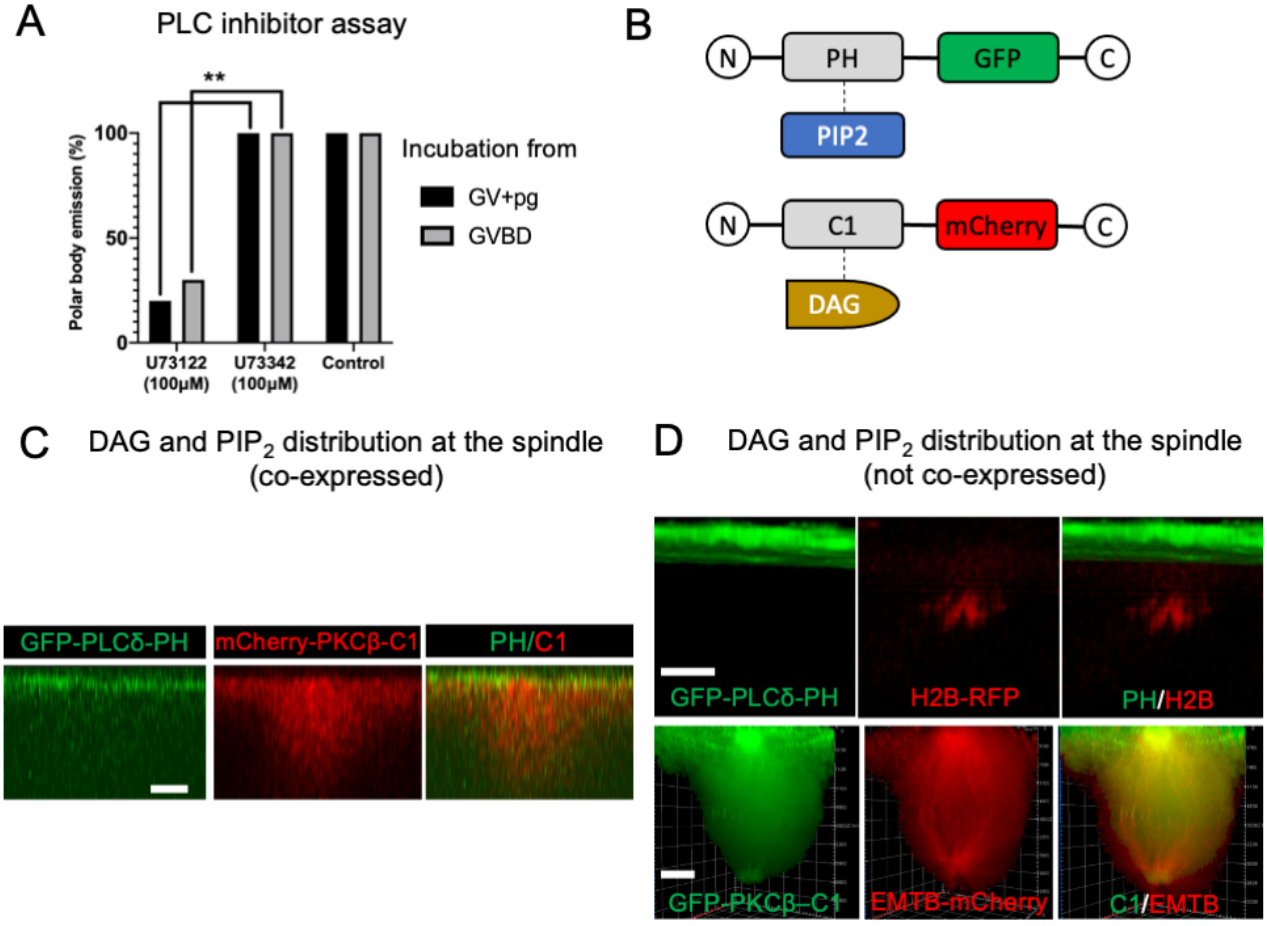

Figure S2 Engagement of PLC-PIP$_2$-DAG pathway in spindle regulation

(A) The PLC inhibitor U73122, rather than its non-active analogue U73342, inhibits polar body emission during *Xenopus* oocyte maturation. The *y*-axis represents the 1st polar body emission rates. GV+pg: Chemicals are applied together with progesterone addition. GVBD: Chemicals are applied from GVBD. n = 10. ** indicates $p < 0.01$.

(B) Schematics show the PIP$_2$ marker GFP-PLCδ-PH (upper) and DAG marker mCherry-PKCβ-C1 (lower).

(C) Live cell imaging (*xz*-plane view) of the spindle in metaphase I oocyte expressing mCherry-PKCβ-C1(DAG) and GFP-PLCδ-PH (PIP$_2$). The distribution of probes indicates that DAG is contained at the spindle region while PIP$_2$ is exclusively at the cortex. Scale bar = 10 μm.

(D) Upper: Live cell imaging (side view) shows PIP$_2$ (GFP-PLCδ-PH) is exclusively at the cortex but not at the spindle (indicated by chromosome marker H2B-RFP). Scale bar = 10 μm. Lower: Live cell imaging (side view) shows DAG (GFP- PKCβ-C1) is expressed throughout the spindle (indicated by microtubule marker EMTB-mCherry). Scale bar = 10 μm.

We next explored the distribution of the key molecules in PLC-mediated PIP_2 metabolism. Following PIP_2 breakdown, hydrophilic IP_3 diffuses into the cytoplasm while DAG that is rich in hydrocarbon chains stays in the membrane (Kadamur and Ross, 2013). A recent study in SH-SY5Y cells (a cell line originated from neuroblastoma) suggested the range of IP_3 action falls in less than 5 μm from its source, due to the hindrance of functionally inactive IP_3R existed in the cytoplasm; hence IP_3 is considered a local signal mediator (Dickinson et al., 2016). It is therefore attempting to speculate a local IP_3 factory positioned right at the spindle or its close neighborhood. However, direct visualization of IP_3 dynamics requires fluorescent resonance energy transfer (FRET)-based techniques and sensitive detecting approaches that are not easily applicable (Matsu-Ura et al., 2019). As an alternative method, we probed *Xenopus* oocytes with the DAG marker mCherry-PKCβ-C1 (C1 domain of PKCβ) and the PIP_2 marker GFP-PLCδ-PH (PH domain of PLCδ)[32] (**Figure S2B**, the schematic of constructs) (Stauffer et al., 1998; Yu and Bement, 2007). Since both molecules are lipophilic, we expected colocalization of DAG and PIP_2 at the membrane-based structure. Surprisingly, DAG was found to be distributed at the whole spindle region while PIP_2 exclusively at the cortex (**Figure S2C**). This observation was further confirmed by expressing the DAG marker and PIP_2 marker separately (**Figure S2D**). Nevertheless, the accumulation of DAG at the spindle suggested the engagement of the PLC-PIP_2-DAG pathway and local production of IP_3 to regulate spindle functions. Furthermore, a report has also shown that DAG is required for Golgi vesicle formation in HeLa cells (Asp et al., 2009); Golgi membrane vesicles are known to promote bipolar spindle assembly through GM130-mediated TPX2 activation (GM130 is a

[32] The plasmids were pCS2-eGFP-C1 and GFP-C1-PLCδ-PH, which were the gifts from William Bement and Tobias Meyer, respectively. GFP-C1-PLCδ-PH was subcloned into pCS2+vectors and made an mCherry variant.

Golgi matrix protein; TPX2 is a spindle assembly factor that has been detailed in **I.1.2.2**) (Guizzunti and Seemann, 2016; Wei et al., 2015), suggesting that DAG serves as a signaling molecule to induce Golgi membrane's action on the spindle assembly. The absence of PIP_2 at the spindle is surprising, given the previous reports showed a clear tubulin-binding specificity of PIP_2 but not the other phospholipids like phosphatidylinositol 3,4,5-trisphosphate, phosphatidylinositol 3-phosphate, phosphatidylinositol, phosphatidylcholine, phosphatidylethanolamine, or IP_3 (Popova et al., 2002); in fact, the protein complex tubulin/PIP2/PLCβ_1 is important in regulating phospholipid metabolism at the plasma membrane (Wolff, 2009). One possible explanation is that there exists a mechanism to actively transport PIP_2 out of the spindle-associated compartment since the *direct binding* of PIP_2 is found to inhibit microtubule assembly (Popova et al., 2002). Intriguingly, research showed that in *Drosophila* oocytes the cortex-exclusive PIP_2 can directly interact with the spindle-associated NuMA, a nuclear protein that serves as a spindle minus-end bundler (introduced in **I.1.2.3**), and thereby helps spindle poles position towards the plasma membrane and stabilizes spindle microtubules (Kotak et al., 2014). Altogether, these studies suggest a complicated relation between PIP_2 and spindle regulation; further investigations, especially loss-of-function studies, are required to elucidate the role of PLC-PIP_2-DAG in regulating spindle organization and its coordination with cell cycle progression.

Vector information of TC1 and TC4

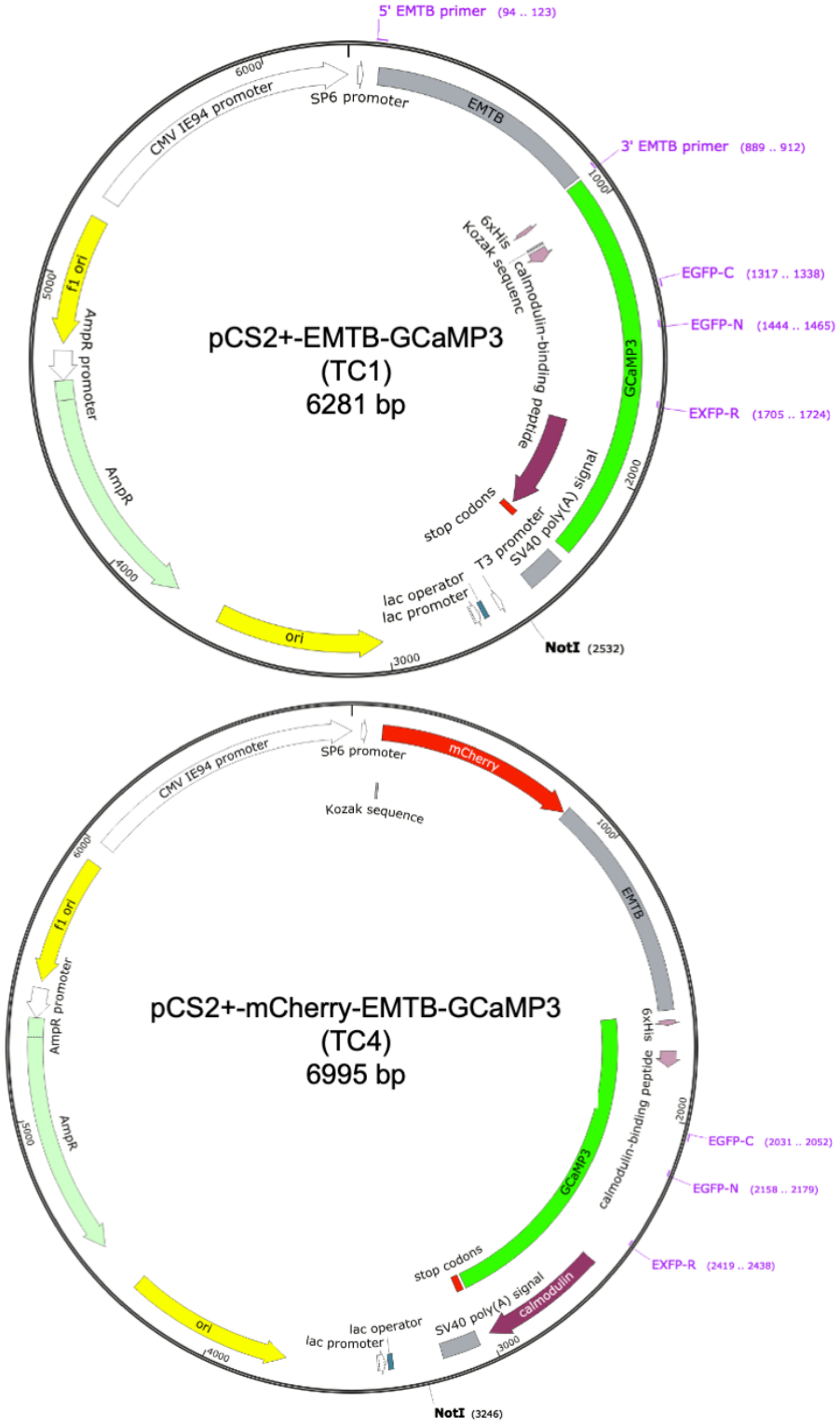

Figure S3 Detailed vector maps of TC1 and TC4

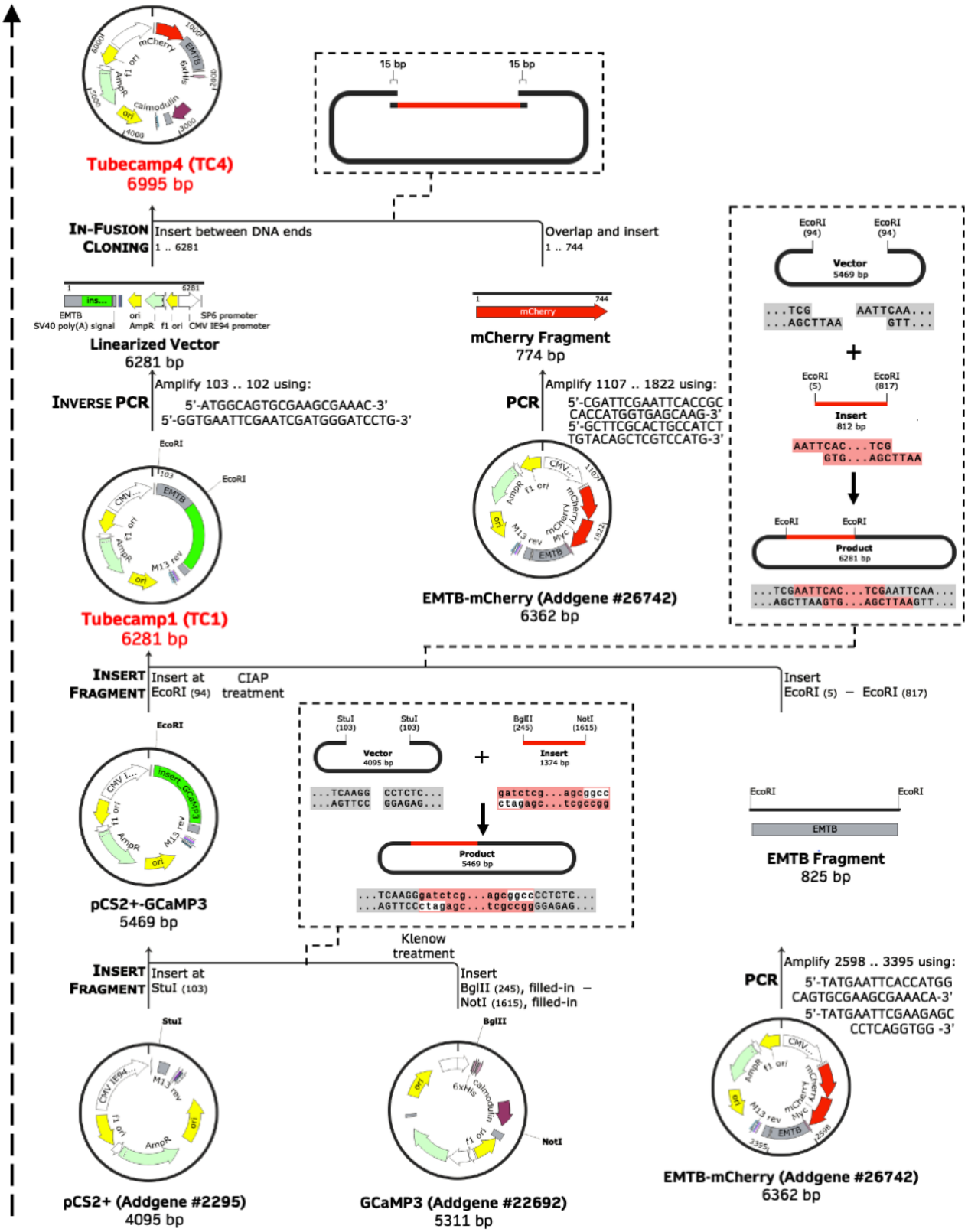

Figure S4 Visualization of the making of TC1 and TC4 in details

Microscopy in results

Table S1 Microscopy in the results

Fig index	Description	Microscope system
3.2	TC1+RGECO or mCherry-EMTB; wound healing	Opterra Swept Field[33]
3.3A	TC1+mCherry-EMTB; oocyte maturation timelapse	MRC-1024[34]
3.3B	TC1+mCherry-EMTB or Rhodamine tubulin; metaphase spindles	LSM880 Airyscan
3.4B	TC1+ H2B-RFP; MII oocyte; prick activation	MRC-1024
3.5A	OG-2+ H2B-RFP; oocyte maturation timelapse	MRC-1024
3.6B	TC1+mCherry-EMTB; STLC-induced monoastral spindle	LSM880 Airyscan
3.7A	TC1+mCherry-EMTB; spindle formation in cell extract	Quorum spinning disk
3.7B	TC1; metaphase spindle in cell extract	LSM880 Airyscan
3.8A	TC1+mCherry-EMTB; cell cycle of HeLa cell	LSM880 Airyscan
3.8B	TC1+mCherry-tubulin; metaphase HeLa cell	Quorum spinning disk
4.1A	BAPTA effect; Extract spindle	MRC-1024
4.1B	BAPTA effect; Monoastral spindle	MRC-1024
4.1C	BAPTA effect; Recovery from colcemid treatment	MRC-1024
4.2A	ER remodeling during extract spindle formation	LSM880 Airyscan
4.2B	ER and extract spindle fate after Triton treatment	MRC-1024
4.3A	GFP-IP_3R1 expression in oocyte extract	Quorum spinning disk
4.3B	IP_3R1 immunofluorescence in oocytes	LSM880 Airyscan
4.3C	OG-2 after IP_3 releasing; metaphase I spindles	MRC-1024
4.4A	Heparin treatment; metaphase I spindles	MRC-1024
4.4B	Heparin treatment; extract spindles	MRC-1024
4.5A	Calmodulin immunofluorescence in oocytes	LSM880 Airyscan
4.5B	GMPCPP protects spindle from BAPTA action	MRC-1024
5.1A	TC4 responding to IP_3 release	MRC-1024
5.2A	TC4 signals during metaphase-anaphase transition	Quorum spinning disk

[33] Opterra Swept Field confocal microscopy is described in Varjabedian *et al.*, 2018.
[34] MRC-1024, Quorum spinning disk and LSM880 Airyscan microscopy are described in **II.4**.

5.3A	OG-2 reports asymmetric $[Ca^{2+}]_i$ rise during polar body emission (3D)	MRC-1024
5.3B	OG-2 reports asymmetric $[Ca^{2+}]_i$ rise during polar body emission	MRC-1024
5.3C	OG-6f reports asymmetric $[Ca^{2+}]_i$ rise during polar body emission	MRC-1024
5.4A	Transient C2 signals at the intercellular bridge (*xy*-plane)	Quorum spinning disk
5.4A'	Transient C2 signals at the intercellular bridge (*xz*-plane)	Quorum spinning disk
S1	Karyotyping *Xenopus* oocytes under different conditions	MRC-1024
S2C	Distribution of DAG and PIP_2 at the spindle	MRC-1024
S2D	Distribution of DAG or PIP_2 at the spindle	LSM880 Airyscan

Contributions of collaborators

1. Dr. X. Johné Liu (My supervisor, University of Ottawa and Ottawa Hospital Research Institute)

   Contributed to the study conception of Chapter **III**, **IV** and **V**. He provided invaluable suggestions to the data interpretation. He also critically commented and edited the thesis.

2. Ms. Ruizhen Li (Liu Lab's technician, Ottawa Hospital Research Institute)

   Contributed to performing the experiments of **Fig III.7A**, **Fig IV.1A**, **Fig IV.1C**, **Fig IV.2B**, **Fig IV.3A** and preparing samples for **Fig IV.3B** and **Fig IV.5A**. She also provided **Fig S1**.

3. Mr. Zackary Swider and Dr. William Bement (University of Wisconsin-Madison)

   Contributed to the construction of TC4. They also provided **Fig III.2**.

4. Dr. Yong Tao (former post-doc of Liu's lab; currently Ottawa Fertility Center)

   Contributed to performing the experiments of **Fig III.8**.

5. Dr. Chloë van Oostende-Triplet (Microscopy specialist, the University of Ottawa)

   Contributed to the imaging of **Fig IV.3B** (upper row).

6. Ms. Terri van Gulik (Administrative assistant, Ottawa Hospital Research Institute)

   Contributed to the proofreading of the thesis.

Curriculum Vitae

Guolong (Sedah) Mo

EDUCATION

- **Doctor of Philosophy** in **Biochemistry.** University of Ottawa, Canada.
- **Master of Science** in **Pharmacology**. China Pharmaceutical University, China.
- **Bachelor of Science** in **Pharmacy**. China Pharmaceutical University, China.

THESIS

- **Ph.D. thesis** (2019) *Calcium nanodomains at spindles*. Advisor: Dr. X. Johné Liu
- **M.Sc. thesis** (2014) *Isoproterenol-induced injury in brain and kidney and drug intervention.* Advisors: Drs. De-zai Dai and Tianhua Yan
- **B.Sc. thesis** (2010) *Study on fermentation conditions and antimicrobial activity of metabolites from marine actinomycete WBF16*. Advisors: Drs. Tao Xi and Yuanyuan Lu

MANUSCRIPT & PREPRINT

- **Mo, G.**, Li, R., Swider, Z., Tao, Y., Mikoshiba, K., Bement, W. and Liu, X.J. (2018) *Calcium nanodomains in spindles*. BioRxiv (preprint). DOI: 10.1101/404715
- **Mo, G.**, Li, R., Leblanc, J., Swider, Z., Bement, W. and Liu, X.J. *Local calcium transients trigger polar body abscission*. In preparation.
- Huang, G.*, **Mo, G.***, Du, T., and Shao, H. *Dissecting the coats of Zebrafish eggs: A proteomic approach*. Submitted. *Co-first authors
- Li, Y., **Mo, G.**, Ortiz, F., Fallahi, M., Bandukwala, H., Liu, X.J. and Dilworth, F.J. *Histone variant H3.3 ensures the activation capability of quiescent satellite cells*. In preparation.

PUBLICATION

- Liu, D.*, **Mo, G.***, Tao, Y., Wang, H. and Liu, X.J. (2017) *Putrescine supplementation during in vitro maturation of aged mouse oocytes improves the quality of blastocysts*. Reprod Fertil Dev. 29, 1392-1400. DOI: 10.1071/RD16061 *Co-first authors
- Tao, Y., Liu, D., **Mo, G.**, Wang, H. and Liu, X.J. (2015) *Peri-ovulatory putrescine supplementation reduces embryo resorption in older mice.* Hum Reprod. 30, 1867-1875. DOI: 10.1093/humrep/dev130
- **Mo, G.**, Li, Y., Du, R., Dai, D., Cong, X. and Dai, Y. (2014) *Isoproterenol induced stressful reactions in the brain are characterized by inflammation due to activation of NADPH oxidase and ER stress: attenuated by apocynin, rehmannia Complex and*

triterpene acids. Neurochem Res. 39, 719-730. DOI: 10.1007/s11064-014-1260-z

- **Mo, G.**, Dai, D., Yan, T. and Dai, Y. (2013) *Novel mechanism and drug targets for Chinese medicine to treat mitochondria disease and aquaporin 4 dysfunction.* Guide of China medicine, 11, 441-443

ORAL PRESENTATION & POSTER

- **Mo, G.** (2017) Oral presentation: *Nanodomain calcium signaling in regulating meiotic spindle functions.* Reproductive group seminar & OHRI WIP seminar.
- **Mo, G.**, Li, R., Liu, X.J. (2016 & 2017) Poster: *Nanodomain calcium signaling in meiotic spindle*. OHRI research day.
- Lavergne, C. L. J., Tao, Y., **Mo, G.**, Liu, X.J. (2017) Poster: *Peri-ovulatory supplementation of L-Ornithine to increase reproductive success in old mice*. OHRI research day.
- **Mo, G.**, Li, R., Liu, X.J. (2016) Poster: *Nanodomain calcium signaling in Xenopus meiotic spindle*. OHRI research day & BMI poster day.
- **Mo, G.** 2016. Oral presentation: *Nanodomain calcium signaling in spindle function*. OHRI WIP seminar.
- Tao, Y., **Mo, G.**, Liu, X.J. (2016) Poster: *Peri-ovulatory putrescine supplementation in aged mice promotes histone deacetylation in the oocytes and improves egg quality*. OHRI research day.
- **Mo, G.** (2015) Oral presentation: *Putrescine supplementation during in vitro maturation of aged mouse oocytes improves the quality of blastocysts.* Reproductive group seminar & BMI seminar day.
- **Mo, G.**, Liu, D., Tao, Y., Wang, H., Liu, X.J. (2015) Poster: *Putrescine supplementation during in vitro maturation of aged mouse oocytes improves the quality of blastocysts.* OHRI research day.

SCHOLARSHIP & AWARDS

- CSC scholarship, China Scholarship Council, 2014-2018.
- Destination 2020 international scholarship, University of Ottawa, 2014-2015.
- Awards for SCI journal publication, China Pharmaceutical University, 2014.
- Scholarship of the project of High-level talents of ethnic minorities. Ministry of Education of China, 2011-2014.
- Admission Scholarship for Key University, China Pacific Insurance Co. Ltd., 2006-2010.
- Outstanding student of China Pharmaceutical University, 2007-2008.
- Outstanding individual of the student association, 2007.